# The Influence of the Intermolecular Synthons on the Molecular Aggregation, Polymorphism, Crystal Growth and Morphology of *p*-Aminobenzoic Acid Crystals from Solution

by

**Ian Rosbottom**

A dissertation submitted in accordance with the requirements for the degree of

Doctor of Philosophy

(Chemical Engineering)

**UNIVERSITY OF LEEDS**

**Institute of Particle Science and Engineering**

**School of Chemical and Process Engineering**

**September 2015**

The candidate confirms that the work submitted is his/her own, except where work which has formed part of jointly authored publications has been included. The contribution of the candidate and the other authors to this work has been explicitly indicated below. The candidate confirms that appropriate credit has been given within the thesis where reference has been made to the work of others.

Ian Rosbottom

**Publications in the Thesis**

**Chapters 5-8 have data that has been published across four publications.**

**Chapter 5: Work included from joint authored publications:**

**Towards an understanding of the nucleation of alpha-*para* amino benzoic acid from ethanolic solutions: a multi-scale approach,** D. Toroz, I. Rosbottom, T. D. Turner, D. M. C. Corzo, R. B. Hammond, X. Lai and K. J. Roberts, *Faraday Discuss.*, 2015,179, 79-114, **DOI:** 10.1039/C4FD00275J

**The solid state, surface and morphological properties of *p*-aminobenzoic acid in terms of the strength and directionality of its intermolecular synthons,** I. Rosbottom, K. J. Roberts and R. Docherty, *CrystEngComm*, 2015, 17, 5768-5788, DOI: 10.1039/C5CE00302D,

**Chapter 6: Work included from joint authored publications:**

**Towards an understanding of the nucleation of alpha-*para* amino benzoic acid from ethanolic solutions: a multi-scale approach,** D. Toroz, I. Rosbottom, T. D. Turner, D. M. C. Corzo, R. B. Hammond, X. Lai and K. J. Roberts, *Faraday Discuss.*, 2015,179, 79-114, **DOI:** 10.1039/C4FD00275J

**Conformational and Structural Stability of Para Amino Benzoic Acid Molecules Expressed in Small Clusters in both the Gas Phase and Continuum Solvent Environment,** D. Toroz, I. Rosbottom, R.B. Hammond and K.J. Roberts, *Crystal Growth and Design, Accepted with Revisions*

**The Stability and Solvation of Pre-Nucleation Clusters of Para Aminobenzoic Acid in relation to its Polymorphic Behaviour**, I. Rosbottom, D. Toroz, R.B, Hammond and K.J. Roberts, *Crystal Growth and Design, Submitted*

**Chapter 7: Work included from joint authored publication:**

**The solid state, surface and morphological properties of *p*-aminobenzoic acid in terms of the strength and directionality of its intermolecular synthons**, I. Rosbottom, K. J. Roberts and R. Docherty, *CrystEngComm*, 2015, 17, 5768-5788, DOI: 10.1039/C5CE00302D

**Chapter 8: Work included from joint authored publication**

**Towards an understanding of the nucleation of alpha-*para* amino benzoic acid from ethanolic solutions: a multi-scale approach**, D. Toroz, I. Rosbottom, T. D. Turner, D. M. C. Corzo, R. B. Hammond, X. Lai and K. J. Roberts, *Faraday Discuss.*, 2015,179, 79-114, **DOI:** 10.1039/C4FD00275J

**My Contribution to Publications**

**Towards an understanding of the nucleation of alpha-*para* amino benzoic acid from ethanolic solutions: a multi-scale approach**, D. Toroz, I. Rosbottom, T. D. Turner, D. M. C. Corzo, R. B. Hammond, X. Lai and K. J. Roberts, *Faraday Discuss.*, 2015,179, 79-114, **DOI:** 10.1039/C4FD00275J

**Sections I contributed to:**

1. Introduction, wrote the majority

2.1. Materials, wrote all

2.2.4 Morphological Prediction and Surface Interface Modelling, wrote all

2.5 Crystal Growth Measurements, wrote all

3.3.1 Stability of Dimers in Ethanol, wrote all

3.3.2 Stability of Tetramers and Octamers in ethanol, wrote all

3.6 Growth Rate Measurements and Morphological and Surface Modelling, wrote all

4. Conclusions, Contributed

**The solid state, surface and morphological properties of *p*-aminobenzoic acid in terms of the strength and directionality of its intermolecular synthons**, I. Rosbottom, K. J. Roberts and R. Docherty, *CrystEngComm*, 2015, 17, 5768-5788, DOI: 10.1039/C5CE00302D

I was the lead author of this paper and the other two author's inputted ideas and offered guidance and corrections during the writing process

**Conformational and Structural Stability of Para Amino Benzoic Acid Molecules Expressed in Small Clusters in both the Gas Phase and Continuum Solvent Environment,** D. Toroz, I. Rosbottom, R.B. Hammond and K.J. Roberts, *Crystal Growth and Design, Accepted with Revisions*

1. Introduction, Contributed

2.1 Solute Molecule selected for Investigation, Contributed

2.3 Comparison of Putative Growth Units for Self-Assembly from Solution using the COSMO Solvation Model, Contributed

3.3 Statistical Thermodynamical Calculations for Growth Units in Solution, Wrote Majority

4. Conclusions, Contributed

**The Stability and Solvation of Pre-Nucleation Clusters of Para Aminobenzoic Acid in relation to its Polymorphic Behaviour**, I. Rosbottom, D. Toroz, R.B, Hammond and K.J. Roberts, *Crystal Growth and Design, In Preparation*

I was the lead author of this paper and the other two author's inputted ideas and offered guidance and corrections during the writing process. D. Toroz carried out the DFT calculations for this paper.

This work is dedicated to the cherished memory of Philip Saravanamuttu, one of the closest and best friends I ever had the privilege of having, you were loved by everyone who knew you. I was proud to carry you to your final resting place. Please watch over the poor souls who must read this thesis!


**Philip Haran Saravanamuttu: 10/05/1989 – 07/09/2012**

## Acknowledgements

I would like to thank Kevin Roberts for his continued drive and enthusiasm for me to achieve the highest standards possible for my research, while still maintaining good humour to make the process enjoyable! I would like to thank everyone who is part of the Crystallisation group at Leeds who has helped me in any small way.

I would like to thank everyone involved in the Critical Mass project at Leeds and Manchester. In particular I would like to thank Dimitrios Toroz for his continued support with his calculations and Joanna Stevens for her advice on NEXAFS spectroscopy. I would like to give a very special thanks to Tom Turner, not only for his excellent research insight that has been very useful during our whiteboard sessions, but also as a close friend who has made our day to day work and many research trips extremely enjoyable.

I would like to thank my family for their continued support of my choice to pursue an academic career and showing enthusiasm for that choice. I would like to thank my parents not only their emotional support, but also their financial support during my undergraduate and at other times which allowed me to succeed in submitting this thesis.

I also recognise the support and advice that has come from the Critical Mass Industrial Advisory Board. In particular, I would like to give a special mention to Bob Docherty who has offered invaluable advice on the molecular modelling work and shown great enthusiasm and positivity about the data I have produced.

I would finally like to thank my friends, partners, housemates and colleagues I have had the pleasure of meeting and spending time with in Leeds, there are too many of you to mention individually! Many of you have kept me company and supported me through the good and bad times during my PhD and made my time during and away from the work genuine pleasure. Many of you I hope to be friends for life. I would also like to leave a special mention for Peter and Daria, along with John and Charlotte, for taking me in when I had nowhere else to stay, I am genuinely grateful to you.

**Abstract**

Intermolecular pairwise interactions (synthons) have previously been used to predict physical properties of molecular crystals, such as polymorphism, morphology and mechanical properties. The overall goal of this research was to correlate the synthon strength and nature found in the crystal structures of the α- and β-forms of 4-aminobenzoic acid to experimentally observed data, assessing their applicability for predicting crystallisation conditions that would produce crystals of desirable physical properties.

The strength and nature of the synthons found in the α-structure were found to significantly vary, while the strength and nature of the synthons in the β-structure were found to be much more similar. These synthons were also found to influence the conformation of the COOH and $NH_2$ groups in both structures.

Water was calculated to favourably bind to the COOH group than ethanol, along with the OH...O H-bonding dimers being calculated to be less stable in aqueous than ethanolic solutions. This suggests that water may hinder the formation of the α form more so than other solvents.

The attachment energy morphological prediction of α-*p*ABA was less needle-like than often observed, probably due to the growth rate of the capping faces growing by a rough interfacial growth mechanism along the long axis of the needle dominated by π-π stacking interactions, being underestimated. Nitromethane (NMe) was calculated to interact more strongly with the phenyl ring than other solvents and hence addition of NMe to ethanolic solutions shortens the long axis of the needle.

The experimentally measured local surface molecular chemisty was found to vary between measurements of the bulk and surface at the (1 0 -1) surface, which is predicted to have unsaturated H-bonds at the surface. Complementing this, spatially resolved measurements across the (1 0 1) surface also showed changes in structure of a supposedly periodic surface.

This study revealed how predicting the strength and nature of the synthons in the bulk structure and at the surface, along with their interaction with solvent molecules and stability in solution, can influence the morphology and polymorphism of the crystals produced from solution.

## Contents

## Table of Figures

## Table of Tables

## Table of Equations

# List of symbols

## Chapter 2

$\Delta H_f$ = enthalpy of fusion

$T_f$ = melting point of the solid solute

$R$ = gas constant

$\Delta S_f$ = molal entropy of fusion

$\mu$ = Chemical potential of a molecule in equilibrium saturated solution

$\mu^*$= Chemical potential of a molecule in a supersaturated solution

$a$ = Solution activity at equilibrium saturation

$a^*$ = Solution activity at supersaturation

γ = activity coefficient at equilibrium saturation

$\gamma^*$ = activity coefficient at supersaturation

$\Delta c$ = dimensionless concentration difference

$c$ = concentration at equilibrium saturation

$\boldsymbol{c}^*$ = concentration at supersaturation

$s$ = supersaturation ratio

$\sigma$ = absolute supersaturation

$G$ = Gibbs free energy

$X(n)$ = Stationary cluster concentration

$C(n)$ = Equilibrium cluster concentration

$fn$ = attachment frequency of monomers

$gn$ = detachment frequency of monomers

$P(n)$ = probability that an n sized cluster will grow to supernucleus size

$Q(n)$ = probability that an n sized cluster will decay back to a monomer

$J$ = nucleation rate

$v$ = molecular volume of a cluster

$\gamma$ = interfacial tension

$c$ = shape factor

$z$ = Zeldovitch factor

$f^*$ = attachment frequency of building blocks to a nucleus

$C_0$ = concentration of nuclei that exist at equilibrium between the nuclei and supersaturated solution

$a_i$ = surface area of a segment (i)

$\sigma_i$ = screening charge density of segment (i)

$\alpha_{eff}$ = effective contact area between two segments

$p_i(\sigma)$ = σ-profile of component i: probability distribution of screening charge densities for an ensemble of segments of component i

$x_i$ = mole fraction

$p_s(\sigma)$ = σ-profile of a mixture: sum of the σ-profiles of all the components of a system weighted by their mole fraction in the mixture

$\mu_s(\sigma)$ = chemical potential of a surface segment within an ensemble

$\mu_i^S$ = chemical potential of compound i in a system s

$G_i^{c,s}$ = combinatorial free energy of compound i in a system s

$r_i$ = dimensionless molecular volume of compound i

$q_i$ = dimensionless molecular area of compound i

$\bar{r}$ = volume of i

$\bar{q}$ = area of i

$\pi_j^S$ = population of conformers with different states of free energy

$KE$ = kinetic energy of an electron

$m$ = mass of an electron

$V$ = voltage across electrodes

$v$ = velocity of electron on impact

$h$ = Plancks constant

$v_{max}$ = largest frequency of radiation produced

$d$ = d spacing

$\theta$ = angle between incident rays and the surface

$\lambda$ = wavelength of X-ray beam

$\mu(\gamma)$ = absorption cross section of X-rays

$\gamma$ = angle between polarisation vector and the symmetry axis of the molecule

$E$ = electric vector of the polarised synchrotron beam

**Chapter 3**

$k_m$ = coefficient of mass transfer

$A$ = area of crystal

$c$ = actual solute concentration of solution

$c^*$ = equilibrium solute concentration

$D$ = coefficient of diffusion

$\delta$ = thickness of stagnant film

$k_d$ = rate constant associated with diffusion

$k_r$ = rate constant associated with growth unit incorporation

$k_G$ = overall crystal growth coefficient

$L$ = characteristic size of the crystal

$r$ = radius corresponding to the equivalent sphere

$\rho_c$ = crystal density

$M_c$ = mass of crystal

$A_c$ = surface area of whole crystal

$v_{hkl}$ = face-specific growth rate

$A_{hkl}$ = area of the faces on the crystal

α = volume shape factor

β = crystal surface shape factor

$n$ = population density per unit volume

$V$ = total suspension volume of the crystalliser

G = linear growth rate

L = crystal size

$R_{hkl}$ = growth rate of surface (hkl)

$\gamma_i$ = surface energy

$A_i$ = surface area

$q$ = fractional charge on an atom

$R_{ij}$ = distance between atoms i and j

D = dielectric constant

$E_{cr}$ = Lattice energy

$V_{exp}$ = Experimental lattice energy

$\Delta H_{sub}$ = sublimation enthalpy

$\varphi_x$ = energy of a bond within the net

$s$ = spin

$\theta^c$ = dimensionless critical roughening temperature

$T^K$ = critical roughening temperature

$\gamma$ = edge free energy of a step

$E_{sl}$ = slice energy

$E_{att}$ = attachment energy

$\alpha_{hkl}$ = alpha factor of a surface *hkl*

$\Delta H(T)_{diss}$ = enthalpy of melting

$E'_{sl}$ = slice energy calculated with the additive at the centre of the slice

$E'_{att}$ = attachment energy of a growth slice containing an additive onto a pure surface

$E''_{att}$ = attachment energy of a pure growth slice onto a surface containing an additive

H-bond = Hydrogen bond

vdW = van der Waals interaction

kcal = kilocalories

K = Kelvin

**Chapter 4**

$\theta$ and $\Phi$ = spherical polar angles

$\lambda$ = translational magnitude

$x_i, y_i$ and $z_i$ = atomic coordinates of mobile molecule

$x'_i, y'_i$ and $z'_i$ = atomic coordinates of stationary molecule

**List of Abbreviations**

*p*ABA = Para Aminobenzoic Acid

H-bonds = Hydrogen Bonds

vdW = van der Waals

NEXAFS = Near Edge X-ray Absorption Fine Structure

DFT = Density Functional Theory

EPSRC = Engineering and Physical Sciences Research Council

NSLS = National Synchrotron Light Source

EtOH = Ethanol

NMe = Nitromethane

QM = Quantum Mechanics

CNT = Classical Nucleation Theory

TSN = Two-Step Nucleation

COSMO-RS = Conductor Like Screening Model for Real Solvents

PXRD = Powder X-ray diffraction

GRD = Growth Rate Dispersion

BCF = Burton, Carbrera and Frank

B & S = Birth and Spread

RIG = Rough Interfacial Growth

BFDH = Bravais, Friedel, Donnay and Harker

SOS = Solid on Solid model

CAS = Chemical Abstracts Service

PTFE = Polytetrafluoroethylene

LARIAT = Large Area Rapid Imaging Analytical Tool

SEM = Scanning Electron Microscopy

GGA = Generalised Gradient Approximation

PBE = Perdew-Burke-Enzerhof

MP2 = Moller-Perturbation Theory

RESP = Restrained Electrostatic Potential

CSD = Cambridge Structural Database

ACN = Acetonitrile

DMSO = Dimethyl Sulfoxide

EtOAc = Ethyl Acetate

EtOH = Ethanol

MeOH = Methanol

# Chapter 1 Introduction and Project Management

*The research subject background is introduced culminating in the problem, hence the research question to be answered. The research question is then related to the aims and objectives of the study*

## 1.1 Introduction and Background

Crystallisation of organic molecules is a widely used purification process in the pharmaceutical and fine chemicals industry, due to the high purity of the resultant crystalline product. The high degree of molecular recognition and subsequent rejection of impurities makes these compounds highly desirable, especially when considering the strict regulations on the required purity of a pharmaceutical product.

With respect to filtering and product formulation, a batch of highly pure, equidimensional and uniform sized crystals are desired. However, the often anisotropic nature of the crystal structures can result in significantly different surface chemistry at the morphologically important surfaces of a crystal. Since batch crystallisation is often undertaken in a solution environment, the surrounding solvent interactions with the solute and crystal surface can influence polymorphism, size and shape of the resultant crystals.

In crystal engineering, intermolecular interactions are often referred to as 'synthons'. The term was coined with respect to the reterosynthesis of organic molecules for fragments of molecules that are involved in synthesis, i.e. making and breaking covalent bonds[10]. This term has evolved to represent 'building blocks' of a material, especially with respect to crystal engineering. Desiraju referred to supramolecular synthons as common building blocks of crystal structures with respect to the design of solid state structures[11]. In this work, a synthon is used to describe the intermolecular interactions that are found within the crystal structures.

The pioneering work by Hartmann and Bennema established the inter-relationship between the directionality of intermolecular synthons with the growth and morphology of molecular crystals, whereby the synthon strengths are calculated using suitable interatomic forcefields[12]. Following this, a method for deriving the habit of molecular crystals from their internal structure and symmetry was demonstrated by Berkovich-Yellin[13]. Computational methods for the routine prediction of the strength, directivity and dispersive nature of intermolecular interactions, together with their summation for predicting crystal lattice and surface attachment energies for morphological prediction, were developed through the HABIT programme[14] by Roberts and co-workers[15]. In parallel to this, within the crystallographic, solid-state and supra-molecular chemistry

community, the importance of hydrogen bonding interactions and graph theory[16, 17] was recognised, in particular their potential importance for understanding polymorphism[18] and for crystal engineering the design of materials[11]. Alongside this work on crystal shape, the field of crystal structure prediction significantly advanced the sophistication of atomistic forcefields, due to the need for highly accurate calculation of the synthon strength between molecules to predict these crystal structures[19-21]. All of these fields recognise the power of intermolecular synthons with respect to their effect on the physical properties of a molecular crystal, along with their use as a tool for predicting these properties.

Though the synthonic influence on predicting and aiding the design of solid state structures[11, 17,19, 22] and crystal morphology is well established, to the authors knowledge there is no such study that attempts to interlink the sythonic strengths to how they influence the crystallisation process from molecular conformation, aggregation, growth and morphology. Rationalising their influence of the synthons found within the crystal structure over the whole crystallisation process could provide more information as to which synthons strongly influence self-assembly and which may more strongly influence crystal growth. This would be helpful with respect to designing an industrial size crystallisation process.

Though calculating the strength of the synthons present within a crystal structure respect to morphological prediction is routinely carried out, the nature of the face-specific synthons with respect to how the surface grows in often overlooked[7, 9, 23, 24]. In addition, there are relatively few studies on the stability of the synthons in solution with respect to polymorphism, most of which have focussed on H-bonding synthons[25, 26]. Therefore, utilising the synthonic information from the crystal structures to select, and asses the stability of molecular building blocks in solution and combining this with quantitative information on how solvent molecules prefer to interact with the single molecule, represents a new combined approach to collect information that indicates how a molecule may de-solvate and self-assemble in solution. In addition, assessing whether the same synthons that are important for the self-assembly of a material are also important for growth, along with quantitative information on the solvent binding to the surface would provide a more complete picture of their influence on the crystallisation process from solution. This combination of techniques could be used to

guide the solvent choice for crystallisation that could be repeated over a variety of systems, without the need for high performance computing resources.

Correlating the influence of the synthons over multiple stages of the crystallisation process encourages a multi technique approach shown in Figure 1-1.

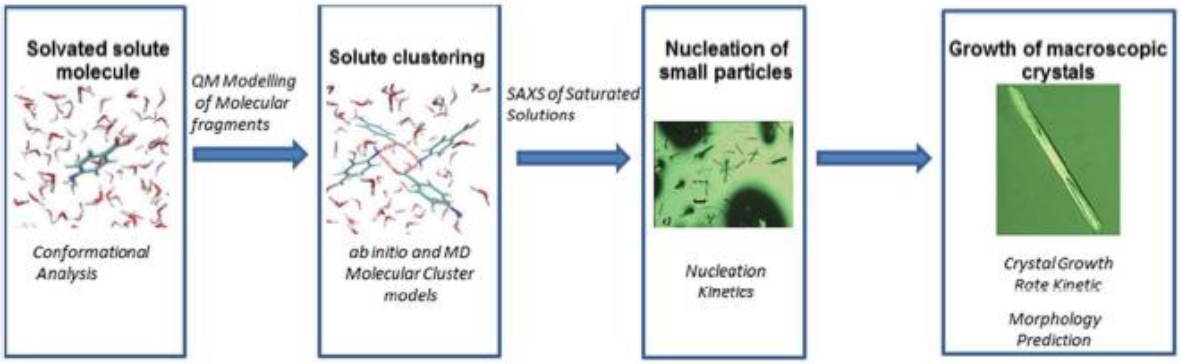


**Figure 1-1: Theoretical pathway of single solvated molecule to macroscopic crystal. Measurements and experiments used to probe each step highlighted on the scheme**

Considering the need to understand the role of the intermolecular synthons over the whole crystallisation process, the influence of the intermolecular synthons on the crystallisation of *p*-aminobenzoic acid (*p*ABA) was investigated by studying how the crystallisation behaviour and morphology of the α and β polymorphs cross-links to the crystal chemistry and molecular building blocks of the crystal structure. This system was chosen for a fundamental study of the crystallisation of organic crystals since it contains hydrogen bonding functional groups that are characteristic of pharmaceutical and fine chemical products, along with the fact that there are two well characterised polymorphs sharing an enantiotropic relationship[27, 28].

## 1.2 Aims

This study will attempt to answer the following question:

**What is the influence of the intermolecular synthons on the molecular aggregation, polymorphism, crystal growth and morphology of *p*ABA crystals from solution?**

This question will be answered through the realisation of the following objectives:

1. Determine the effect of the synthons on molecular conformation

2. Identify the important intermolecular building blocks that influence the molecular aggregation and polymorphism in solution
3. Ascertain the important synthons that influence the face-specific crystal growth and predict the crystal morphology as a function of solvation environment
4. Elucidate the face specific crystal growth mechanisms and relate to the intermolecular interactions at the faces and crystal morphology
5. Compare predicted surface chemistry to experimental surface chemistry and relate to the face specific crystal growth

## 1.3 Delivery Plan

These objectives will be realised through a combined set of computational and experimental activities:

- Calculate the bulk strength of the intermolecular interactions in both polymorphs and through this select likely molecular building blocks for the crystal structures
- Calculate solvation shell of *p*ABA and stability of small clusters in solution
- Predict the morphology based on pair wise intermolecular interactions and elucidate the important intermolecular interactions un saturated at the crystal surfaces
- Elucidate surface molecular geometry through polarisation dependent NEXAFS measurements and compare to molecular models
- Calculate surface binding sights for solute/solvent competition through grid based searching methods and calculate their effect on crystal morphology

## 1.4 Thesis Plan

Successful completion of these objectives should provide data in previously un-studied depth on the influence of intermolecular interactions on the crystal growth process from the early stage clusters to the final surface chemistry of a macroscopic crystal. The flow of work of the thesis is shown is Figure 1-2

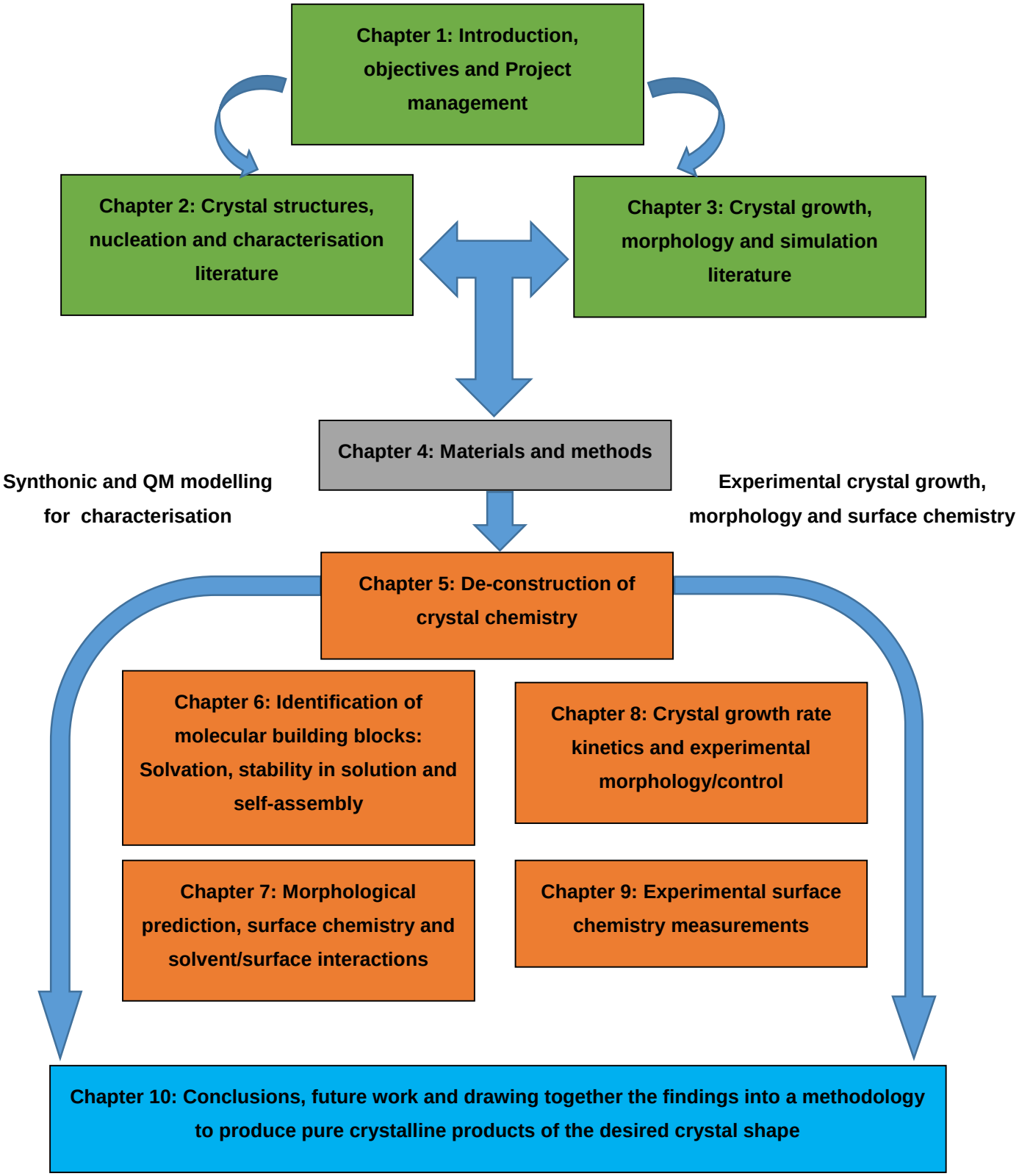


**Figure 1-2: Work flow of the entire study**

## 1.5 Project Management

This study is part of an EPSRC funded joint Critical Mass Project 'Molecules, Clusters to Crystals' with the University of Leeds and University of Manchester. This project is led at the University of Leeds by primary supervisor Professor Kevin Roberts. Dr Xiaojun Lai (co-supervisor) Dr Robert Hammond and Dr Andrew Scott also contributed to this project at the University of Leeds.

Similarly at the team at the University of Manchester is led by Professor Roger Davey and supported by Professor Sven Schroeder. Dr Joanna Stevens has provided valuable advice on the NEXAFS spectroscopic experiments and data analysis.

All synchrotron based experiments (chapter 9) in this study were performed at the National Synchrotron Light Source, Brookhaven National Lab, USA. The work was undertaken on the U7A station and supported by Dr Cherno Jaye and Dr Daniel Fischer.

The modelling of small clusters in continuum solvent conditions would not have been possible without the valuable advice of Professor Andreas Klamt, University of Regensberg, Germany, on the applicability of the COSMO-RS theory for these studies. The optimisations of the small clusters in chapter 6 in Gaussian were performed by Dr Dimitrios Toroz.

Dr Robert Docherty has provided valuable support and advice with regards to morphological prediction and crystal chemistry analysis, particularly with regard to the data presented in chapters 5 and 7.

The crystallisation of *p*ABA from mixed ethanol:nitromethane solvation environments (chapter 8) were performed by Miss Roisin O'Connell, who was a summer project student under my supervision.

# Chapter 2 Crystallography and Crystallisation from Solution

*The key literature associated with the current understanding of crystal structures and the crystallisation process, along with a brief review of key techniques used to characterise structure and crystallisation*

## 2.1 Introduction

Present knowledge of the crystalline state and the crystallisation process from solution is based structural information derived from the early crystallographers, solution kinetics and thermodynamics, along with nucleation and crystal growth theory. Here, the key literature underpinning the crystalline state and crystallisation was reviewed to understand how building blocks of molecules are related to each other to become a crystalline structure, along with how a crystal forms from single molecules in solution. This encompasses the solution phase and saturation along with nucleation theory. The main theory of growth and morphology is covered in chapter 3.

In addition to reviewing the theory of crystal structures and crystallisation, the techniques for characterising crystallisation and understanding solution and nucleation behaviour were also reviewed. Since many of the stages of solution crystallisation occur at the nano-scale, information collected from a variety of techniques can be used to infer information about the crystallisation process. Experimental scattering and spectroscopic techniques can be complimented by multi-scale molecular and crystallographic modelling to rationalise the observations collected.

Understanding crystallisation and the techniques used to understand the process underpins how the data in the thesis was rationalised. Therefore, the important literature related to these processes must be understood.

## 2.2 Crystal Structures

### 2.2.1 Internal crystal structure: Building Blocks, Unit Cells and Lattices

A crystal structure can be defined as 'a regular arrangement of atoms, molecules or ions that repeat infinitely in three dimensions'[29]. The smallest repeating unit (building block) of atoms, molecules or ions is known as the 'asymmetric unit'. Normally, several asymmetric units are related to each other by symmetry to complete the unit cell, which is then repeated infinitely in three dimensions to create a crystal lattice[1].

The unit cell is described by three translational vectors *a, b* and *c*, plus three angles *α, β* and *γ* (Figure 2-1). The asymmetric unit contains *z'* atoms, molecules or ions; and the unit cell contains z asymmetric units.

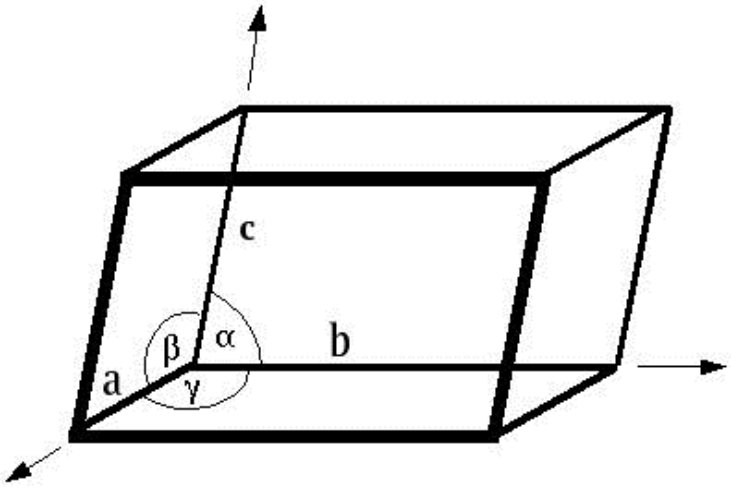


**Figure 2-1: A generalised unit cell showing the lattice vectors and angles that define a unit cell[30]**

There are seven known crystal systems that are shown in Figure 2-2.

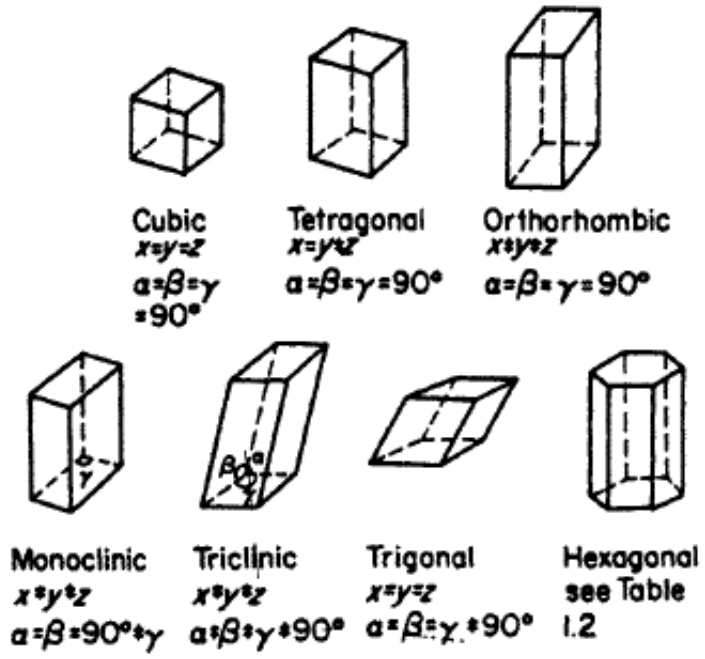


**Figure 2-2: Seven known crystal systems and the unit cell dimensions that define them[1]**

Simple atomic systems are more likely to crystallise in highly symmetric crystal systems, for example sodium chloride crystallises in a cubic lattice. Hence, increasing the complexity of the molecular species in the crystal can result in the molecules crystallising in lower symmetry classes, such as triclinic, monoclinic and orthorhombic. These three systems account for the majority of known molecular crystal structures, such as the ones examined in this study.

### 2.2.2 Lattice Planes and Crystallographic Directions

The planes and crystallographic directions are referenced with respect to the translational vectors of the unit cell *a, b* and *c*. W.H. Miller suggested the concept of Miller indices (*hkl*), defining a planes position as the reciprocal of where the plane intercepts the crystallographic axes (Figure 2-3). The intercepts are defined as A, B and C.

$$h = \frac{a}{X}, \quad k = \frac{b}{Y} \quad \text{and} \quad l = \frac{c}{Z}$$

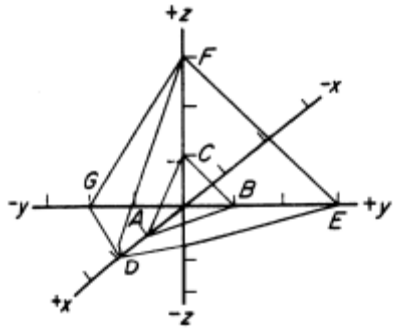


**Figure 2-3: Definition of Miller indices (hkl) and a diagram showing intercepts of planes on the crystallographic axes[1]**

If plane cuts the axis at a distance equal to a full lattice parameter from the origin X, Y or Z then the integer h, k or l is 1. If it cuts the axis at half the lattice parameter then the h, k or l integer is 2 and so on. If the plane is parallel to a crystallographic axis then the intercept is infinity, therefore the Miller index is set to zero. The distance between the planes in a direction is known as the interplanar spacing ($d_{hkl}$) and is shown in Figure 2-4. The interplanar spacing can be calculated from X-ray diffraction data, where it can be a useful measure of the morphological importance of a plane.

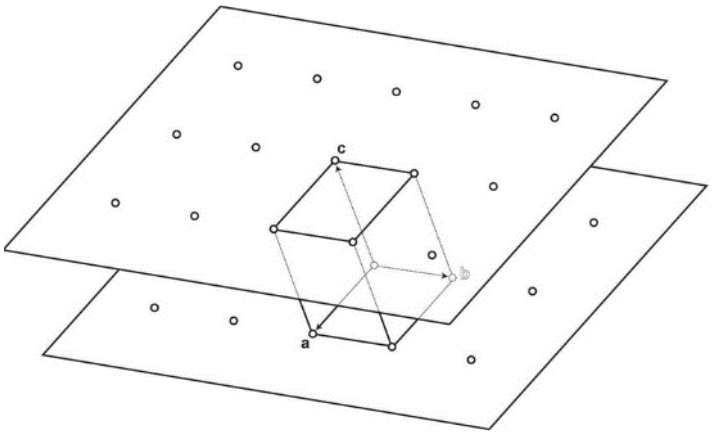


**Figure 2-4: Diagram of interplanar spacing between atoms, ions or molecules in a specific crystallographic direction [hkl][1]**

## 2.3 The Solution State, Solubility and Supersaturation

### 2.3.1 Solubility

The maximum amount of solid that can be dissolved in a solvent to create a homogenous saturated at a given temperature is defined as the 'equilibrium solubility'[31]. In an ideal solution, the solute-solute interactions are the same strength as the solute-solvent interactions and therefore any change in enthalpy can only come from the enthalpy of fusion. In this case, the solubility can be predicted from the Hildebrand equation:

$$\ln x = \frac{\Delta H_f}{R}\left[\frac{1}{T_f}\right] - \left[\frac{1}{T}\right] \quad \textbf{(Equation 2-1)}$$

where $x$ = mole fraction of solute in solution, $\Delta H_f$ = enthalpy of fusion of the solid solute, $T_f$ = melting point of the solid solute, $R$ = gas constant and $T$ = solution temperature. Plotting ln x vs 1/T (Van't Hoff coordinates) should give a straight line because $\Delta H_f = T_f \Delta S_f$ can be written as:

$$ln\, x = \frac{-\Delta H_f}{RT} + \frac{\Delta S_f}{R} \quad \textbf{(Equation 2-2)}$$

where $\Delta S_f$ = molal entropy of fusion. In real systems, the solubility will often vary from ideality. If the measured solubility is greater than ideal, the solute-solvent interactions are stronger than the solute-solute interactions. Conversely, if the solubility is less than ideal then the solute-solvent interactions are weaker than the solute-solute interactions.

### 2.3.2 Supersaturation

It is possible to dissolve more solid in solution than defined by the equilibrium solubility by disturbing the equilibrium, i.e. cooling an unstirred saturated solution below the equilibrium saturation temperature (supercooling) or evaporation of solvent. Once the solution is saturated beyond the equilibrium solubility for a defined temperature, the solution is said to be 'supersaturated'. A solubility curve typically consists of three well defined zones: stable, metastable and labile (Figure 2-5)

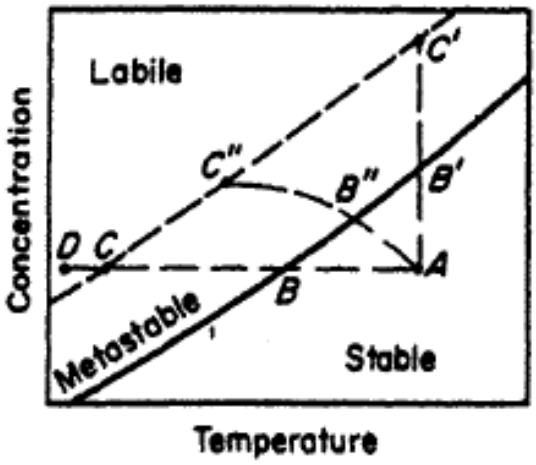


**Figure 2-5: A sample solubility curve of temperature vs concentration of the solution, showing the three main stages of a saturated solution that can be accessed through the supercooling process[1]**

Crystallisation does not occur immediately in the metastable zone due to influences such as kinetic barriers and interfacial tension[32], hence directly affecting how far a solution can be supercooled. The distance between the dissolution temperature and crystallisation temperature of a system is known as the 'metastable zone width' (MSZW). Once the solution enters the labile zone then crystals will nucleate and grow[33].

Thermodynamically, supersaturation (σ) can be thought of as the difference in the chemical potential between a molecule at equilibrium and a molecule in the supersaturated state[33]:

$$\boldsymbol{\sigma = \frac{(\mu - \mu^*)}{RT}}$$ **(Equation 2-3)**

Where $\mu$ and $\mu$* are the chemical potentials of a molecule in a saturated solution and a molecule in a supersaturated solution respectively. The solution activity ($a$) is accounted for in the Gibbs-Dunhelm equation[33]:

$$\boldsymbol{\sigma = ln\left(a/a^*\right)}$$ **(Equation 2-4)**

where $a$ and $a^*$ are the solution activities at equilibrium and supersaturation respectively. Hence, concentration can be included through introducing an activity coefficient γ:

$\boldsymbol{\sigma = ln\left(\gamma c / \gamma^* c^*\right)}$ **(Equation 2-5)**

Often it is difficult to obtain activity coefficients, therefore supersaturation can be viewed as a dimensionless concentration difference Δc:

$\boldsymbol{\Delta c = c - c^*}$ **(Equation 2-6)**

This can also be expressed as the supersaturation ratio (S) and absolute supersaturation (σ):

$\boldsymbol{s = \frac{c}{c^*}}$ **(Equation 2-7)**

$\boldsymbol{\sigma = \frac{\Delta c}{c^*} = s - 1}$ **(Equation 2-8)**

## 2.4 Nucleation

### 2.4.1 Driving Force for Nucleation

The driving force for nucleation can be defined from a general thermodynamic driving force for first order transitions, since it is necessary that the stable solid crystallised occupies a lower free energy state than the metastable solution[34]. The transition can be physically understood as the gain in free energy per molecule going from a metastable solution to a stable crystalline form.

$\boldsymbol{\Delta\mu = \frac{(G_{old} - G_{new})}{M} = \mu_{old} - \mu_{new}}$ **(Equation 2-9)**

The thermodynamic energy gain is offset somewhat by the energy penalty from creation of the resultant interface from a new solid phase existing in solution[35]. This idea is the basis for the concept of critical radius introduced by Volmer[36]. The critical radius can be defined as 'the size of the cluster or nucleus whereby the free energy gain from the internal energy of the cluster is greater than the free energy penalty (surface energy) resulting from the creation of an interface'. Clusters of a greater size than the critical radius should nucleate and grow to a macroscopic crystal.

### 2.4.2 Clusters and Attachment Frequencies

Prior to nucleation, it is thought that molecular clusters form in solution via random attachment and detachment of molecules, whereby clusters of sizes greater than the critical size nucleate and grow and clusters smaller than the critical size dissolve back

into solution[37]. Ter Horst and Kashchiev developed a probability factor for attachment of molecules to a cluster[37], based on White's assumption that the contribution of attaching dimers and trimers etc. is negligible compared to the contribution of monomers[38]. When considering a one component gaseous, liquid or solid phase kept at absolute temperature and supersaturation, where only monomers attach or detach, the stationary and equilibrium cluster size distributions can be given by:

$$\boldsymbol{X(n) = C(n)\left[1 + \sum_{i=2}^{M-1} g2g3 \ldots \frac{gi}{f2f3} \ldots fi\right]^{-1} \times \left[\sum_{i=n}^{M-1} g2g3 \ldots / f2f3 \ldots fi\right]} \text{ (Equation 2-10)}$$
[37]

where $X(n)$ and $C(n)$ are the stationary and equilibrium concentrations of $n$ sized clusters respectively, $fn$ and $gn$ are the attachment and detachment frequencies of monomers from an $n$ sized cluster respectively. A given $n$ sized cluster has a probability $P(n)$ to grow to a supernucleus size $n = M$, conversely it also has a probability $Q(n)$ to decay back to a monomer size. These probabilities are related by:

$$\boldsymbol{P(n) + Q(n) = 1} \text{ (Equation 2-11)}$$

This probability of non-elastic collisions is directly relevant to classical nucleation theory.

### 2.4.3 Classical Nucleation Theory

Since crystal nucleation occurs on the nanoscale, much of the theory around the molecular behaviour in the nucleation transition state has been derived from classical nucleation theory (CNT.) More recently, the observation of dense fluids and disordered clusters prior to the appearance of crystals resulted in the development of two-stage nucleation theory, derived mainly from observations of the behaviour of large protein and inorganic molecules. Much of the underpinning theory behind these schools of thought were comprehensively reviewed by Erdermir et al[39] and Davey, ter Horst and Schroeder in 2013[40].

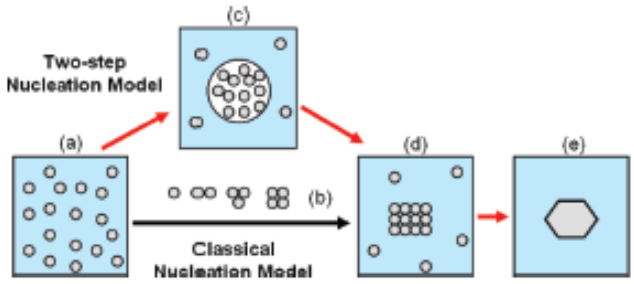


**Figure 2-6: Schematic of the two different proposed pathways from a solution to a crystal proposed by CNT and Two Step Nucleation theory[39]; (a) homogenous solution; (b) clustering process of solute due to solution supersaturation; (c) liquid-like clusters suggested to exist prior to nucleation in two-step nucleation theory; (d) ordered clusters that are structurally analogous to the crystal structure; (e) phase separated macroscopic crystals**

Classical nucleation theory was first postulated by Volmer and Weber[41] and further developed by Becker and Doring[42], Frenkel[43] and Zeldovich[44]. There is a vast body of literature published on refining and testing CNT for various crystalline systems[45]. A major assumption of classical nucleation theory is that clusters formed in solution are of the same structure of the final crystalline material, where the surface energy of a nuclei be the same as the surface energy of a crystalline interface[46]. Though this approximation is probably not true in many cases, valuable data on the crystallisation of a wide variety of materials has been extracted using this method.

CNT is often used to measure the nucleation rates of crystalline particles, *J*, which is defined as the number of crystalline particles that form from a supersaturated solution per unit of volume and time[47]:

$$\boldsymbol{J = A\,\exp\left(-\frac{B}{ln^2 S}\right)} \quad \textbf{(Equation 2-12)}$$

where $S$ is the supersaturation ratio, A and B are constants and the $exp\left(-\frac{B}{ln^2 S}\right) = \frac{W}{kT}$ is considered as the dimensionless energy barrier for nucleation. The utilisation of micro reactor systems, which allow the collection of large amounts of turbidimetric data on a 1ml scale, have led to the development of theories that can derive physical parameters and kinetics from classical nucleation theory using statistical analysis[48, 49].

### 2.4.3.1 Homogenous Nucleation

Homogenous nucleation occurs whereby the clusters of the new phase do not have contact with any other bodies except the old phase. 2.4.1 and 2.4.2 introduced the

idea of a critical nucleus size, which states that for a cluster to undergo a first order phase transition from a liquid phase to a solid crystalline phase, the favourable free energy of cluster formation has to be greater than the energy penalty resulting from the formation of a solid-liquid interface. This can be expressed as Equation 2-13

$\ln x = \frac{\Delta H_f}{R}\ 1 T_{f-\left[\frac{1}{T}\right]}$ (**Equation 2-1**$\Delta G = \frac{4}{3}\pi r^3 \Delta g + 4\pi r^2 \sigma$ (**Equation 2-13**)

This equation assumes a spherical nuclei and the first term is the volume energy of the nucleus. Hence this term is the volume of a sphere multiplied by the difference in free energy per unit volume between the liquid and solid crystalline phase.

Considering a cluster of $n$ building units, the bulk free energy gain of that cluster, depending on supersaturation, is $(-n\Delta\mu)$. The energy penalty can now be described by the 'total interfacial energy', $c(vn)^{2/3}\,\gamma$. This is the surface area of the cluster, where $c$ is a shape factor and $v$ is the molecular volume of the cluster, multiplied by the interfacial tension ($\gamma$). B in Equation 2-14 is the thermodynamic free energy barrier for the formation of a nucleus and is equivalent to:

$B = \frac{4}{27} c^3 v^2 \left(\frac{\gamma}{kT}\right)^3$ (**Equation 2-14**)

The pre-exponential factor, A in equation 2-15, describes the molecular kinetics of the nucleation process. Assuming nucleation is a series of attachments and detachments that form different sized clusters of the nucleating phase (2.4.2), A is expressed as a product of the Zeldovich factor ($z$), the frequency of attachment of building blocks to the nucleus ($f^*$) and the concentration of nuclei that exist at equilibrium between the nuclei and the supersaturated solution such that:

$A = z f^* C_0$ (**Equation 2-15**)

The use of $z$ and $C_0$ accounts for the nuclei that grow to greater than the critical size, but eventually decay due to the effects of Brownian motion.

### 2.4.3.2 Heterogeneous Nucleation

In real solution crystallisation systems, it is often thought that crystals form by heterogeneous nucleation. Heterogeneous nucleation occurs at energetically favourable sites within the system, such as an interface caused by impurities or small

particles in the solution. Therefore, the thermodynamic barrier for nucleation is changed such the interfacial tension is now multiplied by the activity factor.

$$\boldsymbol{B_{HEN} = \frac{4}{27} c^3 v^2 \left(\frac{\gamma_{HEN}}{kT}\right)^3}$$ (**Equation 2-16**)

where $\gamma_{HEN} = \varphi.\gamma$. The foreign bodies that template nucleation have activity factors in the range $0 < \varphi < 1$. Therefore B is reduced, meaning reduced work for nucleation.

### 2.4.4 Two-Step Nucleation

Ten Wolde and Frenkel observed that density fluctuations of the solute in solution, close to the fluid-fluid critical point, have an effect on the route to nucleation[50]. They identified that the formation of dense, liquid like droplets could act as pre cursors for nucleation. This observation resulted in the idea that nucleation can occur by a two-step mechanism, where the formation of ordered liquid-like clusters precedes the nucleation of the stable crystal. To expand, the small angle scattering study of *p*ABA crystallising in supersaturated ethanol solutions by Toroz et al[51] observed increased ordering in solution prior to crystallisation. However, the fractal dimensions of these clusters suggested that there was no well-defined interface between these clusters of more ordered solute, hence the clusters remain similar in nature to the surrounding liquid, i.e. 'liquid-like clusters'. In this theory, it is supposed that the density fluctuation precedes the structural fluctuation[52], rather than both parameters being implicitly assumed to vary simultaneously.

Another important characteristic of two-step nucleation is that it is proposed that crystals nucleate within the metastable precursor phase (Figure 2-7).

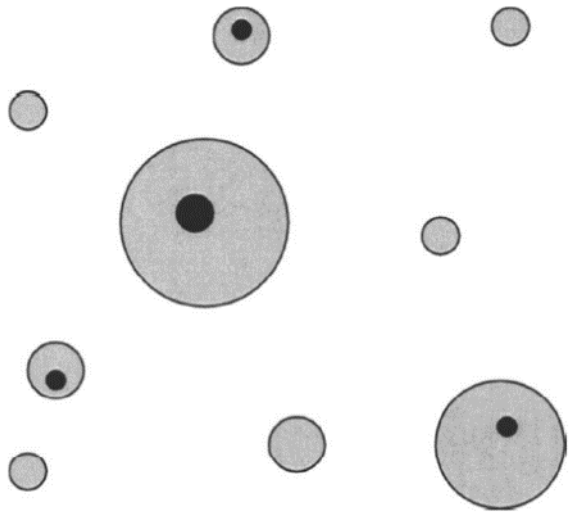

**Figure 2-7: Diagram of two-step nucleation which presumes there is one crystal nucleation event within each dense cluster of the intermediate phase[53]**

Studies of the two-stage nucleation phenomena appear to show that the kinetics of the formation of the crystals becomes dependent on the kinetics of formation of the intermediate phase[52]. The majority of observations that have supported this theory have been on large molecules such as proteins, however there have been studies that have suggested that such pre-aggregation of a metastable phase prior to nucleation can occur in small organic molecules as well[54, 55].

## 2.5 Polymorphism

There are different definitions in the literature for polymorphism, however the definition coined by McCrone in 1965, given as 'a solid crystalline phase of a given compound resulting from the possibility of at least two different arrangements of the molecules of that compound in the solid state'[56], is widely accepted.

It is often observed that the metastable polymorph crystallises prior to the crystallisation of the stable polymorph. This was recognised by Wilhelm Ostwald in 1899, where he postulated that 'when a system leaves an unstable state, it does not seek out the most stable state, but the nearest metastable state which can be reached with a loss in free energy'[57]. Once isolated, the metastable form can remain stable for an extended period of time before converting to the most stable polymorphic form.

### 2.5.1 Enantiotropy and Monotropy

If two polymorphs are enantiotropically related, this means that their order of stability is dependent on temperature. In other words, a reversible transition must occur at a defined temperature where the free energy curves cross for polymorphs to be enantiotropically related. In contrast, when one polymorph has a lower free energy than another polymorph at all temperatures, the two polymorphs are known as being monotropically related, i.e. the free energy curves never cross[58].

### 2.5.2 Conformational Polymorphism

The conformation of a molecule can change significantly between polymorphs, in particular those with several centres of conformational flexibility. Day et al observed that flexible molecules often do not adopt their lowest energy conformations in a crystal structure[59]. Changes in conformation can significantly alter the physical properties between polymorphs, which was perhaps most famously demonstrated in the case of Ritonavir[60].

Ritonavir was an antiviral compound marketed as Norvir which was used to treat Acquired Immunodeficiency Syndrome (AIDS). During development of the compound only one polymorph of Ritonavir was found and 240 lots of Norvir were produced with no stability problems. However, in 1998 capsules started failing the dissolution requirement. Upon examination, a new polymorph of Ritonavir was discovered and characterised (Figure 2-8 and Figure 2-9) displaying both a significant change in molecular conformation and change in H-bonding network.

**(a)**

**(b)**

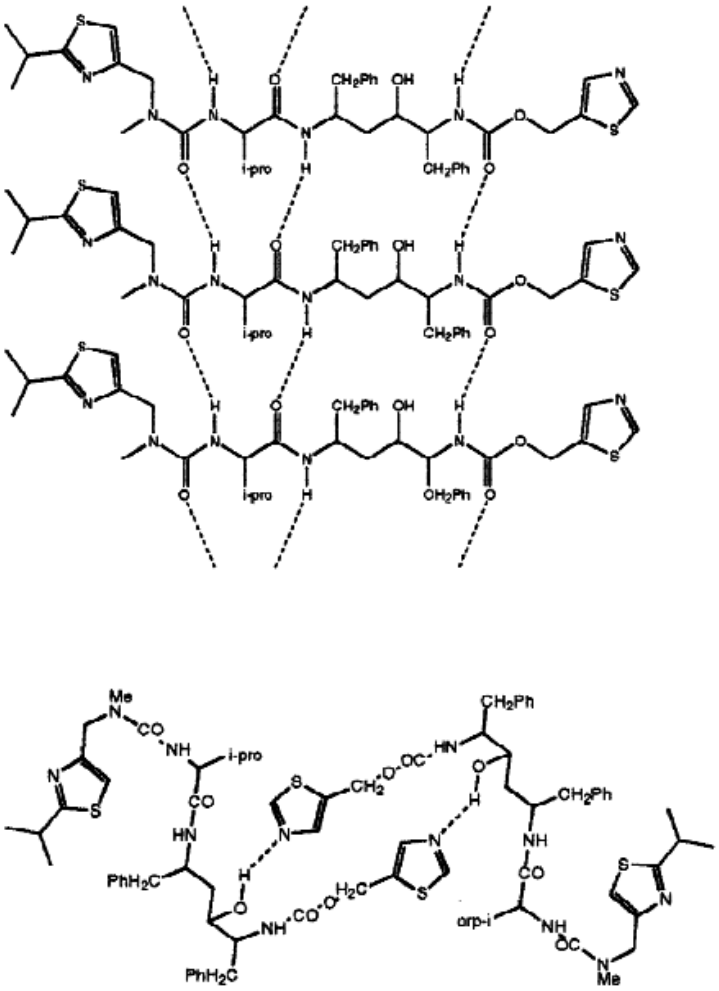

**Figure 2-8: H-bonding network of form I of Ritonavir: (a) beta-like stack; (b) 2-fold screw axis[60]. Not all available H-bonding donor and acceptor sites are being used in this structure**

Within the form I structure, the H-bonding displays two different basic patterns. The amide linkages line up with each other and form NH...O hydrogen bonds to form a beta-like stack along the short crystallographic axis. In addition, the stacks are paired up by a hydrogen bond between the OH group of one molecule with the thiazole group of another molecule.

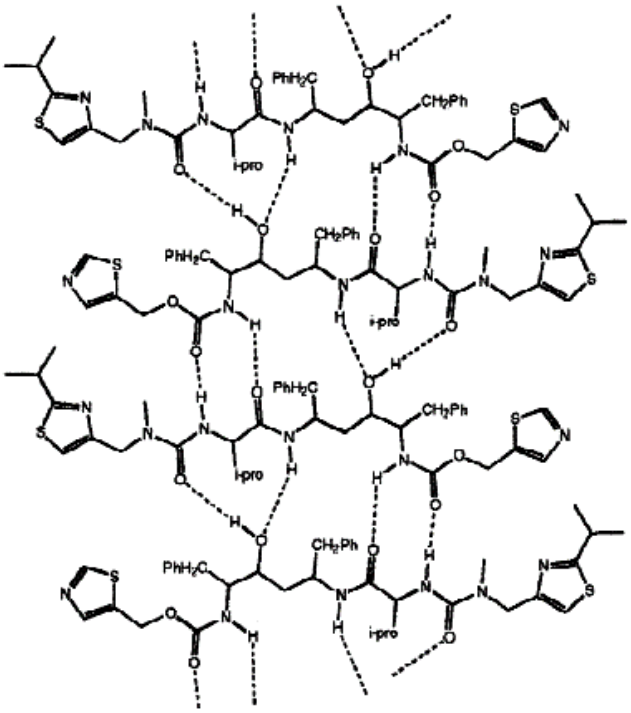

**Figure 2-9: H-bonding network of ritonavir form II[60]. More H-bonding donor and acceptor sites are being used within this structure compared to form I of Ritonavir**

Since crystals of form I have a greater amount of exposed hydrogen bond acceptors and donors than form II, form I has greater solubility in hydrogen bonding solvents. Hence, this is an example of how the effect of different molecular conformations within polymorphs can greatly affect the solubility, and hence effectiveness of a pharmaceutical drug.

### 2.5.3 Solvates and Co-Crystals

Solvates are crystal structures containing either stoichiometric or non-stoichiometric amounts of solvent molecules within the structure. The principle is similar in co-crystals, except that there are one or more molecules within the crystal structure that are not solvent molecules.

The idea of a structural landscape of a crystal is that it includes many possible crystal structures associated with a particular molecule, where this can include polymorphs, solvates and co-crystals[61]. Crystallisation from solution is thought to proceed via the formation of disordered clusters, often thought to be partially solvated. Therefore, considering Ostwalds rule of stages[57], the idea that the most thermodynamically stable

crystal structure can be obtained following a cascade down an energy gradient which contains a number of kinetically stable crystal structures, it is perhaps unsurprising that some of these can contain solvents or other foreign molecules.

### 2.5.4 Polymorphic Control

Since it is generally accepted that pre-nucleation clusters exist in solution, exerting influence over the structure of these clusters can offer a degree of polymorphic control. Previous studies have shown that external factors, such as structure mimicking additives[62] or use of templates to influence molecular self-assembly in solution[63], can be effective in polymorphic control. However, it is sometimes challenging to replicate these conditions and effects in a scale up process, either due to practicalities of implementation in a larger vessel or the cost of templating materials. Therefore, achieving polymorphic control through tuning of the solvation environment is often a much simpler process to implement in a large scale crystalliser and is therefore a much simpler solution to the problem of polymorphic control. The pre-assembly of molecules in solution has previously been conjectured to strongly influence the polymorphic selection during a crystallisation process[64-66].

It has been conjectured that addition of molecules to a growing cluster is not always monomeric and therefore the effect of cluster-cluster interactions on the polymorphic direction of a nucleation process has been studied theoretically[67]. Indeed, it is known that many crystals have growth units that are not monomeric, and these theoretical simulations have suggested that clustering and nucleation may proceed aggregation of small clusters[68]. Further to this, both theoretical and experimental studies have shown that how the solvent environment promotes or hinders hydrogen bonded networks formed in these aggregated clusters can impact on the resultant crystalline form obtained[25, 55].

## 2.6 Computational Crystallisation Characterisation

Since the molecular behaviour during crystallisation is difficult to observe directly, a number of techniques are employed both experimentally and theoretically to derive information on the solution state, nucleation, growth, crystalline structures and surfaces.

Computational techniques based on calculating the internal free energy and intermolecular interactions between molecules can offer insight into molecular behaviour that is difficult to observe, especially in the solution phase.

### 2.6.1 Molecular Mechanics

Molecular mechanics uses classical mechanics to model molecular systems[69]. These ideas were first developed by D.H. Andrews and co-workers by predicting dynamic properties of molecules through these molecular models[70]. Wiberg developed the first computational method for obtaining the minimum energy of a molecule as a function of the bond angles and non-bonded interactions[71], via a steepest descent mechanism.

Molecular mechanics calculates the intramolecular and intermolecular energies through atomistic forcefields derived from experimental data[72-76]. For organic molecules, the vdW interactions are often treated with a Lennard-Jones type potential[77, 78] and often include a term that calculates the coulombic interactions. In addition, some forcefields include a specific term to calculate the hydrogen bonding interactions[73-75].

With respect to organic crystals, molecular mechanics energy minimisation is often used to find the optimum crystal structure geometries, predict crystal structures and calculate lattice energies[19, 20, 22, 79].

### 2.6.2 Molecular Dynamics

Molecular dynamics can model complex systems at the molecular level by solving equations of motion numerically to follow the time evolution of a system[80]. From these computational experiments, the thermodynamic and kinetic properties of a system can be derived.

Molecular dynamics simulations are particularly relevant with respect to modelling solution behaviour, since it is extremely challenging to observe solution behaviour experimentally. Therefore, molecular dynamics has been widely used to observe molecular behaviour in solution prior to and during crystal nucleation[81-83]. It has also been proven particularly effective in predicting what effect the solvent can have on the crystal polymorphism of a system, by understanding a solvents role in promoting certain structural motifs which direct the nucleation of a certain polymorph[25].

### 2.6.3 Quantum Chemistry

Quantum chemistry calculations apply quantum mechanics theory to molecular structures to derive time dependent physical properties of a system. These calculations aim to determine the electronic structure of a molecule or system by solving the Schrodinger equation. Through this, the systems chemical properties can be implied. Since the Schrodinger equation can only be solved exactly for a hydrogen atom[84], methods have been developed to approximate the solution for more complex systems.

#### 2.6.3.1 Valence Bond Theory

Valence bond theory assumes bonds formed between two atoms are localised between the atoms by the donation of one electron per atom[85, 86]. This theory adequately describes the shape of covalent compounds in a qualitative sense, however is inaccurate since many atoms bond using delocalised electrons.

#### 2.6.3.2 Molecular Orbital and Hartree-Fock Theory

An alternative to the Valence Bond theory was developed by Robert Mulliken, whereby he assigned quantum numbers to electrons, such that they are seen to be delocalised over an entire molecule[87-89]. This approach was found to better predict data obtained by spectroscopic methods and through this the Hartree-Fock method was developed.

The Hartree-Fock method seeks to approximately determine the wavefunction and energy of a system by solving the Hartree equation[90], which is an approximation of the Schrodinger equation. Fock recognised that the Hartree equation did not respect the asymmetry of the wavefunction[91], and Hartree reformulated his equations to include exchange[92].

The Hartree-Fock method only became relevant with the development of electronic computers that had the power to solve these more complex equations. The Crystal[93] program was created through the development of using the Hartree-Fock method for periodic systems[94, 95].

#### 2.6.3.3 Density Functional Theory

The Thomas-Fermi model of a quantum ideal gas in a box was the first model to use calculations based on the density of electrons, rather than the wave function. This

became the basis for density functional theory (DFT), which uses the Kohn-Sham method[96]. This splits the density functional up into four parts: kinetic energy, an external potential, exchange and correlation functions. The approach to solving the problem of calculating the wavefunction of interacting electrons is solved by assuming that non-interacting electrons have the same density as interacting electrons. The Kohn-Sham equations include a local effective potential in which the non-interacting particles move.

The majority of work that goes into improving DFT theory is based on improving the exchange and correlation functions. In more recent years, functionals have been improved to account for dispersive interactions between clusters of molecules when utilising DFT calculations[97, 98].

### 2.6.4 Solvent Dielectric Continuum Model

A continuum model is defined as 'a model in which a number of the degrees of freedom of the constituent particles (a large number) are described in a continuous way, usually by means of a distribution function'[99]. The solvation continuum models take their origins from simple physical considerations[100]. Kirkwood extended Bell[101] and Born's[102] considerations of a solutes (M) interaction with a medium represented by a continuous dielectric to quantum descriptions[103]. Onsagers landmark paper developed the idea of the solute being in a cavity, hence the development of the term 'cavity field'[104]. Therefore the simple solvent dielectric continuum model encases the solute molecule within a cavity that is the shape of a molecule and the solvent is treated as a continuum based on the dielectric constant of the solvent.

#### 2.6.4.1 COMSO-RS Model

The conductor like screening model for real solvents (COSMO-RS)[105, 106] utilises a two-step process to calculate thermophysical data in liquids. The first step employs a QM geometry optimisation of the solute within a conducting solvent dielectric continuum cavity, whereby the solvent dielectric polarises the molecule and the molecule back polarises the dielectric. Surface charges are calculated for the solute in this step.

In the second step, thermophysical properties are calculated through a statistical thermodynamics calculation within *COSMO*thermX[107]. The liquid is considered as an

ensemble of almost closely packed ideally screened molecules, where each segment now has a direct contact partner. The segments are defined by area ($a_i$) and its screening charge density ($\sigma_i$). The screening charge densities come from the surface charges calculated from the optimisation in the first step. The vdW, H-bonding and electrostatic interactions between the segments are also dependent on the contact area between the segments ($\alpha_{eff}$). The electrostatic interaction that arises from the contact of screening charge densities (SCD's) is termed the 'misfit' interaction and is calculated using Equation 2-17

$$\boldsymbol{E_{MF}(\sigma,\sigma') = \alpha_{eff}\frac{\alpha'}{2}(\sigma+\sigma')^2}$$ **(Equation 2-17)**

Where σ and σ' are the screening charge densities of the two contacting segments and α' is an adjustable parameter. If a sufficiently negative SCD comes into contact with a significantly positive SCD that contains a hydrogen then the interaction can be described by a specific H-bonding functional form shown in Equation 2-18.

$$\boldsymbol{E_{HB}(\sigma,\sigma') = \alpha_{eff}C_{HB}min\{0;min(0;\sigma_{donor}+\sigma_{HB})max(0;\sigma_{acceptor}-\sigma_{HB})\}}$$ **(Equation 2-18)**

In Equation 2-18, $C_{HB}$ is the H-bonding strength coefficient, $\sigma_{donor}$ is the screening charge density of the donor segment and $\sigma_{acceptor}$ is the screening charge density of the acceptor segment. $\sigma_{HB}$ is a threshold parameter for H-bonding. Therefore, Equation 2-18 is equal to zero unless the more negative of the SCD's is less than the threshold parameter $-\sigma_{HB}$, along with the more positive SCD is greater than the threshold parameter $\sigma_{HB}$. When this occurs the H-bonding energy is the product of the excess screening charge densities, i.e. $(\sigma_{donor}+\sigma_{HB})(\sigma_{acceptor}-\sigma_{HB})$.

Finally, the vdW interactions are calculated from Equation 2-19.

$$\boldsymbol{E_{vdW}(\sigma,\sigma') = \alpha_{eff}(\tau_{vdW}+\tau'_{vdW})}$$ **(Equation 2-19)**

Where $\tau_{vdW}$ and $\tau'_{vdW}$ are element specific empirical parameters.

To describe the composition of the surface segment ensemble with respect to the interactions, only the probability distribution of σ has to be known for all compounds i. These probability distributions $p_i(\sigma)$ are known as 'σ-profiles'. The σ-profile of the mixture is a sum of the σ profiles of the components i weighted with their mole fraction in the mixture $x_i$.

$$\boldsymbol{p_s(\sigma) = \sum_{i \in S} x_i p_i(\sigma)}$$ (**Equation 2-20**)

The chemical potential of a surface segment with a screening charge density σ in an ensemble described by normalised distribution function $p_s(\sigma)$ is given by

$$\boldsymbol{\mu_s(\sigma) = -\frac{RT}{\alpha_{eff}} ln\left[\int p_s(\sigma') exp\left(\frac{\alpha_{eff}}{RT}\left(\mu_s(\sigma') - e(\sigma,\sigma')\right)\right) d\sigma'\right]}$$ (**Equation 2-21**)

Where $e(\sigma,\sigma') = (E_{vdW}(\sigma,\sigma') + E_{HB}(\sigma,\sigma') + E_{mf}(\sigma,\sigma'))/\alpha_{eff})$, the three energy terms $E_{mf}(\sigma,\sigma')$, $E_{HB}(\sigma,\sigma')$ and $E_{vdW}(\sigma,\sigma')$ are calculated using Equations 2-17 to 2-19 respectively. $\mu_s(\sigma)$ is a measure of the affinity of the system S to a surface of polarity σ.

The chemical potential of compound i in system S is calculated by the integration of the σ-potential over the surface of i:

$$\boldsymbol{\mu_i^s = \mu_i^{C,S} + \int p_i(\sigma)\mu_s(\sigma) d\sigma}$$ (**Equation 2-22)**

For the calculation of the chemical potential of a liquid containing more than one component, a combinatorial contribution to the chemical potential is derived from the combinatorial contribution to the free energy:

$$\boldsymbol{G_i^{c,s} = \frac{\delta G_{c,s}}{\delta x_i} = RT[(\lambda_0 + \lambda_1)\sum_i x_i \ln r_i - \lambda_1 \ln(\sum_i x_i r_i) + \lambda_2 \sum_i x_i \ln q_i - \lambda_2 \ln(\sum_i x_i q_i)]}$$ (**Equation 2-23**)

From this, the combinatorial chemical potential of compound i is:

$$\boldsymbol{\mu_i^{c,s} = \frac{\delta G_{c,s}}{\delta x_i} = RT\left[\lambda_0 \ln r_i + \lambda_1\left(1 - \frac{r_i}{\bar{r}} + \ln\frac{r_i}{\bar{r}}\right) + \lambda_2\left(1 - \frac{q_i}{\bar{q}} + \ln\frac{q_i}{\bar{q}}\right)\right]}$$ (**Equation 2-24**)

Where $r_i$ is the dimensionless molecular volume and $q_i$ is the dimensionless molecular area of compound $i. \lambda_0,\ \lambda_2$ and $\lambda_3$ are adjustable parameters. The volume and area of $i$ are defined as:

$$\boldsymbol{\bar{r} = \sum_i x_i r_i}$$ (**Equation 2-25**)

$$\boldsymbol{\bar{q} = \sum_i x_i q_i}$$ (**Equation 2-26**)

In the cases of the selected clusters, the free energy and the σ-profiles will be significantly different. The cluster populations can be calculated relative to each other by utilising the 'automatic conformer detection' option. The population of the different clusters is calculated according to the Boltzmann distribution between states of different free energy $\left(G_j^s = E_{cosmo}^j + \mu_j^s\right)$. The multiplicity $w_j$ is assigned to each

conformer taking into account molecular symmetry. The population of the conformers is given by:

$$\pi_j^S = \frac{w_j \exp\left\{-\frac{E_{cosmo}^j + \mu_j^S}{kT}\right\}}{\sum_k \omega_k \exp\left\{-\frac{E_{cosmo}^k + \mu_k^S}{kT}\right\}} \quad \textbf{(Equation 2-27)}$$

The population of these conformers are expressed as fractions labelled 'normalised weight factor' in the output file.

The COSMO-RS model has provided effective predictions of solubility and solvent screening[108, 109], ionic liquid solution properties[110] and conformational analysis[111], to name a few applications.

## 2.7 Experimental Crystallisation Characterisation

### 2.7.1 X-Ray Diffraction

When an electrically charged particle rapidly decelerates, the kinetic energy (KE) of the particle can be converted to radiation, known as X-rays. When electrons are accelerated towards an electrode their kinetic energy can be calculated by Equation 2-28.

$$KE = eV = {}^{1}/_{2}\, mv^2 \quad \textbf{(Equation 2-28)}$$

Where $m$ = mass of an electron, $v$ = voltage across the electrodes, $e$ = charge of the electron and $v$ = velocity of the electron on impact. The photon energy is calculated by Equation 2-29.

$$eV = hv_{max} \quad \textbf{(Equation 2-29)}$$

Where $h$ = Plancks constant and $v_{max}$ = largest frequency of radiation produced.

The diffraction of waves is due to the phase relations between waves. Path differences in the travel of two waves result in differences of amplitudes. Waves can either combine constructively (in-phase) or destructively (out of phase) shown in Figure 2-10.

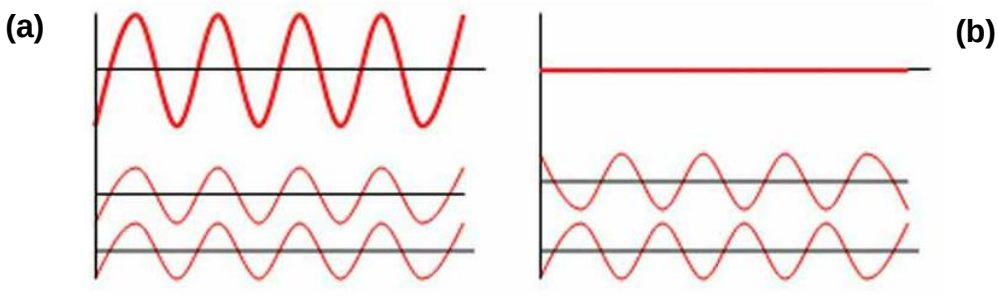


**Figure 2-10: (a) waves combining in-phase to increase the amplitude of the wave; (b) waves combining out of phase to decrease the amplitude of the wave[2]**

### 2.7.1.1 Braggs Law

Figure 2-4 revealed how a crystal can be thought of as a repeating set of planes equally spaced by *d* (interplanar spacing). If an X-ray beam penetrates the surface and reflects off a plane of atoms, it will have travelled a greater distance than an X-ray that has reflected off the surface. For waves to be in-phase they need to have travelled a whole number of wavelengths while inside the material. Figure 2-11 and Equation 2-27 show how Bragg formulated his equation into 'Bragg's Law'.

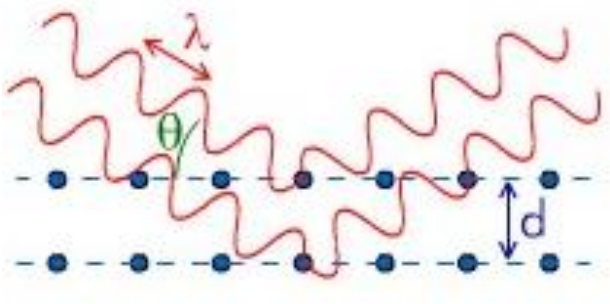


$$n\lambda = 2dsin(\theta)$$ **(Equation 2-30)**

**Figure 2-11: Diagram of X-ray beam reflecting of the surface and a sub-surface plane of a crystal[2]**

Where $d$ = spacing between the atoms; $\theta$ = angle between incident rays and the surface and $\lambda$ = wavelength of X-ray beam. If this equation solves such that n is a whole integer, then the waves combine in-phase and produce a bright spot of a piece of photographic film[112].

### 2.7.1.2 Powder X-Ray Diffraction

Powder X-ray diffraction (PXRD) is carried out on a collection of microscopic crystals, which to the naked eye resembles a powder. The result of using a powdered sample is that every possible crystalline orientation is represented equally. This method is often used for identifying different crystalline phases or product purity; although a full crystal structure can be obtained through a process known as Rietveld refinement.

When the sample is rotated, the diffracted radiation is cone shaped, with each cone representing a crystallographic plane *hkl*.

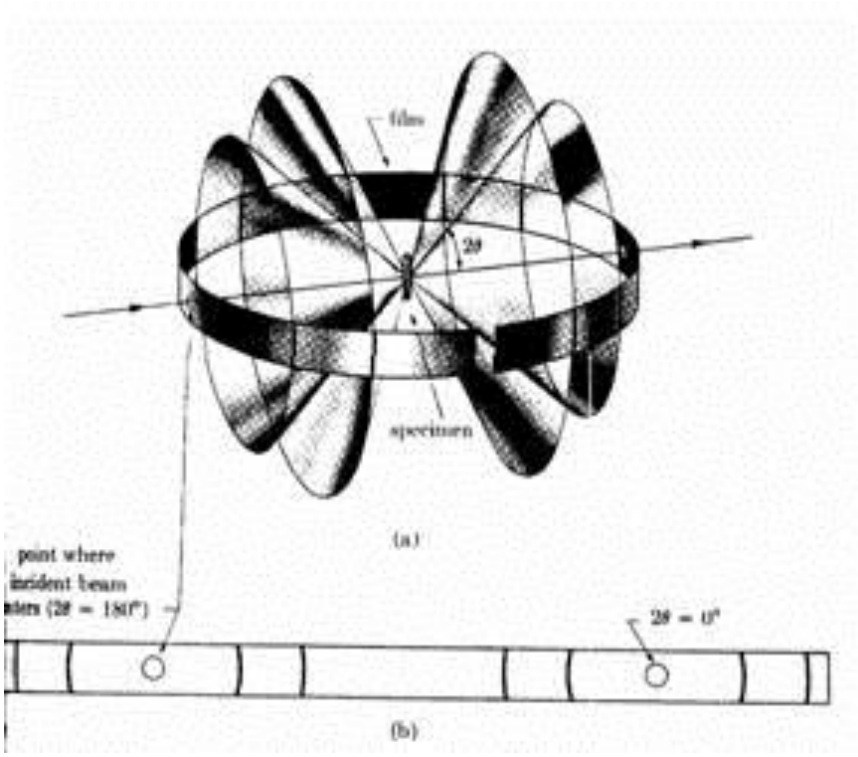


**Figure 2-12: Diagram of cone-shaped X-ray radiation obtained from a rotated powder crystalline sample[113]**

The diffracted cones hit the film and produce a series of lines which correspond to a crystallographic plane *hkl*. From this line $\theta$ and *d* spacing can be calculated.

Most modern powder diffractometers use a Bragg-Brentano design. The detector rotates about the sample to vary the scattering angle $2\theta$.

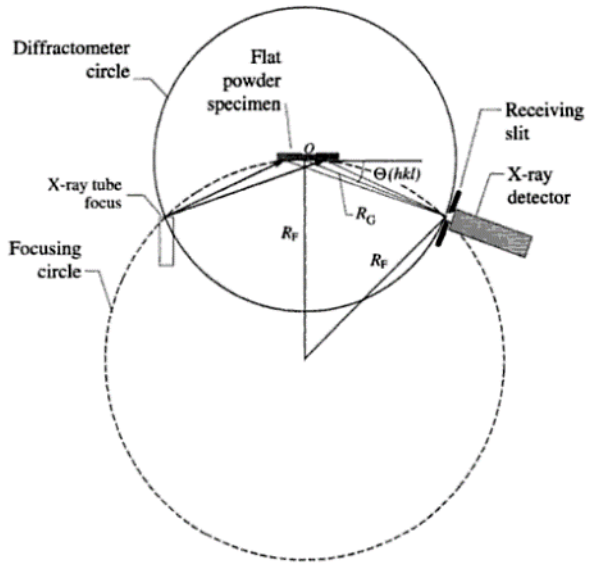


**Figure 2-13: Diagram of the Bragg-Brentano method set-up for powder XRD (divergent beam focussing)[114]**

#### 2.7.1.3 Single Crystal X-Ray Diffraction

To identify the specific position of the atoms within a crystal structure, diffraction patterns can be collected in as many different directions as possible[115]. The diffraction patterns in the different directions can yield an electron density map. With prior knowledge of the species that are expected within the crystal structure, the electron density maps can be used to identify the specific atomic positions within the crystal. A least sum of squares method is usually utilised to fit the atoms to the electron density map to identify the molecular positions and fit the repeating unit cell, hence the crystal structure is produced.

### 2.7.2 Near Edge X-Ray Absorption Fine Structure Spectroscopy

Near edge X-ray absorption fine structure (NEXAFS) spectroscopy is a powerful for examining the electronic structure of low z (molecular weight) molecules, especially with respect to elucidating surface structure[116]. This technique was developed in the 1980's and much of the progression of this technique can be attributed to the studies of Stohr and co-workers.

#### 2.7.2.1 Synchrotron Radiation

Synchrotron radiation is broad spectrum electromagnetic radiation that is generated when charged particles are accelerated through magnetic fields. The radiation has a

characteristic polarization and has frequencies that range over the whole electromagnetic spectrum.

Modern synchrotron radiation sources run with a dedicated storage ring. Electrons are accelerated and injected into the ring, where they are kept at a fixed energy within the orbit of the accelerator by application of a constant magnetic field. The synchrotron radiation is emitted tangentially from the beam orbit at a very small angle called the photon opening angle. The storage ring may be viewed as the device that transforms radio frequency radiation into the broad electromagnetic radiation that is characteristic of synchrotron radiation[117]

The synchrotron sources will generally support numerous experiments at different stations. The stations collect the radiation emitted tangentially as the beam passes through bending magnets and insertion devices. To achieve satisfactory geometry it is sometimes necessary to deflect the beam using a mirror, and also to increase intensity at the sample focussing mirrors are often employed[117]

#### 2.7.2.2 X-Ray Absorption Spectroscopy

The absorption of X-rays by a given molecule can be measured as a coefficient which is a function of energy. An appropriate energy range is selected around the absorption edge of the element of interest where, once the appropriate energy is reached, the absorption will greatly increase as a core electron is excited from an inner shell to an unoccupied molecular orbital. This produces a photoelectron wave which is back scattered by surrounding atoms[118].

The interactions between outgoing and backscattered waves vary with photon energy. The most well studied region of x-ray absorption is the extended region, known as EXAFS (Extended X-ray Absorption Fine Structure). In this region the scattering processes are dominated by the atomic like potentials of the central and backscattering atoms, therefore typically only single backscattering processes are important[119].

#### 2.7.2.3 Development of NEXAFS

Low Z molecules have weak resonances in the EXAFS region, therefore examining the pre-edge (near edge) region can reveal information on the bonding and geometry of such molecules. These low z molecules have more than 50% of the electrons

involved with bonding, which leads to a lack of a sizeable electron core and hence only small backscattering at high kinetic energies[119]. Near the absorption threshold the kinetic energy is low (≤30ev) and therefore scattering processes are influenced by core potentials of the central absorbing atom and its nearest neighbours, and the detailed valence electron charge in the intramolecular region[118]. The NEXAFS spectra can be characterised by complex multi scattering processes.

Though these are complex events, theoretical and experimental study have in fact shown that the K shell NEXAFS spectroscopy is dominated by two types of intramolecular resonances. In molecules where there are unoccupied π* orbital's, there is a resonance that occurs below the ionisation potential (I.P.) for the 1*s* shell, this corresponds to a transition of a 1*s* electron into an empty or partially filled antibonding π* orbital which is lowered below the I.P. by coulomb interaction with the core hole[118]. This excitation to an unoccupied level is also seen as the low energy photoelectron being trapped by the molecular potential and the resulting wave function in the final state leads a large dipole matrix element which results in narrow and intense resonances[119].

The early studies of simple chemisorbed molecules such as CO and NO on the unreactive metal surfaces served as an effective tool for determining the orientation of these molecules. The work by Stohr et al in 1981[120] showed definitively how the absorption intensity of the σ and π resonances of chemisorbed NO and CO on Nickel changed with variation of the angle between the sample and the synchrotron beam.

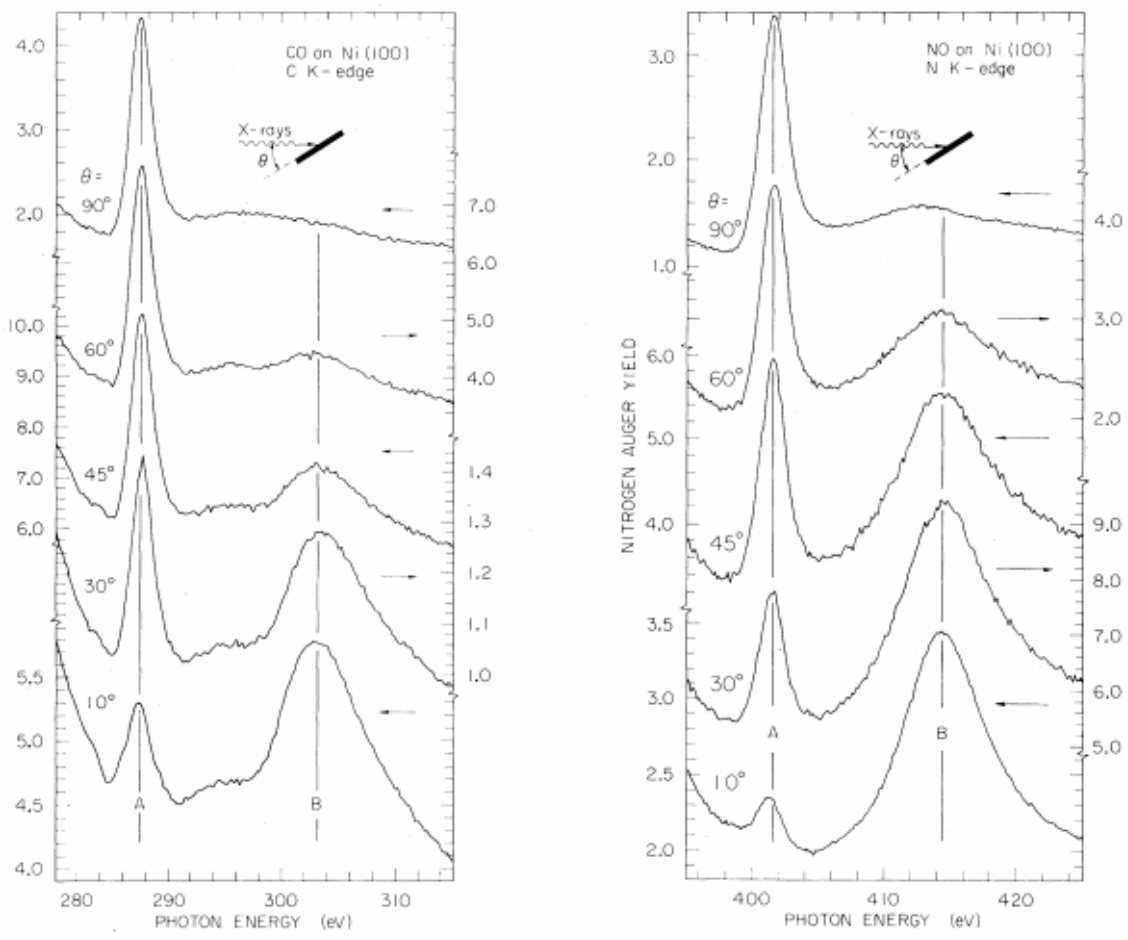


**Figure 2-14: Absorption intensities of chemisorbed NO and CO on NI (100) surface with variation of the polarization angle[120]**

Peak A represents the π shape resonance and is strongest when the beam is at normal incidence (90º). As the polarization is rotated towards grazing incidence, the π resonance starts to decrease while peak B starts to increase in intensity. Peak B represents the σ shape resonance[120].

If we assume circular symmetry for the orientated molecules and linearly polarized light, then a simple equation can calculate the absorption cross section μ.

$$\mu(\gamma) \sim 1 + \frac{1}{2}\beta(3cos^2\gamma - 1)$$ **(Equation 2-31)**

where γ is the angle between the polarization vector and the symmetry axis of the molecule. Therefore, from this equation it is found that for a molecule orientated along the surface normal the σ resonances would be most intense at γ = 0º, while the π resonances would be most intense at γ = 90º.

It is now known that the strongest intensity for an orbital will be observed when the electric field vector (E) is parallel to the orbital. E is perpendicular to the synchrotron beam and is divided into two components, $E_{parallel}$ and $E_{perpendicular}$. $E_{parallel}$ is the dominant component of the electric vector and the degree of linear polarisation P of the electric beam is given by:

$$\boldsymbol{P = \frac{|E_{parallel}|^2}{|E_{parallel}|^2 + |E_{perpendicular}|^2}}$$ **(Equation 2-32)**

The intensity of the peaks that arise from the transitions of core electrons to specific molecular orbitals is represented by the following equations for samples of threefold or higher symmetry. I is made up the parallel and perpendicular components of the beam $I_{parallel}$ and $I_{perpendicular}$.

$$\boldsymbol{I = C\{PI_{parallel} + (1 - P)I_{perpendicular}\}}$$ **(Equation 2-33)**

$$\boldsymbol{I_{parallel} = A(cos^2\theta cos^2\alpha + 0.5 sin^2\theta sin^2\alpha)}$$ **(Equation 2-34)**

$$\boldsymbol{I_{perpendicular} = (0.5 A sin^2\alpha)}$$ **(Equation 2-35)**

Equations 2-31 and 2-32 can be inserted into Equation 2-33 to give:

$$\boldsymbol{I = A[P cos^2\theta (1 - 3/2 sin^2\alpha + 1/2 sin^2\alpha)]}$$ **(Equation 2-36)**

These equations can be used to calculate the orientation of the bonds examined. This is often achieved by measuring the spectra at several different orientations and calculating the peak areas. The angle of the bond is then fitted such that the intensities calculated are the same as the intensities measured.

### 2.7.2.4 Core Hole Excitation and Detection

When an electron is excited out of a core level to a higher molecular state a core hole is created. The existence of a core hole is highly unstable and therefore an electron from a higher bound state will drop down to fill the core hole, and energy is released in the form of a fluorescent photon or auger electron (Figure 2-15):

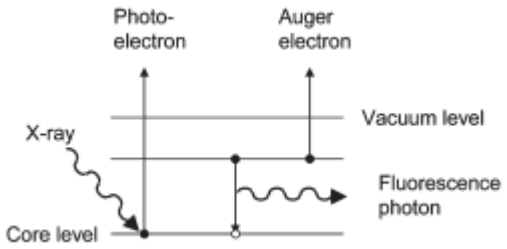


**Figure 2-15: Diagram of photoabsorption process whereby a core electron becomes excited and the core hole is filled. The process results in the emission of a photelectron and a fluorescent photon, which can both be detected during the experiment**

The photoelectron yields information about the surface of the material while the fluorescence data gives information on the bulk structure. These can be detected using the total electron yield technique, which sometimes detects photoemission which can give false NEXAFS data, and partial electron yield which can negate the photoemission peaks.

### 2.7.2.5 NEXAFS and Single Crystals

NEXAFS spectroscopy is often seen as a surface science technique, hence much of the seminal work by Stohr and co-workers focussed on the orientation of single molecules on surfaces[119, 121-124].

However, Roberts and co-workers proved the applicability of this technique for studying single crystals under a variety of conditions[125-129]. Interestingly, these studies revealed structural changes between the surface and bulk of the (0001) surface of benzil single crystals[127] and structural changes upon melting and re-crystallisation of n-alkanes[125].

Despite these proof of concept experiments, there have been relatively few X-ray absorption spectroscopic experiments examining the surfaces of single crystals. This is perhaps due to the high vacuum conditions needed for these experiments and the low vapour pressures of organic crystals. However, there have been some studies of organic materials using such experiments, namely probing H-bonding networks associated with these materials[8, 130-132].

These studies revealed the applicability of probing the directionality of the H-bonding networks within the bulk of an organic material, by comparing the shifts in peaks

between the gas phase and condensed phase. However, the sensitivity to the bond orientation due to the polarised nature of synchrotron beams means that it should be possible to detect the orientation of molecules in molecular crystals. If a material phase separates as a poorly crystalline or amorphous structure it can be impossible to detect the orientation of the molecules through techniques such as X-ray diffraction. Therefore, utilising the sensitivity of the orbital orientation with respect to the beam polarisation would provide information on the molecular orientation of materials that do not display long range order. This would be valuable in understanding the growth of anisotropic, poorly crystalline materials with respect to predicting which synthons are orientated in a particular growth direction.

## 2.8 Closing Remarks

The theory behind crystal structures and crystallisation play a vital role when drawing conclusions on the crystallisation behaviour observed, both through experiments and simulations.

The crystallisation characterisation techniques that have been reviewed in this study are widely used in the crystallisation field, however the theory must be soundly understood in order to draw sense from these techniques and hence obtain sensible conclusions from the data collected.

Multi-technique studies such as this can result in opportunities to advance well-known theory, since it provides a combination of data that has perhaps not been used before. Hence, before advancing the crystallisation theory, one must understand the theory itself.

# Chapter 3 Crystal Growth and Morphology

*The development of the link between crystal growth and morphology is covered, focussing on the development of morphologically predictive modelling.*

## 3.1 Introduction

The morphology of organic crystals can play a substantial role in the downstream processing and formulation of an organic crystalline product. Though the nucleation transition pathway is thought to strongly influence many physical properties (structure, polymorphism etc.) that are displayed by a molecular crystal, it is thought that the crystal growth process has the strongest influence on the final crystal morphology. Both the internal crystal structure and the external growth conditions (temperature, supersaturation, solvent etc.) strongly influence the crystal growth and morphology, hence both should be considered when trying to control crystal morphology. Since this study examined the influence of synthons on crystal morphology, both internal and external synthons, this chapter reviewed the literature on crystal morphology and prediction.

Molecular modelling has been widely used to predict the morphology of crystals[7, 133-135], with these models including properties such as interplanar spacing, symmetrical considerations and, perhaps most widely, the relationship between surface intermolecular interactions and crystal growth rate. The intermolecular interactions are often calculated using interatomic potentials derived from experimental data. However, increases in computing power and sophistication have resulted in the ability to predict the intermolecular interaction strength from first principles *ab initio* calculations.

Continually improving models of crystal growth and morphology will improve the ability of practitioners to predict the correct conditions for crystallisation that will produce crystals of desired size and shape. Therefore, understanding the current literature and models can result in such improvements.

## 3.2 Crystal Growth

The anisotropic nature of molecular crystals often results in significantly varied surface chemistry at the crystal faces, as defined by specific Miller planes (*hkl*). This variation in surface chemistry can result in considerably different face specific growth rates that can produce anisotropic crystal morphologies, such as needles. Figure 3-1 shows how the slow growing faces dominate the final morphology of a crystalline particle.

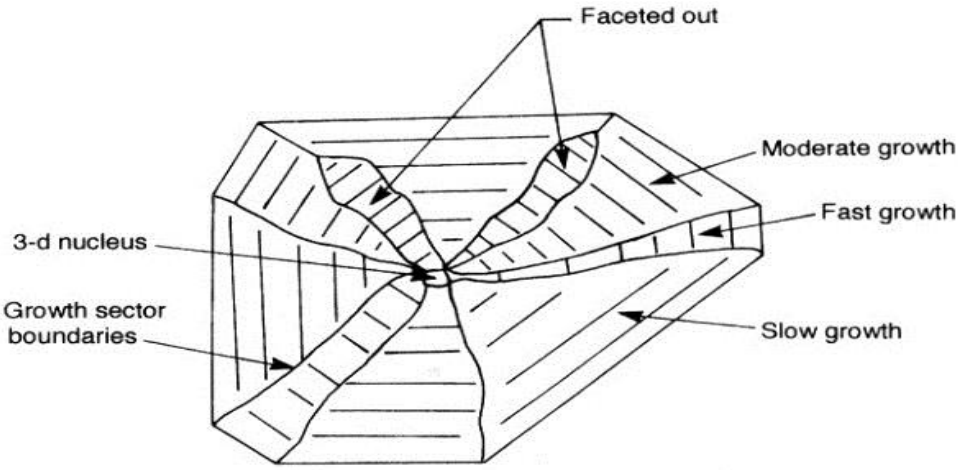


**Figure 3-1: Representation of a cut through a particulate grain boundary showing that the final three-dimensional morphology is created from a series of two dimensional growth processes. 3D morphology dominated by slow growing faces[6]**

The fastest growing faces are usually the smallest, or they can even 'grow out' and not be present in the final crystal morphology. Therefore, one must understand the process of crystal growth and its effect on crystal morphology.

## 3.2.1 Diffusion and Mass Transfer

### 3.2.1.1 Diffusion Reaction Theory

The theory introduced by Noyes and Whitney in 1897 assumed that crystallisation is simply the reverse of dissolution[136]. They proposed that the driving force for crystallisation is the concentration difference between the bulk solution and at the solid/solution interface.

$$\frac{dm}{dt} = k_m A(c - c^*)$$ **(Equation 3-1)**

Where $m$ = crystal mass deposited over time; $A$ = surface area of the crystal; $C$ = solute concentration of the solution; $C^*$ = equilibrium concentration and $k_m$ = coefficient of mass transfer. This can also be written as:

$$\frac{dm}{dt} = \frac{D}{\delta} A(c - c^*)$$ **(Equation 3-2)**

where $D$ = coefficient of diffusion of the solute and $\delta$ = thickness of the stagnant film.

The crystal growth process is thought to proceed via two processes: solute molecules are transported from the bulk liquid phase to the crystal surface (diffusion), followed

by their incorporation into the crystal lattice at the surface (adsorption) (Figure 3-2). Both of these processes are thought to affect the crystal growth rate.

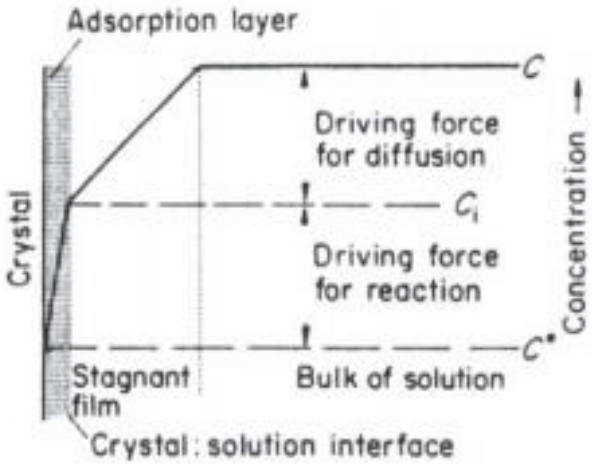


**Figure 3-2: Concentration driving forces for the diffusion and adsorption stages of crystal growth[1]**

Therefore the driving force for crystallisation (Equation 3-2) is split up into driving force for diffusion and adsorption.

**Diffusion:** $\frac{dm}{dt} = k_d A(C - C_i)$ **(Equation 3-3)**

**Adsorption:** $\frac{dm}{dt} = k_r A(C_i - C^*)$ **(Equation 3-4)**

Where $k_d$ = rate constant associated with diffusion; $k_r$ = rate constant associated with growth unit incorporation and $C_i$ = solute concentration in the solution at the crystal/solution interface.

The challenge associated with applying Equations 3-3 and 3-4 is that they involve interfacial concentrations that are difficult to measure. Therefore, the term $C_i$ is often replaced with an overall concentration driving force$(C - C^*)$. This results in a general equation for crystallisation that can be written as:

$\frac{dm}{dt} = k_G A(C - C^*)^g$ **(Equation 3-5)**

where $k_G$ = overall crystal growth coefficient. The exponent $g$ is usually referred to as the 'order' of the overall crystal growth. In this case, the exponent is applied to the concentration difference and does not give any indication of the number of elementary

species involved in the crystal growth process; hence it should not be confused with the conventional order term used in chemical kinetics.

### 3.2.2 Crystal Growth Rates

The crystal growth rate has three well known expressions: mass deposition rate $R_G$ (kgm$^{-2}$s$^{-1}$); mean linear velocity $\bar{v}$ (ms$^{-1}$) or an overall linear growth rate $G$ (ms$^{-1}$)[1]. These quantities are related by Equation 3-6:

$$\boldsymbol{R_G = K_G \Delta c^g = \frac{1}{A}\frac{dm}{dt} = \frac{3\alpha}{\beta}\rho_c G = \frac{3\alpha}{\beta}\rho_c \frac{dL}{dt} = \frac{6\alpha}{\beta}\rho_c \frac{dr}{dt} = \frac{6\alpha}{\beta}\rho_c \bar{v}} \quad \textbf{(Equation 3-6)}$$

Where $L$ = characteristic size of the crystal; $r$ = radius corresponding to the equivalent sphere; $\rho_c$ = crystal density; α and β = volume and surface factors of the crystals; $m$ and $A$ = mass and area of the crystal.

Crystal growth rates can be thought of as face-specific, overall mass growth rate or linear growth rate that changes the characteristic dimension of the crystal.

#### 3.2.2.1 Face-Specific Crystal Growth Rate

The velocity of the movement of a surface perpendicular to the direction of the crystallographic face is the face-specific growth rate ($v_{hkl}$). In the case of anisotropic crystal structures, which are common in molecular crystals, the face-specific growth rates are often found to be quite different. Hence measurement of the face-specific growth rates as a function of supersaturation can yield face-specific crystal growth mechanisms.

#### 3.2.2.2 Overall Mass Growth Rate

The total mass flux to all the crystallographic faces is used to express an average growth rate of the crystal expressed as the overall mass growth rate, $R_G$ (kg/m$^2$s):

$$\boldsymbol{R_G = \frac{1}{A_c}\frac{dM_c}{dt} \; or \; R_G = \frac{\rho_c}{A_c}\sum v_{hkl} A_{hkl}} \quad \textbf{(Equation 3-7)}$$

where $M_c$ = mass of crystal; $A_c$ = surface area of whole crystal; $v_{hkl}$ = face-specific growth rate and $A_{hkl}$ = area of the faces on the crystal. The determination of the growth rate is often obtained through a gravimetric method by weighing the mass of crystals formed as a function of time under controlled conditions such as supersaturation and temperature. These kind of measurements are often used for the design of a batch scale-up crystallisation process[137].

### 3.2.2.3 Overall Linear Growth Rate

The overall linear growth rate (G) is commonly used within population balance theory for expressing the change of crystal shapes over time to predict crystal size distributions in a bulk crystalliser[138, 139]. G can be expressed as:

$$\boldsymbol{G = \frac{dL}{dT}}$$ **(Equation 3-8)**

the overall linear growth rate and overall mass growth rate can be related by Equation 4-9.

$$\boldsymbol{R_G = \frac{1}{A_c}\frac{dM_c}{dt} = \frac{1}{\beta L^2}\frac{d(\alpha \rho_c L^3)}{dt} = \frac{3\alpha\rho_c}{\beta}\frac{dL}{dt} = \frac{3\alpha\rho_c}{\beta} G}$$ **(Equation 3-9)**

Since it is an overall growth rate, the shape of the crystal must also be accounted for to calculate the mass and area of a crystal with Equation 3-10 and 3-11.

$$\boldsymbol{M_c = \alpha . \rho_c . L^3}$$ **(Equation 3-10)**

$$\boldsymbol{A_c = \beta . L^2}$$ **(Equation 3-11)**

Where α = volume shape factor and β = crystal surface shape factor. If the crystals are spherical or cubic ($^{\beta}/_{\alpha} = 6$) then the overall growth rate can be expressed by Equation 3-12.

$$\boldsymbol{R_G = \frac{1}{2}\rho_c . G}$$ **(Equation 3-12)**

The crystal size distribution under defined conditions can be obtained from the population balance model utilising Equation 3-13.

$$\boldsymbol{\frac{\partial(nV)}{\partial t} + \frac{\partial(GnV)}{\partial L} = 0}$$ **(Equation 3-13)**

Where $n$ = population density per unit volume; $V$ = total suspension volume of the crystalliser; G = linear growth rate; L = crystal size and t = time.

## 3.2.3 Growth Rate Dispersion

Even similar size crystals of the same material do not always grow at the same rate when exposed to identical conditions, a phenomenon known as growth rate dispersion (GRD)[140-142].

White and Wright first observed this phenomena that found the size dispersion of a batch of sucrose crystals increased significantly over time[143]. This was expanded by

Wang and Mersmann[144] and Mitrovic[145] who established that there was a link between initial size of crystal seeds and crystal growth rates.

Since GRD has a direct effect on the crystal size dispersion of product crystals which is related to product quality, the large body of research that has been directed into this area has resulted in three models to rationalise this phenomena.

#### 3.2.3.1 Constant Crystal Growth Model

The constant crystal growth model[141] proposed that the nuclei form with a distribution of growth rates at constant crystallisation conditions, whereby the relative growth rate of each nuclei remains constant over time.

#### 3.2.3.2 Random Fluctuation Model

The random fluctuation model proposed that the growth rate fluctuates around an average constant growth rate[138]. These fluctuations were proposed to be caused by changes in local surface structure over time as the crystal grows, resulting in face specific growth rate deviation.

#### 3.2.3.3 Fast Growers, Slow Growers Model

The 'fast growers, slow growers' model proposed that differences in lattice strain between different sized secondary nuclei could account for this growth rate dispersion[146]. Larger crystals that are produced by a surface breeding mechanism result in the surface features being removed by attrition, in contrast to the small crystals which are produced my mechanical breeding and hence contain increased lattice strain.

### 3.2.4 Crystal Growth Mechanisms

The understanding of individual face-specific growth kinetics can reveal information on how a molecule integrates itself into the crystal lattice at that surface. Relating the face-specific growth rates of the crystal surfaces with supersaturation can reveal whether the face grows by one of three well established crystal surface growth rate mechanisms, Burton Carbrera and Frank (BCF), Birth and Spread (B&S) or Rough Interfacial Growth (RIG) (Figure 3-3).

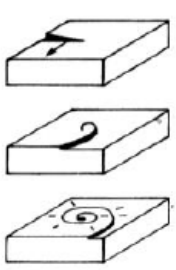

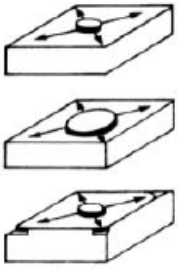

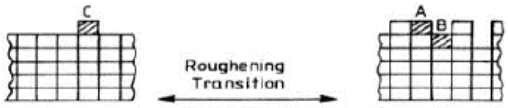


**BCF**: The incorporation of growth units onto the stepped surface provided by protrusion of dislocations leads to the formation of a growth spiral over the crystal surface creating a permanent source of growth steps at the crystal surface.

**B&S**: In the absence of steps surfaces develop through the nucleation (birth) and growth (spread) a monolayer. After nucleation, further molecules can absorb and integrate into the existing monolayer thus enabling it to spread over the surface followed, in turn, by further 2D nucleation events when the surface layer has fully spread over the surface.

**RIG:** At high supersaturation, the growth interface undergoes surface roughening providing through this abundant sites for surface integration with a lot more step and kink sites thus resulting in a much higher growth rate.

$$R_{hkl} = A\sigma^2 tanh\left(\frac{B}{\sigma}\right) \qquad R_{hkl} = A_1\sigma^{5/6} exp\left(\frac{5}{6}\right) \qquad R_{hkl} = A\sigma$$

**Figure 3-3: Diagrams and short description of three major growth mechanisms that can be elucidated from relating growth rate to supersaturation. The BCF growth via spirals, B & S growth via 2D nucleation and the surface and RIG via a roughening polynucleation mechanism[1]**

At low supersaturations, the BCF[147] mechanism is common in the presence of screw dislocations, whereby a molecule can integrate at the surface and growth occurs by spirals. At growth surfaces where the presence of screw dislocations is unlikely, the supersaturation builds at the boundary layer, until a nucleation event takes place and molecules can adsorb into a monolayer until it spreads across the surface, resulting in the B&S[148] mechanism. At high supersaturations, a surface can undergo a roughening transition, and molecules can adsorb at multiple surface integration sites, resulting in a linear relationship between supersaturation and growth rate.

Variation in surface chemistry can lead to different crystal growth mechanisms at the surfaces of a molecular crystal, which often can lead to undesirable crystal shapes. A surface growing by an RIG mechanism will grow so much faster than the other faces

that an elongated, needle like morphology, will often occur[3, 51]. It has previously been well studied that different crystal growth mechanisms at different surfaces can strongly influence crystal morphology[149-151].

## 3.3 The shape of Molecular Crystals

The shape (morphology) of molecular crystals is dependent on the packing of the molecules within the crystal lattice, since the structures of these crystals are often strongly anisotropic. Therefore, to understand the morphology of the crystals one must be able to identify the crystallographic directions with respect to the crystal lattice, as surfaces are often labelled with three numbers in a bracket, known as Miller indices. The following section will show how this labelling of a crystal surface relates to the crystal structure and ultimately can reveal which synthons are directing the growth in a particular crystallographic direction.

### 3.3.1 The Law of Rational Indices

Haüy proposed that the shape of crystals was directly related to the shape of the unit cell, since this is repeated infinitely in all directions. This is why highly symmetric crystal structures produce isotropic crystal shapes and low symmetry structures can often produce anisotropic morphologies. Therefore the directionality of the growth facets that present at the crystal surface can be related to the dimensions of the unit cell through the ‘law of rational indices’. This law proposes that the intercepts of a plane on the crystallographic axes will be ratios of integers, i.e. rational numbers. Therefore a crystal face is described by the reciprocal of the lattice intercepts, i.e. the (1 1 1) surface would represent the growth plane that intercepts each axis at one unit cell length.

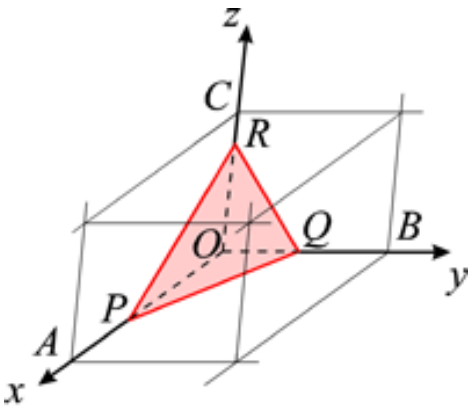


**Figure 3-4: Schematic representation of the law of natural indices showing the intercepts on a set of crystallographic axes[152]**

The law of rational indices is demonstrated in Figure 3-4, whereby the intercepts *OP*, *OQ*, *OR*, of the natural faces of a crystal form with the unit cell axes *a*, *b*, and *c* are inversely proportional to the prime integers *h, k, l*.

The *h, k, l* values are known as the Miller indices of the crystal face. For the morphologically important surface, these are often small due to the corresponding lattice planes being the densest and therefore have a low interplanar spacing.

Haüy deduced the law of rational indices from the observation of the stacking laws required to build the natural faces of crystals by the stacking of elementary blocks, such as cubes. For instance, he observed that this law holds for the construction of the {1 1 0} faces of the rhomb-dodecahedron observed in garnets (Figure 3-5).

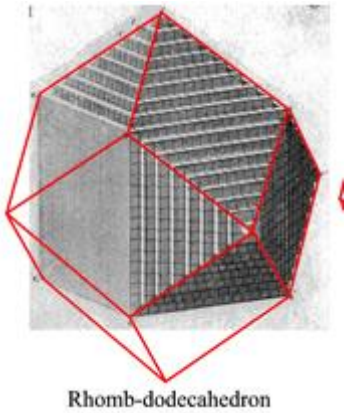


**Figure 3-5: Application of stacking laws to cubic blocks used to construct the {1 1 0} form of the rhomb-dodecahedron observed in garnets[152]**

### 3.3.2 Equilibrium Morphology and the Wulff Plot

In 1875 Gibbs postulated that the three dimensional shape of a crystal will be the one in which the total free energy is at a minimum, according to Equation 3-14.

$\sum_i \gamma_i A_i$ **Equation 3-14**

Whereby $\gamma_i$and $A_i$ are the surface energy and surface area of the i$^{th}$ face. In 1901, Wulff developed this theory such that the equilibrium crystal habit would consist of crystal faces whose distance from the origin is proportional to the specific surface energies of the faces and the crystal growth rates away from the nucleation centre (Figure 3-6).

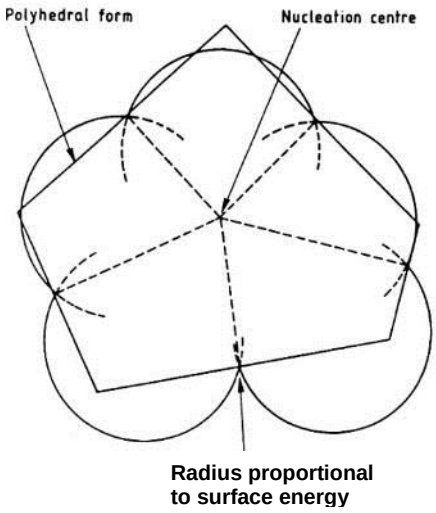


**Figure 3-6: Diagram of Wulff plot of the equilibrium morphology of a crystal[9]**

Routine molecular drawing programs such as Shape[153] and Mercury[154] can take crystallographic information and relative crystal growth rates expressed as the nucleation centre to crystal face distance, and construct a Wulff plot of the resulting crystal morphology. Therefore, using the law of rational indices it is possible to know the packing in a particular direction, hence also at a surface. Therefore, it can be deduced that the growth rate of a surface is dependent on the strength on the intermolecular interactions between the molecules in that particular direction. If the relative strengths of the intermolecular interactions in the crystal structure can be calculated, then the relative growth rates of the surfaces, along with a prediction of the crystal morphology can also be calculated.

## 3.4 Synthonic Engineering

As was discussed in chapter 1, the term ‘synthon’ is used to describe a growth unit of a crystalline material. As discussed in the previous section, the strength of the intermolecular interactions that are directed in a particular direction are thought to govern the growth rates in that direction, and hence the overall shape of the crystal. Synthonic engineering is focussed on calculating the strength and nature of these interactions.

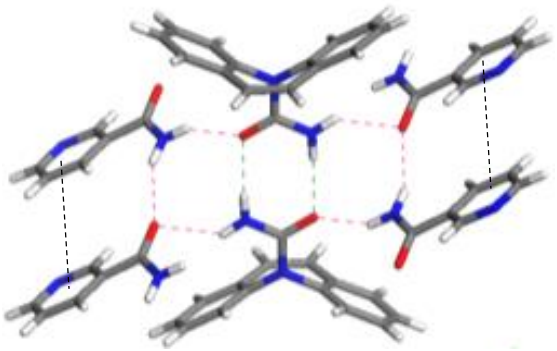

**Figure 3-7: Intermolecular interactions (synthons) made up of directional hydrogen bonds (pink and blue) and more isotropic vdW interactions (black)**

The fully satisfied intermolecular interactions that are present within the bulk of the material are known as ‘intrinsic synthons’, while the unsaturated intermolecular interactions exposed at the surface of a material are known as ‘extrinsic synthons’. The strength and directionality can be calculated utilising crystallographic modelling programs, such as HABIT[14]. The nature, strength and directionality of these synthons can direct physico-chemical properties of a crystalline material such as nucleation, crystal growth, polymorphism and purity. Therefore, through calculation of the strength and nature of both the intrinsic and the extrinsic synthons present at the surface of molecular crystals, these properties can be accurately predicted.

### 3.4.1 Crystal Chemistry and Intermolecular Potentials

The internal structures of molecular crystals are often dominated by 'weak' intermolecular interactions such as hydrogen bonds (H-bonds), π-π stacking interactions and less specific van der Waals interactions (vdW). The molecules pack in arrangements that maximise these attractive interaction energies, while still being in energetically favourable conformations.

The strength of the intermolecular interactions is a major factor in directing the growth rates in specific crystallographic directions, and hence the morphology of the final crystalline particle. Traditionally, the strength of intermolecular interactions has been calculated using empirical interatomic potentials derived from experimental data[73-75, 155, 156]. In recent years, as computing power has vastly increased, the sophistication of *ab initio* calculations of molecular energies has developed. Density functional theory (DFT) based calculations are of the ground state, however the development of functionals, such as the M06[157] and Grimme's[97] functional, are parameterised to account for dispersion effects of neighbouring molecules. Despite this, these calculations are often computationally expensive and time consuming and as of yet, are unproven to offer significantly more accurate results than empirical intermolecular potentials.

The calculation of a pairwise intermolecular interaction is often achieved through the 'atom-atom method'[158], which sums the individual atom-atom interactions between the two molecules. Equation 3-15 shows a Lennard-Jones potential used to calculate vdW interactions, including a Coulombic term to calculate electrostatic interactions (Equation 4-15):

$$\boldsymbol{V_{ij} = -A/r_{ij}^{6} + B/r_{ij}^{12} + q_i q_j / D r_{ij}}$$ **(Equation 3-15)**

where A and B are atom-atom interaction specific parameters, $q_i$ and $q_j$ are fractional charges on atoms *i* and *j* separated by distance R, and D is the dielectric constant. For molecular crystals where hydrogen bonding is important, which is common in organic crystals representative of pharmaceutical drugs, a specific part of the potential is parameterised to calculate H-bonds[73-75]. This part of the potential is applied when considering hydrogens covalently bonded to a polar atom, such as O or N, which is forming a non-bonded contact with another polar atom.

### 3.4.2 Lattice Energies and Potential Validation

The lattice energy ($E_{cr}$) is the sum of all of the non-bonded interactions that hold together a crystal. This can be routinely calculated using molecular modelling programmes such as HABIT[14]. HABIT constructs a series of unit cells in three dimensions and calculates the non-bonded energy between a central molecule and all other molecules in the central and surrounding unit cells. The lattice energy is summed according to Equation 3-16:

$$E_{cr} = {}^{1}/_{2} \sum_{k=1}^{N} \sum_{i=1}^{n} \sum_{j=1}^{n'} V_{kij}$$ **Equation 3-16**

The calculated lattice energy can be compared to experimentally obtained sublimation enthalpies ($\Delta H_{sub}$) to test the suitability of an intermolecular potential. The 'experimental lattice energy' ($V_{exp}$) is related to the sublimation enthalpy through Equation 3-17:

$$V_{exp} = -\Delta H_{sub} - 2RT$$ **Equation 3-17**

where the 2RT is the correction for the difference between the gas phase enthalpy and the vibrational contribution to the crystal enthalpy. Good agreement between the sublimation enthalpy and calculated lattice energy suggests that the potential is suitable to predict the strength of the interatomic interactions for the atoms involved, and hence predict the strength of the intermolecular interactions.

There are generalised potential parameters available in the literature that have previously provided good predictions of the strength of intermolecular forces between organic molecules[73-75, 156, 159]. These potentials are parameterised to handle a range of molecules, and as such some computational scientists argue that the absolute values of the intermolecular bond strengths cannot be wholly accurate. This leads to some workers preferring to optimise potentials against known crystal structures, experimental data and *ab initio* energy calculations to create a potential that is suited to a specific molecule or system[21, 22, 160]. Though in many cases this improves the accuracy of the calculation of intermolecular force strength, the process can be time consuming. Optimisation of the potential is more common within the crystal structure prediction community, where the absolute values of intermolecular interactions are far more important, since it is the lowest energy crystal structure that is usually taken as the most likely prediction and the energies are often quoted with accuracies of less a

kj/mol[161-163]. However, for the prediction of crystal morphologies the relative strength of the intermolecular interactions is often found to be most important[7, 133]. If the relative strengths of the intermolecular interactions are correct, then the exact numbers for the intermolecular interaction strengths that are given from different potentials have been found to make little difference in the crystal morphological prediction[164].

#### 3.4.2.1 Lattice Energies Calculations for Solid Form Selection

The lattice energy is a sum of all the intermolecular interactions within the crystal. Therefore, the lattice energy can be calculated by summing all the interactions of one of the asymmetric units with all of the other molecules within the unit cell and surrounding unit cells. The calculation of lattice energy is often set up so that the intermolecular interactions are calculated within a spherical radius where the reference asymmetric unit is at the centre of the sphere. Figure 3-8 shows how the lattice energy change as the sphere radius is increased.

Figure 3-8 demonstrates at what distance from the origin the important intermolecular

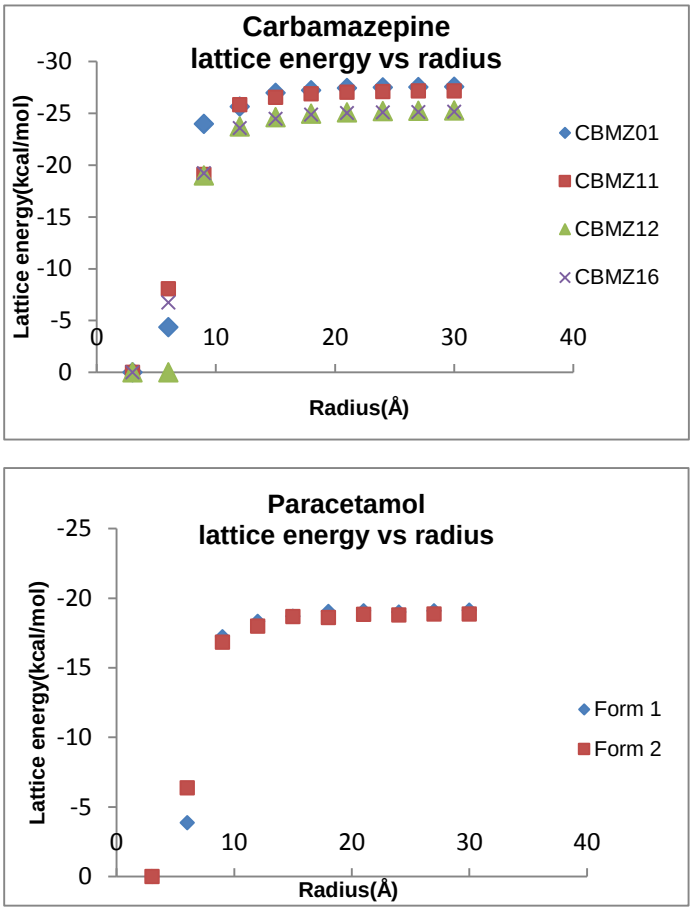


**Figure 3-8: Lattice energy convergences of the polymorphic forms of carbamazepine (top) and paracetamol (bottom) as a function of limiting radius, i.e. cluster size**

interactions become satisfied, such that the lattice energy converges. If the lattice energy converges at a lower radius, then it suggests that clusters or nano-crystals that show structural analogies with the crystal structure could become stable at small sizes. In addition, if the lattice energy converges to a sensible number at a realistic distance, it suggests that the potential is fit for purpose.

### 3.4.3 Selection of Morphologically Important Surfaces

Early relationships of interplanar spacing to morphological importance, linked with lattice geometry, lead to the Bravais, Friedel, Donnay and Harker model (BFDH)[9, 165-168]. This model is still used to identify the morphologically dominant faces (*hkl)*. The rule suggests that, after allowances have been made for space group symmetry, the crystallographic forms[169] with greatest

interplanar spacing $d_{hkl}$ will be morphologically important at the surface of the crystalline particle.

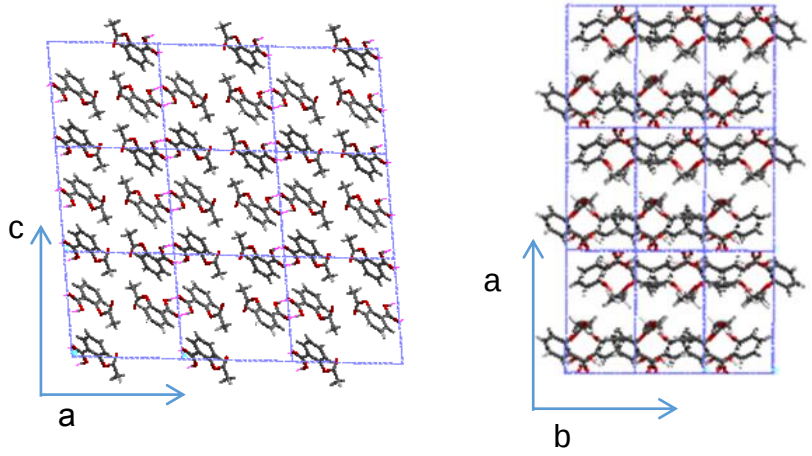


**Figure 3-9: Crystal packing of the published crystal structure of aspirin (Cambridge structural database reference for the structure ACSALA01) {0 0 1} form (left) and {1 0 0} form (right) showing how the structure is repeated in the [0 0 1] direction but not the [1 0 0], resulting in reduction of the morphological importance of the {0 0 1} but not the {1 0 0} form. Note. {h k l} indicates crystallographic form; [h k l] crystallographic direction and (h k l) crystallographic face**

Figure 3-9 shows how, in the case of aspirin with a $P2_1/n$ space group, the crystal structure repeats within a unit cells length along the [0 0 1] direction, but in the [1 0 0] direction this does not happen. Hence, the morphological importance of the {0 0 1} form is reduced to {0 0 2} as the effective interplanar spacing is $d_{hkl}/2$. In contrast, the {1 0 0} form remains morphologically important.

Using information from the crystal structure computer programmes, such as Morang[168], can calculate the interplanar spacing in specific crystallographic directions and therefore efficiently predict the likely morphologically important surfaces.

### 3.4.4 Periodic Bond Chain Theory

The BFDH rule does not take into account the effect of the intermolecular forces on face specific crystal growth in a molecular crystal. This weakness was recognised by Hartmann and Perdok in 1955, with the derivation of the 'periodic bond chain' theory and first use of the term 'attachment energy'[12].

The periodic bond chain theory suggests that crystallographic faces with strong stoichiometric bonds running in-plane at the surface will be slow growing, and

therefore morphologically important. This theory divides crystal faces into three types: F, S and K faces (Figure 3-10).

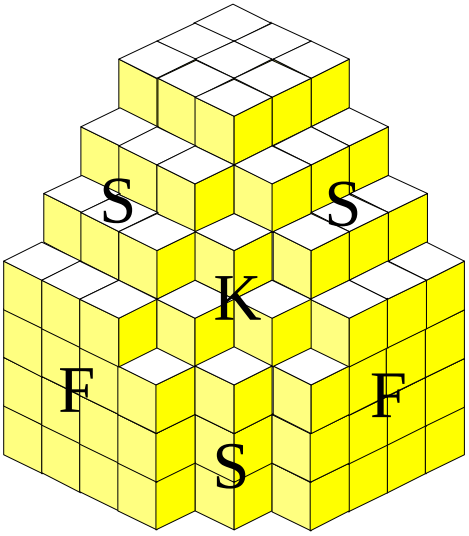


**Figure 3-10: Types of crystal faces as defined by PBC theory indicating the amount of bonds available to form with an incoming molecular growth unit[170]**

A simple way to differentiate between these classes of faces and their speed of growth is to consider which strong intermolecular interactions grow in-plane at the surface, and which interactions need to be formed to incorporate the building unit at this surface. An F (flat) face will have two or more strong intermolecular interactions in-plane at this surface, hence the interactions that are formed when incorporating a building block at this surface will be relatively weak, therefore slow growth and a large face. An S (stepped face) may only have one or less strong intermolecular interactions in-plane at the surface, hence at least one strong intermolecular interaction will need to be formed when incorporating the growth unit at this surface, therefore faster growth and a smaller face will be expected. Finally, a K (kinked) face will have no strong intermolecular interactions in-plane at this surface, hence all the strong intermolecular interactions will need to be formed when incorporating the growth unit at this surface, therefore fastest growth will be expected and these surfaces will be smallest, or even not be present in the final crystal morphology.

### 3.4.5 Graph Sets and Connected Net Analysis

As a further extension on the PBC analysis, the idea of connected nets is introduced. Connected nets have an overall thickness $d_{hkl}$ whereby all units are connected to each other and they consist of at least two sets of PBC's[171]. The influence of connected nets and morphology, especially with respect to roughening transitions, has been strongly established by Bennema, Meekes and co-workers[172, 173].

#### 3.4.5.1 Roughening Transition Temperature

Onsager derived a calculation of the exact free energy for the Ising model on a rectangular net[174]. This two dimensional model expresses the energy of a solid/fluid interface according to Equation 3-18.

$$\boldsymbol{E = -\sum_{<i,j>} \varphi_{i,j} s_i s_j}$$ **(Equation 3-18)**

Where $\varphi_x$ = energy of the bond between units $i$ and $j$ within the net and $s$ = spin, whereby the spin can take only two values: +1 for a solid or -1 for a liquid. From this, the critical roughening temperature can then be obtained from equation 3-19.

$$\boldsymbol{sinh\left(\frac{2\varphi_x}{kT}\right) sinh\left(\frac{2\varphi_y}{kT}\right) = 1}$$ **(Equation 3-19)**

Therefore, this implies for an isotropic rectangular net whereby the intermolecular bond energies are equal, that the dimensionless critical temperature is given by Equation 3-20.

$$\boldsymbol{\theta^c = (kT/\varphi)^c \cong 2.27}$$ **(Equation 3-20)**

Since this model is based only on one layer, to attempt to model a more realistic interface multiple layer models have been developed. One of the most widely used models is the solid on solid (SOS) model[175]. Above the roughening temperature steps can form on the surface due to random equilibrium fluctuations, such that an approaching molecule has a good chance of coming into contact with a kink site and the molecule no longer needs a screw dislocation or an edge formed by 2-D nucleation to incorporate at a surface. The crystal growth rate has a linear dependence on supersaturation in these conditions.

#### 3.4.5.2 Connected Nets and the Roughening Transition

From the 'solid on solid' (SOS) model, a roughening transition temperature is defined in the following way[133, 176].

$$\boldsymbol{T < T^R \rightarrow \gamma > 0}$$ **(Equation 3-21)**

$$\boldsymbol{T \geq T^R \rightarrow \gamma = 0}$$ **(Equation 3-22)**

Where $T$ = temperature of growing face; $T^K$ = critical roughening temperature of that face and $\gamma$ = edge free energy of a step. Equations 3-21 and 3-22 imply that when the temperature of the growing face is above the roughening transition temperature, the edge free energy of a step will be zero and essentially there will be no energetic 2-dimensional nucleation barrier to integration of a molecule at a surface.

### 3.4.6 Attachment Energy Morphological Prediction

#### 3.4.6.1 Attachment Energy and α-Factor Calculations

Once the lattice energy has been calculated, it can then be partitioned into slice ($E_{sl}$) and attachment ($E_{att}$) energies for faces predicted to be morphologically important by the BFDH rule. The lattice, slice and attachment energies are related by Equation 3-23.

$$\boldsymbol{E_{cr} = E_{sl} + E_{att}}$$ **(Equation 3-23)**

The slice energy is the summation of all the interactions between the central molecule and all other molecules within the slice boundary, whereas the attachment energy is the summation of all the interactions between the central molecule and molecules outside the slice boundary. HABIT routinely calculates this, and the process is shown in Figure 3-11.

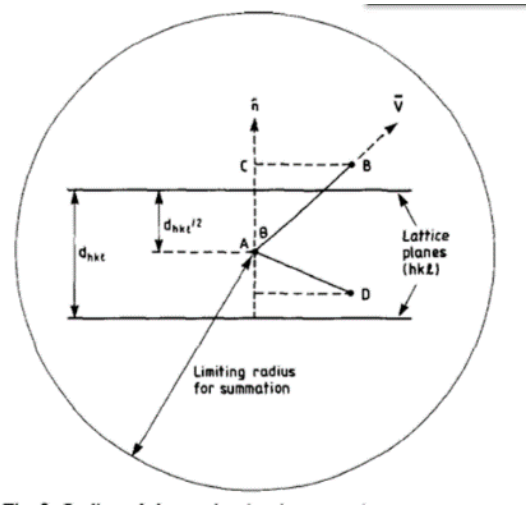


**Figure 3-11: Diagram of lattice energy partitioning into slice and attachment energies within the limiting radius. A is the central molecule, B is a molecule outside the slice, D is a molecule within the slice, N⁺ is the growth normal to the planes [$d_{hkl}$], N- is the growth normal to the planes ($\bar{h}\bar{k}\bar{l}$), AB and AD are intermolecular bond vectors, $d_{hkl}$ is the interplanar spacing, θ is the angle between the growth normal and the bonding vector and AC is the component of the vector AB which is parallel to the growth normal. The slice boundary can be optimised to find the most stable slice[14].**

In this model, it is assumed that the attachment energy is proportional to the growth rate according to Equation 3-24.

$$R \propto E_{att}$$ **(Equation 3-24)**

These calculated attachment energies are then converted into centre to face distances and then used to construct a Wulff plot of the predicted morphology.

Once the lattice energy has been divided into slice and attachment energies, the morphological stability of a growth interface can be assessed by calculation of the α factors[177].

$$\alpha_{hkl} = (E_{sl}/E_{cr})(\Delta H(T)_{diss}/RT)$$ **(Equation 3-25)**

In Equation 3-25, $\Delta H(T)_{diss}$ is the enthalpy of melting, R is the gas constant and T is the melting temperature. $E_{sl}/E_{cr}$ is known as the anisotropy factor and is a measure of the extent of intermolecular interactions satisfied for a molecule exposed at a growth surface, compared to a fully satisfied bulk molecule.

### 3.4.6.2 Attachment Energy Morphological Prediction

Once the suitability of the intermolecular potential has been validated through lattice energy calculations, the attachment energies can be used to predict the morphology. Generally, morphological predictions created in this way give the best match to crystals grown in the vapour phase or at low driving force, as these conditions are closest to the equilibrium conditions in which the attachment energy morphology is predicted.

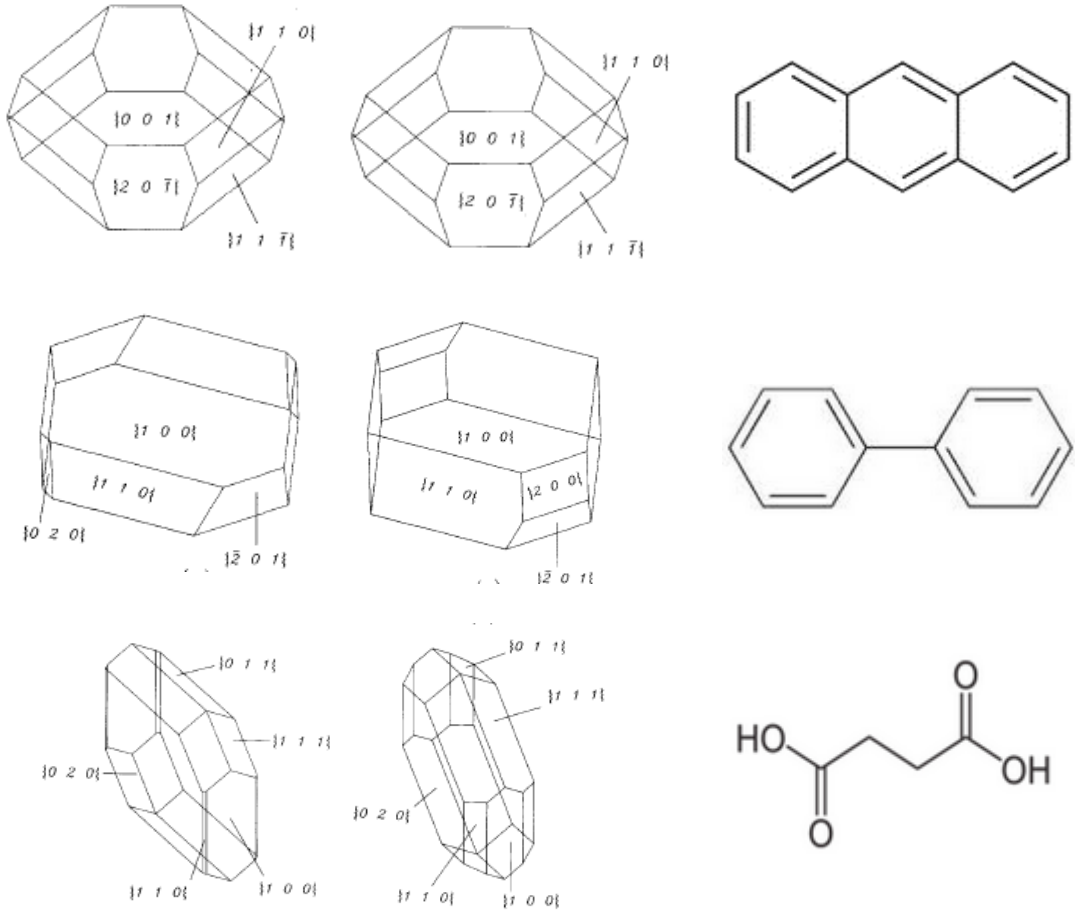


**Figure 3-12: Observed (left) and attachment energy calculated (right) morphologies for anthracene (top), biphenyl (middle) and succinic acid (bottom). Molecular structures shown on the right hand side[7]**

Figure 3-12 shows how the attachment energy model can give a good prediction of the shape of molecular crystals with varied functionality. The morphological prediction of anthracene almost completely matches the experimental crystal morphology. Biphenyl and succinic acid give a good match to the general shape of the experimental morphologies. However, biphenyl shows under estimation of the (-2 0 1) surface and

the succinic acid prediction is slightly thinner and over estimates the size of the (1 1 1) surface compared to the experimental morphologies. The morphologies predicted here are all rather equant, suggesting that the faces grow by stable crystal growth mechanisms such as BCF or B&S. Expanding on this idea, it is perhaps not surprising that the best match of prediction to experimental is anthracene, as this molecule can only form weak vdW interactions and also has no flexibility, probably resulting in stable, slow crystal growth.

## 3.5 Influence of Solution Environment on Crystal Morphology

The attachment energy morphological prediction is essentially a prediction of crystal morphology at equilibrium from the vapour phase. However, since the vast majority of industrial crystallisation processes take place in the solution phase, it is important to consider the effect of the surrounding solvent interactions at the crystal/solution interface on the growth of the important crystal faces. In addition, the crystal growth kinetics in solution can have a significant effect on crystal morphology.

### 3.5.1 Influencing the Morphology with Tailor Made Additives

Utilising additives that mimic the molecular conformation of a polymorph has been utilised for effectively suppressing the crystallisation of an unwanted polymorph[62]. The same principles can be applied with respect to suppressing the growth of a fast growing face by utilising molecular recognition at crystal interfaces[178, 179].

Roberts and co-workers developed a method of modelling the morphology of crystals in the presence of additives through the HABIT programme. The additives were split into 'blocking modifiers[180]' and 'disrupting modifiers[134]'. Blocking modifiers retard to the growth rate of a face by blocking the movement of the surface step/kink terraces, whilst the disrupting modifiers disrupt the intermolecular bonding networks. Figure 3-13 shows a schematic of the two different additive modification mechanisms.

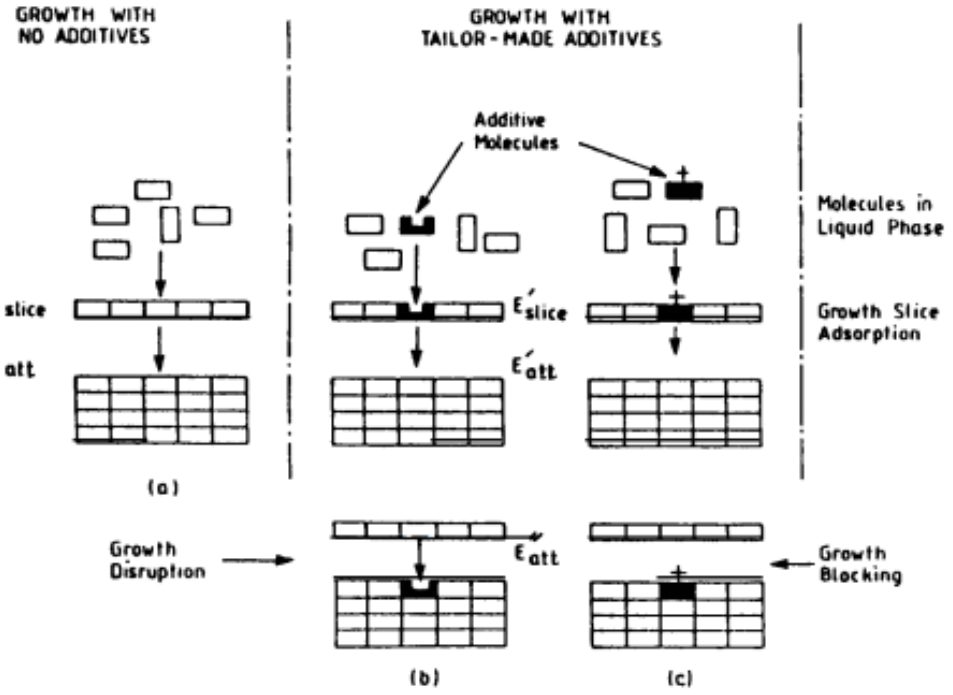


**Figure 3-13: Schematic showing the definition of the energy terms $E_{att}$, $E'_{att}$, $E''_{att}$, $E_{sl}$ and $E'_{sl}$ used in the morphological modelling of (a) pure systems; (b) systems containing disruptive type tailor-made additives and (c) blocker-type tailor-made additives[134, 180]**

Modelling the growth rate as a function of an additive resulted in the introduction of some new terms[134, 180] to expand Hartman and Perdok's classical attachment energy theory. $E'_{sl}$ is the slice energy calculated with additive at the centre of the slice; $E'_{att}$ is the attachment energy of a growth slice containing an additive onto a pure surface and $E''_{att}$ is the attachment energy of a pure growth slice onto a surface containing an additive.

### 3.5.2 Solvent Induced Modification of Crystal Morphology - Benzophenone

Figure 3-14 shows how the morphology of benzophenone is strongly modified when crystallised from toluene solutions. The size of the (0 2 1) surface is greatly enhanced whereas other surfaces, such as the (0 2 0) surface, are observed to grow out.

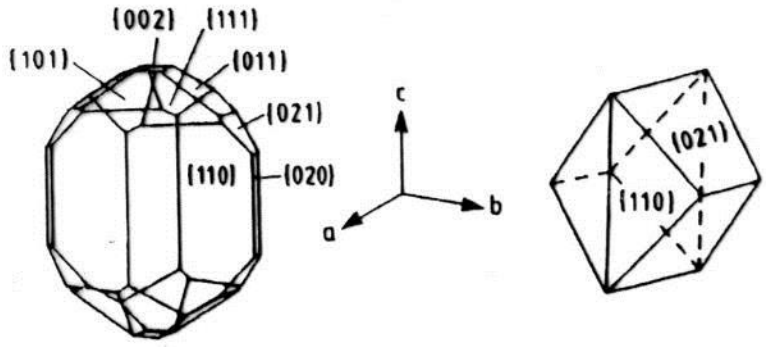


**Figure 3-14: Benzophenone morphology from most solvents (left) and from toluene (right)[4]**

Comparing how toluene interacts with the (0 2 1) and (0 0 2) surfaces can rationalise why the (0 2 1) surface is greatly enhanced in size, compared to the other faces, when benzophenone is crystallised from toluene.

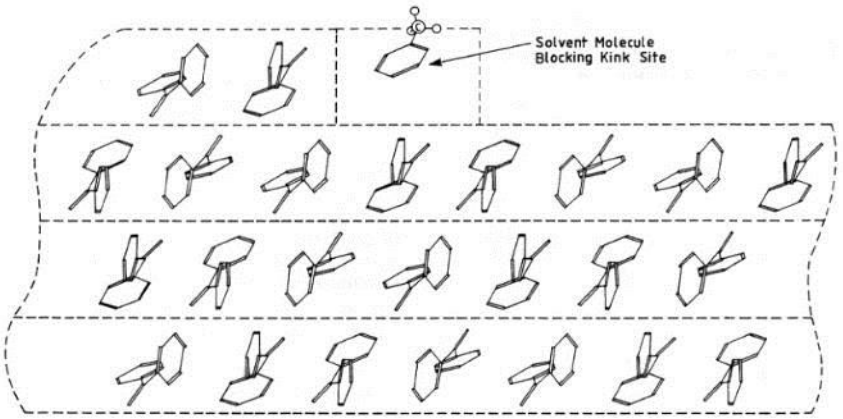


**(0 2 1)**

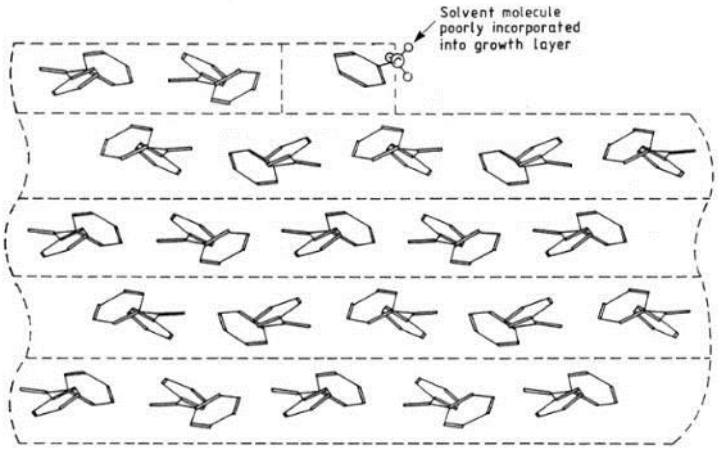


**(0 2 0)**

**Figure 3-15: Predicted solvent molecule incorporation at the (0 2 1) surface and (0 2 0) surfaces of benzophenone[4]**

The toluene molecule is observed to incorporate much more easily into the growth layer of the (0 2 1) surface compared to the (0 2 0). Therefore, the de-solvation of the (0 2 1) surface will be much slower and will have the effect of slowing down the growth rate of this surface and increasing the surface area. Compared to the (0 2 0), where toluene incorporation into the growth layer is much more difficult, growth will not be hindered and hence the face grows out and is not observed at the surface of benzophenone crystals grown from toluene.

Crystal morphology modification has been well studied, particularly in the cases of problematic needle-like morphologies[24, 181-184] that can be difficult to process and result in pipe blockages. Since morphology control has obvious industrial applications there are a variety of studies that utilise molecular modelling techniques to predict how crystal morphologies may be controlled.

### 3.5.3 Grid Based Methods for Predicting Solvent Induced Morphologies

If one wanted to predict the morphology of a range of crystals from different solutions, it would be computationally expensive and extremely time consuming to run MD simulations for a large range of solution environments. Hence, using computationally efficient grid based methods to calculate solute and solvent binding energies can allow prediction of solvent induced morphologies from calculations performed on a standard desktop computer in a matter of minutes.

#### 3.5.3.1 Grid Search Method for Modelling Extrinsic Synthons

The SYSTsearch programme[35] creates a three-dimensional grid near the surface of a crystal where a probe molecule explores every point to find the most favourable point at where a molecule may interact with a crystal surface.

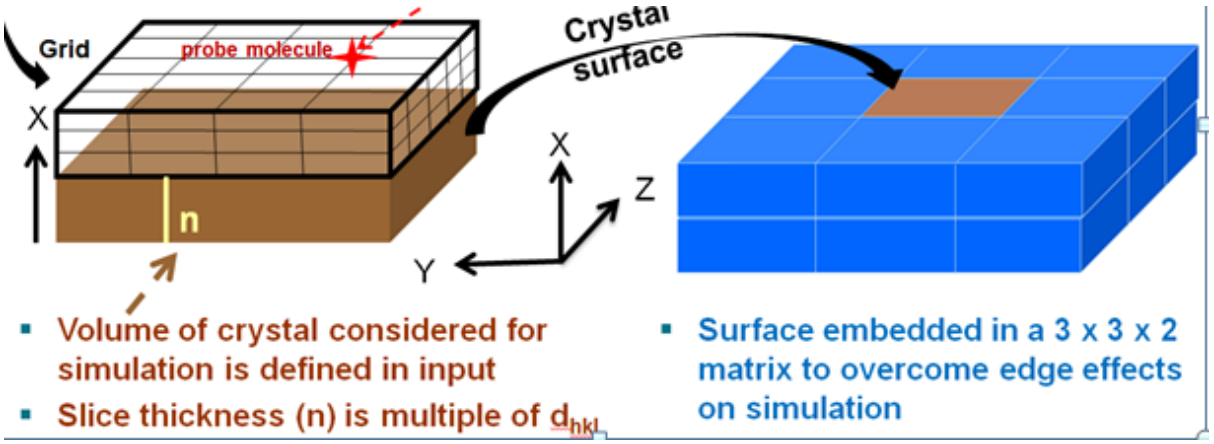


**Figure 3-16: Schematic of the how the SYSTsearch programme creates the grid around a given surface for a probe molecule to translate and rotate to find the most stable point[5]**

In addition to translating across the grid, the probe molecule is also allowed to explore rotational degrees of freedom at each point to find the most stable geometry. The most stable grid point can be outputted, or the distribution of interactions at each surface. This can allow prediction as to how solute or solvent molecules will preferentially bind to a given surface.

### 3.5.3.2 Aspirin Case Study

The SYSTsearch method for calculating the solute/solvent binding energies was used to calculate the solvent mediated morphology of aspirin[5]. The strongest solute and solvent binding energies to each surface was The binding energy of aspirin, ethanol and water molecules to the morphologically important surfaces of an aspirin crystal[5] were calculated using the SYSTsearch grid search of the surfaces. The attachment energies were then modified to account for the strength of the solute/solvent binding sites and the concentration of the solution, which resulted in the calculation of a solvent mediated morphology. The Figure 3-17 shows a comparison of the vacuum state morphology prediction, solution mediated morphology prediction and experimentally crystallised aspirin (both from a 62:38 ethanol:water mixture):

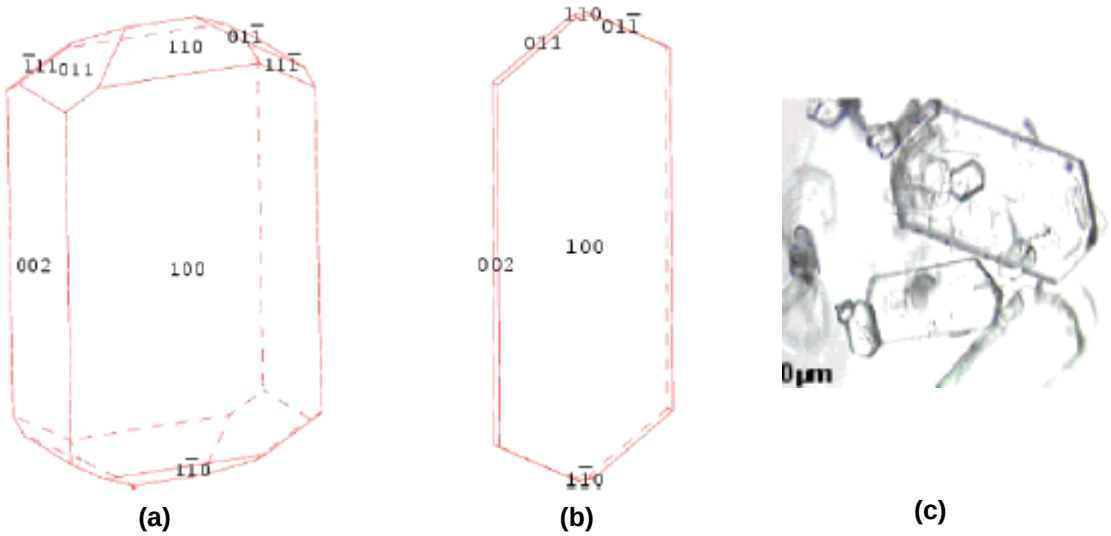


**Figure 3-17: Solution mediated attachment energy morphology prediction of aspirin crystals using the solute/surface and solvent surface interactions calculated using grid-based calculations: (a) Vacuum attachment energy morphology prediction. (Middle) Solution mediated morphology prediction in 62:38 ethanol: water mixed solvent. (Right) Experimental crystals from 62:38 ethanol: water mixes[5]**

The solution mediated morphology showed excellent agreement to the experimental crystals. Compared to the vacuum state morphology prediction, it is clear that the growth of the (1 0 0) surface has retarded significantly compared to the other major surfaces. Examination of this surface revealed that it has exposed carbonyl and hydroxyl groups at the surface, which hence are expected to strongly interact with the surrounding solvent and slow down the de solvation at this surface.

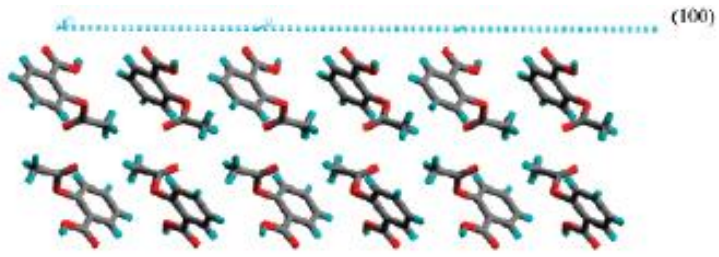


**Figure 3-18: Aspirin (1 0 0) surface cleaved in the perfect termination of the crystal structure showing the exposed hydrophilic carbonyl and hydroxyl functional groups[5]**

### 3.5.4 Molecular Dynamics

Molecular dynamics can be a powerful tool to simulate the path a solute, solvent or additive molecule takes when diffusing from solution to crystal surface[185]. The simulation of the molecular motion can provide a more accurate model of the surface in contact with solution and can offer improved insight into how solute and solvent approach a surface.

Molecular dynamics calculations can either be single growth units approaching a surface[185, 186] or, with increasing computing power, a full solvation layer of several hundred molecules at a surface can be modelled[187].

## 3.6 Material of Study: Para Aminobenzoic Acid

### 3.6.1 Structural Details of *p*ABA

The molecular structure of *p*ABA consists of a phenyl ring with a carboxylic acid group and amino group in the para position.

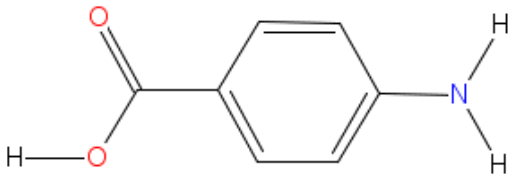


**Figure 3-19: Molecular structure of *p*ABA**

*p*ABA is known to crystallise in two well-characterised polymorphs, α[188] and β[189]. A recent study has revealed a third polymorph, this has an orthorhombic crystal structure, which was found by crystallising from aqueous solutions containing *p*ABA and selenous acid[190], but this latter structure was not considered here.

There are two published structures for α-*p*ABA and one published structure for β-*p*ABA. The crystallography details are shown in Table 3-1.

**Table 3-1: Crystallography details for the published structures for *p*ABA[188, 191, 192]**

| Polymorph | CSD Ref Code | Space Group | a (Å) | b (Å) | c (Å) | β (°) | Cell Volume (Å$^3$) |
|---|---|---|---|---|---|---|---|
| α | AMBNAC01 | $P2_1/n$ | 18.55 | 3.86 | 18.64 | 93.56 | 1332.32 |
| α | AMBNAC06 | $P2_1/n$ | 18.57 | 3.86 | 18.63 | 93.67 | 1327.06 |
| β | AMBNAC04 | $P2_1/n$ | 6.28 | 8.58 | 12.36 | 100.13 | 655.91 |

The intermolecular packing from the AMBNAC01 and AMBNAC04 crystal structures is shown in Figure 3-20.

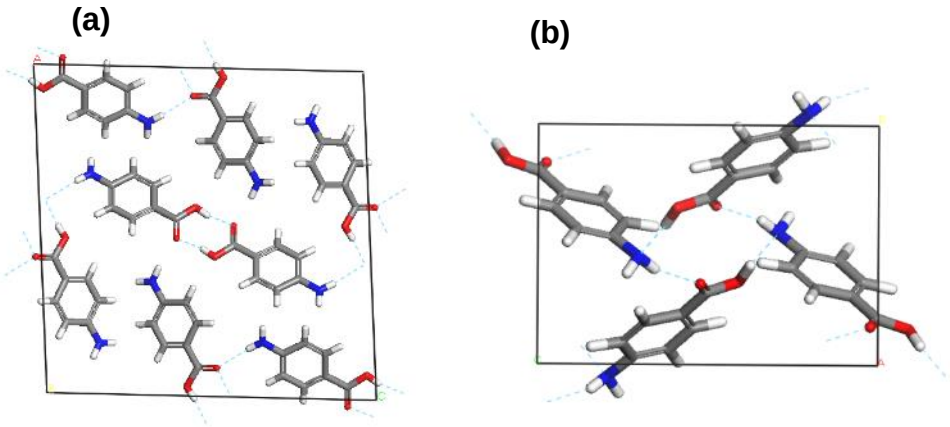


**Figure 3-20: Details of unit cells of α-*p*ABA (a) and β-*p*ABA (b) displaying their associated packing motifs. α packing comprising of COOH...HOOC H-bonding dimers and NH...O H-bonds. β packing consists of a 4 membered H-bonding ring with identical OH...N and NH...O interactions.**

Figure 3-20(a) shows that the packing of the α form is dominated by the formation of non-equivalent OH...O H-bonding dimers between neighbouring carboxylic acid groups. In addition, the *p*ABA molecules create a head to head stacking motif in the b direction creating strong interactions between the π orbitals associated with the phenyl ring. The interatomic forces themselves are usually relatively weak, however the close stacking of the molecules results in a large amount of atoms close to each other and interacting, therefore resulting in a stronger intermolecular force. Figure 3-20(b) shows that the packing of the β form is characterised by a 4 membered H-bonding ring motif consisting of alternating OH…N and NH…O H-bonds. In addition, the *p*ABA molecules also create head to tail stacking motifs creating strong π-π stacking interactions.

The α and β forms have been well characterised and are thought to have an enantiotropic relationship. The transition temperature has been reported as between 13.8°C and 16 °C[27, 28], with the alpha form being more stable thermodynamically above this temperature. Interestingly, even crystallisation experiments carried out below the transition temperature frequently yield crystals of the alpha form[192].

The beta polymorph crystallises as rhombic like prisms and was first reported by Groth in 1908 [193]who stated that the crystals found were monoclinic with axial ratios 1.4403:1:0.7312, β = 100.10° and density 1.393 g/cm$^3$. These early observations were confirmed by Prasad et al[194] who reported unit cell dimensions of *a* = 12.26 Å, *b* = 8.61 Å and *c* = 6.30 Å and β = 100.10°. Interestingly, this contribution highlights problems encountered when attempting to crystallise the beta form in that the driving force, supersaturation, must be kept small to obtain the beta phase in this instance by crystallisation from aqueous alcohol. Later Alleaume et al[195] confirmed that the beta form is monoclinic and reported unit cell dimensions *a* = 6.275 Å, *b* = 8.55 Å, *c* = 12.80 Å and β = 108.30°; *Z* = 4 and the space group $P2_1/c$. A re-determination of the crystal structure of the beta form was reported by Gracin and Fisher in 2005[189] (AMBNAC 04) who found cell dimensions *a* = 6.2782 Å, *b* = 8.5831 Å, *c* = 12.3649 Å and β = 100.13°; *Z* = 4 albeit with a different setting of the monoclinic space group 14 as $P2_1/n$. In 1965, Killean et al[196] attempted to repeat the experiment reported by Groth and Prasad by re-crystallising commercially available PABA from methanol, ethanol, acetic acid, acetone and dioxane solutions. They characterised three crystallographic forms but none of them corresponded to the rhombic crystals observed previously. Form *II* and form *III* were later shown by Grimm et al[197] to be solvates containing, respectively, acetone and dioxane. Form *I* found by Killean was later shown to be consistent with what is now known as the alpha form with unit cell dimensions of *a* = 18.55 Å, *b* = 3.86 Å and *c* = 18.64 Å, β = 93.56°; *Z*= 8 and the space group $P2_1/n$, published by Lai and Marsh[191] in 1967 (AMBNAC 01). The crystals of the alpha polymorph were observed to be long fibrous needles. The structure was revisited by Athimoolam et al[188] in 2007 (AMBNAC 06) who reported unit cell dimensions *a* = 18.57 Å, *b* = 3.84 Å, *c* = 18.63 Å, β = 93.67°, *Z* = 8 and the space group is $P2_1/n$. The intermolecular packing for these two structures quite similar with the Lai and Marsh structure refined with a slightly

pyramidal amino group, while the Athimoolam structure is refined with a planar amino group.

## 3.7 Conclusions

The prediction of crystal morphology through attachment energy theory has established the link between crystal growth rates, morphology and intermolecular interaction strengths and directionality[7, 13, 133, 178]. Morphological prediction of crystal structures with more isotropic crystal structures and experimental morphologies are found to give better agreement to these experiment morphologies. This is probably because crystals of this nature mostly grow by BCF and B&S crystal growth mechanisms, which facilitate slow stable growth.

Morphological prediction and control of needle-like morphologies is still significant challenge to crystallisation scientists[24, 182]. It can often be the case that needle-like morphologies appear in the case of unwanted metastable polymorphs crystallising alongside the desired polymorph. Otherwise, it could simply be that the desired polymorph presents as a needle, which is difficult to process due to their tendency to block pipes and often be very brittle.

The structural nature of the clusters that form in solution prior to nucleation can strongly influence the polymorphic form crystallised from a certain solvent(refs). Whereas the shape of the crystal is mostly governed by the growth process, which is strongly influenced by the face-specific crystal chemistry, i.e. synthons that can form at a specific crystal surface. Morphological prediction can identify such synthons that govern the face-specific growth, however calculating how different solvent environments influence the crystal morphology due to the competition between solute and solvent binding, along with how this affects crystal growth mechanisms can often be much more complex. Analogously, predicting the pre-nucleation solution structure and how this governs the polymorphic selection can also be extremely complex.

Therefore, it is apparent that understanding the solute-solute and solute-solvent interactions influence on the self-assembly in that solvent, along with the subsequent growth post-nucleation would result in being able to more accurately being able to predict the polymorph and shape of a crystal produced from that solvent. Molecular

dynamics simulations can sometimes provide information on microscopic molecular behaviour, both at the pre-nucleation clustering stage and at the crystal/solution interface. However, the complexity and computational expense of these types of simulations can make it difficult to perform these on a range of compounds.

This results in the need for simple to perform calculations that can provide a guide to the structural behaviour in pre-nucleation clusters and at the crystal solution interface, along with being able to rationalise these results against sensible experimental data. The solvent dielectric and statistical thermodynamic COSMO-RS approach offers a computationally efficient way of looking at the stability of single molecules in solution, whereby it has the potential to be expanded to clusters. The attachment energy theory can identify the synthonic nature of crystal surfaces. This knowledge can be combined with grid-based searching methods to identify more specific solute and solvent binding sites at a particular surface to complement the data from the attachment energy method. Therefore, this study will attempt to combine data from these different techniques for modelling intermolecular interactions and clusters to attempt to create a novel procedure for identifying their influence on polymorphism and morphology from specific solvents. This data will be compared to experimental data to attempt to correlate molecular and structural data to trends in experimental data, such as polymorphism and crystal growth mechanisms.

Development of computationally efficient methods for predicting the influence of solvent on polymorphism and crystal morphology would be significant step forward in enabling the digital design of a crystallisation process. Combination of microscopic data with more macroscopic models, such a computational fluid dynamics, could result in efficient design of a batch industrial crystallisation process.

# Chapter 4 Materials and Methods

*This chapter provides a guide to the experimental and computational methods that were utilised in this study. This should allow anyone to repeat and understand the work done in the thesis should it be needed.*

## 4.1 Introduction

This chapter provides a detailed summary of the calculations and experimental procedures utilised to collect the data described in this thesis. In this, the experimental details of the crystal growth experiments are described, including the methods for obtaining the solubility data. The details of the beamline and settings for the NEXAFS experiments undertaken at the synchrotron are outlined, along with details of sample mounting. Finally, the settings and functions used for the simulation data are detailed in the chapter to aid the reader's understanding of how the simulation data was obtained.

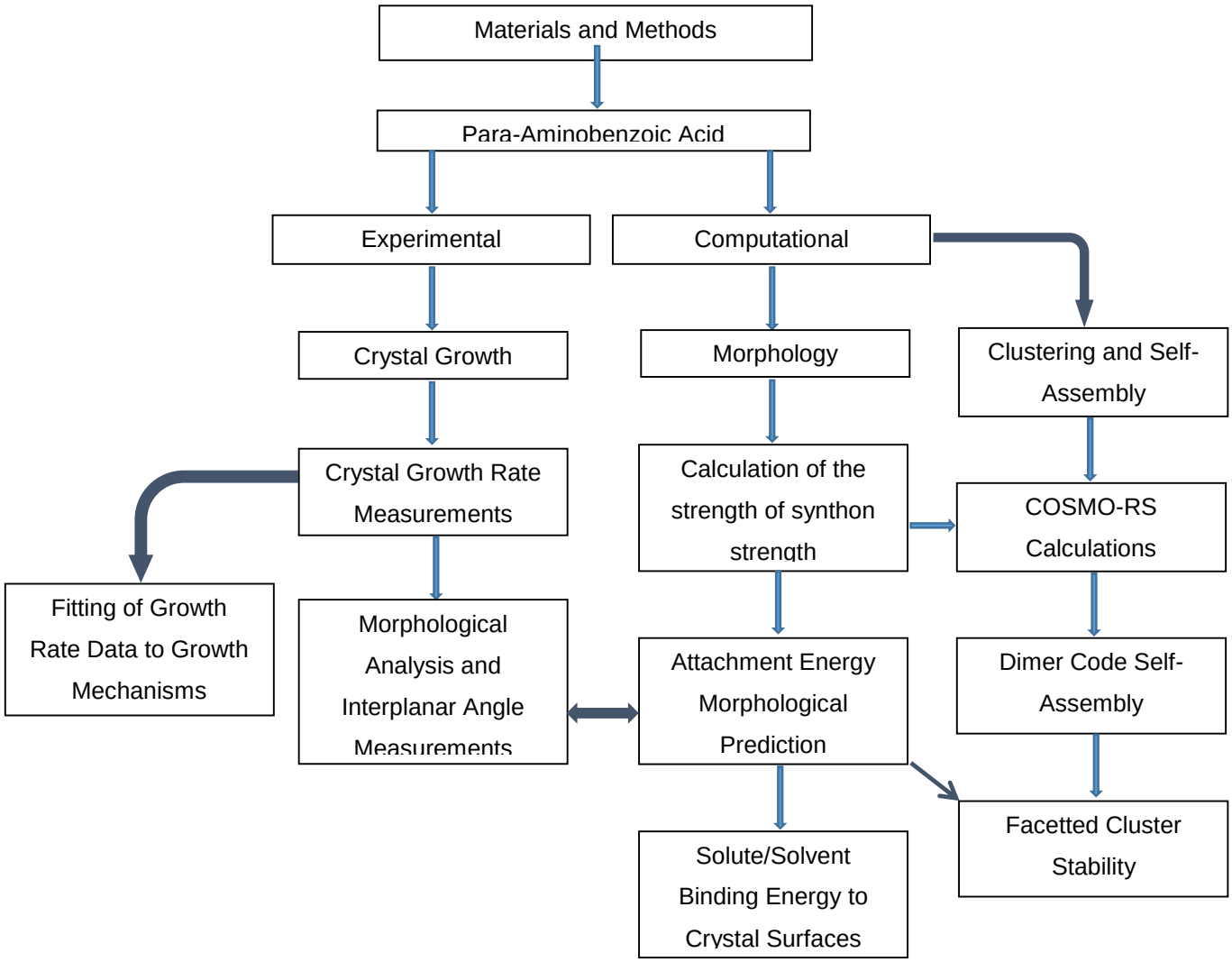


**Figure 4-1: Flow of methods used throughout the study**

## 4.2 Materials

### 4.2.1 Para Amino Benzoic Acid

99% purity powder α-*p*ABA was purchased from Sigma Aldrich and used as the starting material for all experimental work described in this study.

### 4.2.2 Solvents

#### 4.2.2.1 Nitromethane

99+% purity nitromethane was purchased from Acros Organics, CAS number 75-52-5.

#### 4.2.2.2 Ethanol

Absolute ethanol (purity 99.5+%) was purchased from VWR chemicals, CAS number 64-17-5.

## 4.3 Experimental Methods

### 4.3.1 Solubility Measurements

#### 4.3.1.1 Gravimetric Analysis

10 g of solvent was measured into a glass vial. At room temperature, α-*p*ABA powder was added into the solution and the solution shook by hand to dissolve the powder. Once the powder had stopped dissolving into solution upon shaking, the vial was sealed with a screw top and wrapped with parafilm. The vial was then placed into a Barstead Labline MaxQ 2000 shaker attached to a Jelabo F25 circulator. The circulator was set to 20°C and the vial was agitated for 24-48 hours. After agitation, the vial was checked to observe that the solid had not dissolved. The solution was left to equilibrate for 12 hours, remaining in the shaker so to hold the temperature of the solution.

For the measurement of the mass in the solution, a fresh vial was weighed on a four figure balance, including the lid. Including the lid is important when working with volatile solvents as solvent evaporation during weighing must be minimised. The supernatant was pipetted from the vial in the shaker into the pre-weighed vial, and the

vial, top and solution was weighed. The vial containing the supernatant was then placed in an oven set at 65°C, with the lid removed, for at least three days. After three days, no visible solvent could be seen and the vial plus lid was re weighed. The sample was placed back in the oven and the process repeated the next day to check if the weight of the vial plus sample had changed. Once no change in weight was observed it was accepted that all the solvent had evaporated from the sample.

The solubility in $g_{solute}/g_{solvent}$ was calculated from the following equations:

The mass of the supernatant taken from the saturated solution was calculated.

$$g_{solution} = g_{vial+lid+solution} - g_{vial+lid}$$ **Equation 4-1**

The mass of the solid left in the vial was then calculated.

$$g_{solid} = g_{solid+vial+lid} - g_{vial+lid}$$ **Equation 4-2**

Finally, the mass of the evaporated solvent was calculated.

$$g_{solvent} = g_{solution} - g_{solid}$$ **Equation 4-3**

Therefore, dividing the mass of solid by the mass of solvent reveals the solubility in grams of solute per grams of solvent.

$$Solubility_{g/g} = g_{solute}/g_{solvent}$$ **Equation 4-4**

## 4.3.2 Seeded Crystal Growth Rate Measurements

### 4.3.2.1 Growth of Crystal Seeds

Solid α-*p*ABA powder was added to 10 g ethanol at room temperature until no more solid would dissolve, and excess solid was left at the bottom of the vial. A magnetic stirrer bar was added to the solution and the solution was heated and stirred using a magnetic hotplate/stirrer. Once the solution had become clear, it was left at room temperature for around 24 hours, where crystals were observed to appear in solution. The solution was filtered and high quality seeds were selected from the bulk crystals. All crystals selected did not have enough mass to show on a four figure balance, i.e. less than 0.0001 g. This procedure was repeated in pure nitromethane to produce single crystals for analysis by single crystal X-ray diffraction.

#### 4.3.2.2 Crystal Growth Rate Measurements

The crystal growth rates were measured on seed crystals inserted into the vial. The seeds were grown from ethanol solutions. A room temperature supersaturated solution of ethanol was heated while stirring using a magnetic hotplate stirrer. The solution was allowed to cool to room temperature until crystals appeared. The crystals were filtered and high quality small single crystals were used for the measurements.

Solid α-*p*ABA powder was weighed on a four figure balance and then added to 10 g of solvent to create the desired supersaturated solutions. A magnetic stirrer bar was added to the solution and the solution heated and stirred until it became clear. Once the solution was clear, a small amount was transferred into a 0.8 ml glass cuvette cell using a plastic 1 ml Pasteur pipette. A pre-selected crystalline seed of α-*p*ABA was then added to the solution using a pair of tweezers. The lid of the cuvette was then wrapped in parafilm and placed inside the growth cell, which was held in place using a small piece of PTFE shaped in an arch. The cell was then placed on an Olympus IMT-2 inverted microscope with attached infinity analyse camera.

Two water circulating baths were employed to create a crash cool effect. One bath was set at 40°C to dissolve the crystal of as much surface imperfection as possible. Once the crystal had been dissolved the desired amount, the second circulator, set at 20°C was attached through using plastic quick change fittings. The temperature of the bath was confirmed using a hand held PT-100 temperature probe. Once the desired temperature was reached, images were captured at 1-2 minute intervals over usually a 10-20 minute period. The length and width of the crystals were measured using the Infinity Analyse2 software.

#### 4.3.2.3 Fitting of Measured Crystal Growth Rates to Growth Mechanism Equations

The crystal growth rate measurements were tabulated as a function of supersaturation within the OriginPro 8.5.1 data analysis and graphing software. Scatter plots were created using the ‘symbol’ and ‘y-error’ graphing functions for both the length and the width of the crystals, so the error from the fact that the growth rates were an average of 3-5 measurements was accounted for.

The crystal growth mechanism was then elucidated by fitting the equations associated with the BCF, B&S and RIG mechanisms (Figure 3-3, Section 3.2.4) to the crystal growth rates vs supersaturation curves. The BCF and B&S equations were fitted using the 'non-linear curve fit' module within Origin. The RIG fitting was done using the 'linear curve fit' module, also within Origin. The fitting was performed using a least sum of squares fit, and the goodness of fit was measured by how close the $R^2$ value was to 1. The growth mechanism where the equation relating growth rate and supersaturation fitted giving the closest $R^2$ value to 1 was then assumed to be the growth mechanism for the given surface.

### 4.3.3 Near Edge X-ray Absorption Fine Structure Spectroscopy

The near edge X-ray absorption fine structure (NEXAFS) spectroscopy was carried out on the U7A beamline at the National Synchrotron Light Source (NSLS) located at Brookhaven National Laboratory, Upton, New York, USA.

#### 4.3.3.1 Crystal Growth

The NEXAFS spectroscopy experiments required large single crystals. For preparation of large single crystals for surface chemistry analysis using NEXAFS spectroscopy, crystals were grown from slow solvent evaporation from 90:10 ethanol:nitromethane mixed solutions. Undersaturated solutions were prepared by dissolving powder α-*p*ABA in 90:10 ethanol:nitromethane mixes and the solution was transferred to pyrex circular dishes. The dishes were covered with perforated parafilm and the solvent allowed to evaporate over the course of up to three weeks.

#### 4.3.3.2 Beamline Details

Partial electron yield (PEY) spectra for the C, N, and O Kedges were collected via a channeltron electron multiplier with the sample. A monochromator with a 600 l/mm grating was used for the C and N Kedges, providing energy resolution of 0.1 eV for C and ~0.15 eV for N and photon flux of ~2 × 1011 photons/s; and 1200 l/ mm for the O K-edge with an energy resolution of ~0.15 eV and photon flux of ~1 × 1011 photons/s (comparable to the XPS Al Kα source). After collection, the spectra were normalized by the simultaneously recorded drain current (total electron yield, TEY) from an in situ gold-coated, 90% transmission grid (I0) placed in the incident X-ray beam to eliminate the effect of incident beam intensity fluctuations and beamline optics absorption

features. The monochromator energy scale was calibrated using the 285.1 eV first π* transition of an amorphous carbon grid for the C K-edge, 400.6 eV first π* on a titanium nitride grid for N, and I0 first minimum at 531.2 eV for O.

#### 4.3.3.3 Conventional Angular-Dependent NEXAFS

A single crystal of α-*p*ABA was mounted onto a 3-circle goniometer using double sided copper tape. The goniometer had rotation about 3-axes θ, Φ and in-plane azimuthal rotation (Figure 4-2).

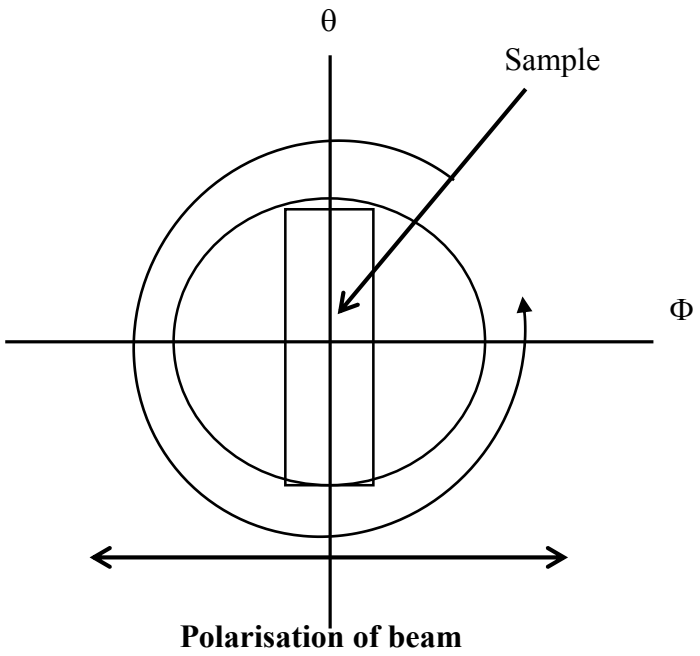


**Figure 4-2: Schematic of the mounted α-*p*ABA crystal on the goniometer showing the axes of rotation available. The beam is directed perpendicular to the plane of the page**

The sample was rotated about all three axes while the angle of the beam was kept constant, with the beam polarisation held horizontal. The principle of NEXAFS experiments involves the detection of emitted photons as a result of exciting electrons from core orbitals. To excite the electrons, a synchrotron beam was focussed on the crystal and the energy scanned from just below to above the C, N and O k-edge. The k-edge represents the energy needed to excite an electron from a 1S core orbital. The auger electrons that escape from the surface, which give information about the surface

structure, are detected as the electron yield. Whereas the fluorescence photons that escape from deeper into the sample, providing information on the bulk structure, is detected as fluorescence yield.

The detection of emitted photons at different energies prior to the absorption edge is related to what sort of bonding environment the electrons are in, e.g. π or σ bonds, along with the elements that are involved in the bond. The polarisation of the beam also affects the intensity of the peaks, so the sample was rotated in the in-plane azimuthal angle, the ϕ and the θ angles shown in Figure 4-2. All of the conventional NEXAFS experiments were performed on the same crystal.

#### 4.3.3.4 NEXAFS Imaging

Four large single crystals were mounted onto a bar of copper tape and moved along into the path of the incident beam. The LARIAT Mk1 (Large Area Rapid Imaging Analytical Tool) NEXAFS microscope at the U7a station at the National Synchrotron Light Source (NSLS) magnetically guides electrons to a detector to create a NEXAFS image with spatial resolution of 50μm[198].

The imaging soft X-ray beam was rastered across an 18 X 13mm$^2$ sample area. Electrons followed magnetic field lines to the rapid parallel processing magnetic field electron yield optics detector where a series of two-dimensional images were produced as the incident X-ray beam was scanned above the C, N and O *K* edges. The image stack gave information of the structural chemistry at the top ~10nm of the crystal surface.

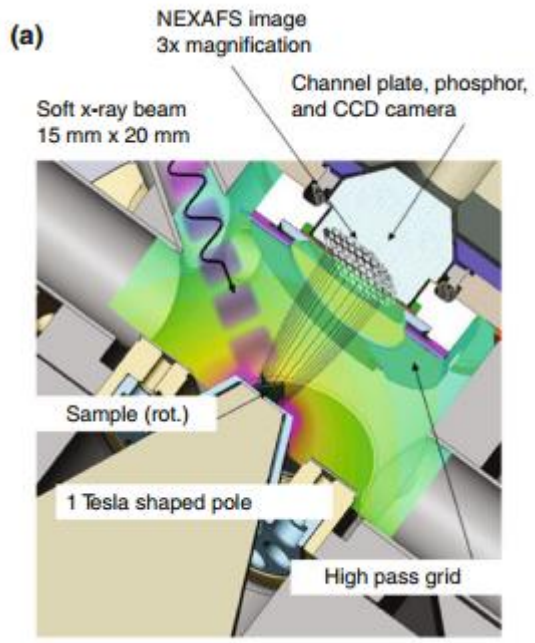


**Figure 4-3: Schematic of the inside of the NEXAFS imaging chamber used at U7A[199]**

Figure 4-3 shows how the soft x-ray beam comes in from the left hand side (purple) and strikes the sample. The sample(s) are mounted on a copper bar where they can be tilted about the axis coming up from the page shown in Figure 4-3. The tesla shaped pole magnetically guides the excited electrons emitted from the surface to a detector and CCD camera. The detector is a full field parallel process magnetic field electron yield optics detector which produces a series of two dimensional NEXAFS lateral images. The image stack reveals information on the chemistry of the surface with 50μm resolution.

For these experiments 4 crystals were mounted on the copper bar at different azimuthal angles. The samples were measured at the C, N and O K-edge to produce images of the bond chemistry associated with each element.

#### 4.3.3.5 Data Processing and Analysis

The conventional angular dependent NEXAFS data was processed using Athena[200, 201]. Peak fitting and fitting of arc tangent steps for the ionisation potentials was also carried out within Athena using the 'peak fitting' tool. Gaussian peaks were fitted to the relevant resonances associated with the bonds.

The data was imported into Athena, where the PEY or FY was plotted over the reference channel, the values from the upstream standards described in Section 4.3.3.2. To achieve the most accurate relative peak sizes, the pre-edge and post-edge lines were manipulated as such that they were as flat and parallel as possible, as shown in Figure 4-4.

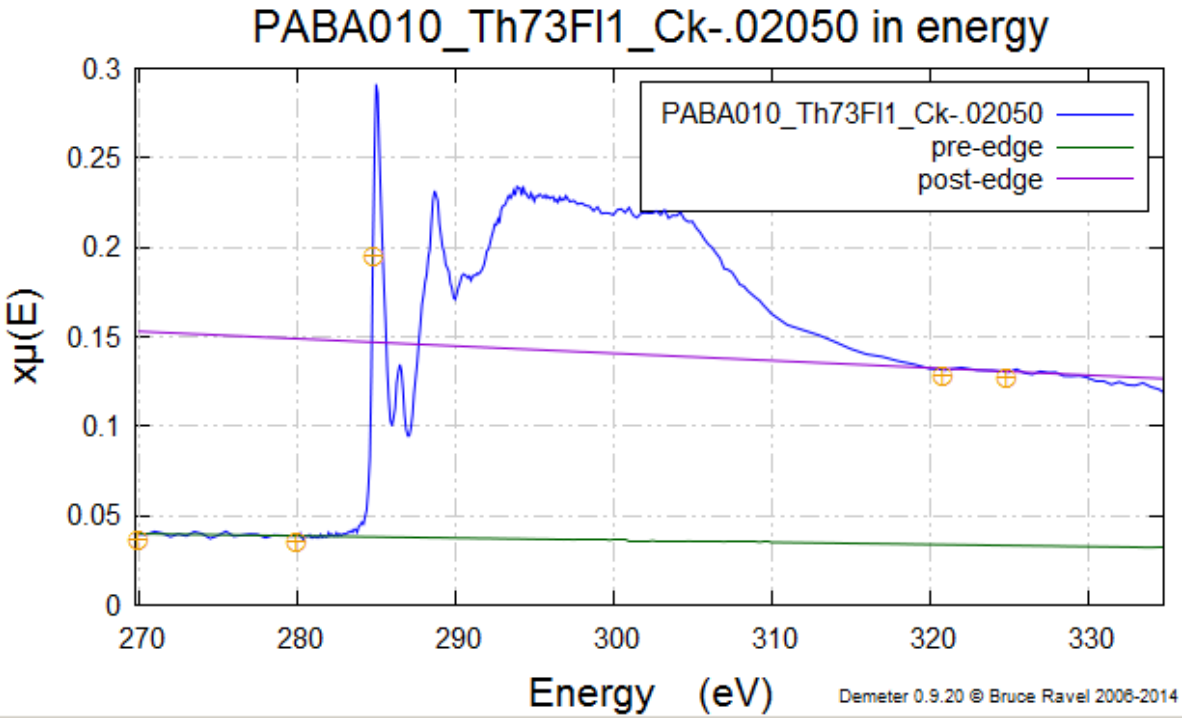


**Figure 4-4: Carbon K-edge NEXAFS spectra showing how the pre- and post-edge is defined from the purple and green lines. The energy range of the pre- and post-edge can be manipulated (the orange circles) to give as straight and as parallel lines as possible. The middle orange circle is $E_0$ (absorption edge)**

The energy ranges of the pre- and post-edge were manipulated such that both lines were parallel and straight, therefore the relative peak sizes could be most accurately measured.

## 4.3.4 X-Ray Diffraction

### 4.3.4.1 Powder X-Ray Diffraction

PXRD was used as a tool for polymorph characterisation on a regular basis for confirming the purity of the two phases of *p*ABA. This was carried out using a Bruker D8 advanced x-ray diffractometer[i] which used Cu Kα radiation and a germanium

primary monochromator in Bragg-Brentano reflection geometry. The step size used was 0.033 2θ and the step time used was 0.7 s/step over a 2θ range of 4-39.8 2θ. The detector used was a Vantec-1 position sensitive detector.

#### 4.3.4.2 Single Crystal X-Ray Diffraction

A crystal was mounted on a MiTeGen loop and X-ray diffraction data were collected on an Agilent SuperNova diffractometer with Cu-$K\alpha$ radiation ($\lambda$ = 1.54184 Å) at 100(1) K. Data were corrected for Lorentz and polarization effects, and absorption corrections were applied using multi-scan methods. The structure was solved by direct methods and refined by block-matrix least-squares on $F^2$ using the CrysAlis$^{Pro}$ 5.2[202].

### 4.3.5 Scanning Electron Microscopy

The Hitachi Bench Top TM3030Plus SEM was used to analyse the morphology of some of the crystals. A beam of electrons are accelerated with a potential of 5 – 15kV towards a sample mounted on a black carbon sticker on a metal stub. The specimen is scanned and an image is created either from the detection of high energy back scattered electrons that originated from the accelerated electron beam, or low energy secondary electrons that originated from within the sample surface

## 4.4 Computational Methods

### 4.4.1 Molecular Structure Analysis

#### 4.4.1.1 Torsion and Bond Angle Measurements

The torsion and bond angles were measured using Materials Studio 5.5[203]. For both types of angle measuring the measure tool was used. The torsion angles were four body, where the amino group torsion was a measure of the torsion angles between the plane of the phenyl ring carbons and the hydrogens attached to the nitrogen defined as C-C-N-H. Similarly, the carboxylic acid group torsion was defined as the torsion angles between the plane of the phenyl ring carbons and the oxygens of the carboxylic acid group.

The bond angles measured were three body and the varying bond angles are defined in the results section.

#### 4.4.1.2 Optimisation of Molecular Structure

The optimisation of the molecular structure of the molecules associated with the different polymorphs of *p*ABA was achieved using the Density Functional Theory programme DMol3[204, 205] module within Materials Studio 5.5[203]. The structures were optimised at the DNP (double numerical with polarisation) level of theory using a GGA/BLYP functional. The core treatment was set to 'all electron'.

The DNP basis is known as a split valence basis set. The different orbitals of the split have different spatial extents, the combination of different vectors in the basis set allows the electron density to adjust its spatial extent appropriately for the molecular environment.

#### 4.4.1.3 Data Searching within the Cambridge Structural Database

The 'Draw' function within Conquest 1.17 was used to draw the COOH and $NH_2$ fragments. For the torsion angle measurements, the 'Define Parameters' function within the '3D' menu was used to define the atoms involved within the torsion. Similarly, for analysis of interatomic distances of structures within the CSD containing OH…O, NH…O and OH…N hydrogen bonds, the interacting fragments were drawn and the hydrogen bonds defined using 'Define Non-Bonded Contact'. The results were transferred to Mercury 3.5 using the 'Analyse Data' function. The histograms of number of hits as a function of bond angle were created using the 'Plots' function within the 'Data Analysis' module of Mercury 3.5.

### 4.4.2 Calculation of Synthon Strength and Morphological Prediction

HABIT98[14, 206] was used for the calculation of the pairwise intermolecular interactions and lattice energy. HABIT98 takes structural information and constructs a series of unit cells in three dimensions. From a molecule in the origin cell, the non-bonded energy between it and all other molecules in the other unit cells are calculated within a user-defined radius.

#### 4.4.2.1 Input Files for HABIT98

The structural information of the crystal was read in the form of a fractional coordinate .cssr file. A .cif file was taken from the CSD and imported into Materials Studio 5.5, where the crystal structures were optimised using the Dreding potential[75], then the

structure was exported as a .car file. The .car file was converted to a .cssr file using CrystalManipulate08.

Since the .cssr file contains on the fractional coordinates of the asymmetric unit, the position of the other asymmetric units that are symmetrically related to the initial unit to make up the unit cell are calculated using a symmetry matrix, known as symmetry operators.

```
 1  0  0  0  1  0  1  0  0  1  0  0  1  0  1
-1  0  0  1  2  0  1  0  1  2  0  0 -1  1  2
-1  0  0  0  1  0 -1  0  0  1  0  0 -1  0  1
 1  0  0  1  2  0 -1  0  1  2  0  0  1  1  2
```

**Figure 4-5: Example of the symmetry matrix used in the HABIT98 calculations for *p*ABA. Each line corresponds to a position of the molecule within the origin unit cell. Each pattern of 5 numbers in a line corresponds to the position in x, y and z, hence 15 numbers per line**

Figure 4-5 shows an example of a symmetry operators matrix. Each line corresponds to an asymmetric unit in the unit cell, with the first line being the origin asymmetric unit. Each set of 5 numbers on a line corresponds to the position in the x, y and z directions, with respect to the unit cell parameters. The first three numbers consist of two zeros and a +/-1. The position of the +/-1 reveals which direction is being referred to, if it is the first number then it is travelling in the x direction, the second then it is in the y direction and if it is the third then it is in the z direction. The +/- is direction with respect to the origin. The last two numbers in each matrix correspond the distance travelled with respect to the unit cell length in each direction, ‘0 1’ corresponding to a full unit cell length in that direction and ‘1 2’ corresponding to half of that unit cell length in that direction.

#### 4.4.2.2 Lattice Energy and Synthon Strengths

To calculate just the synthon strengths and lattice energy, HABIT98 was ran using ‘LATT’ mode. The ranking of the intermolecular interactions by strength was outputted using the DEBUG-1 function. The α form has two molecules in the asymmetric unit (α1 and α2) and the lattice energy was averaged over the summations with respect to the two molecules. Therefore the ranking of intermolecular interactions had to be partitioned between α1 and α 2.

The intermolecular interactions were calculated using the Momany force-field[73] containing a Lennard-Jones potential for the vdW interactions (Equation 4-5), a specific 10-12 H-bonding potential (Equation 4-7) and a Coulombic term with respect to the electrostatic interactions.

$$U_{NB}(r_{ij}) = \sum_{i=1}^{n}{}' \sum_{j=1}^{M}{}' \left( {A^{k1}}/{r_{ij}}^{12} - {C^{k1}}/{r_{ij}}^{6} \right)$$ **Equation 4-5**

Where $A^{k1}$ is a parameter that indicates the minimum of the repulsive well from the average calculation over a number of crystals[73], $r_{ij}$ is the distance between the interacting atoms and $C^{k1}$ was calculated from Equation 1-6.

$$C^{k1} = \frac{3}{2}\left[\frac{e\hbar}{m_e^{1/2}}\right]\frac{\alpha_k \alpha_l}{(\alpha_k/N_k)^{1/2}+(\alpha_1/N_l)^{1/2}}$$ **Equation 4-6**

Where $\alpha_k \alpha_l$ are experimentally determined polarisabilities[207], $N_k$ and $N_l$ are the effective number of electrons for atom types $k$ and $l${**Scott, 1966 #473**}**,** $e$ is the elementary charge, $\hbar = h/2\pi$ and $m_e$ is the mass of an electron.

Since the non-bonded interactions between a hydrogen covalently bonded to a more polar atom, such as oxygen, and an adjacent polar atom are stronger than the other vdW interactions, a specific potential is used to calculate these strengths in equation 4-7.

$$U_{GHB}(r_{H\ldots X}) = \sum_{i=1}^{n}\sum_{j-1}^{M}(A_{H\ldots X}/r_{H\ldots X}^{12} - B_{H\ldots X}/r_{H\ldots X}^{10})$$ **Equation 4-7**

Where $r_{H\ldots X}$ is the distance between the hydrogen and the adjacent polar atom, $A_{H\ldots X}$ and $B_{H\ldots X}$ are parameters that depend on the polar atom involved in the H-bond, derived from molecular orbital calculations[208].

$$U_{e1}\left(r_{ij}\right) = \sum_{i=1}^{n}\sum_{j=1}^{M} {332.0qiqj}/{Dr_{ij}}$$ **Equation 4-8**

Where $qi$ and $qj$ are the fractional charges calculated for each atom and D is taken to be 2 and known as the 'effective dielectric constant'. The dielectric constant is set to 2 as changing the dielectric constant per crystal would be complex and require a new H-bonding potential.

For the calculations of the electrostatic interactions, the Restrained Electrostatic Potential (RESP) charges based on *ab initio* MP2/aug-cc-pvtz theory derived from the Antechamber within Ambertools were calculated{D.Toroz, 2015 #237}. The single

molecule of *p*ABA was optimized at the MP2/aug-cc-pvtz level and the optimized structure's electrostatic potential was calculated with Gaussian09[209]. The ESP data created from Gaussian is converted into a RESP format in Antechamber and finally the RESP fit is applied with Ambechamber to calculate the actual RESP charges.

#### 4.4.2.3 Lattice Energy Calculations and Functional Group Contributions

The breakdown of lattice energy per molecule, atom type and functional group was achieved using the DEBUG-2 function. For the purposes of molecular analysis, *p*ABA was sub-divided into three molecular components: amino, phenyl and carboxylic acid. The functional group contributions to the lattice energy reflect the summation of the individual contribution of the atoms involved within each component. The contributions per functional group and per atom type were summed over the asymmetric unit.

The nomenclature used to label the interactions identified the strongest interaction as capital A (i.e. alphabetically), with α or β referring to the polymorphic form and 1 or 2 relating to the different crystallographically independent molecules within the asymmetric unit (α-structure). The packing diagrams were annotated to show some of the strongest interactions with two labels on, e.g. Dα1/Dα2, indicates the intermolecular interactions between the two molecules within the asymmetric unit.

This basic nomenclature was also used to characterise the surface-specific interactions a given surface (*hkl).*

#### 4.4.2.4 Morphological Prediction

The morphologically important forms [169] as defined by the BFDH rule (section 3.4.3) were calculated using Morang[168]. Morang utilises the unit cell information and calculates the interplanar spacing in each crystallographic direction and then ranks them in descending order. The faces with greatest interplanar spacing are thought to be morphologically important.

The lattice energy was then sub divided into slice and attachment energy per form using the 'FULL' mode within HABIT98, according to the equations in Section 3.4.6. The 'automatic slice shift' routine was employed to find the most stable slice.

The attachment energies were checked to make sure that all the energies were negative. All of the energies were then divided through by the lowest absolute value,

to create a relative centre to face distance from the nucleation centre to the crystal surface. The crystallographic data and relative centre to face distances were then inputted into Shape[153] to draw a Wulff plot of the predicted morphology (section 1.3.2)

Additionally, activating the 'DEBUG -1' option when the programme is running in 'FULL' mode results in output of which intermolecular interactions are contributing to the slice energy and which are contributing to the attachment energy of each of the morphologically important faces that were selected for examination.

#### 4.4.2.5 Interfacial Angle Measurements

The interfacial angle calculations were based on the angles between crystallographic planes calculated using Morang[168]. The unit cell parameters were inputted into the program and the 'angle between two planes' option selected, where the miller indices of the two planes were entered. These were compared to experimentally measured interfacial angles.

### 4.4.3 Explicit Cluster Energies

The crystal structures of the α and β forms of *p*ABA were sub divided into pairwise interactions based on the strength of the intermolecular interactions calculated and the other remaining interactions within the unit cell. These dimers were then used to build up related tetramer and octamer clusters based on the crystal structures.

The explicit intermolecular interaction energy between molecules within either solute-solute or solute-solvent clusters were calculated using HABIT. The fractional coordinates and charges were entered into HABIT, with only the identity symmetry operators inputted, along with only one unit cell. The amount of molecules in the cluster was made equal to 'amount of molecules in the asymmetric unit', so the interactions between all the molecules inputted was examined. The total energy of all the intermolecular interactions between all the molecules was summed and displayed as 'cluster energy' in the results.

### 4.4.4 Implicit Solvation Treatment of Solute Clusters

Solution thermodynamic properties of these dimers, tetramers and octamers were calculated through the COSMO-RS approach (described in section 2.6.4.1). This combined DFT and statistical mechanics approach involves the optimisation of the

clusters using a solvent continuum DFT approach and then calculation of the intermolecular interactions using a statistical mechanics ensemble.

#### 4.4.4.1 DFT/Solvent Continuum Optimisation

Initial optimisations were carried out using the DMol3[204, 205] module within Materials Studio 5.5[203]. The optimisations were carried out at the DNP level of theory using the GGA/PBE functional (similar to the optimisations described in section 4.4.2), as this functional has been parameterised for use within the COSMO-RS theory. The 'Use Solvation Model' box was checked within the 'electronic' tab and the desired solvent selected. This activated the use of a solvent dielectric continuum during the optimisation (described in section 2.6.4). If the solvent wasn't available then the dielectric constant was entered manually from literature values.

For calculations requiring a higher level of DFT theory, the quantum chemical package Gaussian09[209] was employed. These calculations used a 6-31G* basis set to better describe the orbital spatial distributions, which are even more important for clusters since the valence electrons may now be taking part in interatomic non-bonding interactions which can distort the orbitals shape. In addition, the M06 functional also can better calculate the dispersion forces between the molecules in the cluster to correctly find the optimum geometry.

#### 4.4.4.2 Statistical Thermodynamics Calculations

The statistical mechanics calculations were carried out within COSMOthermX version C30_1501[107]. All of the .cosmo files produced from the DFT calculations could be loaded directly into the COSMO*therm* program.

#### 4.4.4.3 Normalised Weight Factor

The relative stabilities of different molecules/clusters were compared in COSMO*therm*, provided that they were both the same molecular weight. Up to 10 different molecules/clusters (referred to as conformers) could be compared at a time, where the relative stability of each was normalised against the Boltzmann distribution to provide a relative population of each user inputted conformers (see Section 2.6.4.1).

Within COSMO*therm* the 'mixture' property within the 'chemical potential' tab was selected. The clusters were selected by labelling each cluster of the same molecular

weight (i.e. dimer, tetramer or octamer) with the label 'paba' and a number between 0 and 9. The 'automatic conformer detection' box was checked that allowed the .cosmo files with the 'paba' labelling that are found within the same file to be treated as conformers of each other. The relevant parameterisation based on the previous DFT calculation was selected, PBE/DNP if the DFT calculation had been carried out within DMol3 and TZVP if the DFT calculation had been carried out within Gaussian09. The relevant solvent .cosmo file was selected and the concentration set to infinite dilution for the solute, the 'activate conformer treatment' box checked and the temperature set to 25°C before running the calculation.

### 4.4.5 Grid-Based Molecular and Surface Searching

Grid based search calculations for finding favourable binding sites for solute and solvent, first to a single molecule of *p*ABA and then to a surface, were performed.

#### 4.4.5.1 Molecular Pair Searching

The most favourable binding sites of a *p*ABA molecule solvent molecules to a single molecule, or OH...O interacting dimer, of *p*ABA were tested using the dimer SYSTsearch code[210, 211]. The programme operates with a stationary and mobile phase, this this case they can be single molecules or dimers so will simply be referred to as a 'body'.

The programme operates by keeping the coordinates of the stationary body frozen, while the mobile body moves along a user defined grid. The mobile body moves in a spherical polar coordinate system around the stationary body (Figure 4-6).

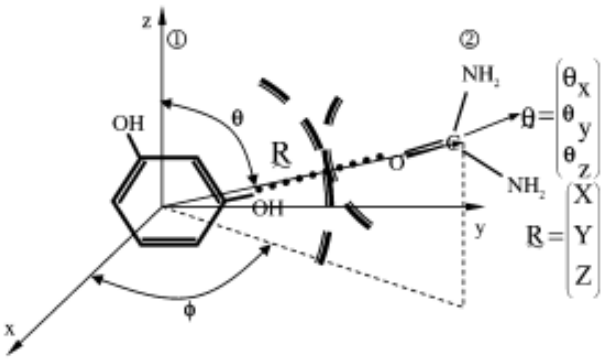


**Figure 4-6: Cartesian coordinate system for assessing molecular pairs in isolation[210]**

Within the Cartesian spherical polar coordinate system, translational steps are defined by a translational magnitude (λ), and a unit vector defined by two spherical polar angles (θ) and (Φ), where the grid points are spaces at angular intervals of Δθ and ΔΦ. The orientation of the mobile molecule is defined by three orientation angles ($\theta_x$, $\theta_y$ and $\theta_z$), therefore;

$$\begin{pmatrix} x_i' \\ y_i' \\ z_i' \end{pmatrix} = \mathbf{M} \begin{pmatrix} x_i \\ y_i \\ z_i \end{pmatrix} + \lambda \mathbf{R}$$

Where $x_i, y_i$ and $z_i$ are the atomic coordinates of the mobile molecule at the starting location, $x_i', y_i'$ and $z_i'$ are the final coordinates following transformation, $\mathbf{M}$ is a rotation matrix (a function of $\theta_x$, $\theta_y$ and $\theta_z$), $\mathbf{R}$ is the position vector of the centre of the coordinates of the mobile molecule and $\lambda$ is a translational magnitude that is minimised with respect to the intermolecular pair potential energy. Typical van der Waals radii are used to determine the minimum separation between the centre of the fixed and mobile molecules for each direction selected for translation of the mobile molecule. The identified distances are used as the starting point for a one dimensional minimisation of the pair potential energy to determine the final location of the mobile molecule for a given orientation and direction of translation. The atom-atom forcefield parameters used are the same as described in Section 4.4.2.1.

For the calculations in this study, solvent molecules of water, ethanol and nitromethane were searched round either a stationary single molecule, or an associated OH...O dimer of *p*ABA. The energy of all the interactions between the mobile body at a point on the grid and the stationary body are calculated and ranked.

For this study, the top energy structure was selected as the input coordinates for the second run. Therefore, the original coordinates plus the selected solvent position are frozen and another solvent molecule is searched around the new stationary body. This is repeated for as many molecules as is desired. No optimisation is calculated between the addition of the solvent molecules.

### 4.4.5.2 Surface Searching

The grid based principle was also applied to searching for the most stable binding site of solute and solvent molecules to a crystal surface rather than a single molecule[5, 35]. An input file for the surface search programme is shown below.

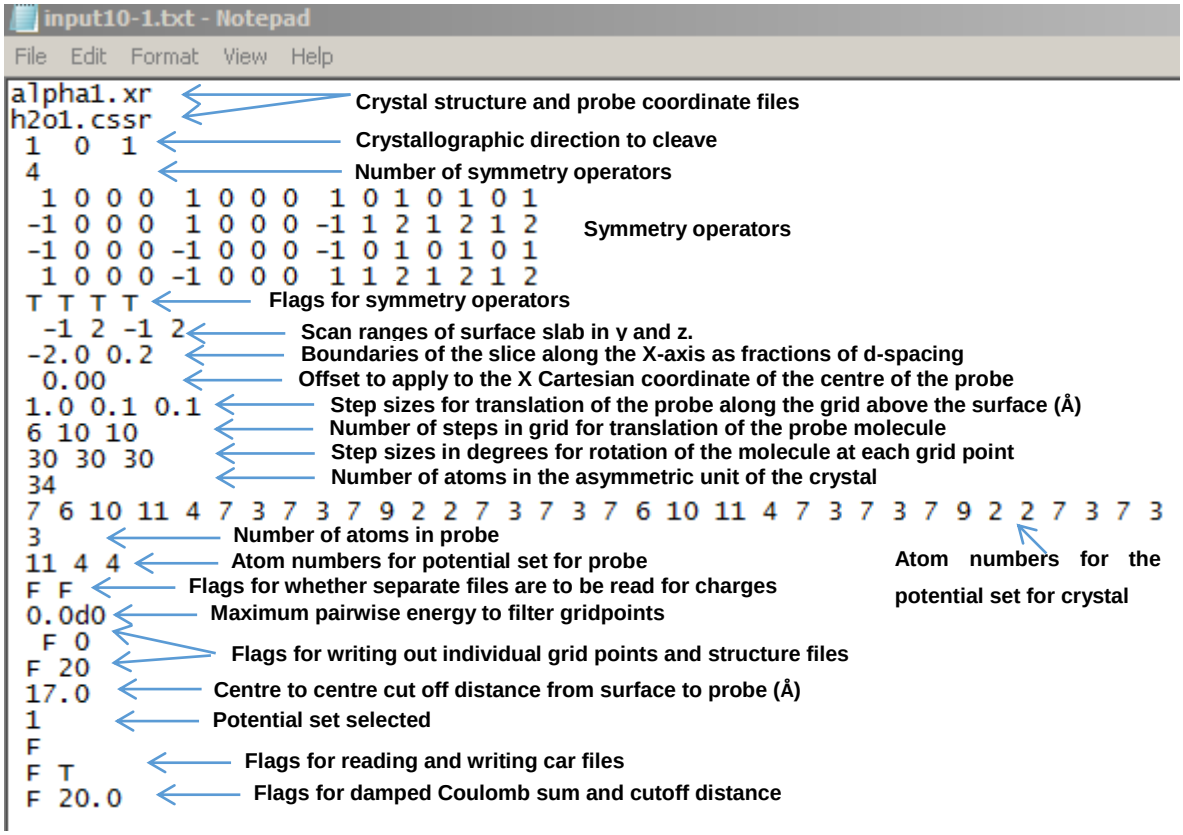


**Figure 4-7: Input file for the surface search programme. Parameters for the grid size around the surface, step size for the translation and rotation of the probe and the thickness of the surface slab are included**

The fractional coordinates of the asymmetric unit of the crystal are read in and treated with symmetry operators to create the asymmetric unit, in much the same way as described in Section 4.4.2.1. The crystal is then cleaved in a crystallographic direction to create a crystal surface, with the thickness being described in terms of d-spacing (Figure 4-8).

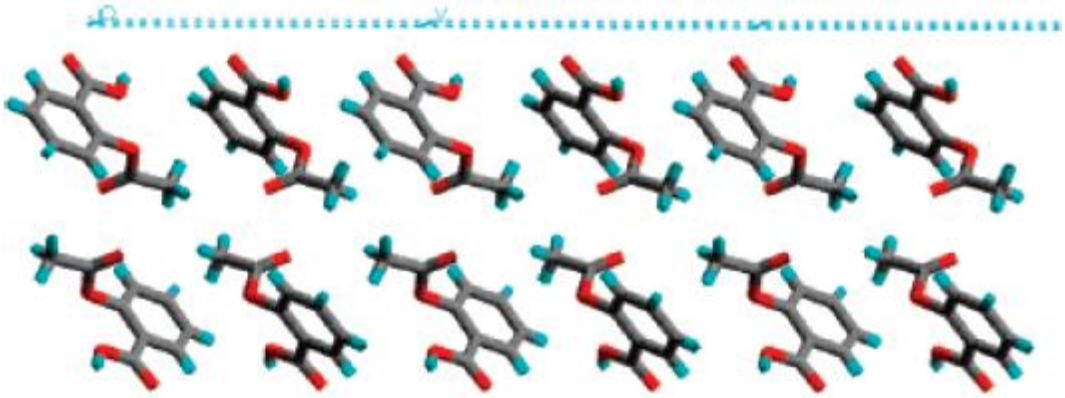

**Figure 4-8: Cleave of the (1 0 0) surface of aspirin constructed using the systematic surface search programme**

The fractional coordinates of the cell are transformed such that the x-axis is pointing up away from the surface. The probe searches an origin unit cell, where there are unit cells constructed either side of the origin to avoid any edge effects. The step sizes in y and z are defined in fractions of the unit cell vector in that direction, whereas the x direction which is going up from the unit cell is defined in angstrom step sizes. The probe can be offset in the x direction so it does not spend too much time crashing into the surface. At every grid point the molecule is rotated about the three different axes and the step size in degrees is defined by the user. At every grid point and every rotation the intermolecular energy between the probe and the surface is calculated. These energies are ranked in the output file.

## 4.5 Closing Remarks

The methods described in this chapter can be utilised to provide a multi technique analysis of the crystal growth and surface chemistry of the material. The experimental techniques are complemented by multi-scale modelling of the solid and solution state. This results in the modelling being able to provide confident rationalisation of the experimental data collected in both the solid and liquid form.

# Chapter 5 Crystal Chemistry, Conformation and Lattice Energy

*The crystal structure is broken down into pairwise intermolecular interactions and the strength of these interactions is calculated along with their contributions to the lattice energy and effects on molecular conformation*

## 5.1 Introduction

The packing of a molecular crystal can viewed as a combination of the molecular conformation and the intermolecular chemistry (synthons). The molecular conformation and synthon strengths are thought to strongly influence some physical properties of a crystal, such as morphology and mechanical properties[7, 13, 135, 212, 213]. Therefore, the nature of the synthons in the crystal structures of α- and β-*p*ABA was determined, along with a calculation of their intermolecular strength through an interatomic forcefield calculation outlined in section 4.4.2. The synthon strengths were used to calculate which parts of the molecule contribute strongly to the lattice energy of each structure, along with relating the molecular conformation in the structure to the synthon strength.

The molecular conformations and interatomic distances of the major interactions were then compared to similar molecular crystals found in the Cambridge Structural Database (CSD) utilising the techniques described in Section 4.4.1. This assessed the statistical likelihood of these types of interactions occurring in molecular crystals, whereby their statistical likelihood was linked to stability.

The calculation of the nature and strength of the synthons presented in this chapter underpins the identification of intermolecular building blocks (objective 2), along with calculation of the face-specific surface chemistry and morphology prediction (objective 3). This strength and directionality of these synthons will be linked to many of the physico-chemical properties of *p*ABA observed in this study. The link between synthon strength and directionality to molecular conformation directly addresses objective 1. Figure 5-1 shows the work flow of the chapter.

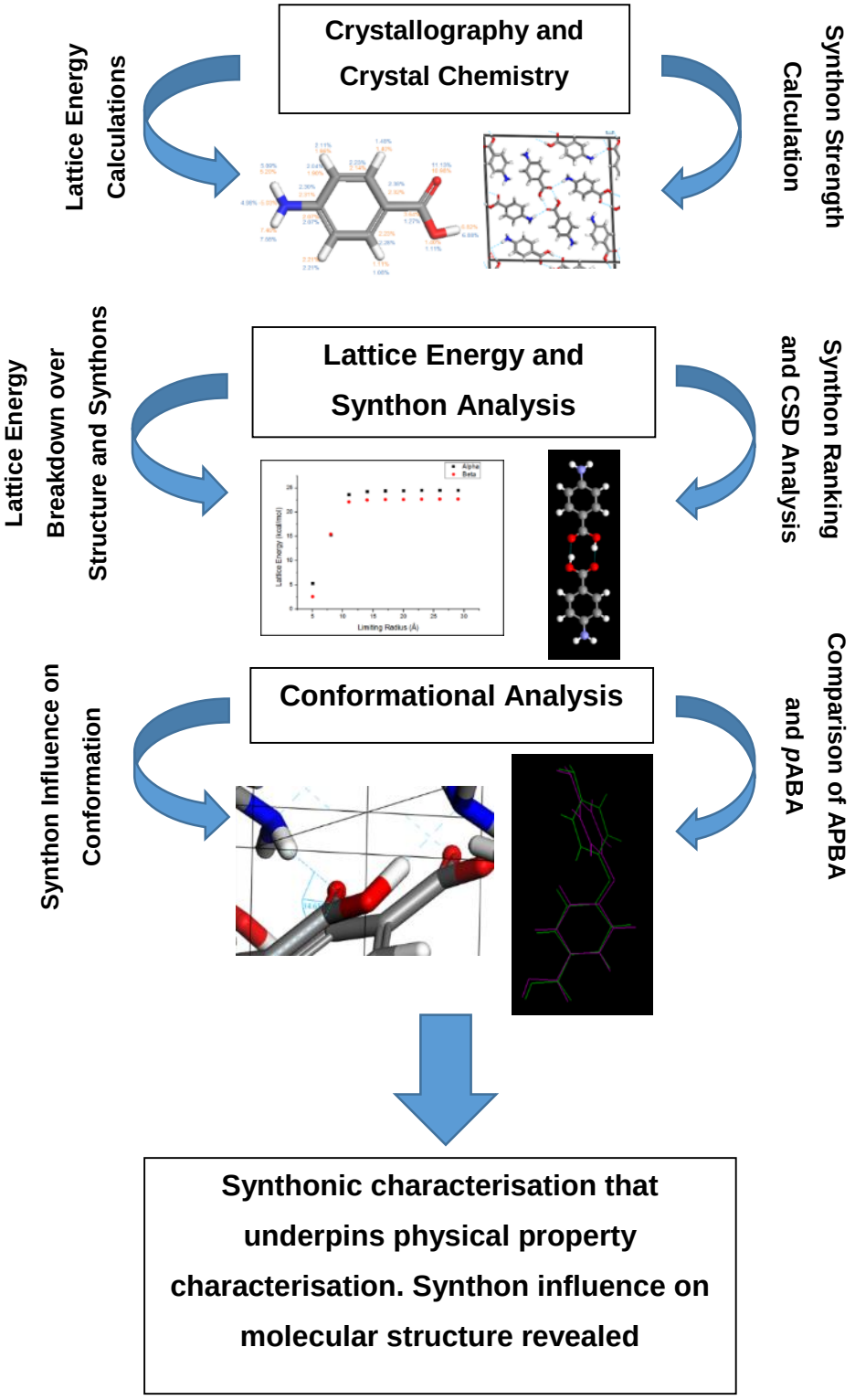


**Figure 5-1: Work flow associated with chapter 5 highlighting what information is gained from this part of the study**

## 5.2 Crystal Chemistry

For α-*p*ABA, there were found to be two crystal structures[188, 191] published in the Cambridge Structural Database (CSD), and one for β-*p*ABA[189]. In addition to the two well characterised polymorphs, a further polymorph of *p*ABA was discovered in 2014[190]. Though this polymorph is yet to be formally labelled, for the purposes of this study I have labelled it γ-*p*ABA. The crystallography details of the structures are shown in Table 5-1:

**Table 5-1: Crystallographic details of the α, β and γ polymorphs of *p*ABA found in the Cambridge Crystallographic Database**

| Polymorph | Ref Code | Year Published | Z/Z' | Space Group | A (Å) | B (Å) | C (Å) | α (°) | β (°) | γ (°) |
|---|---|---|---|---|---|---|---|---|---|---|
| A | AMBNAC01 | 1967 | 2/8 | $P2_1/N$ | 18.55 | 3.86 | 18.64 | 90.00 | 93.56 | 90.00 |
| A | AMBNAC06 | 2007 | 2/8 | $P2_1/N$ | 18.57 | 3.84 | 18.63 | 90.00 | 93.67 | 90.00 |
| B | AMBNAC04 | 2005 | 1/4 | $P2_1/N$ | 6.27 | 8.58 | 12.36 | 90.00 | 100.13 | 90.00 |
| Γ | AMBNAC09 | 2014 | 2/8 | Pna21 | 26.99 | 3.73 | 12.67 | 90.00 | 90.00 | 90.00 |

The α form was found to have two molecules in the asymmetric unit and eight molecules in the unit cell, while the β form was found to have one molecule in the asymmetric unit and four molecules in the unit cell. Figure 5-2 shows the packing diagrams for α and β *p*ABA.

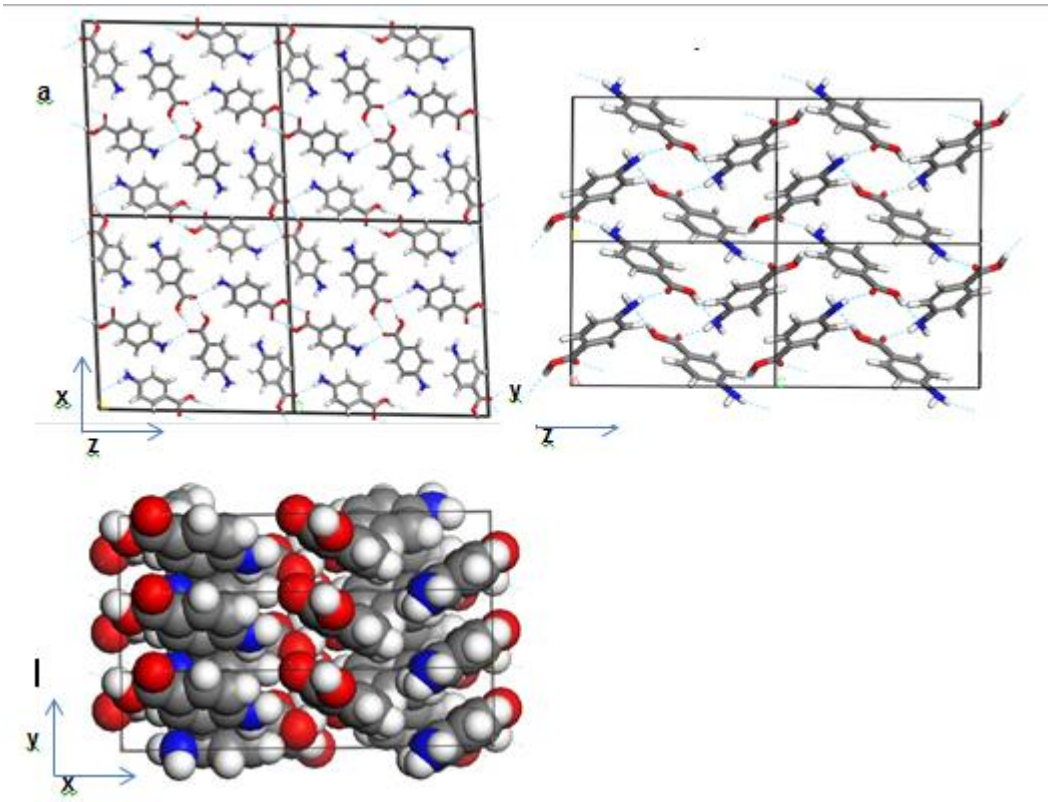


**Figure 5-2: 2 by 2 unit cells in stick model (a) in the x and z directions for α-*p*ABA; (b) in the y and z directions for β-*p*ABA; (c) 1 by 3 space fill model in the x and y directions for α-*p*ABA**

The packing of the α-form was found to comprise of non-equivalent centrosymmetric OH...O H-bonding dimers, formed between neighbouring carboxylic acid groups. In addition, NH...O hydrogen bonds were found to link the non-equivalent dimers[188, 191]. Figure 5-2(c) shows that the *p*ABA molecules were found to stack head-head, directed close to parallel to the y axis of the α-*p*ABA structure.

The packing of the β-form was found to consist of a four membered H-bonding ring consisting of two identical OH...N and NH...O interactions[189]. In addition, the molecules were also found to stack head to tail in approximately the y,z direction.

## 5.3 Lattice Energy Calculations and Bulk Synthon Strengths

### 5.3.1 Interatomic Potential Validation

Table 5-2 shows the lattice energies for α- and β-*p*ABA that were calculated using interatomic potentials which have previously shown a good agreement of calculated and experimental lattice energies for organic molecules with H-bonding and π-orbital functionality[7, 9, 135]. Both structures were optimised using the Dreiding interatomic in Materials Studio 5.5 potential prior to lattice energy calculation, as outlined in Section 4.4.2.

**Table 5-2: Calculated lattice energies for the crystal structures of α and β *p*ABA found in the CSD using the potential sets from Momany[73], Nemethy[74] and Dreiding[75]**

| Structure | Polymorph | Potential | Lattice Energy (kcal/mol) | Crystal Density (g/Å$^3$) |
|---|---|---|---|---|
| AMBNAC01 | α | Momany | -24.54 | 0.82 |
| AMBNAC01 | α | Nemethy | -26.79 | 0.82 |
| AMBNAC01 | α | Dreiding | -12.58 | 0.82 |
| AMBNAC06 | α | Momany | -22.43 | 0.82 |
| AMBNAC06 | α | Nemethy | -24.75 | 0.82 |
| AMBNAC06 | α | Dreiding | -25.61 | 0.82 |
| AMBNAC04 | β | Momany | -21.59 | 0.83 |
| AMBNAC04 | β | Nemethy | -12.20 | 0.83 |
| AMBNAC04 | β | Dreiding | -13.51 | 0.83 |

The experimental lattice energy, based on sublimation enthalpy data, for α-*p*ABA was found to be between 26.77kcal/mol[214] measured at 373K using a torsion effusion method and 27.25kcal/mol[215] also measured at 373K using a calorimetric method. Table 5-2 shows that calculating the lattice energy using the Momany potential gave a sensible lattice energy for both α and β *p*ABA, while the lattice energy calculated for α-*p*ABA matched well to the experimental sublimation enthalpy. The prediction of the

lattice energies of organic molecules with well-defined H-bonding and π-orbital functionality using the Momany forcefield has previously shown good agreement with experimental data[7, 9, 135]. Both structures of pABA that were examined in this study contain strong H-bonding interactions, therefore it seemed prudent to select a forcefield that contained a specific term to calculate the H-bonds (Section 4.4.2.2). The Momany forcefield was parameterised to calculate the interactions between OH...O H-bonding dimers[73], similar to those present within the α-structure. Since Table 5-2 shows that both the Nemethy and Dreiding forcefields overestimate some of the repulsive interactions within the α- and β-pABA structures such that the lattice energy does not closely match the sublimation enthalpy, the Momany potential was the most sensible choice for the forcefields tested. To the authors knowledge there is no published sublimation enthalpy for β-*p*ABA.

### 5.3.2 Lattice Energy Convergence

To assess which intermolecular interactions need to be satisfied to converge the lattice energy, the sphere of calculation within HABIT98 from the central molecule was increased in 3Å steps to include more molecules within the origin and surrounding unit cells. This technique was outlined in Section 4.4.2.

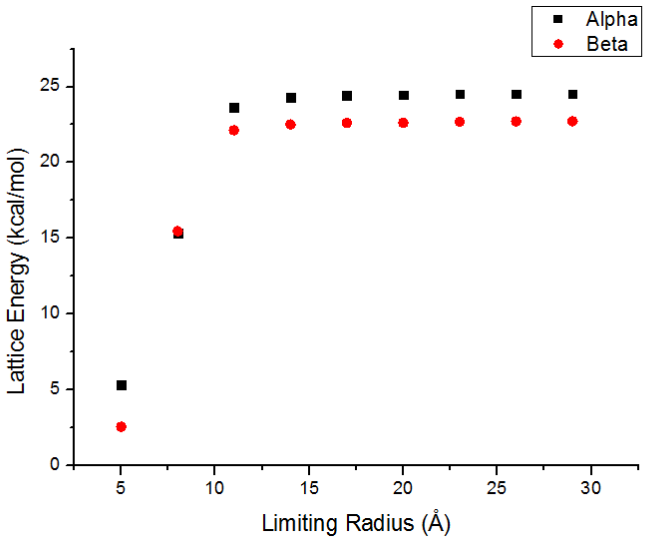


**Figure 5-3: Convergence of lattice energy of *p*ABA α and β calculated as a function of limiting radius. Radius of convergence similar for both polymorphs. β lattice energy lower than α at 8Å radius before all the important H-bonding in α becomes satisfied.**

The lattice energies for α- and β-*p*ABA were both found to converge at around 10-12Å. It was found that for both structures, it was formation of the major H-bonding and π-π stacking interactions that resulted in the convergence of the lattice energy.

Figure 5-3 revealed that the fully converged lattice energies of the α polymorph was calculated to be lower than the β form, though an interatomic potential calculation is a 0K calculation and β is the low temperature form. Though the interatomic potential calculation is technically done at 0K, the parameters are often derived from more ambient conditions experimental data. The solubility of both forms is very similar[28, 192], suggesting that the free energy of both forms are very close. Price et al computed the lattice energies of *p*ABA in the correct order using an interatomic forcefield[216], however the lattice energies were found to be within less than a kilojoule of each other. This study focusses on the relative energy of the synthons and their effect on crystal morphology and it has been shown that the morphology prediction of organic crystals are relatively insensitive to the intermolecular potential used[164], therefore this forcefield was deemed suitable for the study.

## 5.4 Bulk Intrinsic Synthons

### 5.4.1 Calculated Synthon Strengths from the Crystal Structures

The calculated synthon strength within the α- and β-*p*ABA crystal structures are shown in Figure 5-4 and Figure 5-5 and Table 5-3 and Table 5-4. These were calculated in HABIT98 using the Momany interatomic potential set[73], utilising the methods described in Section 4.4.2.

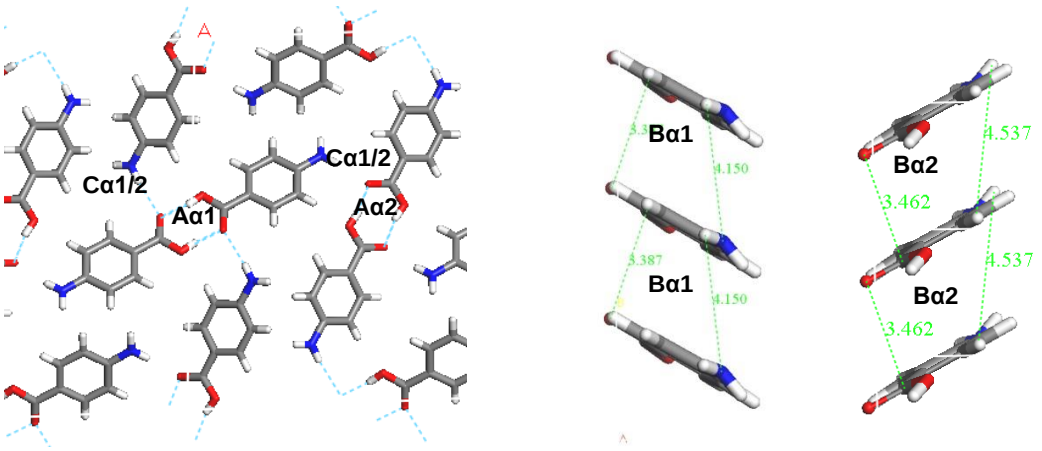


**Figure 5-4: Strongest synthons in the α-pABA structure labelled on the α packing diagram. Combination of H-bonding interactions (A, B and D) and π-π stacking (C) indicating that both types of interactions are important in the formation of α. Interactions tabulated in Table 5-3a and b.**

**Table 5-3: 7 strongest intermolecular interactions from α molecule 1(a) and 2 (b). Distance (column 3) reflects centre of mass to centre of mass of the molecules involved in the interaction (herein and after). Total energy of interaction is energy of the bond multiplied by the multiplicity**

(a)

| Bond | Multiplicity | Distance (Å) | Intermolecular Energy (kcal/mol) | Percentage Contribution to Lattice Energy | Dominating Interatomic Interaction Type | COOH % Contribution to Interaction | $C_6H_4$ % Contribution to Interaction | $NH_2$ % Contribution to Interaction |
|---|---|---|---|---|---|---|---|---|
| Aα1 | 1 | 8.23 | -5.67 | 23.1 | H-Bond | 96.4 | 4.0 | -0.4 |
| Bα1 | 2 | 3.86 | -2.68 | 21.8 | π-π Stacking | 14.5 | 72.6 | 13.00 |
| Cα1 | 1 | 7.90 | -2.27 | 9.3 | H-Bond | 41.7 | 20.7 | 37.6 |
| Dα1 | 1 | 7.75 | -2.00 | 8.2 | H-Bond | 38. 8 | 26.1 | 35.1 |
| Eα1 | 2 | 7.96 | -2.26 | 9.2 | vdW | 79.9 | 21.0 | -0.9 |
| Total | | | 18.65 | 71.6 | | | | |

(b)

| Bond | Multiplicity | Distance (Å) | Intermolecular Energy (kcal/mol) | Percentage Contribution to Lattice Energy | Dominating Interatomic Interaction Type | COOH % Contribution to Interaction | $C_6H_4$ % Contribution to Interaction | $NH_2$ % Contribution to Interaction |
|---|---|---|---|---|---|---|---|---|
| Aα2 | 1 | 8.34 | -5.63 | 22.9 | H-Bond | 96.7 | 3.6 | -0.4 |
| Bα2 | 2 | 3.86 | -2.66 | 21.7 | π-π Stacking | 14.5 | 72.6 | 13.0 |
| Cα2 | 1 | 7.90 | -2.27 | 9.3 | H-Bond | 41.7 | 20.7 | 37.6 |
| Dα2 | 1 | 7.76 | -1.21 | 4.9 | H-Bond | 38.8 | 26.1 | 35.1 |
| Fα2 | 2 | 6.94 | -1.9 | 7.7 | vdW | 80.8 | 20.0 | -0.9 |
| Total | | | -16.33 | 66.5 | | | | |

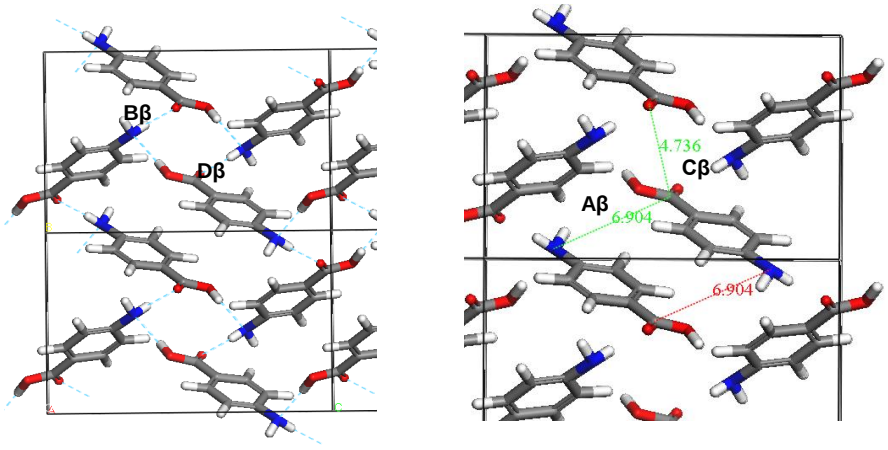


**Figure 5-5: Strongest interactions of β-*p*ABA labelled on the β packing diagram. Combination of H-bonding ring interactions (B and D) and offset stacking with interactions between the $NH_2$ and COOH groups (A and C) indicating that both types of interactions are important in the formation of β. Interactions tabulated in Table 5-4**

**Table 5-4: Eight strongest intermolecular interactions from β-*p*ABA. Total energy of interaction is energy of the bond multiplied by the multiplicity**

| Bond | Multiplicity | Distance (Å) | Intermolecular Energy (kcal/mol) | % Contribution to Latt Eng | Dominating Interatomic Interaction Type | COOH % Contribution to Interaction | $C_6H_4$ % Contribution to Interaction | $NH_2$ % Contribution to Interaction |
|---|---|---|---|---|---|---|---|---|
| Aβ | 1 | 4.17 | -2.57 | 11.9 | π-π stacking | 33.3 | 65.2 | 1.5 |
| Bβ | 2 | 8.11 | -2.45 | 22.7 | H-Bond | 46.5 | 15.7 | 37.7 |
| Cβ | 2 | 5.73 | -2.39 | 22.2 | vdW | 37.8 | 34.0 | 28.2 |
| Dβ | 2 | 6.74 | -1.46 | 13.6 | H-bond | 9.1 | 44.5 | 46.4 |
| Eβ | 1 | 6.53 | -1.01 | 4.4 | vdW | 15.7 | 80.2 | 4.1 |
| Total | | | -16.18 | 74.8 | | | | |

Figure 5-4 and Table 5-3(a) and (b) revealed that the strongest interactions in the α form were found to be the H-bonding dimers between the carboxylic acid groups, contributing approximately 23% to the calculated lattice energy (Aα1 and Aα2). Interestingly bond Cα, which involves the more isotropic vdW forces due to π-π interactions between close packed molecules of *p*ABA stacking along the b-axis, was found to contribute approximately 22% of the total calculated lattice energy. This indicates that the interactions due to the π-π stacking of phenyl rings are as influential in the packing of this crystal structure as the more directional hydrogen bonds, which are often thought to be the most important interactions within molecular crystal structures[16, 17, 217].

Figure 5-5 and Table 5-4 revealed that the strength of the interactions in the β-form were found to be more evenly spread in comparison to the α-form. The top four

interactions all were found to contribute above 10% of the lattice energy. The two that contributed most to the β-*p*ABA lattice energy (Aβ and Cβ) were found to contribute around 22% to the lattice energy, which were found to be dominated by the OH...N H-bond and the polar interactions between the two COOH head groups respectively.

The functional group contribution analysis, with respect to their % contributions to the intermolecular interaction strengths, was determined in columns 7-9 in

Table 5-3 and Table 5-4. For example, the carboxylic H-bonded dimers (Aα) were found to have over 96% of its interaction centred on the COOH group, while the π-π stacking interaction (Bα) was found to be more centred on the phenyl ring, with over 72% of the interaction contributed by the phenyl ring.

The functional group contribution to the synthon is interesting with respect to considering how molecules may have to orientate prior to forming a synthon. Considering the Dα synthon which has 96% of its energy focussed on the COOH group, the molecules involved in making this synthon would have to find the orientation such that the COOH groups could interact with this end on orientation. Comparing to the Bα synthon, where the spread of the intermolecular energy around the molecule was found to be more isotropic and 72% of the energy was centred on the phenyl ring, it can be seen as more of the intermolecular energy is spread over a larger area of the molecule. Therefore, it can be postulated that a greater area of the molecule can initiate the formation of the Bα synthon compared to the Aα synthon, despite the greater amount of intermolecular energy that is resultant from the formation of the Aα synthon.

### 5.4.2 Contributions to the Synthon Strength

The list of atomic charges for the α-*p*ABA are shown in Figure 5-6, calculated using the methods outlined in 4.4.2.

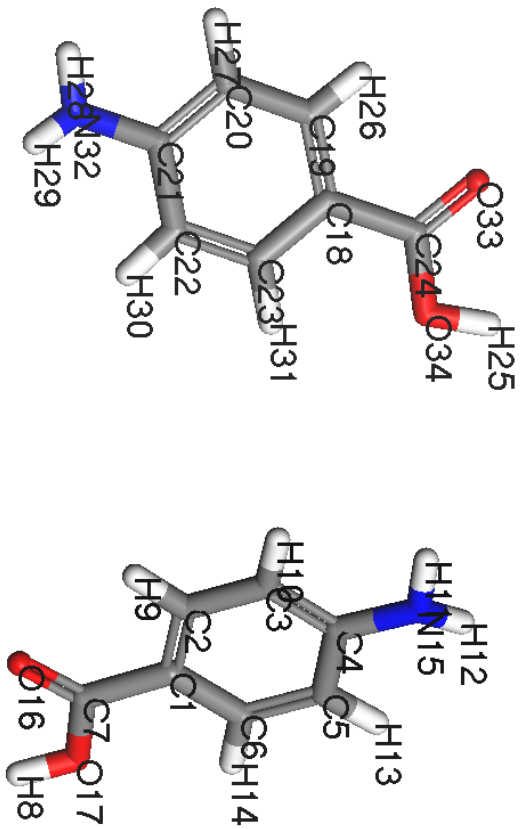


| Atom | Charge |
|---|---|
| C1 | 0.0323 |
| C2 | -0.0412 |
| C3 | -0.0596 |
| C4 | -0.0148 |
| C5 | -0.0670 |
| C6 | -0.0413 |
| C7 | 0.2949 |
| H8 | 0.3617 |
| H9 | 0.0255 |
| H10 | 0.1270 |
| H11 | 0.3633 |
| H12 | 0.3633 |
| H13 | 0.1169 |
| H14 | 0.0870 |
| N15 | -0.7445 |
| O16 | -0.4368 |
| O17 | -0.3666 |

| Atom | Charge |
|---|---|
| C18 | 0.0323 |
| C19 | -0.0412 |
| C20 | -0.0596 |
| C21 | -0.0148 |
| C22 | -0.0670 |
| C23 | -0.0413 |
| C24 | 0.2949 |
| H25 | 0.3617 |
| H26 | 0.0255 |
| H27 | 0.1270 |
| H28 | 0.3633 |
| H29 | 0.3633 |
| H30 | 0.1169 |
| H31 | 0.0870 |
| N32 | -0.7445 |
| O33 | -0.4368 |
| O34 | -0.3666 |

**Figure 5-6: (a) Asymmetric unit of AMBNAC01 α-*p*ABA crystal structure; (b) list of atomic fractional charges calculated in Section 4.4.2**

The intermolecular energy for the synthons in the α-*p*ABA structure was divided into attractive and repulsive forces due to the H-boning and vdW interactions, along with the attractive electrostatic interactions. This is shown in Table 5-5.

**Table 5-5: (a) Division of how the forces due to vdW, H-bonding and coulombic forces contribute to the synthons listed in Table 5-3(a) for the synthons from one of the molecules in the α-*p*ABA asymmetric unit; (b) for the synthons listed in Table 5-3(b) for the other molecule in the asymmetric unit**

**(a)**

| Bond | Distance (Å) | Att (kcal) | Rep (kcal) | Coul (kcal) | Total (kcal) |
|---|---|---|---|---|---|
| Aα1 | 8.23 | -7.65 | 4.38 | -2.40 | -5.67 |
| Bα1 | 3.86 | -4.51 | 1.47 | 0.37 | -2.68 |
| Cα1 | 7.90 | -2.75 | 1.60 | -1.12 | -2.27 |
| Dα1 | 7.75 | -2.77 | 1.57 | -0.80 | -2.00 |
| Eα1 | 7.96 | -1.25 | 0.36 | -0.32 | -1.21 |

**(b)**

| Bond | Distance (Å) | Att (kcal) | Rep (kcal) | Coul (kcal) | Total (kcal) |
|---|---|---|---|---|---|
| Aα2 | 8.34 | -7.07 | 3.94 | -2.50 | -5.63 |
| Bα2 | 3.86 | -4.60 | 1.60 | 0.34 | -2.66 |
| Cα2 | 7.90 | -2.75 | 1.57 | -0.80 | -2.27 |
| Dα2 | 7.76 | -1.25 | 0.36 | -0.32 | -1.21 |
| Eα2 | 6.94 | -1.66 | 0.69 | 0.02 | -0.95 |

Table 5-5 shows that the Coulomb forces strongly influence the H-bonding dimers, contributing to almost half of the intermolecular interaction for Aα1 and Aα2, compared to the more isotropic vdW interaction where the contribution of the Coulomb forces is much less. This is due to the greater fractional charges on O16, O33, H8 and H25 (Figure 5-6).

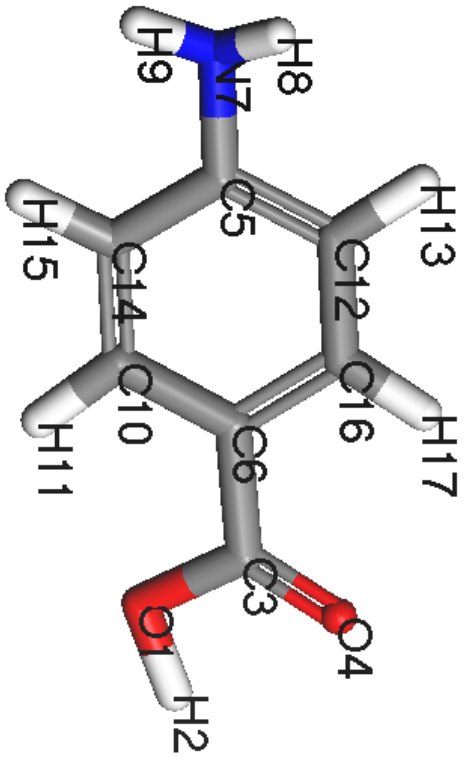


| Atom | Charge |
|---|---|
| O1 | -0.3666 |
| H2 | 0.3617 |
| C3 | 0.2949 |
| O4 | -0.4368 |
| C5 | -0.0148 |
| C6 | 0.0323 |
| N7 | -0.7445 |
| H8 | 0.3633 |
| H9 | 0.3633 |
| C10 | -0.0412 |
| H11 | 0.0255 |
| C12 | -0.0670 |
| H13 | 0.1169 |
| C14 | -0.0596 |
| H15 | 0.1270 |
| C16 | -0.0413 |
| H17 | 0.0870 |

**Figure 5-7: (a) Asymmetric unit of AMBNAC01 α-*p*ABA crystal structure; (b) list of atomic fractional charges calculated in Section 4.4.2**

The intermolecular energy for the synthons in the β-*p*ABA structure was also divided into attractive and repulsive forces due to the H-boning and vdW interactions, along with the attractive electrostatic interactions. This is shown in Table 5-6.

**Table 5-6: Division of how the forces due to vdW, H-bonding and coulombic forces contribute to the synthons listed in Table 5-4 for α-*p*ABA**

| Bond | Distance (Å) | Att (kcal) | Rep (kcal) | Coul (kcal) | Total (kcal) |
|---|---|---|---|---|---|
| Aβ | 4.17 | -3.88 | 1.35 | -0.04 | -2.57 |
| Bβ | 8.11 | -4.19 | 3.39 | -1.64 | -2.45 |
| Cβ | 5.73 | -3.44 | 1.80 | -0.76 | -2.39 |
| Dβ | 6.74 | -2.18 | 1.03 | -0.30 | -1.46 |
| Eβ | 6.53 | -1.03 | 0.13 | -0.11 | -0.92 |

The contribution of the coulombic force to such H-bonds in both the α- and β-*p*ABA structures is in good agreement with a previous study on α-lactose monohydrate, where the coulombic interactions were found to be much more dominant in hydrogen bonding compared to the vdW interactions[218]. In addition, H-bonding dimers of water molecules, which are similar in nature to the OH...O H-bonding dimers, have previously reported an intermolecular energy of around 5 kcal/mol, in good agreement with what is calculated here[219]. Hence, this suggests that the combination of dispersive, H-bonding and Coulomb forces calculated here are reasonably accurate, suggesting the forcefield choice and charge set choice were sensible and fit for purpose.

Comparing the functional group contributions to the synthons of α- and β-*p*ABA, β-*p*ABA showed a more equal spread of the intermolecular energy across the whole molecule for the major synthons than α-*p*ABA. Figure 5-8 shows the isolated major pairwise interactions for the α- and β-*p*ABA crystal structures.

**(a) α-*p*ABA Important Synthons**

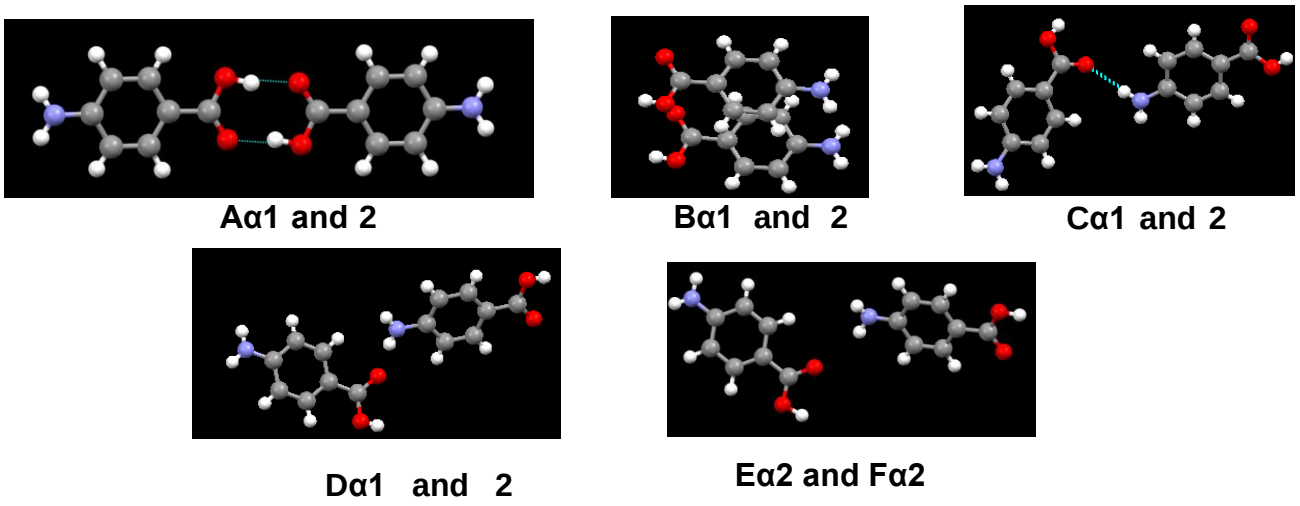


**(b) β-*p*ABA Important Synthons**

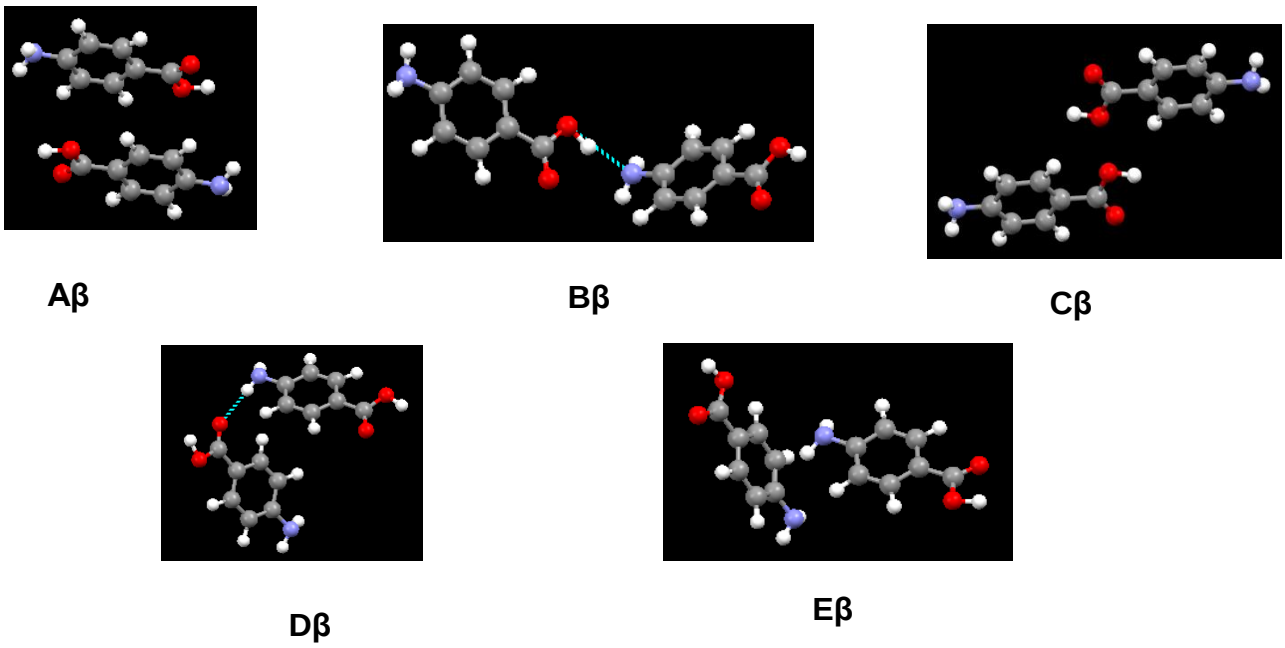


**Figure 5-8: Important bulk synthons as specified in tables 1-4 and 1-5 for both forms of *p*ABA that are required to be satisfied to converge the lattice energy. Pairwise interactions visualised for clarity. Combination of H-bonding and vdW interacting synthons important for both structures.**

The geometry of the molecules involved in the synthonic interactions in β-*p*ABA resulted in them being closer to each other, compared to α-*p*ABA. This allowed more

of the molecule to be involved in the intermolecular interaction, hence the more isotropic spread of the contribution to the intermolecular interactions of the functional groups shown in Table 5-7, compared to those within the α-*p*ABA structure. In addition, this correlates with the crystal density shown in Table 5-2 where β-*p*ABA was shown to have greater crystal density than α-*p*ABA. Dunitz et al suggested that the greater the packing density then the more stable the crystal structure, which is probably why β-*p*ABA is the low temperature stable form[220]. However, it should be noted that, similar to the solubility, the packing density difference between the two polymorphs is extremely small.

It is interesting to observe that both structures were found to contain a π-π stacking motif, with the α structure containing a head to head stack and the β structure containing a head to tail stack.

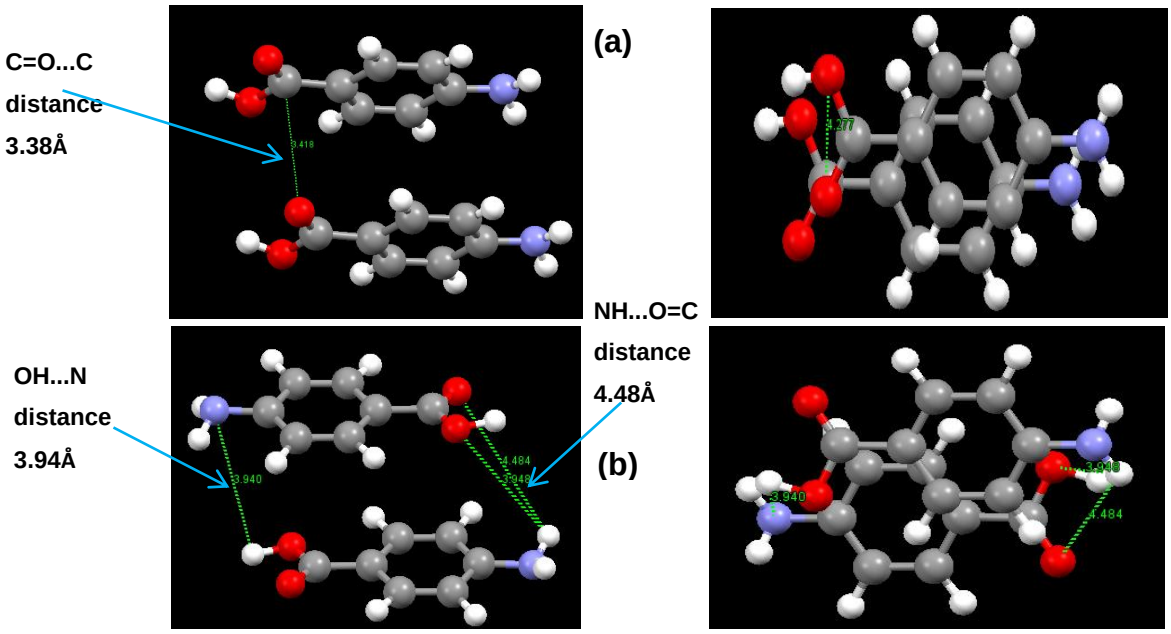


**Figure 5-9: (a) (above left and right) α π-π stacking dimer, head to head stacking 3.8Å intermolecular distance between the corresponding $NH_2$ and COOH groups. Molecules slightly offset creating stronger interactions between the functional groups. (b) (below left and right) β π-π stacking. Head to tail stack around 4Å distance between functional groups. Molecules more offset than α to maximise strength of interactions between $NH_2$ and COOH groups.**

The Bα stacking motif was found to be slightly offset so that the more electronegative nitrogen and electropositive hydrogen atoms can form stronger atom-atom

electrostatic interactions at one end, whilst the electronegative oxygen and electropositive carbon can interact in the same way at the other end.

Figure 5-9(a) shows the β motif to be a head to tail stack that was found to be even more offset than the α stacking motif. This suggests that the electrostatic interactions between the more polar atoms in the $NH_2$ and COOH functional groups are important interatomic interactions in this dimer. This is despite the interatomic distances of the strongly interacting atoms being slightly longer in the β stack compared to that present in the α stack. The head to tail stacking motif was predicted to be the strongest synthon in the β structure, although the energies of this interaction and the OH...N and NH...O H-bonding interactions are very similar.

### 5.4.3 Lattice Energy Contributions

In a similar approach to dividing the intermolecular interactions over the functional groups in

Table 5-3 and Table 5-4, the lattice energy was partitioned over the individual atoms of the asymmetric unit of the α and β structures, which is shown in Figure 5-10.

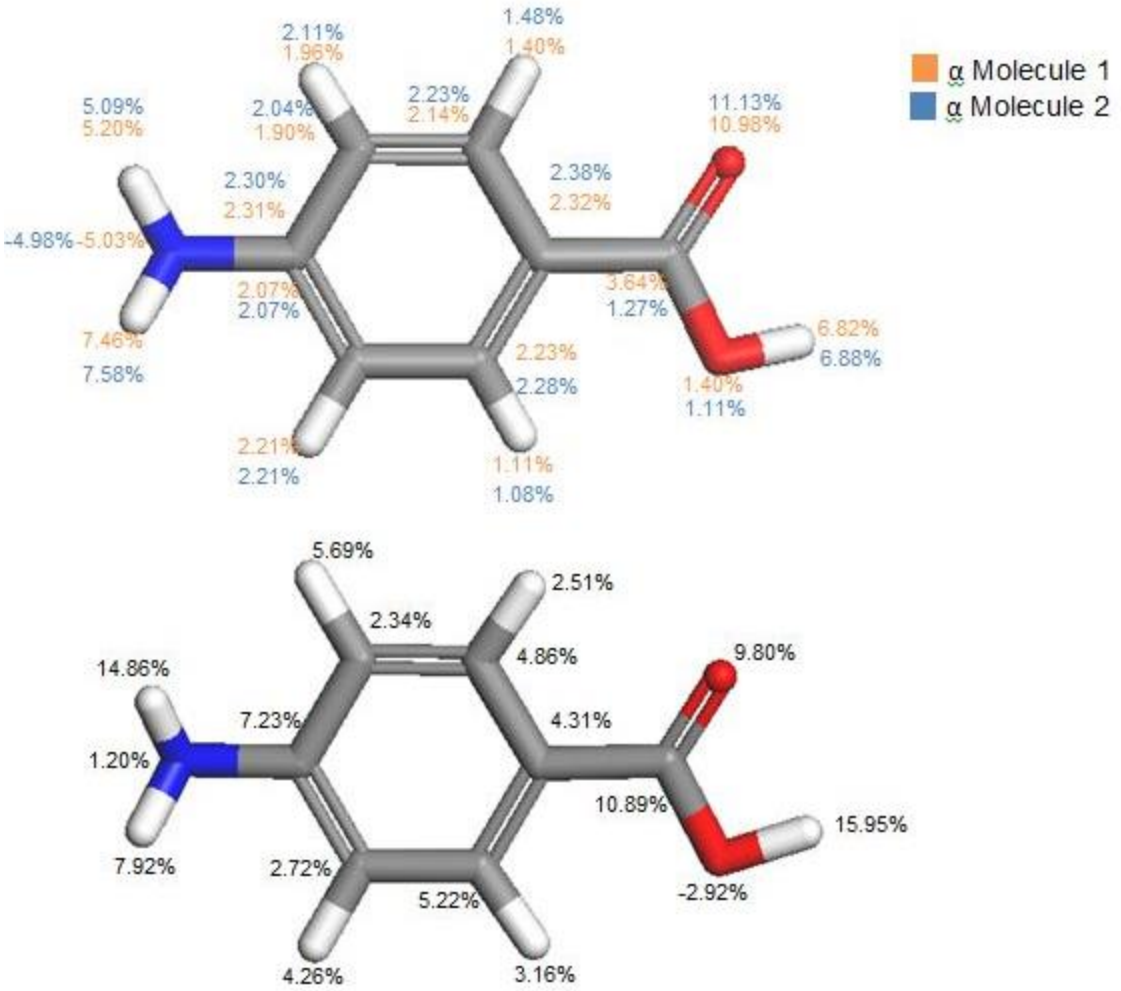


**Figure 5-10: Molecular structures of *p*ABA highlighting the percentage contribution of the lattice energy of α (top) and β (bottom) per atom calculated using the DEBUG-2 function.**

In addition, the total functional group contributions were also summed in Table 5-7:

**Table 5-7: Functional group contributions of the AMBNAC01 and AMBNAC04 crystal structures. Functional group contributions are summed from the individual atomistic contributions shown in Figure 5-10**

| Polymorph | Ref Code | $NH_2$ Contribution | $C_6H_4$ Contribution | COOH Contribution |
|---|---|---|---|---|
| α | AMBNAC01 | 15.33% | 39.81% | 44.86% |
| β | AMBNAC04 | 23.8% | 42.5% | 33.7% |

The contributions of the two molecules in the asymmetric unit of α are broadly similar due to the similar environments of the atoms, whereas the β form shows increased importance of the amino hydrogens and hydroxyl hydrogen, and decrease in contribution from carbonyl oxygen. The increase in COOH contribution to the lattice energy in α is probably due to the packing including the strong OH...O H-bonding interactions, while in the β-structure the OH...N and NH...O H-bonds are not as strong as the OH...O H-bonds found in α. In addition, the $NH_2$ group was found to have an increased contribution to the lattice energy of the β structure since it acts as a H-bonding donor and acceptor in β, but only as a donor in α.

From this analysis, it was possible to identify what parts of the molecule must interact to result in lattice energy convergence and hence aid the prediction of what may be the important building blocks with respect to the self-assembly and stabilisation of a crystal structure. For α-*p*ABA, the highest percentage of the lattice energy was provided by the COOH group (44.86%), while the $NH_2$ group was found to only contribute 15.33% of the lattice energy. Hence, it would be expected that the major synthons that result self-assembly and stabilisation of the α structure would involve the COOH and phenyl groups. In contrast, the spread of the lattice energy across the β-*p*ABA asymmetric unit was found to be slightly more even, with all three major groups making a significant contribution to the lattice energy. However, the phenyl ring group was found to be the major contributor to the lattice energy and hence would be expected be part of the most important molecular building blocks for the β-*p*ABA structure.

Though there are significant studies on improving the accuracy of lattice energy calculations, especially calculating the differences between the energies of polymorphs[221-223], detailed analysis of the contribution of different parts of the molecule to the lattice energy are often overlooked. This technique is relatively simple, yet can yield information about what parts of the molecule need to be available for the self-assembly of a particular polymorph, hence what parts of the molecule would probably need to be hindered to inhibit the formation of an unwanted polymorph.

## 5.5 Packing Anisotropy between α- and β-*p*ABA

Figure 5-11 and Figure 5-12 how the packing of the molecules has resulted in intermolecular interactions forming between the crystallographic planes for α- and β-*p*ABA.

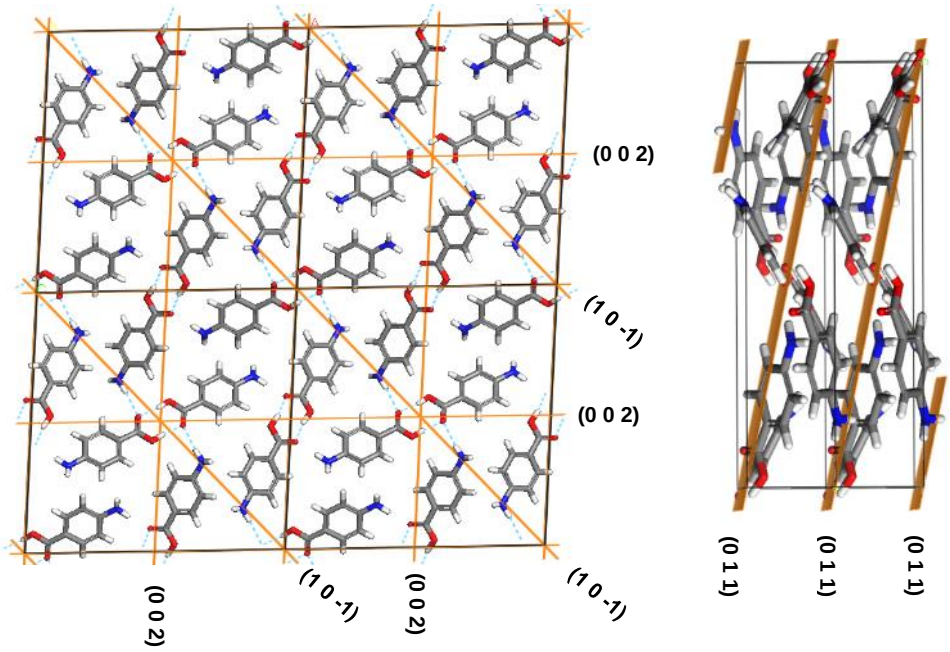


**Figure 5-11: α-*p*ABA crystal structure showing which low index miller planes bisect the important synthons within the structure**

Within the α-*p*ABA crystal structure, the Aα1 and Aα2 synthons were found to be almost perfectly bisected by the (1 0 -1) and (0 0 2) planes. In addition, the molecules stack close to parallel to the b-axis forming the π-π stacking interactions, i.e. almost bisected by the (0 1 1) plane. From this, the strongly anisotropic and directional nature of the structure would suggest that the growth would be most prominent perpendicular to these miller planes that bisect these intermolecular interactions.

This packing is in contrast to the β-*p*ABA crystal structure, where the isotropic 4-memebered ring structure that was found to be directed in three dimensions resulted in the strongest synthons in the structure pointing in different directions.

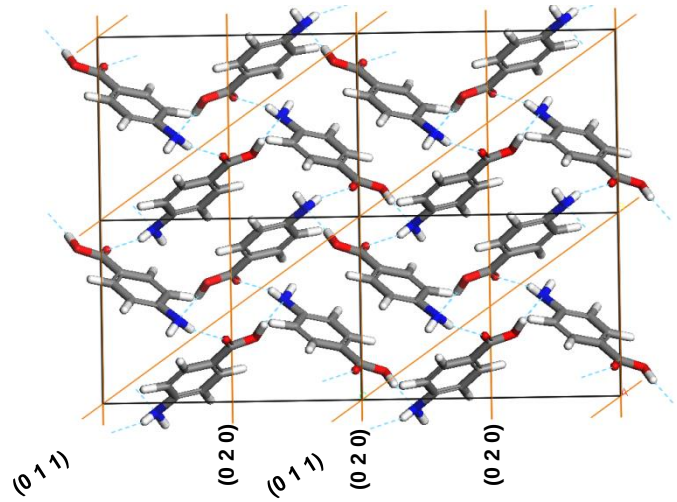


**Figure 5-12: β-*p*ABA crystal structure showing the low index Miller planes that bisect some of the important intermolecular synthons within the structure**

Though the (0 1 1) and (0 2 0) planes appear to bisect some of the important synthons present within the β-*p*ABA crystal structure, it is important to remember that the ring structure is orientated in three dimensions, i.e. that some of the synthons that have been broken are actually pointing in and out of the page. In that, the synthons that might be seen as being broken at the surface are actually directed more in-plane. Therefore, such an isotropic structure with the synthons pointing in more than one defined direction, the growth would be expected to be more isotropic and equal in the major crystallographic directions.

## 5.6 CSD Analysis of Important H-bonding Interactions

Figure 5-13 shows the density of hits in the CSD of the OH...O, OH...N and NH...O interactions as examined as a function of distance and angle:

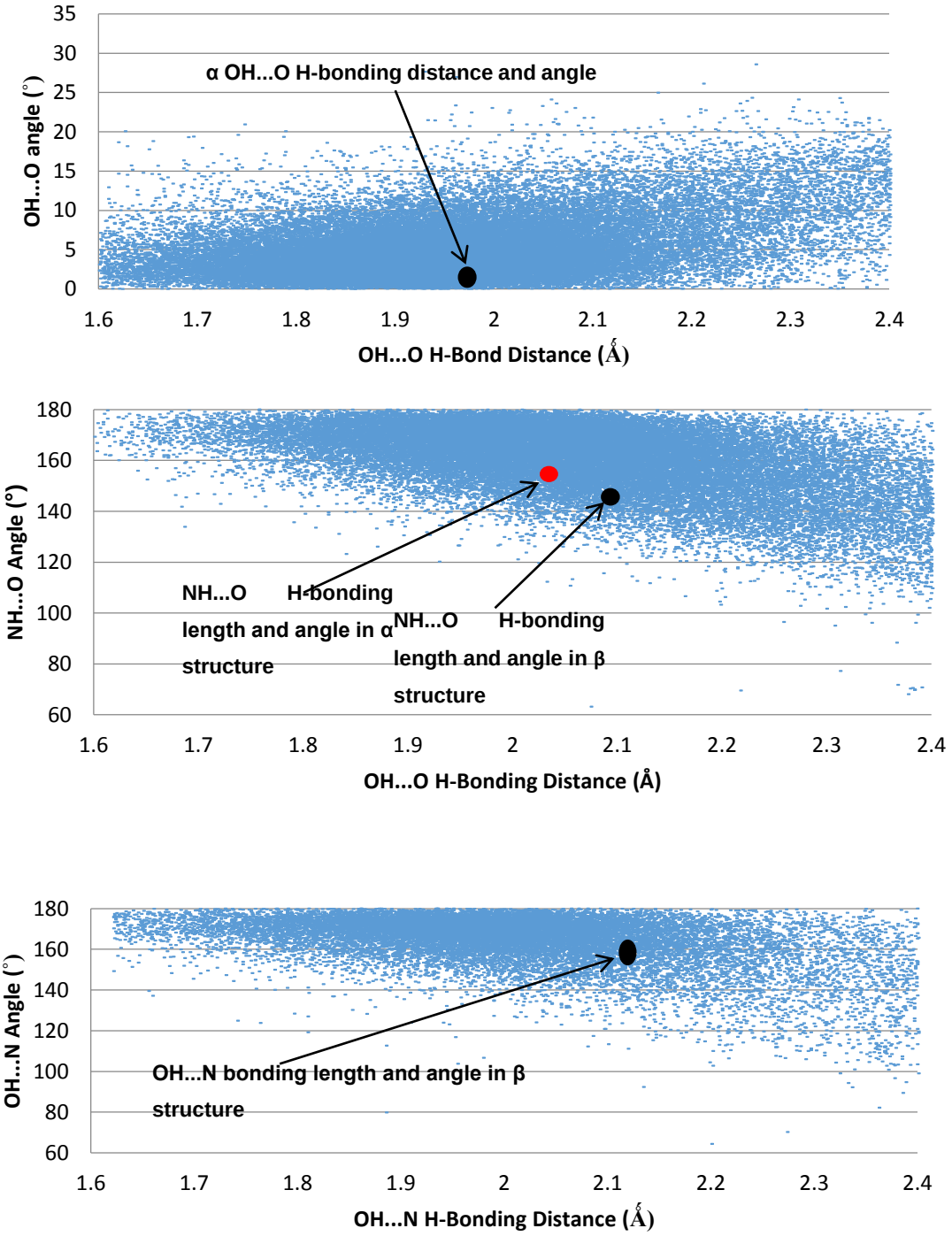


**Figure 5-13: H-bonding data from the CSD of H-bonding angles and distances of OH...O (top), NH...O (middle) and OH...N (bottom) interacting groups.**

Figure 5-13 revealed that the hit density of structures with OH...O H-bond lengths between 1.8Å and 2.1Å was very high. It also showed that the more linear the bond angle between the molecules, then the higher the amount of hits. The H-bond length

and orientation of the carboxylic acid H-bonding dimer interactions in the α structure were found to be close to the centre of this dense area of structures, consistent with this being a common and stable interaction.

The majority of the OH…N H-bonding interactions found in the search of the CSD were between 160˚ and 180˚ and had bond lengths of 1.8Å-2.1Å. The OH...N H-bonding length of 2.15Å in the β structure was also found to be within a dense area of structures containing a similar bond length, once again suggesting that this is a common stable interaction that is a key synthon in the molecular self-assembly and formation of the β structure.

The spread of hits for the NH...O interactions in the CSD was found to be a little wider in terms of bond length compared to the OH…O and OH…N interactions, though the highest density of hits was found to be around 2Å. The shorter interactions tended to have more linear interactions. However, as the NH…O bond length increased, the bond angle was found to move away from a linear conformation. This suggests that these structures could be more amenable to a change in geometry as the NH...O bond length increases, mindful that these interactions would be expected to be weaker and possibly not the major interactions that stabilise the crystal structure. This appears to be the case for the NH...O interactions present in the α and β forms of *p*ABA.

## 5.7 Conformational Analysis

Though *p*ABA is a relatively inflexible molecule, the main centres of rotation are of the COOH and $NH_2$ functional groups with respect to the phenyl ring. The torsion angles of the molecular structures from the AMBNAC01 and AMBNAC06 structures for α-*p*ABA, along with the AMBNAC04 structure for β-*p*ABA (Table 5-1) are shown in Figure 5-14.

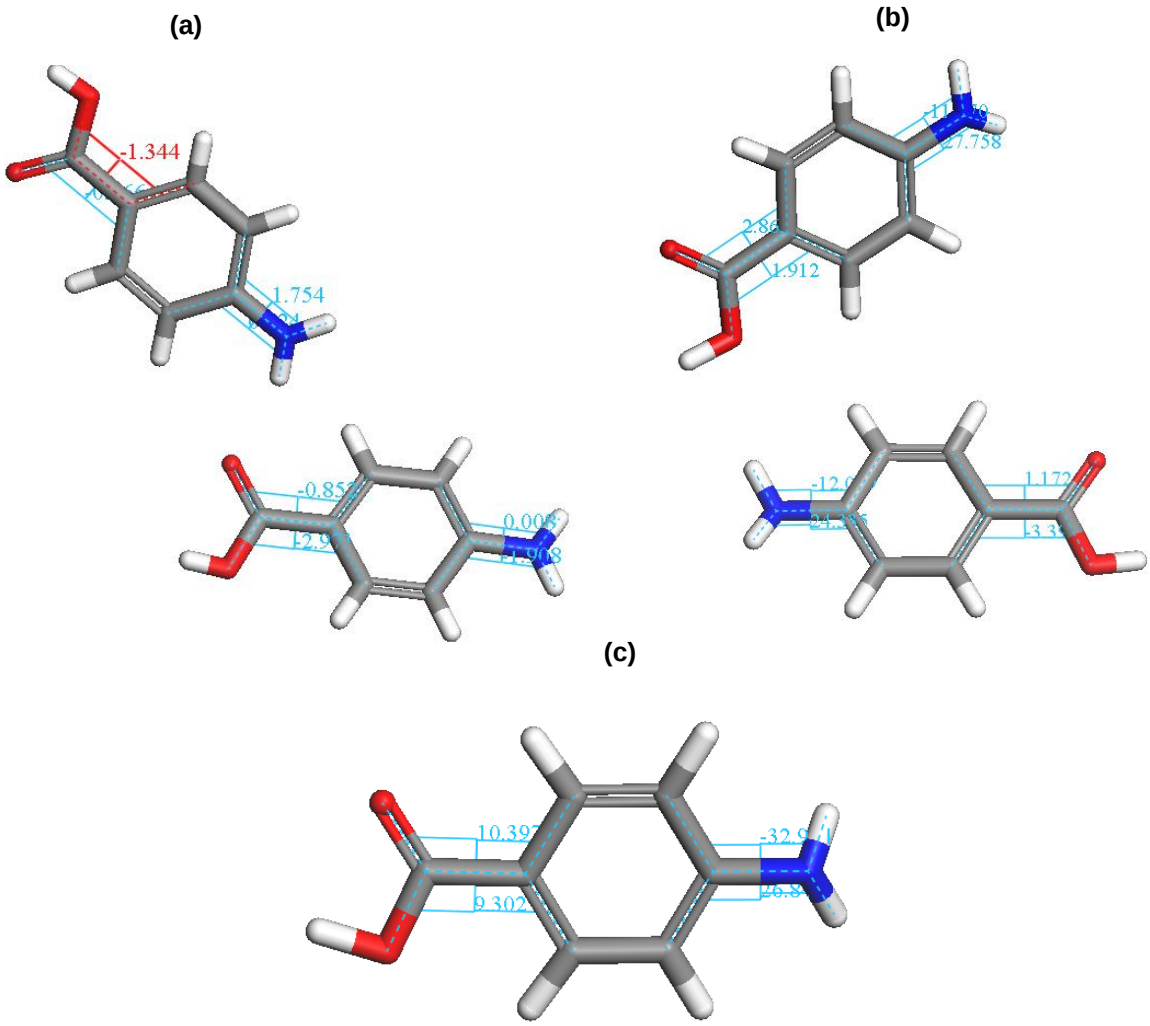


**Figure 5-14: Asymmetric units of (a) α-*p*ABA AMBNAC06 crystal structure; (b) α-pABA AMBNAC01 crystal structure; (c) β-*p*ABA AMBNAC04 crystal structure. Four body torsions around the functional groups shown**

This is demonstrated in the fact that the AMBNAC01, AMBNAC04 and AMBNAC06 structures were all found to contain different intramolecular geometries with respect to the $NH_2$ group. In addition, the COOH group displays a slightly different conformation between the α and β structures.

Table 5-8 shows the measured four body torsion angles for the COOH and $NH_2$ functional groups with respect to the phenyl ring of the molecules in the asymmetric units of the crystal structures found in the CSD. All of the torsion angles quoted in this chapter are the four body torsions shown in Figure 5-14.

**Table 5-8: Conformational Analysis of the COOH and $NH_2$ functional group torsion angles for the published crystal structures in the CSD for *p*ABA α and β. Two values given for the α structures as there are two molecules in the asymmetric unit.**

| COOH Torsion Angle (°) | Polymorph | Ref Code | Lead Author | Year Published | C-C-N-H Torsion Angle (°) |
|---|---|---|---|---|---|
| 2.865, 1.172 | α | AMBNAC01 | Lai | 1967 | 12.03, 11.17 |
| 0.866, 0.852 | α | AMBNAC06 | Athimoolan | 2007 | 0.024, 0.008 |
| 10.397 | β | AMBNAC04 | Gracin | 2005 | 26.844 |

Table 5-8 shows the COOH group of the α structures were found to be almost completely planar with respect to the phenyl ring, while the β structure was found to have a torsion angle of around 10°. The formation of the OH...O H-bonding dimers that run planar to the phenyl ring probably holds the COOH groups planar with respect to the phenyl ring, while the NH...O and OH...N interactions in the β form are not directed planar to the ring and hence the torsion angle was found to be around 10° away from the plane of the ring. Figure 5-15(a) reveals that the majority of crystal structures with a COOH group attached to a phenyl ring in the CSD are close to planar.

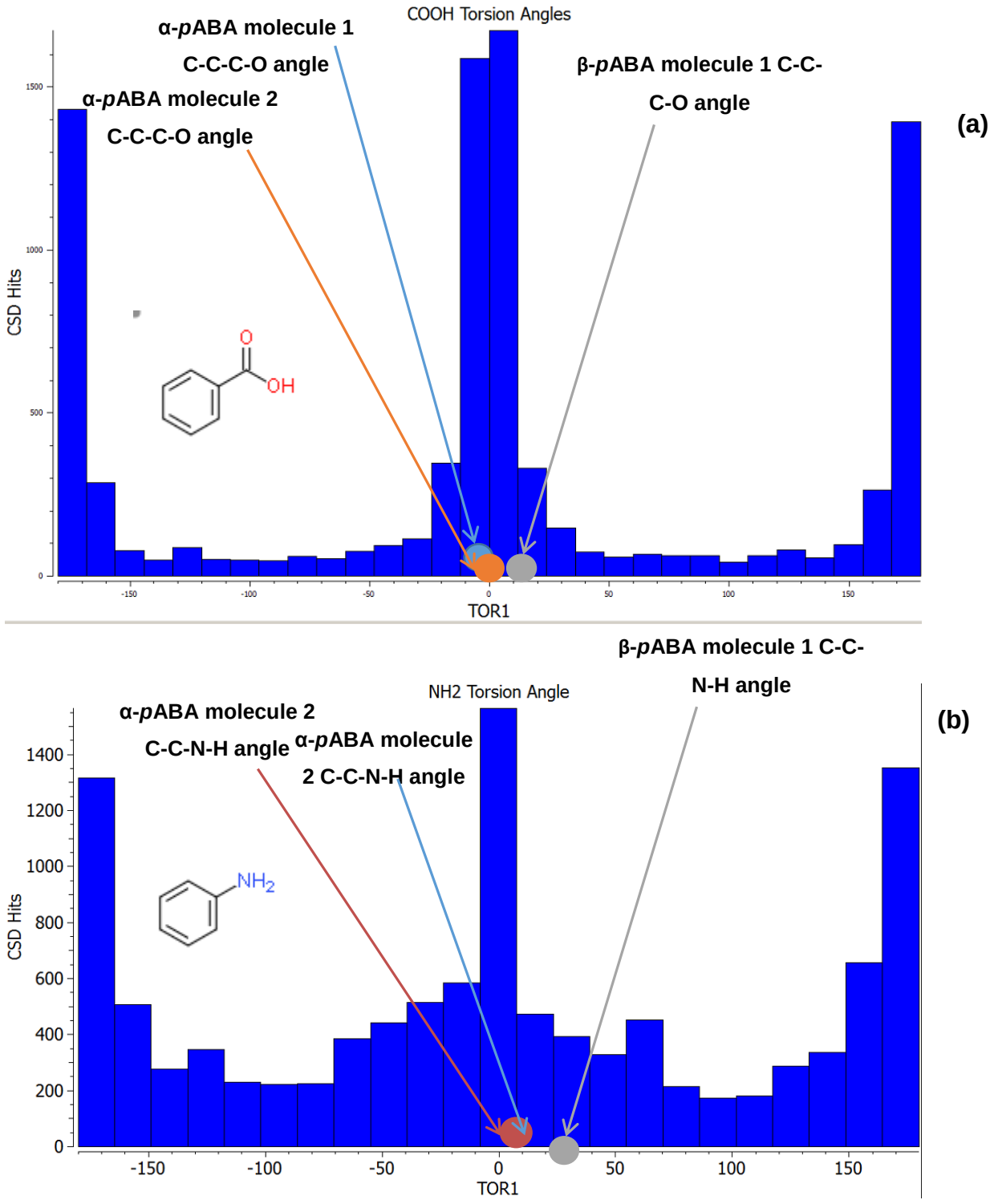


**Figure 5-15: (a) Histogram of the torsion angles of COOH groups attached to a phenyl ring found in the CSD. (b) Histogram of the torsion angles of $NH_2$ hydrogens from the phenyl ring found in the CSD. (180° rotation is essentially a planar torsion). The fragment searched is shown on both histograms**

The conformation of the $NH_2$ group is of some interest as the two structures published in the CSD have different conformations. Figure 5-14 showed that the structure published by Lai et al[191] showed a torsion angle of around 12° from the plane of the phenyl ring, while the more recent structure from Athimoolan et al[188] found it to be planar. The β-*p*ABA structure also presented a pyramidal $NH_2$ geometry[189]. It is worth observing that the two structures that show a more pyramidal $NH_2$ group both had the hydrogen positions found from analysis of the electron density maps[189, 191], whereas the hydrogen positions in the α structure with the more planar $NH_2$ were geometrically placed[188].

In addition, Figure 5-15(b) showed that the majority of structures found had linear C-C-N-H torsion angles. However, a greater proportion of structures were found to have non-linear torsion angles than for the COOH group. Optimisation of the single molecules from the crystal structures is shown in Figure 5-16 (only one molecule optimised from each α structure as the molecular conformations are very similar).

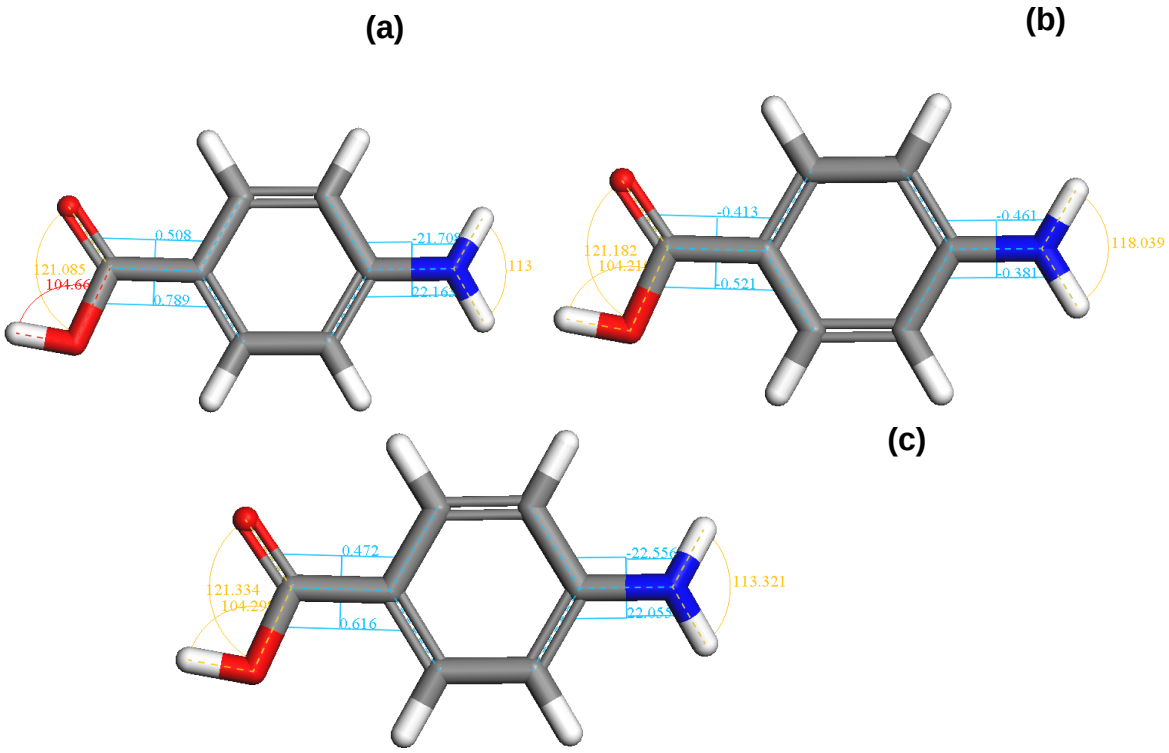


**Figure 5-16: Resulting conformations from *ab initio* geometry optimisation of the molecular structures from (a) α-*p*ABA AMBNAC01 crystal structure; (b) α-*p*ABA AMBNAC06 crystal structure; (c) β-pABA AMBNAC04 crystal structure**

The geometry optimisations resulted in very similar conformations from the optimisation of the AMBNAC01 and AMBNAC04 structures, showing a pyramidal $NH_2$ with a torsion angle of around 21°. The $NH_2$ group remained close to planar upon optimisation of the AMBNAC06 molecular structure. The energy and conformations of the optimised molecular structures was compared in Table 5-9.

**Table 5-9: Conformations of the COOH and $NH_2$ functional groups upon *ab initio* optimisation of the molecular structures taken from the crystal structures in the CSD. Atomic energies of the structures quoted along with the relative energies**

| Polymorph | Ref Code | C-C-N-H Torsion Angle (°) | COOH Torsion Angle (°) | Energy (kcal/mol) | Relative Energies (kcal/mol) | Relative Energies (kj/mol) |
|---|---|---|---|---|---|---|
| A | AMBNA C01 | 21.71, 22.16 | 0.51, 0.79 | -298843.23 | +0.01 | 0.04 |
| α | AMBNA C06 | 0.46, -0.38 | -0.41, -0.526 | -298842.77 | +0.47 | 1.96 |
| B | AMBNA C04 | 22.41, 22.40 | 0.84, 1.02 | -298843.24 | 0 | 0 |

The relative energies of the optimised molecular structures for the AMBNAC01 and AMBNAC04 crystal structures are found to be almost identical. The energy of the optimised AMBNAC06 structure is found to be almost 2kj/mol higher than the energy of the most stable AMBNAC04 conformation, hence indicating that the conformation from the AMBNAC06 optimisation is a local minimum, rather than the global minimum. The fact that the more pyramidal $NH_2$ group has been found to be more stable suggests that the planar $NH_2$ group found in the AMBNAC06 structure is a function of the geometric placement used in the structure refinement[188].

The conformation of the COOH group is consistently planar in all three structures; therefore the difference in energy between the conformers seemed to be due to the pyramidilisation of the $NH_2$ group. This is in good agreement with the results of the conformational analysis of the structures from the CSD shown in Figure 5-15, where the vast majority of the structures are found to have a planar COOH group. In comparison, through the majority of $NH_2$ groups found in the CSD were found to have a planar conformation, there was a greater proportion of structures with a non-planar conformation compared to the COOH group.

### 5.7.1 Relation of the Functional Group Conformation to Crystal Chemistry

The subtle conformational changes associated with the molecular structures within the α and β crystal structures can reflect the crystal chemistry and intermolecular packing of each structure.

#### 5.7.1.1 α-pABA COOH Group

Figure 5-17 shows the hydrogen bonding interactions that the COOH group in α-*p*ABA forms with the surrounding molecules.

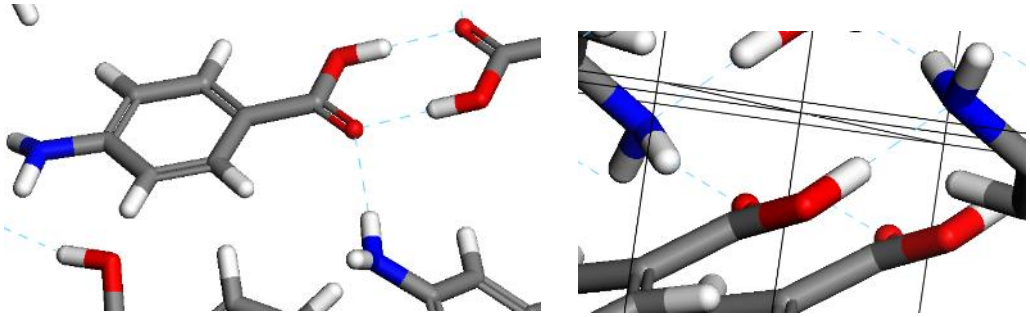

**Figure 5-17: Zoom in of the H-bonds formed by the COOH group in the α-*p*ABA AMBNAC01 and β-pABA AMBNAC04 crystal structures**

Table 5-8 and Table 5-9 revealed that the COOH conformations of the gas phase optimised molecule and crystal structure molecule are both very close to planar with respect to the phenyl ring for α-*p*ABA. Considering that the COOH group forms OH...O and O...HN interactions in the α-structure, the torsion angle between the plane of the C-C bond of the carboxylic acid and the neighbouring hydrogen which is interacting with the carbonyl group was measured for both the neighbouring NH and OH groups forming H-bonds to the COOH group (Figure 5-18).

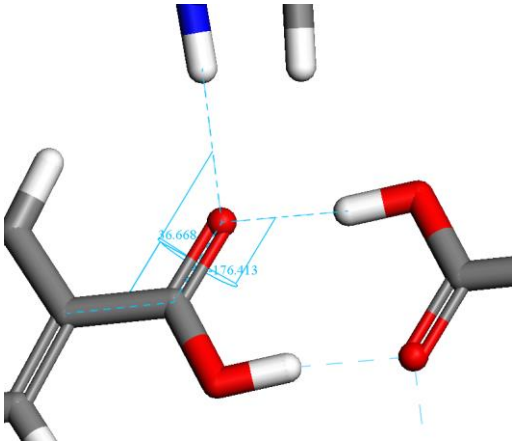


**Figure 5-18: Torsion angles from plane of the C-C bond within the COOH group and the interacting hydrogens from the neighbouring the OH and NH groups forming H-bonds to the carbonyl oxygen within the α-*p*ABA AMBNAC01 crystal structure**

The C-C-O-H torsion angle associated with the OH...O interactions was found to be around 4°, whereas the corresponding torsion angle for the NH...O interaction was found to be around 37°. Since the COOH group remains relatively planar with respect to the ring it is supposed that the OH...O interactions, rather than the NH...O, direct the conformation of this functional group.

### 5.7.1.2 β-*p*ABA COOH group

The COOH group within the β-*p*ABA structure has an increased torsion away from the plane of the phenyl ring compared to α-*p*ABA. The intermolecular environment around the COOH groups in α- and β-*p*ABA is shown in Figure 5-19.

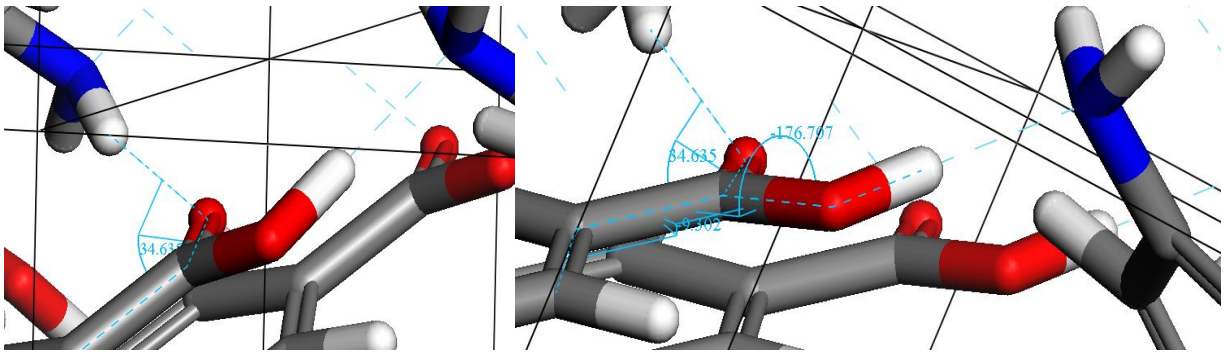


**Figure 5-19: Torsion angle from the plane of the C-C bond within the COOH group and the interacting hydrogen forming the NH...O hydrogen bond with the carbonyl oxygen (left) within the β-*p*ABA AMBNAC04 structure. Torsion angle from the plane of the ring to the OH oxygen and the torsion angle from the plane of the C-C bond in the COOH group to the OH hydrogen within the β-*p*ABA AMBNAC04 structure**

Considering rotation about the C-C bond of the COOH group, the C=O and O-H groups form hydrogen bonds in different directions. The NH...O interaction is almost 35° away from the plane of the C-C bond, while the OH...N interaction is almost in a straight line from the OH covalent bond to the nitrogen. To accommodate both of these interactions, the C=O group was found to be torsioned around 9° above the plane of the ring, alongside the OH bond that was found to bend around 3° from the plane of the C-C bond. This suggests that the OH...N interaction is the dominant synthons of these two hydrogen bonding interactions; hence it can exert greater influence over the geometry of the COOH group.

#### 5.7.1.3 $NH_2$ group

The $NH_2$ groups most stable C-C-N-H torsion angle was found to be around 21° from the plane of the phenyl ring. Table 5-8 showed that the α-*p*ABA $NH_2$ group was found to have a decreased torsion angle. In contrast, the β-*p*ABA $NH_2$ group has an increased torsion angle, compared to the optimised molecular geometry. Figure 5-20 shows the intermolecular bonding environment around the $NH_2$ groups of α- and β-*p*ABA.

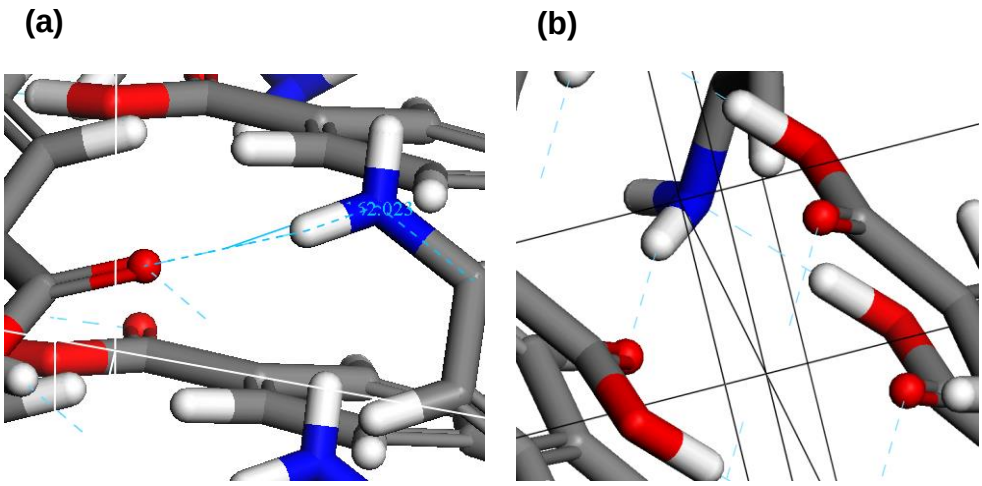


**Figure 5-20: (a) Torsion angle from plane of C-N bond to the oxygen from neighbouring carbonyl group forming the NH...O hydrogen bond within the α-*p*ABA crystal structure. (b) Zoom in of $NH_2$ group within the β-*p*ABA crystal structure showing the H-bonding interactions to this group**

Figure 5-20(a) showed that the NH...O hydrogen bond within the α-*p*ABA structure was found to have a torsion of around 18° away from the plane of the C-N bond.

Hence, the formation of the NH...O hydrogen bond interaction probably reduces the C-C-N-H torsion angle.

In contrast, the increased torsion within the β-*p*ABA crystal structure is probably due to the $NH_2$ group acting as both a hydrogen bonding donor and acceptor. Figure Figure 5-20(b) showed that the OH...N and NH...O interactions are, to some extent, pulling the nitrogen and hydrogen of the $NH_2$ group involved within these interactions in opposite directions, hence increasing the C-C-N-H torsion angle. Figure 5-21 shows the bond angle between the C-N bond and the adjacent H-bonding hydrogen.

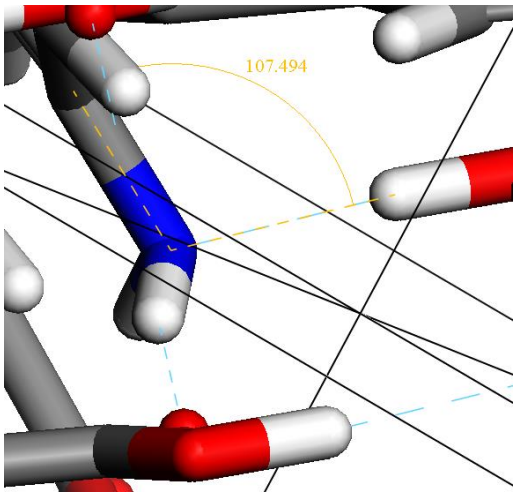


**Figure 5-21: 3 body bond angle C-N-H between the C-N bond and the hydrogen forming the OH...N H-bonding interaction. 4 body torsion angle C-N-H-O from plane of C-N bond to oxygen forming the NH...O interaction**

Figure 5-21 shows that the C-N...H bond angle was found to be around 107°, hence the OH...N H-bonding interaction could be expected to pull the nitrogen out of the plane of the ring and slightly bend the C-N bond. In addition, it appears that the angle of the NH...O interaction might be expected to actually direct the hydrogens to a more planar geometry. Hence, from this analysis it appears that the OH...N interaction may well be the dominant synthon associated with the $NH_2$ group within the β-*p*ABA structure, and as such exerts a greater influence on the geometry of the $NH_2$ group by creating a slightly greater torsion angle between the $NH_2$ hydrogen and the ring. This postulation is reinforced by the fact that the H-N-H bond angle of the $NH_2$ group is slightly decreased from 113° to 111° (Figure 5-20) compared to the optimised

molecular structure, suggesting the NH...O interaction does relatively little to widen the bond angle.

## 5.8 Synthons and the Packing of a Crystal Structure

It is interesting to observe that for both structures the molecular conformation has moved away from the computational minimum. This is in line with studies conducted on more flexible molecules[59] whereby it may be expected that the conformation plays a greater role on polymorphism, however this study did observe that often molecules of any size become distorted when packing into a crystal structure.

This chapter has not only observed the conformational change, but also characterised the synthons that induce the changes in molecular conformation. An understanding of what functional groups or intermolecular interactions are likely to induce conformational changes could assist in the prediction of whether the conformation is likely to play a role in polymorphic preferences during crystallisation.

## 5.9 Conclusions

The synthonic character of the α and β crystal structures was determined, along with their effect on molecular conformation, together with which synthons and functional groups are important for lattice energy stabilisation. These results are summarised in Table 5-10.

**Table 5-10: Summary of questions and problems identified and addressed in this chapter**

| Question/Problem | Information gained from this chapter | Relevance to Study |
|---|---|---|
| What are the strongest synthons in the α- and β-*p*ABA structures? | • α dominated by OH...O carboxylic acid H-bonded dimers and head-head π-π stacking interactions<br>• β synthons are of more equal energy. Major synthons include head-head π-π stack and NH...O and OH...N H-bonds | Strongest synthons likely to be building blocks for self-assembly and to strongly influence crystal growth |
| How do the different functional groups contribute to the lattice energy in the two polymorphs? | • α mostly focussed on COOH and phenyl ring group<br>• More even spread of lattice energy across the functional groups of β-*p*ABA | Identifies which parts of the molecule must be satisfied to converge the lattice energy of each structure |
| How do the conformation and interatomic distances of the synthons compare to other similar structures in the CSD? | • The synthons in both α- and β-*p*ABA exhibit similar conformations and interatomic distances as other structures in the CSD<br>• NH...O synthon seems to be most amenable to changes in interatomic distance and conformation | Synthons in *p*ABA are probably stable, since there are many other similar ones in the CSD.<br>The amenability of the NH...O synthon suggests that it is influenced by the more dominant synthons, therefore is a weaker, more secondary synthon |

| | | |
|---|---|---|
| How do the synthons affect the molecular conformation of *p*ABA in the crystal structures? | • Both structures were found to have slightly higher energetic conformations than the global minimum<br>• H-bonding synthons were found to affect the $NH_2$ and COOH conformations | Conformations of even inflexible molecules are affected by H-bonding synthons much more than vdW interactions. The intermolecular energy being focussed on one or two atoms affects the molecular structure |

The differences in calculated synthon strength, direction and nature of the α- and β-*p*ABA crystal structures was found to strongly influence which functional groups dominated the lattice energy convergence. In addition the H-bonding networks were also found to affect the COOH and $NH_2$ conformations, even though *p*ABA is quite an inflexible molecule.

The OH…O dimer synthon and the π-π stacking synthon are dominated by the COOH and phenyl ring groups respectively. Hence, the functional group contribution to the lattice energy of α-*p*ABA was found to be dominated by the COOH and phenyl ring groups. In contrast, there was significant contribution from all three major parts of the *p*ABA molecule to the dominating synthons of the β-*p*ABA structure and the spread of the lattice energy round the functional groups within the β-*p*ABA structure was found to be more even.

The conformation of the *p*ABA molecule was found to be affected by the intermolecular synthons in both α- and β-*p*ABA. The hydrogen bonding interactions were found to have an influence over the conformation of the COOH and $NH_2$ functional groups. This is probably because the intermolecular energy is focussed more onto a single atom, compared to more isotropic vdW interactions which usually encompass many more interatomic interactions. This suggests that for relatively inflexible molecules, where the conformational change may be small and the energetic increase may also be small, that the formation of synthons is the determining factor in stabilising the crystal structure.

Understanding the energetic balance between conformational energy penalties caused by formation of synthons can reveal the energy barriers associated with

crystallisation, thereby revealing how crystallisable a material may be. This can aid with the design of a crystallisation process and predictions of how easily a molecule may crystallise from solution. The strength and directionality of the synthons calculated in this chapter underpin the completion of objectives 2 and 3 relating to predicting molecular building block aggregation and crystal morphology. In addition, the detailed relation of the synthonic structure to the molecular conformation satisfied objective 1

# Chapter 6 Molecular Modelling of Solvation and Self-Assembly of Molecules to Clusters

*The explicit solvation of the* p*ABA molecule is explored and combined with implicit QM continuum solvation calculations, whereby these results are linked to the polymorphic behaviour of the material.*

## 6.1 Introduction

The de-solvation of single solute molecules and subsequent aggregation into pre-nucleation clusters within solution is extremely challenging to monitor experimentally. Therefore molecular modelling techniques are often applied to attempt to extract more information about this transition pathway. Therefore this chapter aimed to correlate binding energies of solvent to *p*ABA and the calculated stability of small clusters in solution, to how the solute molecules may aggregate in certain solvents and in turn influence the polymorphic form of the resultant crystals.

The molecular grid search technique (Section 4.4.4) was used to examine the preferred binding sites of explicit solvent molecules to the single molecule of *p*ABA to determine which functional groups may be hindered by a certain solvent. These calculations were then complemented by quantum mechanical solvent continuum and statistical thermodynamics calculations of the relative comparative populations of small clusters in solution based on synthons of α- and β-*p*ABA defined in chapter 5. These populations indicated which molecular building blocks associated with each crystal structure were favoured in solvents from which *p*ABA is known to crystallise from. In turn, a self-assembly pathway from single molecule to dimers, tetramers and octamers was proposed for the α- and β-*p*ABA structures.

This work contributed to the completion of objective 2, since the molecular solvation can directly influence the aggregation of the molecules in solution. Correlating how hindered a functional group may be due to solvent binding with calculating the stability of small aggregates in solution can offer insight into the transition from single molecules to clusters, prior to nucleation. This knowledge is important with respect to designing a crystallisation environment that promotes the desired polymorphic form. The principles of where a certain solvent preferentially solvates and which molecular building blocks are important for self-assembly can be related to the growth and morphology of the material, which is part of objectives 3 and 4. Figure 6-1 shows the work flow for this chapter.

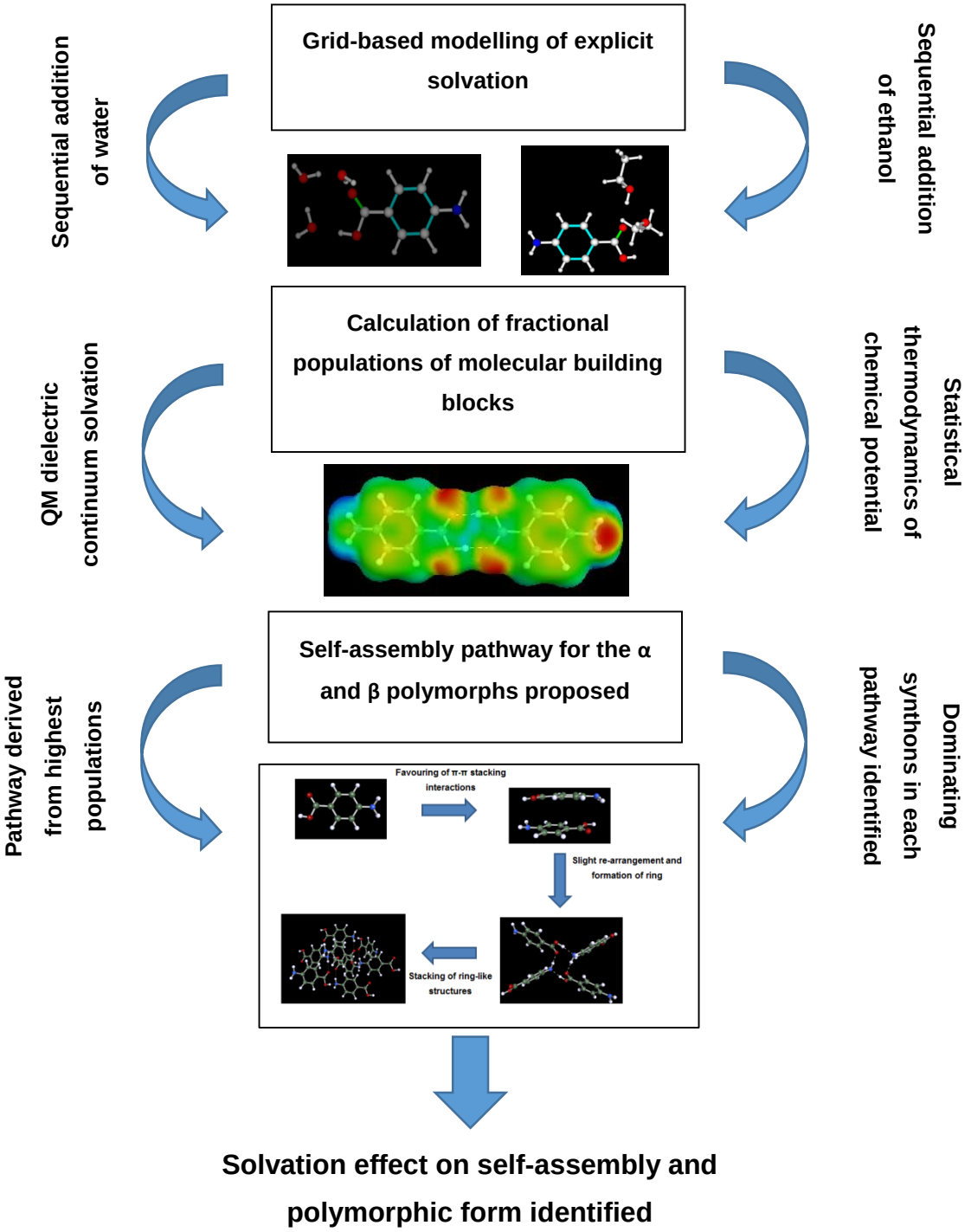


**Figure 6-1: Work flow associated with chapter 6 highlighting what information is gained from this part of the study**

## 6.2 Explicit Solvent Binding

The single molecule on single molecule grid search technique outlined in Section 4.4.4 was used to identify the most favoured binding sites of water and ethanol to a single molecule of *p*ABA. The molecules could only be searched sequentially and the programme works by holding one body rigid while the other body was moved around the grid, so once a molecule of solvent was added it remained rigid during the search of the sequentially added molecules.

Figure 6-2 to Figure 6-4 show the preferred binding sites for single molecules of water and ethanol added sequentially.

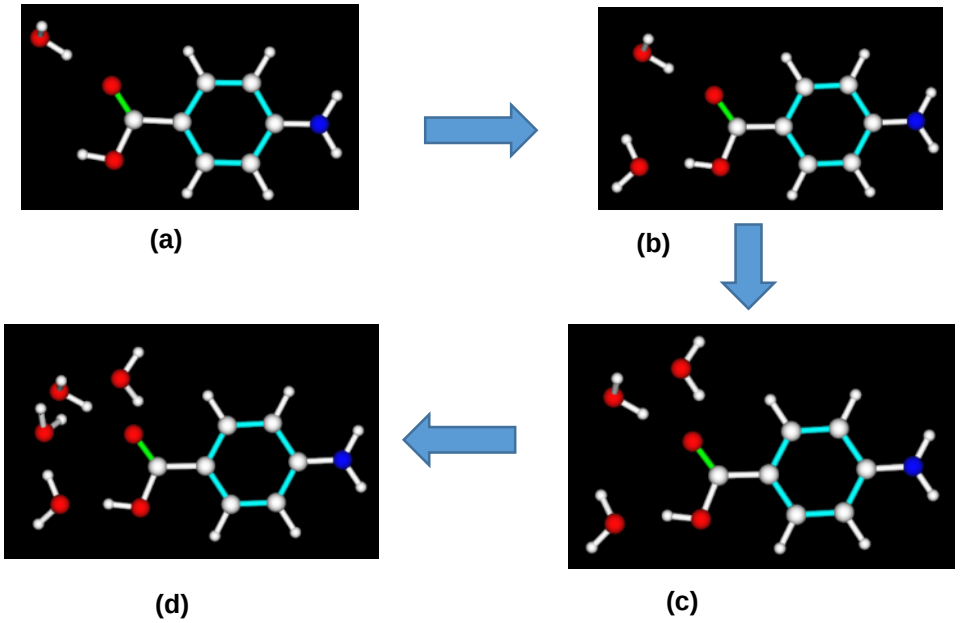


**Figure 6-2: Sequential systematic searching of water on a single molecule of *p*ABA. For the third addition, the preferred self-association of water to itself was ignored**

Water was found to strongly prefer to bind to the COOH group of *p*ABA, compared to anywhere else on the molecule. The addition of two molecules of water formed a bridge between the carbonyl oxygen and the hydroxyl hydrogen through a H-bonding network (Figure 6-2b). Addition of the third molecule revealed that the most favoured binding site was for the water molecule to interact with itself (Figure 6-3). However, the third water molecule also strongly preferred to hydrogen bond to the remaining lone pair of electrons on the carbonyl oxygen. Addition of a fourth water molecule

revealed that the entirety of the top fifty structures consisted of the fourth molecule of water binding to the already added water molecules.

**Figure 6-3: Most favoured structure upon addition of a third water molecule to a single molecule of *p*ABA**

The binding of water molecules was compared to the binding of ethanol molecules in Figure 6-4.

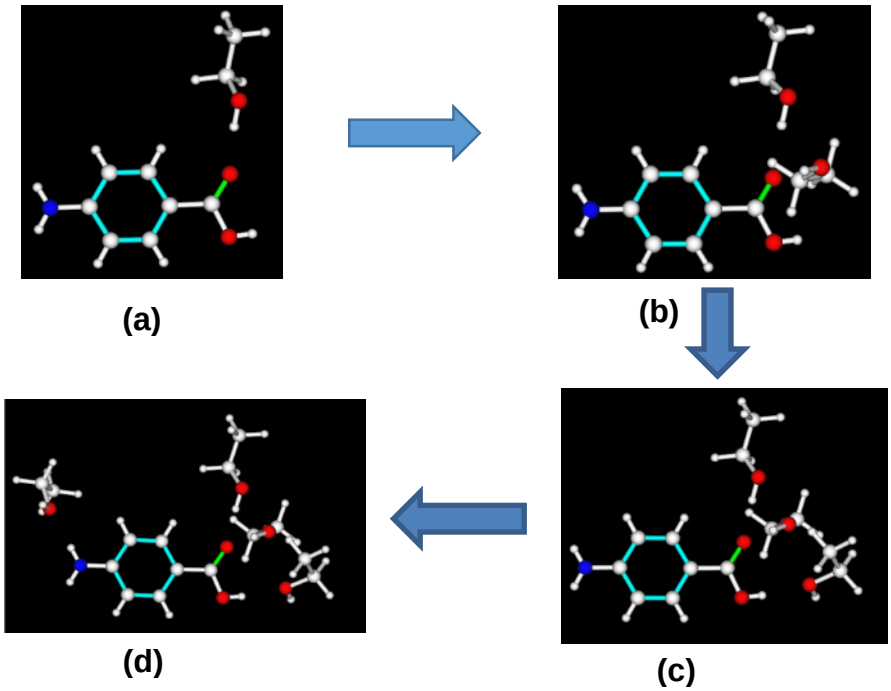


**Figure 6-4: Sequential systematic searching of ethanol on a single molecule of *p*ABA For the third and fourth addition, the preferred self-association of ethanol to itself was ignored**

Similarly to water, the first three ethanol molecules are able to bind to the COOH group. However, the addition of a 4$^{th}$ ethanol molecule found that the 29$^{th}$ most stable binding site was to the $NH_2$ group, with all the other more stable structures consisting of ethanol binding to itself. This suggests that water more strongly prefers bind to itself, in preference to *p*ABA, than ethanol does. This could be one of the reasons why the

solubility of *p*ABA in water is found to be so much lower in water than in ethanol, as water would poorly solvate the phenyl ring since the phenyl ring rather hydrophobic.

Since the systematic search only calculates the energy between the rigid and mobile bodies, the intermolecular interactions were calculated and summed to give an intermolecular cluster energy, using the methodology described in Section 4.4.3. The results are displayed in Table 6-1.

**Table 6-1: Intermolecular cluster energy calculated from sequential addition of up to four molecules of ethanol and water to a single molecule of *p*ABA**

| Water | | | Ethanol | |
|---|---|---|---|---|
| **ΔE/Molecule Added (kcal/mol)** | **Cluster Energy (kcal/mol)** | **Addition** | **Cluster Energy (kcal/mol)** | **ΔE/Molecule Added (kcal/mol)** |
| -4.08 | -4.08 | 1st | -4.14 | -4.14 |
| -4.91 | -8.99 | 2nd | -7.95 | -3.81 |
| -3.86 | -12.85 | 3rd | -11.40 | -3.45 |
| -3.49 | -16.34 | 4th | -13.27 | -1.87 |

The cluster energy gained from adding water molecules was greater than for adding ethanol molecules. This probably reflects that water strongly solvates the COOH group forming a stable network around it. In addition, water also was found to form favourable interactions with itself. The stronger bonds made in the solvation shell around the COOH group for water compared to ethanol probably hinders the formation of the OH...O carboxylic acid dimer in water more than ethanol. This could be part of the reason that water seems to favour the β form of *p*ABA more so than other solvents[192, 224].

## 6.3 Solvent Dielectric Continuum and Statistical Thermodymanics Calculations of the Stability of Small Clusters

Thermophysical data relating to the stability of small clusters of *p*ABA in solution was calculated to predict the relative fractional populations of these clusters and free energy of formation. The pairwise synthons strengths calculated in Chapter 5 were used as a guide in selecting the dimer pairs to examine, whereby tetramers and octamers were built from these constituent dimers. The first letter in the label represents the size of the cluster, e.g. D for dimer, along with the second letter in the dimer labelling referring to the strength of the synthons calculated in Chapter 6 (Section 6.4, Tables 6-3 and 6-4). Figure 6-5 to Figure 6-7 show the clusters examined by this method.

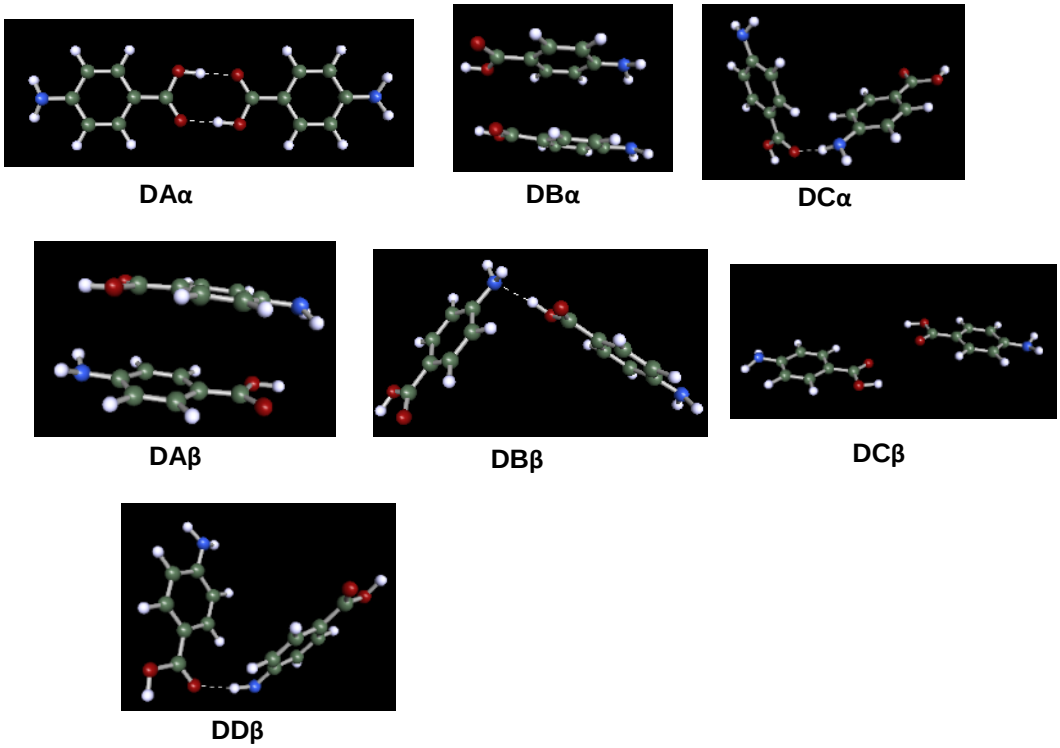


**Figure 6-5: Important dimer molecular building blocks derived from the α- and β-*p*ABA crystal structures**

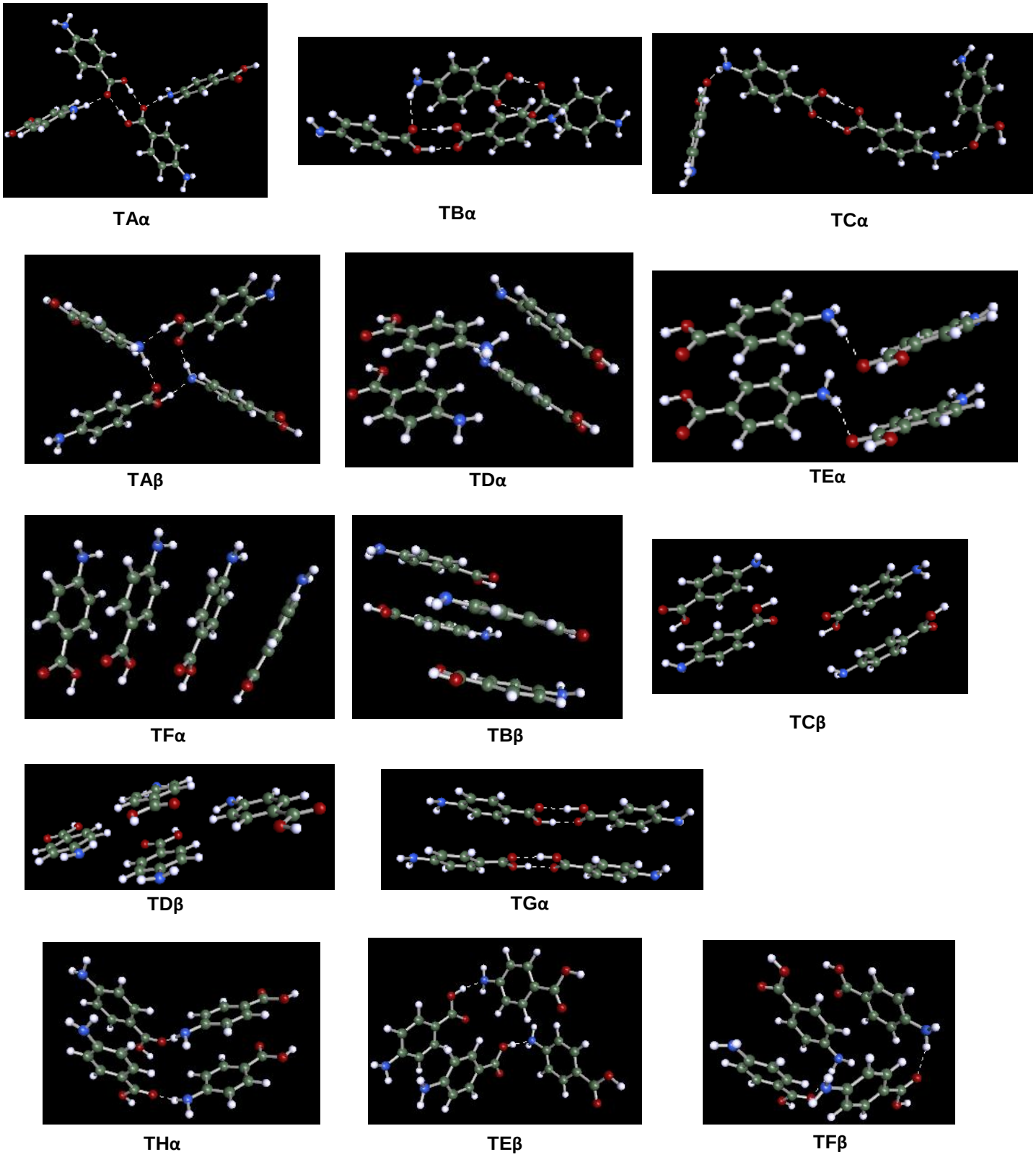


**Figure 6-6: Tetramers based on the crystal structures and important molecular building blocks of α- and β-*p*ABA**

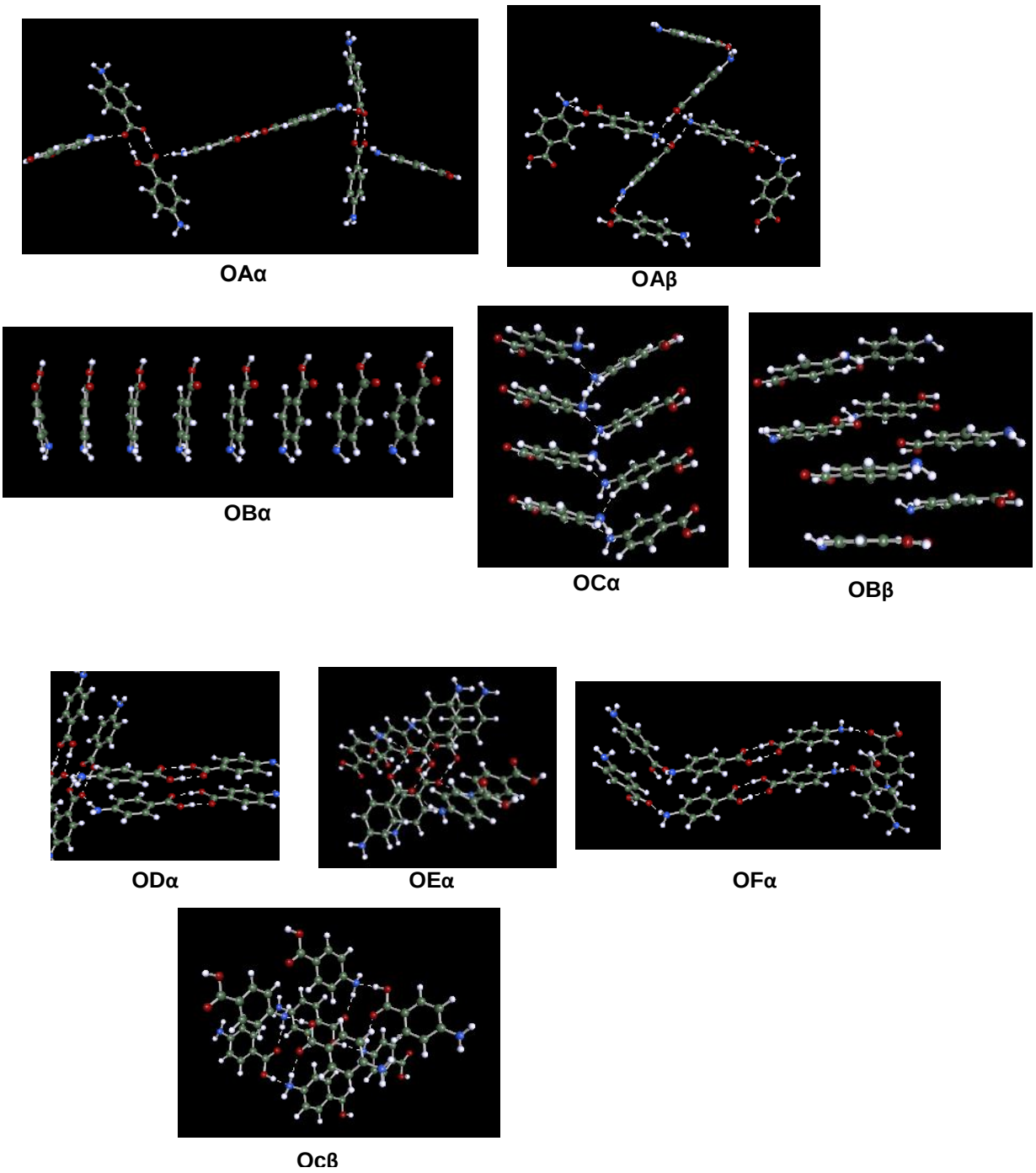


**Figure 6-7: Octamers derived from the crystal structures of α and β *p*ABA containing mixed H-bonding and vdW interactions**

### 6.3.1 Synthon Analysis of the Clusters

Since the tetramers and octamers were built from the constituent synthonic building blocks, the clusters can be analysed in terms of which synthons are present in each cluster. The intermolecular energy between the molecules within the clusters was calculated using the methodology described in Section 4.4.3.

**Table 6-2: Synthonic makeup of the tetramers and octamers along with the energy of their total interactions present within each cluster**

| Cluster | Constituent Synthons | Cluster Energy (kcal/mol) |
|---|---|---|
| TAα | 2 X DAα and 2 X DCα | -13.61 |
| TBα | 1 X DAα and 2 X DCα | -10.21 |
| TCα | 1 X DAα and 2 X DCα | -11.01 |
| TAβ | 2 X DBβ and 2 X DDβ | -7.90 |
| TDα | 2 X DBα | -5.36 |
| TEα | 2 X DBα and 2 X DCα | -9.90 |
| TFα | 3 X DBα | -8.04 |
| TBβ | 2 X Daβ | -5.14 |
| TCβ | 1 X DCβ and 2 X Daβ | -9.92 |
| TDβ | 1 X DAβ and 2 X DHβ | -5.94 |
| TGα | 2 X DAα and 2 X DBα | -16.70 |
| THα | 2 X Bα and 2 X DCα | -10.70 |
| TEβ | 2 X DBβ | -4.90 |
| TFβ | 2 X DDβ | -2.92 |
| OAα | 3 X DAα and 4 X DCα | -26.09 |
| OBα | 7 X DBα | -18.76 |
| OCα | 6 X DBα | -16.08 |
| ODα | 4 X DAα, 4 X DBα and 2 X DCα | -37.94 |
| OEα | 2 X DAα, 4 X DBα and 4 X DCα | -31.14 |
| OFα | 2 X DAα, 4 X DBα and 4 X DCα | -31.14 |
| OAβ | 4 X DBβ and 4 X DDβ | -15.64 |

| | | |
|---|---|---|
| OBβ | 4 X DCβ | -9.56 |
| OCβ | 4 X DBβ and 4 X DDβ | -15.64 |

Table 6-2 revealed that the tetramers and octamers that are made up of the DAα and DBα dimers were calculated to have the greatest intermolecular cluster energies.

## 6.3.2 Stability of Dimers in Solution

### 6.3.2.1 Dimer Energetics

The internal energy of the electronic structure of the dimers was calculated in the first step of the COSMO-RS calculation outlined in Section 4.4.3, corresponding to the theory described in Section 2.6.4. This energy is the internal energy of the *p*ABA molecules after optimisation of the cluster within the solvent dielectric continuum. The utilisation of the M06 functional resulted in calculation of dispersion interactions between the *p*ABA molecules within the cluster. Figure 6-8 shows the calculated internal energies ($E_{COSMO}$) of the Daα, DBα, DCα, Daβ, DBβ, DCβ and DDβ.

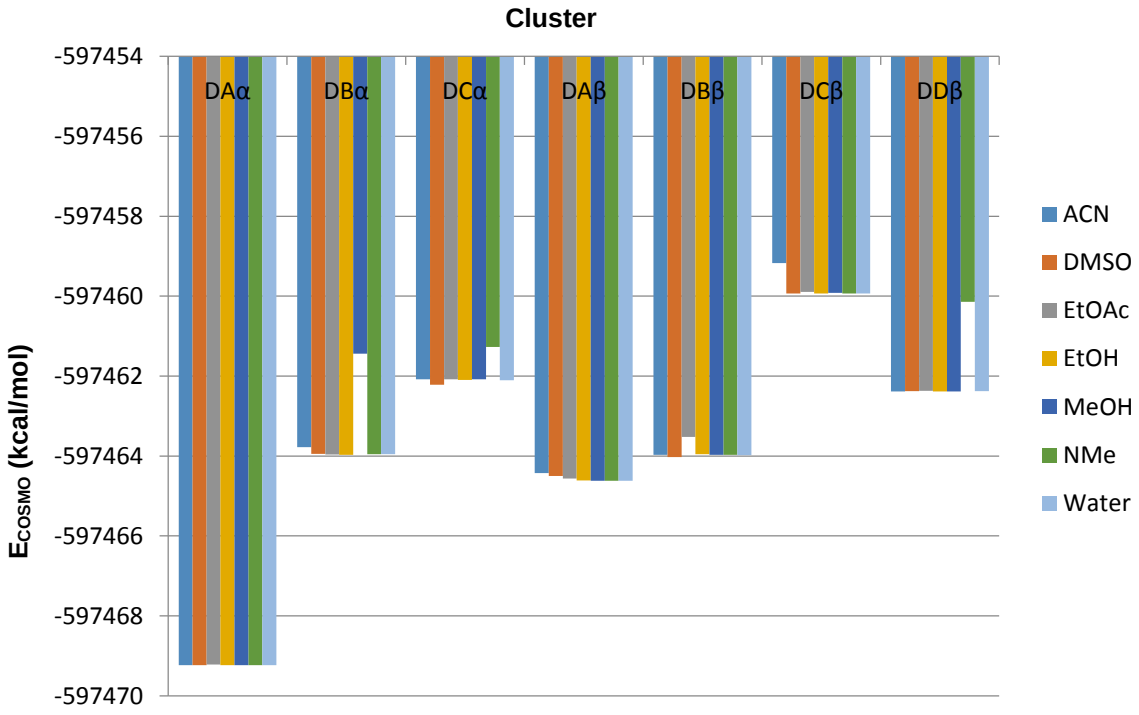


**Figure 6-8: The internal energy of the dimers shown in Figure 6-5 calculated from the DFT geometry optimisation, using a 6-31G* basis set and M06 functional. Dielectric continuum conditions were used for the solvation conditions**

Figure 6-8 shows that the DAα dimer was found to have the lowest internal electronic energy in all of the solvents tested. The energy variances calculated for the clusters in the different solvents was found to be relatively low. The DAα dimer contains the OH...O H-bonds (Figure 6-5), so it is perhaps unsurprising that the internal energy of that dimer is lowest. However, since this energy is only derived from the internal energy of the molecules and how the dielectric nature of the solvent polarises the molecule, further calculations would be helpful to provide more information as to how the clusters may more explicitly interact with the surrounding solution. This was provided by using the statistical thermodynamics methods described in Section 2.6.4.1.

#### 6.3.2.2 Dimer Fractional populations

The combination of the internal energy and the 'chemical potential' (Section 2.6.4) can be utilised to provide a fractional population of each cluster in solution according to equation 2-24. Equation 2-24 has previously been used to examine the relative stabilities of multiple conformers of the same molecule[225, 226]. However, in an approach similar to the one used by Di Tommaso and co-workers[26, 227], the dielectric continuum approach was used to examine the relative stabilities of different clusters in the continuum solvation environment. The conformers calculation (Equation 2-24) is parameterised to examine different species of the same molecular weight, therefore the species examined must have the same molecular weight. Therefore the calculation of the fractional populations is always on clusters of the same size, i.e. dimers, then tetramers and then octamers. The clusters were inputted together to the solvent dielectric continuum to create a mixture of clusters at infinite dilution (the clusters only interact with the surrounding solvent and not with each other). The calculation of the populations of the different clusters comes from the Boltzmann distribution over different states of free energy (section 2.4). The combined internal energy and chemical potential of each cluster is calculated with respect to the total internal energy and chemical potentials of all the components in the system.

Figure 6-9 (below) shows the fractional populations of the major intermolecular interacting dimers from the α and β forms of *p*ABA.

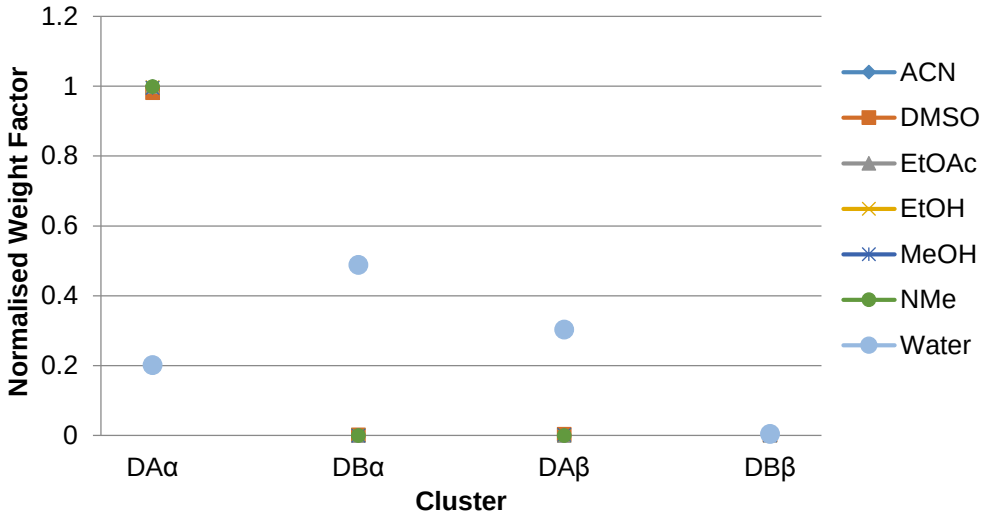


**Figure 6-9: Fractional populations of strongest H-bonding and vdW interacting dimers in solvents that *p*ABA is known to crystallise from. Populations calculated from internal energy plus chemical potential of clusters compared to those for the whole system**

In all solvents apart from water, the DAα dimer was found to have a fractional population of almost 1, while all the other dimers had almost zero contribution to the fractional population. This would suggest that, in a situation where the early stages of pre assembly of solute molecules began with monomers forming dimers, the DAα carboxylic acid H-bonding dimer would be the most favoured building block to form that is associated with either crystal structure. In contrast, the DBα and DAβ dimers were found to have a higher fractional population than the DAα dimer in water. This favourability of the π-π stacking dimers over the DAα dimer in water could be the reason that β-*p*ABA has been observed to more reliably nucleate from water than any of the other solvents[224].

### 6.3.3 Chemical Potentials of Dimers

The chemical potentials of the surface segments and whole compound were calculated from Equations 2-21 and 2-22 respectively. This is calculated from the interactions between the polar segments described in Section 2.6.4. The electrostatic, H-bonding and vdW interactions between the segments, and hence molecules, was calculated from Equations 2-17 to 2-19 respectively. This gives an indication of how

the cluster would interact with the surrounding solvent. Hence combining the internal electronic energy of the molecules within the continuum ($E_{COSMO}$), along with the chemical potential calculated from the interacting segments can result in a more complete calculation of the stability of the clusters in solution.

Figure 6-10 revealed the internal energy difference for the clusters between different solvents was small. However, Figure 6-9 revealed that the calculated fractional populations in water were found to be quite different to all the other solvents. Since the second step of the calculation combines the internal energy and chemical potential, the chemical potential must play a significant role in the increased fractional populations of the DBα and DAβ dimers above the DAα dimer in water. Figure 6-10 shows the chemical potentials for the Daα, DBα, DAβ and DBβ dimers.

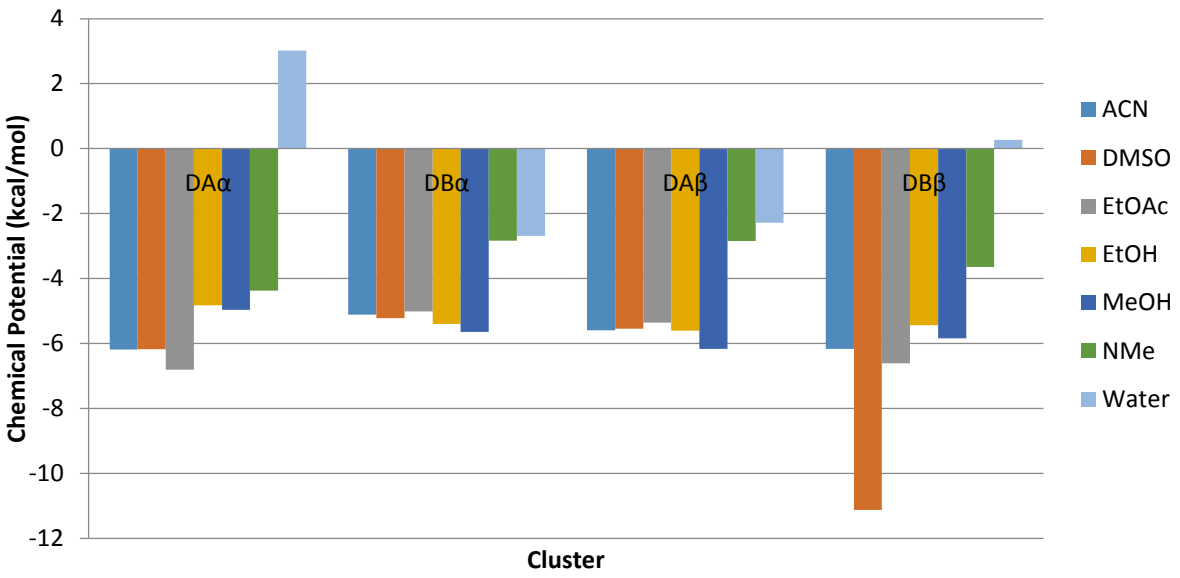


**Figure 6-10: Chemical potentials of the energetically favoured DAα, DBα, DAβ and DBβ dimers in the major solvents that *p*ABA is known to crystallise from**

Figure 6-10 shows that the chemical potentials of all the clusters were found to be higher in water than the other solvents. However, the chemical potential of the DAα dimer was found to be much more positive in water than the other solvents, hence it was found that water has very little affinity for the DAα dimer. There was found to be

around a 7kcal/mol difference between the chemical potential of the DAα dimer in water and the other solvents. Additionally, the chemical potential of the DAα dimer was found to be around 5kcal/mol higher than the DBα and DAβ dimers in water. The polarity of the surfaces (from the calculated surface charges in the QM optimisation) that make up the surface segments in the DAα, DBα and DAβ clusters are shown in Figure 6-11.

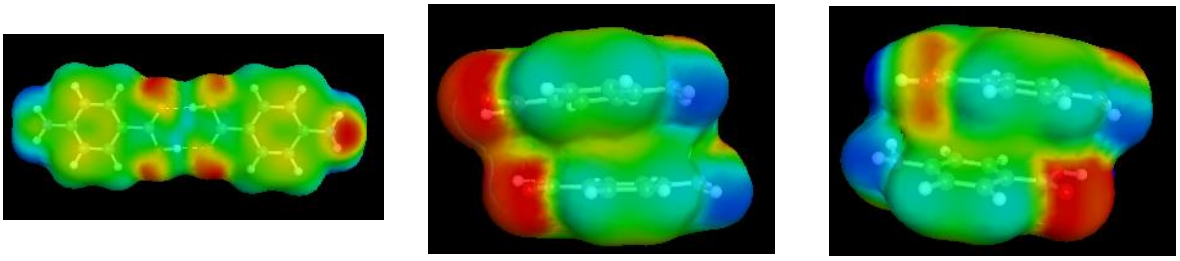

**DAα** **DBα** **DAβ**

**Figure 6-11: Sigma surfaces from the COSMO QM calculation showing how strongly or weakly charged a surface is. Red is negative, blue positive and green and yellow more neutral**

The chemical potential of the DAα dimer in water is probably more positive due to the large area of this dimer that is hydrophobic. Figure 6-11 shows that the majority of the DAα dimer is green or yellow, indicating that the surface charges were found to be close to neutral. In contrast, the DBα clusters have more area that is deep red or blue, indicating that in these areas the surface charges were found to be more polar.

The chemical potential is calculated from the interacting segments of the clusters with each other and the surrounding solution based on mole fraction and surface area of the clusters. Since the solubility of *p*ABA in water is low, then the vast majority of the interactions that the DAα cluster would form in solution would be with the solvent. The major hydrophilic part of this cluster is the COOH group, which has two out of the three possible H-bonding sites that this group can form satisfied. The phenyl rings make up a large area of the DAα cluster and these are relatively hydrophobic. Therefore, with the COOH group being relatively unavailable and the majority of the rest of the molecules being hydrophobic, the water molecules would offer little stabilisation to this motif, resulting in this more positive chemical potential.

In contrast, the DBα and DAβ clusters have available COOH groups that can strongly H-bond with the water molecules. In addition, the phenyl ring groups are stacked close to each other in the DBα and DAβ clusters and therefore form π-π stacking interactions that can stabilise the phenyl ring area of the molecule. Hence, each part of the molecule can form dispersive or H-bonding interactions when it is part of the DBα or DAβ dimer, hence the much more favoured chemical potential.

Comparing the chemical potentials of these clusters in other solvents which appear to favour the crystallisation of the α-form, the chemical potentials are relatively similar. None of the other solvents tested gave a positive chemical potential for the DAα cluster that was found for water. It would be expected that, to some extent, all of the other solvents could provide some vdW stabilisation to the phenyl ring structures of the DAα dimer. Combining the favourable internal energy from the H-bonds formed within the DAα cluster, with the extra stabilisation from the more favourable chemical potential, resulted in the DAα dimer dominating in all solvents apart from water.

Explicit solvation of a single molecule of *p*ABA shown in Figure 6-2 revealed that water molecules preferentially to bind to the COOH group or self-associate. Combining with the calculated lack of affinity of water for the DAα dimer, suggests that water is likely to both strongly solvate the COOH group and even try to attack the COOH groups in the DAα dimer break up this cluster. This is probably why the β-polymorph has only been reliably observed to crystallise in water due to suppression of the formation of the major synthon of the α-structure.

### 6.3.4 Tetramer Energetics and Normalised Weight Factors

The internal $E_{COSMO}$ energy, previously described for the dimers in Section 2.6.4 and in Section 6.3.2, was calculated for the tetramers and presented in Figure 6-12, shown below.

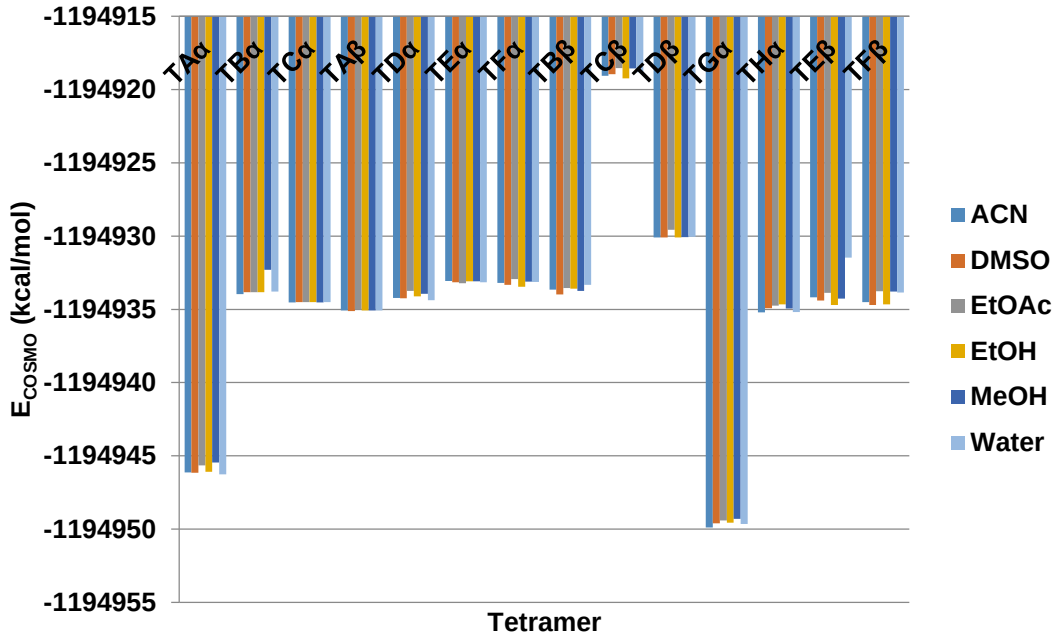


**Figure 6-12: $E_{COSMO}$ energies for the tetramers shown in Figure 6-6**

The most stable tetramers were found to be the TAα and TGα clusters. The energy gap between the TAα and TGα tetramers compared to the other clusters is over 10kcal/mol. Compared to the dimeric clusters, the energy gap between the most stable clusters for the tetramers has now grown. Figure 6-13 shows the normalised weight factors for the tetramers from the α- and β-*p*ABA crystal structures.

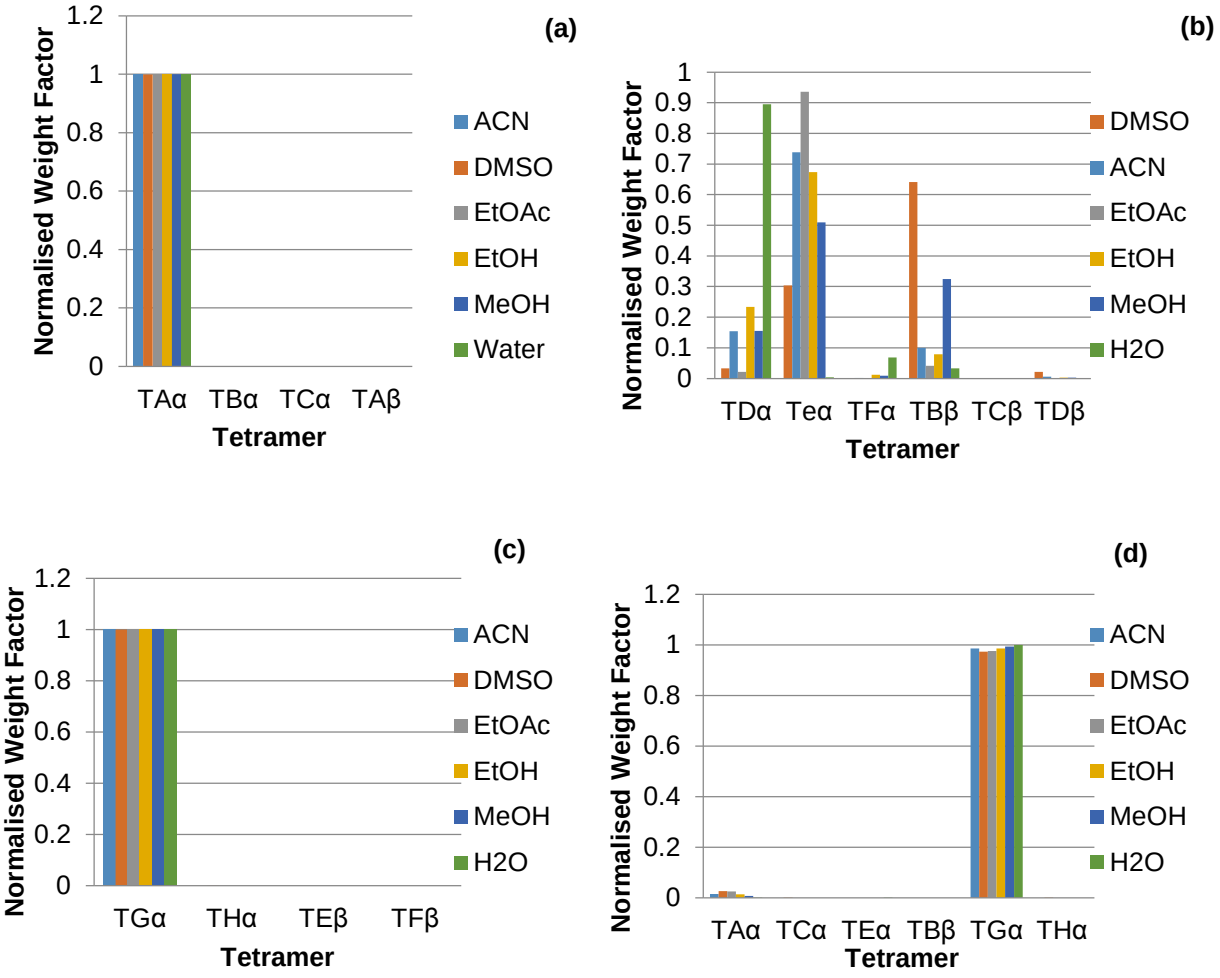


**Figure 6-13: (a) Normalised weight factors of H-bonding interacting tetramers; (b) normalised weight factors of π-π interacting tetramers; (c) normalised weight factors of mixed H-bonding and π-π interacting tetramers; (d) normalised weight factors of the two most favoured tetramers from the Figure 6-13(a), (b) and (c)**

Figure 6-13(a) and Figure 6-13(b) shows that the TAα tetramer and TGα tetramer were found to have calculated fractional populations of almost 1 and the other tetramers having fractional populations of almost 0 for the H-bonding and mixed tetramers respectively. In addition, Figure 6-13(d) shows that the TA7 tetramer was found to be dominant when compared to either H-bonding or π-π interacting tetramers. The TA7 tetramer contains the OH...O H-bonding dimers stacked together to create π-π stacking interactions as well. This suggests that the self-assembly of the α form may go via the stacking of these DA1 like dimers to form the observed crystal structure.

For the dimers, it was observed that the chemical potentials could overcome the internal energies of the clusters and influence the calculated populations. For the tetramers, it was observed that the tetramers with most favourable internal energy dominated the calculated populations for all the solvents. The calculated chemical potentials are shown in Figure 6-14

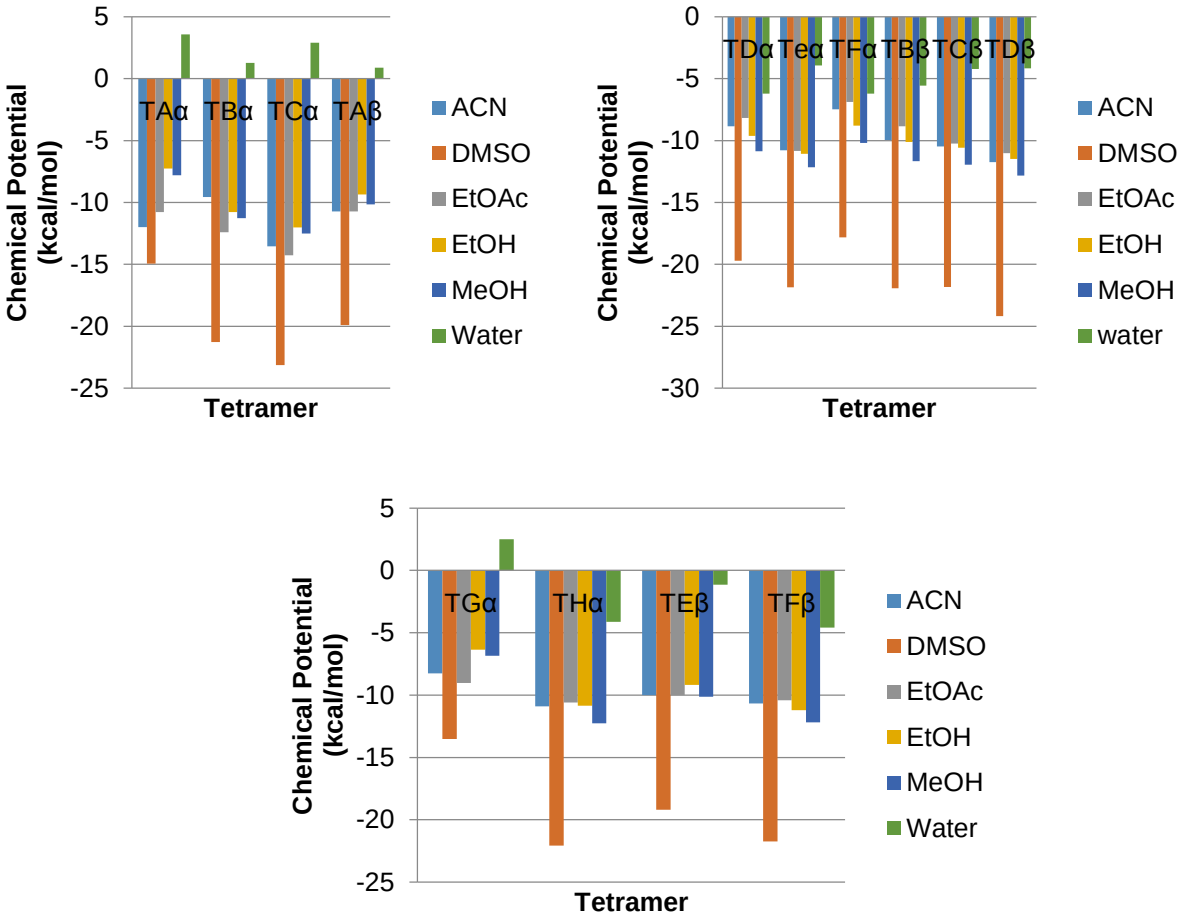


**Figure 6-14: Chemical potentials for the tetramers shown in Figure 6-6. (a) Tetramers dominated by H-bonds between them; (b) tetramers dominated by vdW interactions between them and (c) tetramers where there are important vdW and H-bonding interactions**

The relative chemical potentials of the tetramers in each solvent were found to be more similar to each other than for the dimers; this is especially the case for the H-bonding and vdW interacting tetramers. The TA7 cluster has a positive chemical potential in water, however this lack of affinity of the water to the TA7 tetramer does not overcome the strong internal energy from the combination of the H-bonding carboxylic acid dimers and the π-π stacking interactions. This suggests that the large difference in internal energy between TA1 and TA7 with the rest of the clusters resulted in these tetramers dominating the calculated fractional populations. This gives an indication that as the important synthons of α-*p*ABA self-assemble in solution they quickly gain favourable free energy.

Interestingly, it was observed that upon optimisation, the TA1 tetramer was found to re-orientate to form a stronger π-π stacking interaction (Figure 6-15).

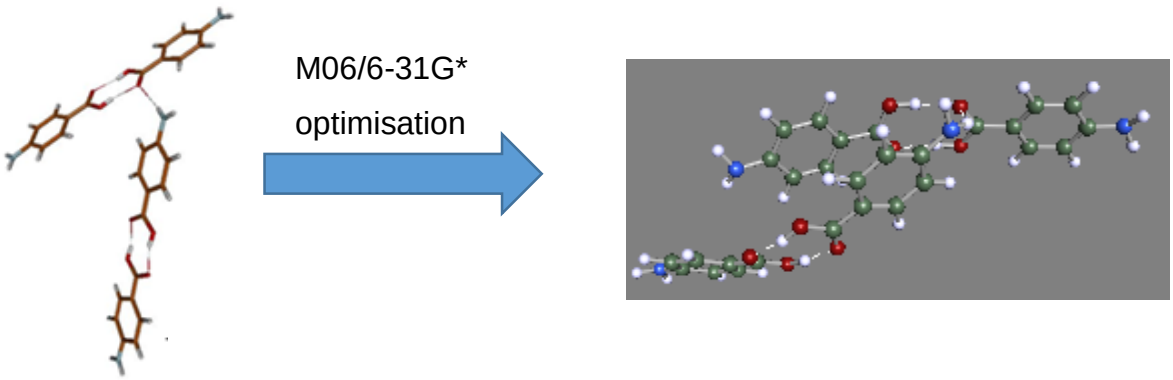


**Figure 6-15: Resulting change in orientation of the TA1 tetramer upon geometry optimisation**

The re-orientation shown in Figure 6-15 highlights that these type of clusters favour the formation of these π-π stacking interactions and that they are probably important in stabilising the α-like clusters. Considering that DA1 is now not solely a H-bonding tetramer, the three remaining H-bonding tetramers were compared in ethanol and water in Figure 6-16 shown below.

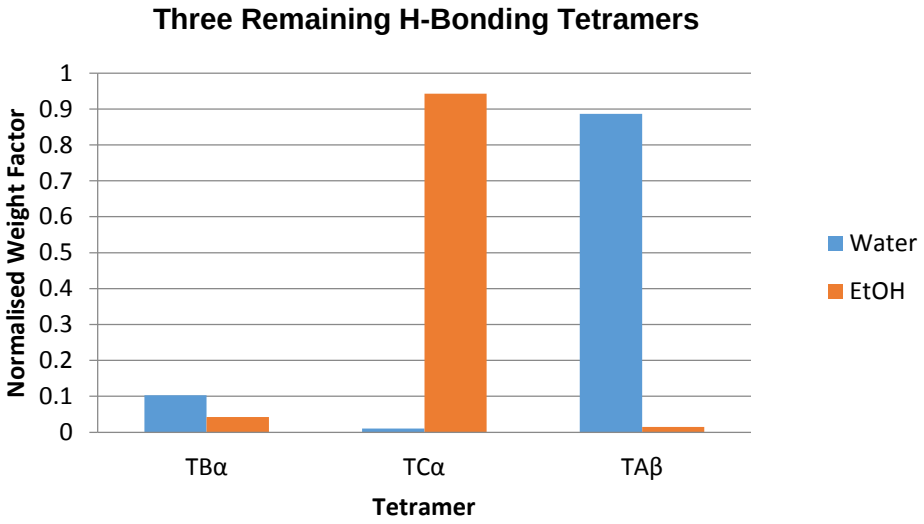


**Figure 6-16: Normalised weight factors of the H-bonding tetramers apart from DA1 in water and ethanol**

Figure 6-16 reveals that in water the TBα tetramer was now found to be the most stable compared to the other α-like H-bonding tetramers, whereas the TAβ tetramer is found to be most stable in ethanol. Considering α-like tetramers that were tested in water, only the clusters containing combined H-bonding dimers and the π-π stacking interactions were found to dominate the fractional populations, compared to the β-like tetramers. Tetramers containing only H-bonding dimers and NH...O H-bonds that would have been thought to be very stable, are in fact found to have a lower fractional population when compared to the β-like H-bonding ring structure (TAβ) (Figure 6-16).

### 6.3.5 Octamer Normalised Weight Factors

The COSMO internal energies of the octamers are shown in Figure 6-17.

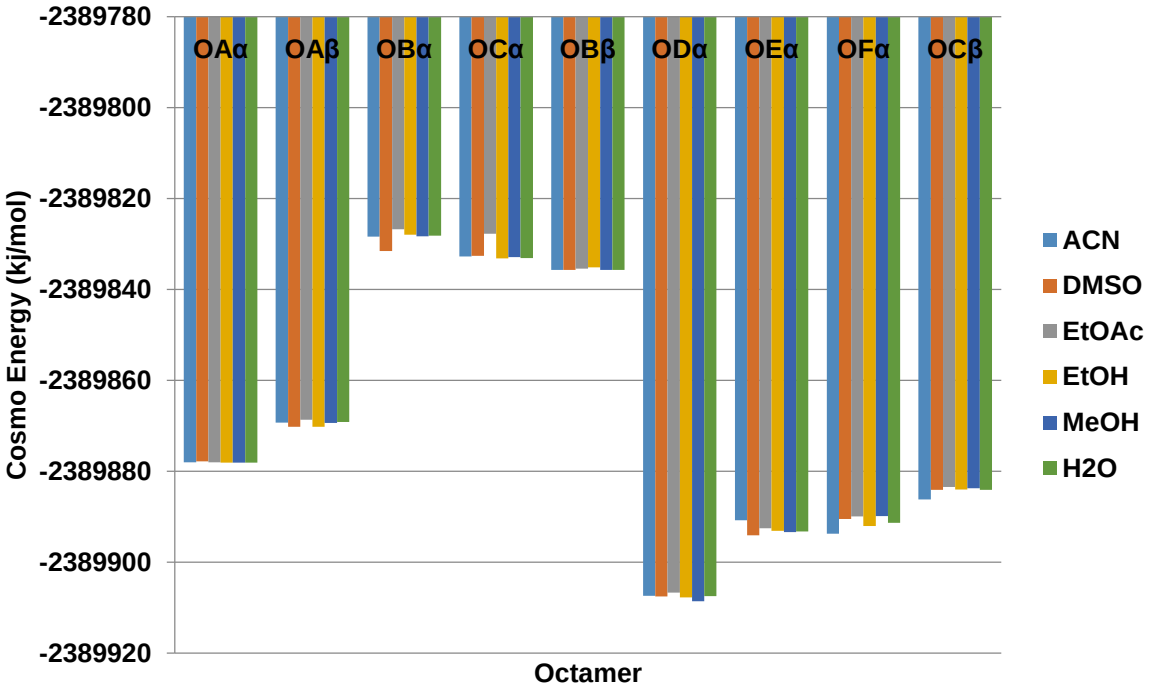


**Figure 6-17: COSMO energies calculated for the octamers at the 6-31G*/M06 level of theory**

The mixed H-bonding and vdW interacting octamers were found to be significantly more stable than the octamers dominated by only H-bonding or vdW interactions. The internal energy gained by having intermolecular interactions within the cluster that satisfy all the potential intermolecular interacting sites within the *p*ABA molecule resulted in a greater internal energy of the cluster. The most favoured tetramer was

found to be TA7, which contained two stacked dimers that are linked by an NH...O hydrogen bond. The calculated fractional populations for the octamers are shown if Figure 6-18.

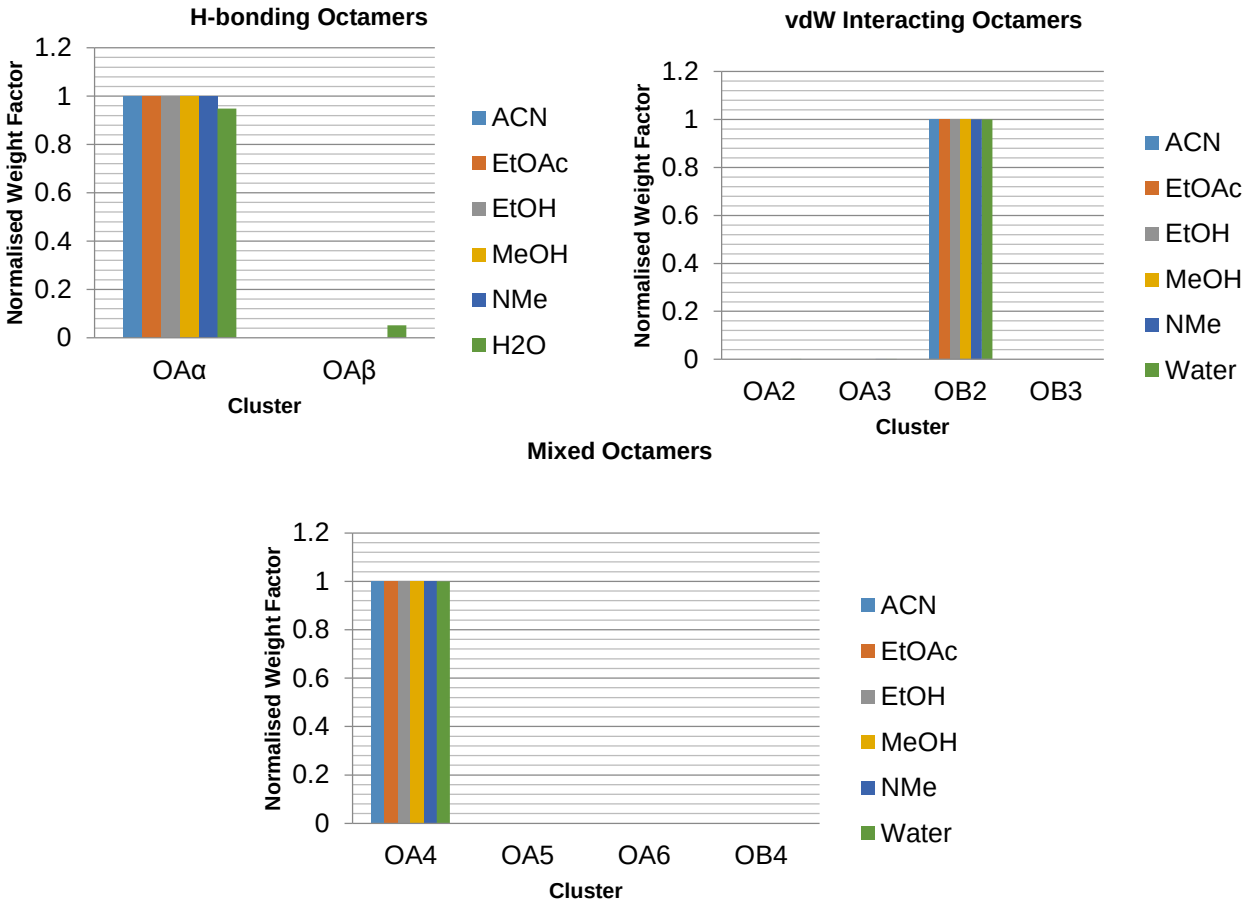


**Figure 6-18: Calculated fractional populations for the (a) H-bonded octamers; (b) vdW interacting octamers and (c) Mixed H-bonding and vdW interacting octamers**

Comparing the populations of the H-bonding, vdW and mixed octamers, for each type of cluster the one with the most stable internal energy was found to dominate the fractional populations. In much the same way as the tetramers, once the internal energy has increased past a certain point, the chemical potential has little effect on the calculated fractional population. Therefore it can be expected that a solvent favouring the formation of these small molecular building blocks can have a strong

influence on the self-assembly and polymorphic selection during the crystallisation of a molecular crystal.

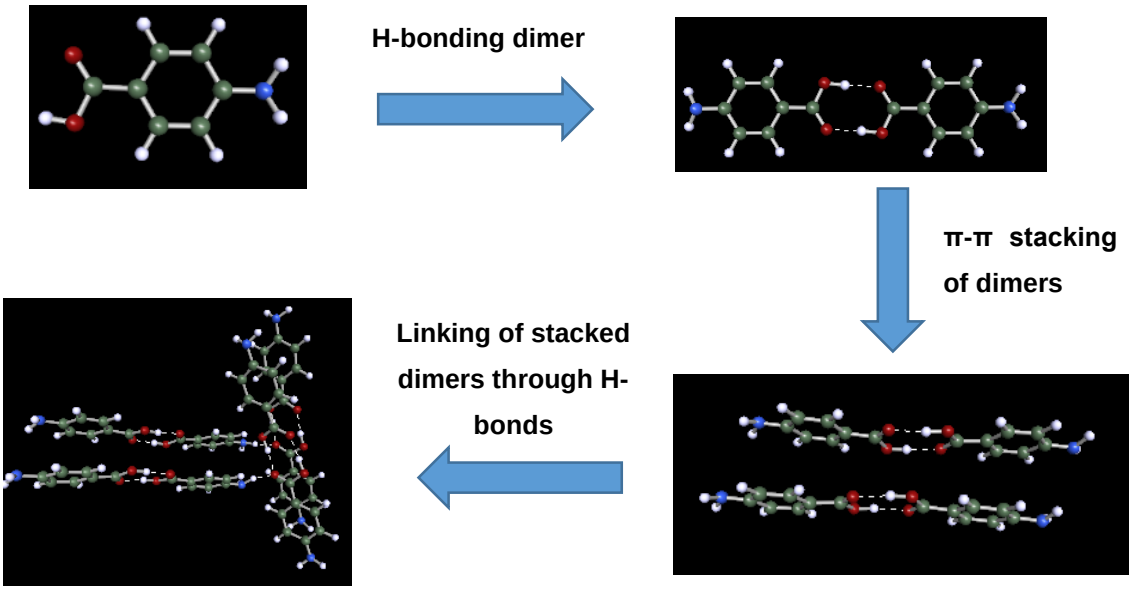


**Figure 6-19: Potential self-assembly pathway of the α-*p*ABA structure based on the dimers,**

Figure 6-19 suggests that, if the solution environment only has a choice to self-assemble towards molecular building blocks associated with the α and β crystal structure, the carboxylic acid dimers would initially form, followed by stacking of these dimers together and then linking of these stacked H-bond dimers by NH...O bonds. These calculations suggest that in all the solvents tested apart from water this pathway is very stable. However, the calculations suggest that within the water solutions the carboxylic dimer is less stable and that probably disturbing that motif in the early stages of self-assembly can lead to the formation of the β-*p*ABA structure in the mechanism shown in Figure 6-20.

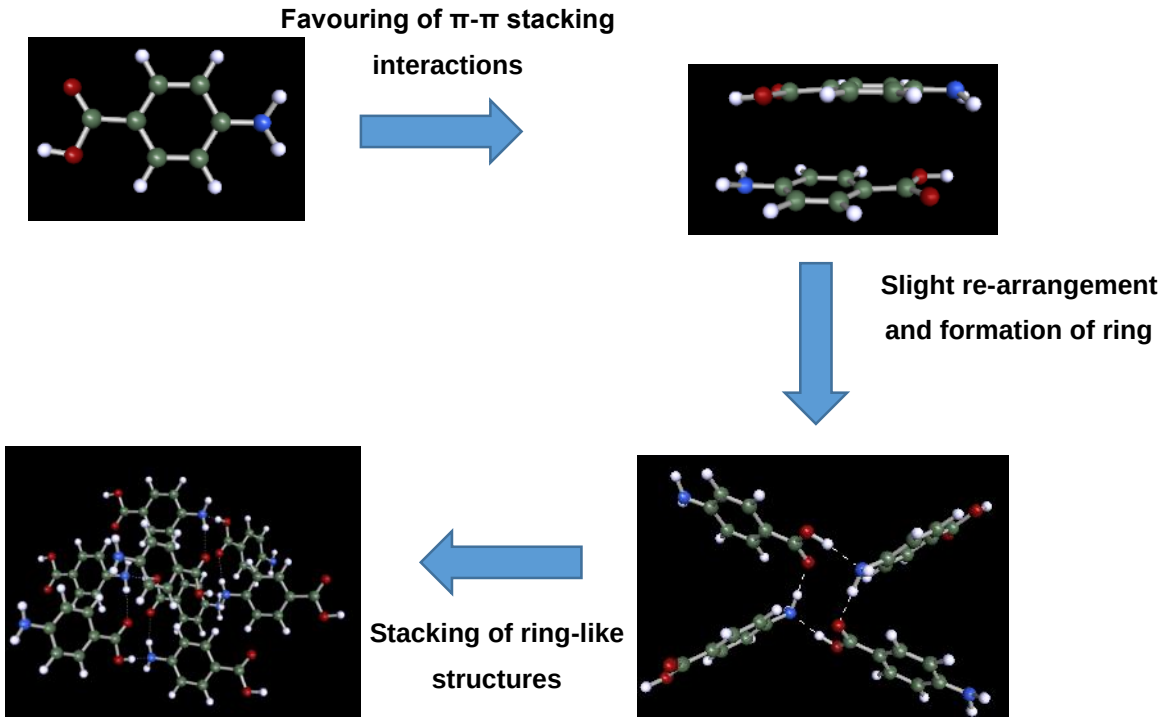


**Figure 6-20: Potential self-assembly pathway of β-*p*ABA in water based on the fractional populations of β like fragments**

Though these are the most stable β-like clusters found from the calculations, it is important to note that if the α carboxylic acid H-bonding dimers start to stack up and form the π-π stacking interactions (TA7 and OA4) then these clusters dominate the fractional population of the clusters, even in water. Therefore, it appears that preventing the initial carboxylic acid H-bonding dimer formation and the apparent stabilisation of the π-π stacking motifs in water could be the early stages that direct the observed nucleation of β-*p*ABA in water.

Since conformation was postulated to play a relatively small role in the polymorphic behaviour of *p*ABA in the previous chapter, the role of the pre-aggregation of molecules probably has a decisive role in the polymorphic direction of the system, since it is thought that pre-nucleation clusters influence the nucleation mechanism during solution crystallisation[65, 66, 228]. The correlation of H-bonding networks to polymorphism[25, 217] was the inspiration for looking at the pairwise interactions effects on polymorphism. However, this approach has showed the influence of the stability of

π-π stacking interactions on the polymorphism, as well as H-bonds, even on a small molecule.

## 6.4 Conclusions

Chapter 6 identified the most important molecular building blocks for the α and β crystal structures and how their stability and interactions with surrounding solvent can be used to predict the polymorphic form produced from solution. The major questions addressed by chapter 6 are summarised in Table 6-3.

**Table 6-3: Major questions or issues addressed by the work in chapter 6**

| Question/Problem | Information Provided from the Chapter | Relevance to the Study |
|---|---|---|
| Where do ethanol and water molecules preferentially bind to *p*ABA? | • Water strongly prefers to bind to the COOH group and itself<br>• Ethanol also prefers the COOH group but has more preference for the $NH_2$ than water | The COOH group is probably less available to form synthons in water than ethanol. The strong preference of water to bind to itself is probably the reason for the low solubility of *p*ABA in water |
| What are the major building blocks of the α and β structures? | • α structure probably proceeds via formation of OH...O H-bonds, that stack up to form π-π stacking interactions<br>• β structure probably proceeds via initial head to tail stacking and then formation of the 4-membered H-bonding ring | Controlling polymorphic form is often achieved by hindering/promoting the major molecular building blocks that facilitate the self-assembly of a particular structure |
| What is the comparable stability of the molecular building blocks of α- and β-*p*ABA in water and ethanol? | • OH...O H-bonding dimers less stable in water than ethanol<br>• Water has lack of affinity to the OH...O H-bonding dimer due to a large amount | Water probably hinders the formation of the OH...O H-bonding dimers and hence promoting the self-assembly of the β form. In contrast ethanol |

| | | |
|---|---|---|
| | of the dimer being hydrophobic | can stabilise the OH...O H-bonding dimers |

The calculations presented in this chapter have suggested that the OH...O H-bonding carboxylic acid dimer influences the often observed crystallisation of α-*p*ABA, even in conditions where the β form is thought to be thermodynamically stable. The stacking up of these dimerised motifs to form H-bonding interactions was also calculated to be very stable, hence the combination of strong H-bonds and satisfying the more hydrophobic ring area of the molecule with π-π interactions is probably the catalyst for the self-assembly of the α-structure. In contrast, the self-assembly of β form is probably initiated by the head-head π-π stcking interaction, whereby they can combine together to form the 4-membered H-bonding ring structure.

Since water has been reported to be the solvent that favours formation of β-*p*ABA the most, the stability of the building blocks in water and ethanol was compared. This revealed water preferred to solvate the COOH group of *p*ABA more so than any other part of the molecule, thus hindering the initial formation of the DAα dimer. In addition, water offers little vdW interaction with *p*ABA and therefore will offer little stabilisation of the ring area of the DAα cluster, suggesting that it may attack the OH...O H-bond so water can once again solvate the COOH group. This is reflected in the positive chemical potential calculated in water for the DAα.

The approaches in this chapter gave good qualitative data on the solvation and self-assembly. However, to achieve accurate qualitative data an extended molecular dynamics benchmarking calculations may be necessary. This is especially so with the systematic search solvation. The sequential addition of molecules neglects the fact that in reality all the solvent molecules would approach *p*ABA at roughly the same time. Therefore, the geometry of the solvation shell would be strongly influenced by how they adopt around each other and the single molecule of *p*ABA.

As previously discussed, the use of a solvent dielectric continuum to calculate the stability of small clusters (dimers) has previously been adopted by Di Tommaso and co-workers[26, 227], giving sensible results. Therefore, extending utilising a solvent

dielectric continuum with the extra statistical thermodynamics calculation that improves the prediction as to how the cluster would interact with the surrounding solution should be a sensible approach. In addition, the COSMO-RS approach has been used on small clusters of molecules whereby explicit water molecules were added to a single molecule and encased in a cavity. The calculations in this case showed good correlation with experimental data, suggesting that the COSMO-RS approach adequately handles small clusters of molecules despite being usually used on single molecules. It should be noted, however, that the H-bonding and vdW forces calculations within the chemical potential are derived from empirical parameters, similar to the forcefield used for the solvation binding in section 6.2. Therefore, the explicit numbers can only be counted as approximate, therefore it is more pertinent to examine the relative energies of the solvation sites and the clusters stabilities discussed in this chapter.

This chapter was the main body of work behind the completion of objective 2 and is foundation work for objective 3.

# Chapter 7 Molecular Modelling of Crystal Morphology

*Crystal morphology predictions are presented along with identification of the synthons that are important for the crystal growth of each surface. The solute/solvent binding to the morphologically important surfaces are also calculated.*

## 7.1 Introduction

The control of crystal morphology is vital with respect to filtering and processing within an industrial crystallisation process. The crystal growth and morphology of a molecular crystal can be highly dependent on the face specific surface chemistry due to the often anisotropic nature of the crystal structures. Hence, this chapter uses the knowledge of the synthon strength calculated in chapter 5 and the solvation behaviour calculated in Chapter 6 to determine the important synthons in the face specific growth, along with the solute-solvent and solute-solute interactions at the important surfaces of α- and β-*p*ABA.

The attachment energy morphology prediction is based on what synthons are predicted to be unsaturated at the morphologically important surfaces, where the more 'broken' strong synthons there are at a surface, the faster the growth. However, this does not take into account solvent environment or how easily a solute molecule may incorporate into a certain surface. Therefore, this chapter not only identifies the synthons which contribute to the crystal growth of a surface, but how the competition between solute and solvent molecular binding may impact how the solute molecules integrate at a surface and therefore how quickly a surface grows.

Determining the important synthons for the face specific growth and predicting how the solute and solvent molecules could bind to these surfaces can aid in the selection of growth conditions to obtain a desirable crystalline morphology. This work forms the basis of the completion of objective 3 and strongly relates to objective 4.

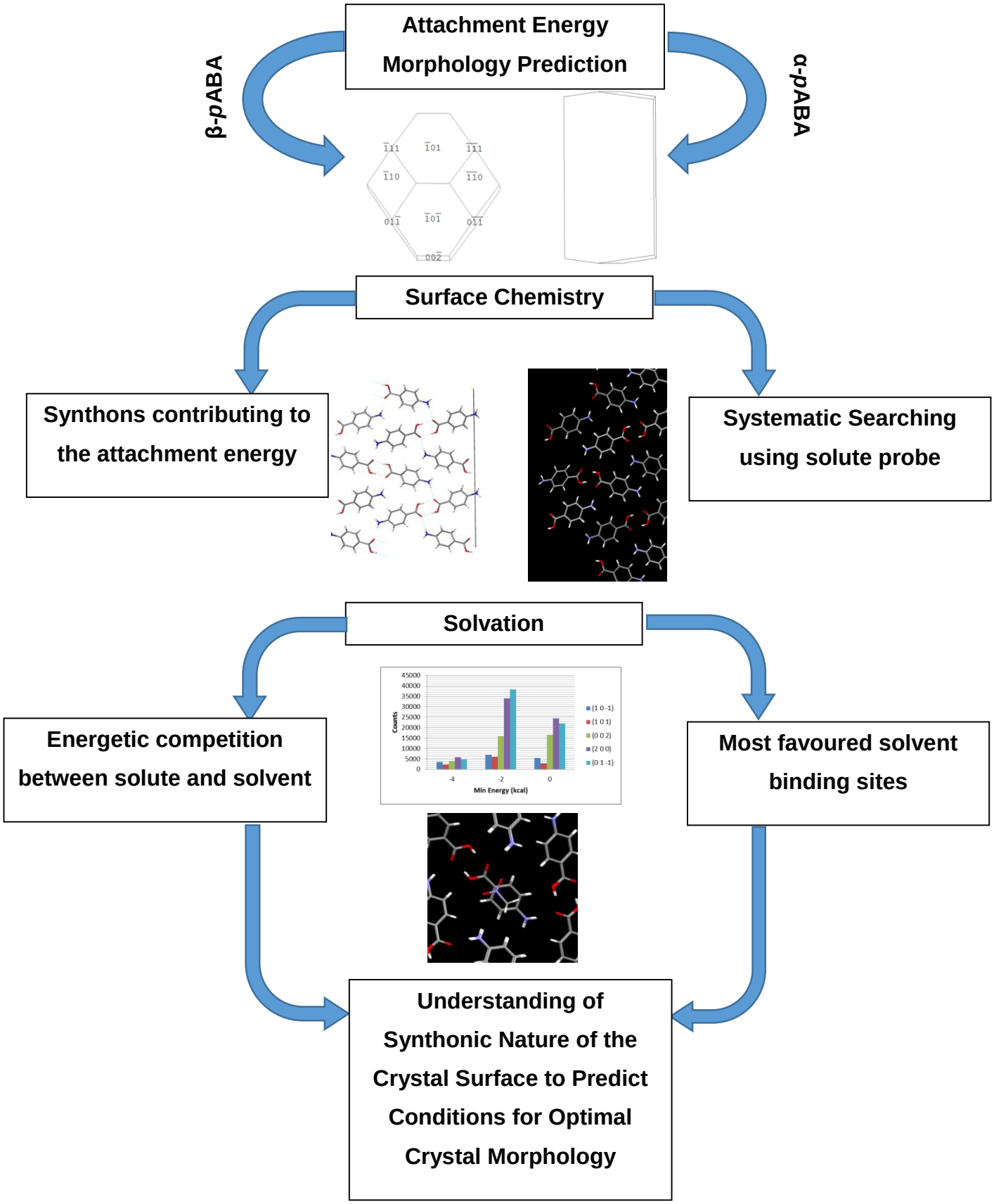


**Figure 7-1: Schematic of work flow of chapter 7**

## 7.2 Morphological Prediction

### 7.2.1 Attachment Energy Calculations

The calculated attachment energies (division of the lattice energy according to Equation 4-23) for the major faces identified from the BFDH model for α- and β-*p*ABA (section 3.4.3) for both forms are shown in Table 7-1. For α-*p*ABA, the calculation first assumed that the growth unit was a monomer and then it was performed assuming that the growth unit was an OH...O H-bonding dimer. This was done since a previous study suggested that in some solvents the OH...O H-bonding dimer synthon may pre-associate in solution prior to nucleation[51]

**Table 7-1: (a) Slice, attachment and anisotropy factor of the important faces predicted by the BFDH rule of α-*p*ABA in monomer mode; (b) Slice, attachment and anisotropy factor of the important faces predicted by the BFDH rule of α-*p*ABA in dimer mode; (c) Slice, attachment and anisotropy factor of the important faces predicted by the BFDH rule of β-*p*ABA.** (a)

| Face (hkl) | $d_{hkl}$ (Å) | Slice Energy (kcal/mol) | Attachment Energy (kcal/mol) | % Saturation of Surface Molecule (Anisotropy Factor) |
|---|---|---|---|---|
| 1 0 1 | 12.7 | -22.9 | -1.6 | 92.4 |
| 1 0 -1 | 13.6 | -14.1 | -10.4 | 67.5 |
| 0 1 -1 | 3.8 | -9.2 | -15.4 | 36.1 |
| 1 1 -1 | 3.7 | -8.2 | -16.3 | 34.3 |
| 1 -1 0 | 3.8 | -9.1 | -15.5 | 39.1 |
| 0 0 2 | 9.3 | -14.7 | -9.8 | 59.7 |
| 2 0 0 | 9.3 | -15.0 | -9.6 | 60.8 |

(b)

| Face (hkl) | $d_{hkl}$ (Å) | Slice Energy (kcal/mol) | Attachment Energy (kcal/mol) | % Saturation of Surface Molecule (Anisotropy Factor) |
|---|---|---|---|---|
| 1 0 1 | 12.7 | -26.6 | -8.3 | 76.1 |
| 1 0 -1 | 13.6 | -20.7 | -14.3 | 59.2 |
| 0 1 -1 | 3.8 | -9.4 | -25.4 | 27.0 |
| 1 1 -1 | 3.7 | -7.6 | -27.3 | 21.8 |
| 1 -1 0 | 3.8 | -8.5 | -26.4 | 24.4 |
| 0 0 2 | 9.3 | -20.7 | -14.2 | 59.3 |
| 2 0 0 | 9.3 | -21.5 | -13.4 | 61.6 |

(c)

| Face (hkl) | $d_{hkl}$ (Å) | Slice Energy (kcal/mol) | Attachment Energy (kcal/mol) | % Saturation of Surface Molecule (Anisotropy Factor) |
|---|---|---|---|---|
| 0 1 1 | 5.2 | -12.2 | -10.5 | 53.8 |
| 0 0 2 | 6.0 | -8.9 | -13.8 | 39.2 |
| 1 0 -1 | 7.0 | -10.6 | -12.2 | 46.5 |
| 1 0 1 | 4.9 | -12.0 | -10.7 | 53.0 |
| 1 1 1 | 5.0 | -10.5 | -12.2 | 46.2 |
| 1 1 0 | 6.1 | -11.5 | -11.2 | 50.8 |
| 1 1 -1 | 3.09 | -8.34 | -14.39 | 36.7 |

Table 7-1(b) shows that the lattice energy is different for the monomer and dimer growth unit. This is because the calculation was constructed so that the interactions between the molecules that form OH...O H-bonds are ignored. Therefore, the interactions are now between two sets of two molecules, rather than between two monomers. Hence, these stronger interactions result in an increased lattice energy that cannot be thought of as a true lattice energy, since a true lattice energy is with respect to free molecules in the gas phase and they would be monomers.

The degree of satisfaction of the synthons associated with a molecule exposed at a surface, compared to a saturated molecule in the bulk of the crystal, can be related to how labile a surface is to accepting solute molecules from solution and therefore how fast a given surface will grow (anisotropy factor Equation 4-25). Table 7-1(a) shows that the anisotropy factor, assuming a monomer growth unit, for the different surfaces of α-*p*ABA is distinctly different. The slow growing (1 0 1) surface was found to have approximately 93% of possible interactions satisfied, whereas the capping (0 1 -1), (1 -1 0) and (1 1 -1) surfaces were found to have approximately 35-39% of interactions satisfied. Hence, it is expected that the capping faces would grow significantly faster than the (1 0 1) surface. This reflects the experimental observation that the morphology of α-*p*ABA often appears as an anisotropic needle-like shape[3, 188, 191, 192], probably due to the anisotropic saturation of molecules at the crystal surfaces. Considering a dimeric growth unit, the anisotropy factor of the (1 0 1) surface drops, suggesting that this surface would grow faster compared to a monomeric growth unit. The calculation with a dimeric growth unit also predicted that the molecules at the (1 0 -1) surface would be more satisfied if the growth unit was a carboxylic acid dimer, reflecting that the growth of this surface is dominated by H-bonding interactions.

The anisotropy factors of the morphologically important surfaces of β-*p*ABA were found to be much more similar than α-*p*ABA. The least satisfied face was found to be only 17% less satisfied than the most satisfied face. This reflects that the synthonic nature of the crystal surfaces is quite similar and hence the more isotropic morphology experimentally observed for β-*p*ABA than α-*p*ABA.

## 7.2.2 Confrontation of Morphology Simulations with Experimental Crystal Morphologies

### 7.2.2.1 α-*p*ABA

The attachment energies calculated assuming a monomeric growth unit in Table 7-1(a) resulted in the flat lathe-like morphological prediction shown in Figure 7-2(a) and Figure 7-2(c). A comparison of the attachment energies calculated for α-*p*ABA using the dimer growth unit revealed that the attachment energy of the (1 0 1) surface was increased when compared to that calculated for the monomer form, with the attachment energies of the (1 0 -1) and the capping surfaces being relatively reduced. This reduction of the attachment energy of the capping surfaces resulted in the prediction of a less plate like morphology shown Figure 7-2(b) and d, with the predicted inclusion of the (0 0 2) and (2 0 0) surfaces. These predictions were compared to the experimentally grown crystals from ethanolic solutions shown in Figure 7-3.

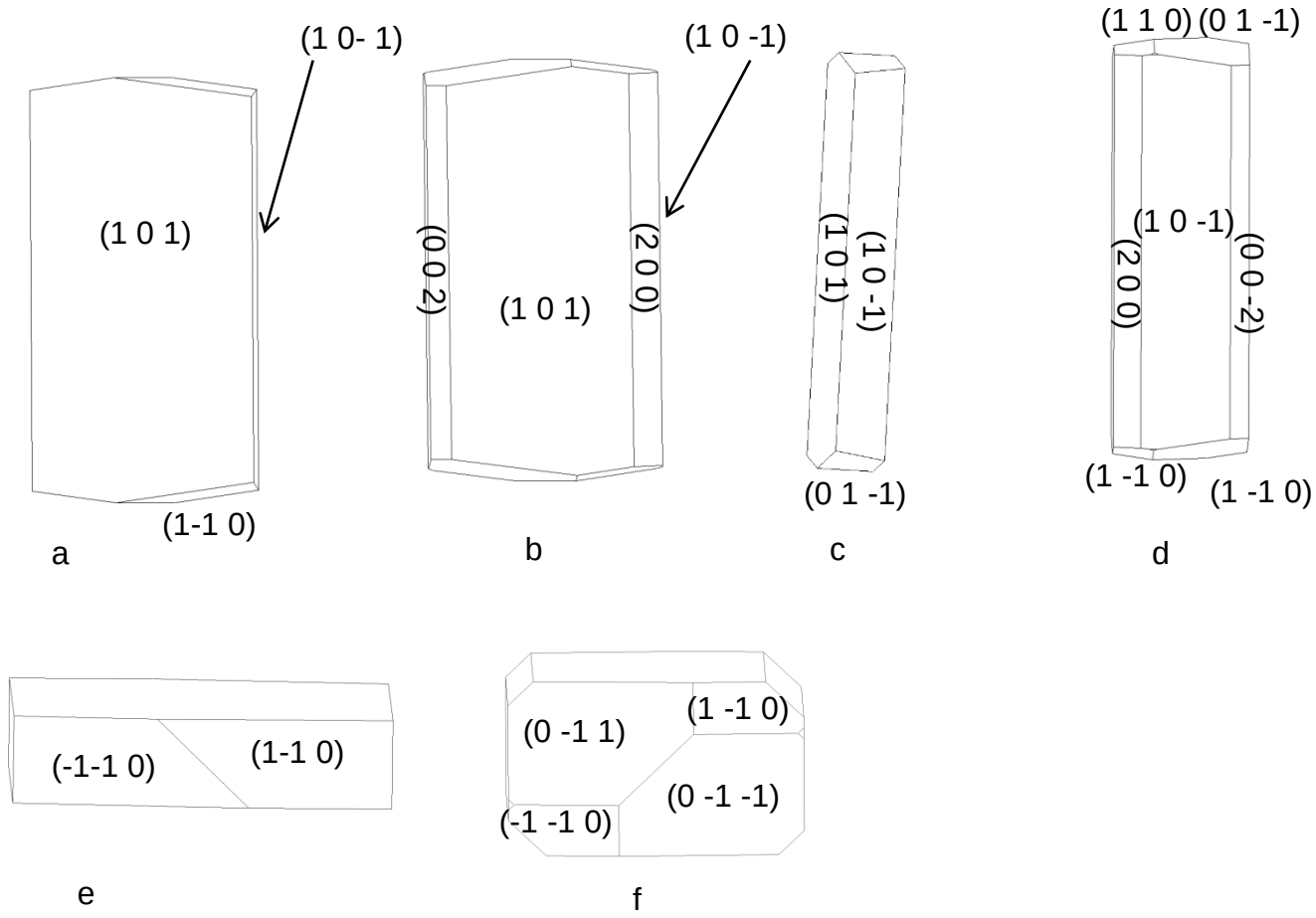


**Figure 7-2: (a, c and e) Attachment energy morphological prediction of α-*p*ABA, assuming the attaching growth units are monomers, showing the major faces that are predicted in the final morphology. (b, d and f) Attachment energy morphological prediction of α-*p*ABA, assuming the attaching growth units are carboxylic acid H-bonding dimers, showing the major faces that are predicted in the final morphology.**

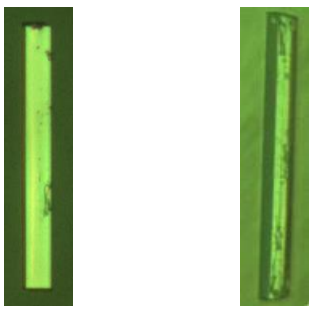


**Figure 7-3: (a) α-*p*ABA grown in EtOH at σ = 0.23 for ten mins; (b) α-*p*ABA grown in EtOH at σ = 0.27 for ten mins. Crystals grown in growth cell utilising the methods described in Section 4.3.3.2**

Both monomer and dimer based morphological simulations were found to have lower aspect ratios with respect to those observed from the experimentally grown seed

crystals from supersaturated ethanol solutions (methodology described in Section 4.3.3.2) shown in Figure 7-3. Figure 7-3(a) showed that at lower supersaturations α-*p*ABA appears to present a more flat and lathe-like morphology. Though still longer than the monomer morphology prediction, the general flat shape appears to correlate to the low supersaturation crystal featuring a dominant flat face being the (1 0 1) surface. Figure 7-3(b) shows at σ = 0.27, the shape of the crystal appeared thicker and seemed to include more faces in the b-axis zone of the crystal, which were probably the (0 0 2) and (2 0 0) surfaces that appear in the dimer morphological prediction. Recent work by Sullivan and Davey suggests that the (1 0 1) and (1 0 -1) surfaces do not completely dominate the b-axis zone of facets Figure 7-4(b) and (d)), and that the morphology is 6 or even 8 sided, with increased importance of the (0 0 2) face[3].

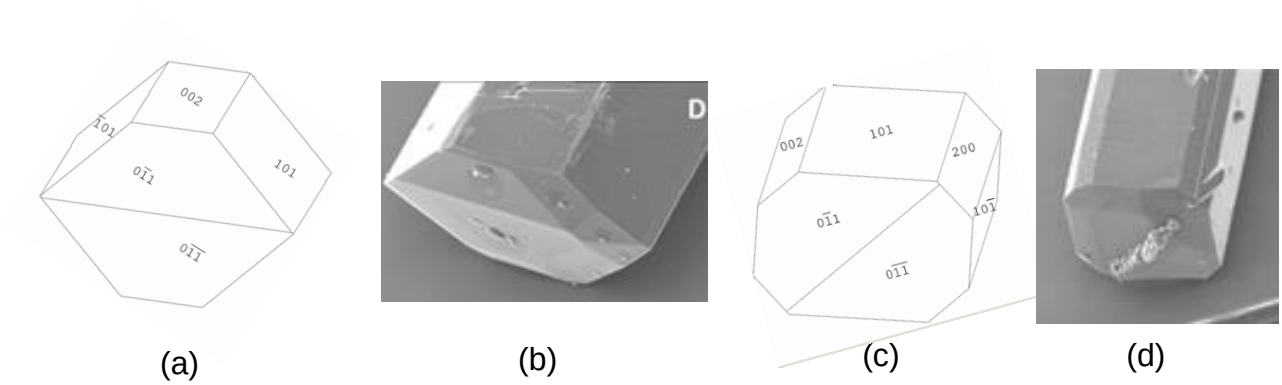


**Figure 7-4: (a) 6-sided morphological sketch of α-*p*ABA adapted to match Figure 7-4(b); Figure (b) α-*p*ABA crystal grown from slow solvent evaporation of EtOH; (c) 8-sided morphological sketch adapted to match Figure 7-4(d). (d) α-*p*ABA crystal grown from slow solvent evaporation of EtOAc. Figure 1-3b and d reproduced with permission from Sullivan and Davey CrystEngComm, 2014[3]**

The morphological sketch in Figure 7-4(a) suggests that in the 6 sided shape in Figure 7-4(b), the extra face is indeed the (0 0 2) surface. However, the morphological sketch in Figure 7-4(c) suggests that the (0 0 2) and (2 0 0) surfaces are consistent with the faces that are present in Figure 7-4(d). Table 7-1(a) and (b) showed that the predicted attachment energy for these minor habit surfaces were found to be very similar to each other for both the monomer- and dimer-based calculation. The latter would suggest that the growth rates for these faces would be very similar, hence there would be a competition between these two faces in terms of them appearing in the final growth morphology. Table 7-2 shows experimental interplanar angles in the (0 1 0) zone for

an α-*p*ABA crystal with respect to those calculated based on the unit cell parameters utilising the methods described in section .

**Table 7-2: Consecutive measurement of interplanar angles of an α-*p*ABA crystal grown from slow solvent evaporation of ethanol matched with the faces via calculated angles**

| Plane angle measured | Calculated angle (°) | Measured Angle (°) |
|---|---|---|
| (0 0 2) → (1 0 1) | 43.3 | 43 |
| (1 0 1) → (2 0 0) | 43.13 | 45 |
| (2 0 0) → (1 0 -1) | 46.69 | 46 |

The interplanar angles were found to match well to the calculated interplanar angles, suggesting a match to the (0 0 2) and (2 0 0) faces that are predicted in Figure 7-4(c).

As with the b-axis zone of the crystal facets, the end capping faces were also found to show variations in the final experimental growth morphology, with respect to predictions. The monomer attachment energy prediction Figure 7-2(e)) showed the (1 -1 0) and (-1 -1 0) faces at the end of the crystal. However, the attachment energies of the (0 1 -1) and (1 -1 0) faces were seen to be very similar (Table 7-1(a)), suggesting that the appearance of these faces at the capping end of the crystal is very competitive.

#### 7.2.2.2 β-*p*ABA

Figure 7-5(a) and (b) show the attachment energy morphological prediction of β-*p*ABA was found to be a diamond-shaped morphology, with more equal growth in the different crystallographic directions. This is consistent with the attachment energies calculations given in Table 7-1(c).

The attachment energy prediction for the β polymorph compared to experimentally grown crystals is shown in Figure 7-5(a) and (b) and revealed that the morphological prediction gave a good match to the shape of the experimentally grown β-*p*ABA crystal shown in Figure 7-5(c).

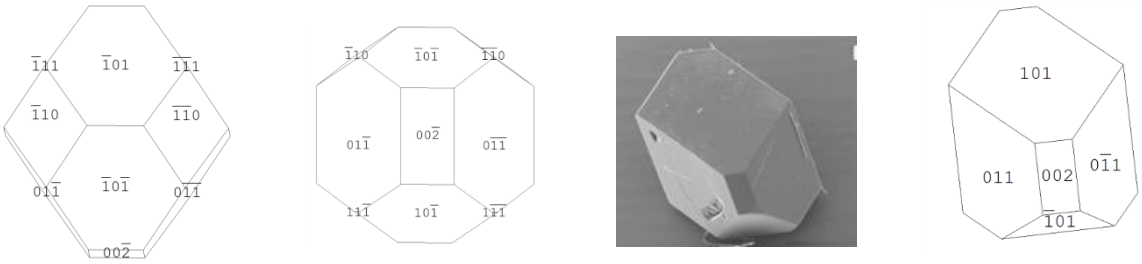


**Figure 7-5: (a and b) Attachment energy morphological predictions of the crystal structure of β-*p*ABA. (c) SEM of β-*p*ABA grown from water showing flat top face, no evidence of multi faceting; (d) Morphological sketch of β-*p*ABA made to resemble the experimental crystal in Figure 7-5c; Figure 7-5c reproduced with permission of Sullivan and Davey, CrystEngComm, 2015[3]**

However, the simulation shown in Figure 7-5(a) shows a multifaceted top surface, whereas Figure 7-5(c) shows a flat top surface. From the morphological sketch in Figure 7-5(d), it would appear likely that the dominating top face is the (1 0 1) surface. The similar calculated attachment energies for β-*p*ABA suggested that the crystal growth mechanisms are probably quite similar. This is in contrast to α-*p*ABA and is probably a factor as to why the attachment energy morphological prediction of β-*p*ABA gave a greater resemblance to experimental crystals when compared to α-*p*ABA.

## 7.3 Molecular Modelling of Surface Chemistry

### 7.3.1 α-*p*ABA

The synthons that were found to contribute to the attachment energies of the morphologically important surfaces of α-*p*ABA were determined and related to the growth rates of the crystal surfaces. The surface chemistry and strongest synthons contributing to the attachment energy for the (1 0 -1) surface is shown in Figure 7-6.

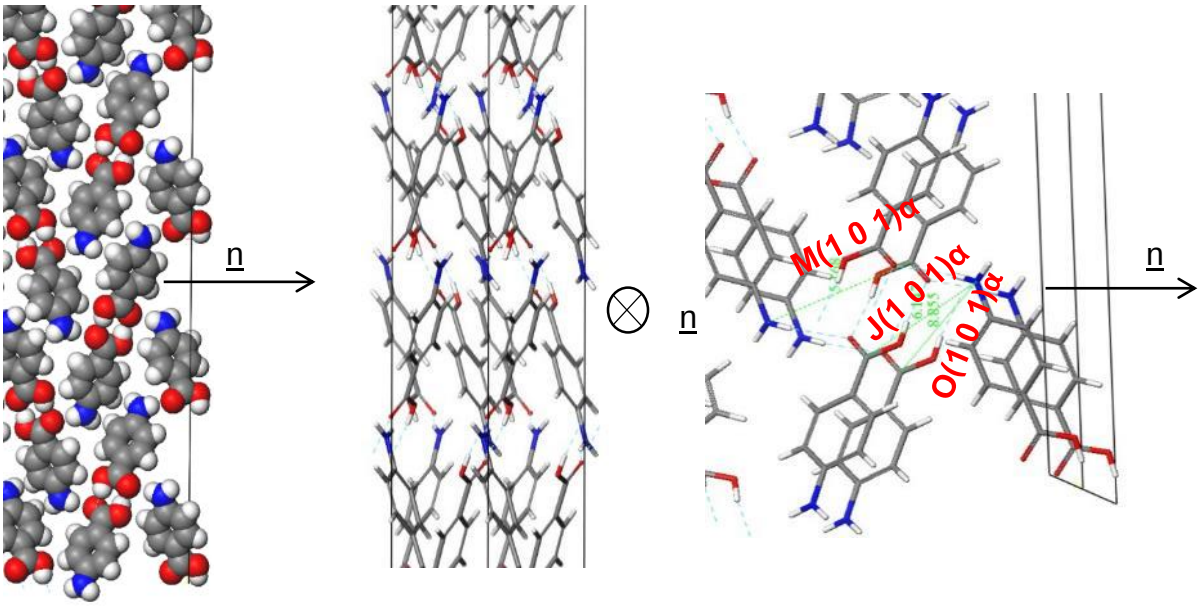


**Figure 7-6: Crystal chemistry of the (1 0 1) surface of α-*p*ABA: (a) space fill model of side view; (b) stick model of plan view; (c) stick model of side view.**

**Table 7-3: Extrinsic synthons contributing to the attachment energy of the α-*p*ABA (1 0 1) surface. Strongest interaction contributing to (1 0 1) growth is the Jth strongest in the bulk interactions, hence slow growth.**

| Bond | Multiplicity | Distance (Å) | Intermolecular Energy (kcal/mol) |
|---|---|---|---|
| J(1 0 1)α | 2 | 6.9 | -0.7 |
| M(1 0 1)α | 2 | 6.7 | -0.4 |
| O(1 0 1)α | 2 | 8.9 | -0.2 |

Figure 7-6(a) shows that the carboxylic acid H-bonding dimers were found to run in-plane at the (1 0 1) surface and Figure 7-6(b) shows the π-π stacking in the b direction were found to be perpendicular to the growth direction of the (1 0 1) surface, and therefore not contributing to the attachment energy. Table 7-3 shows the extrinsic synthons were found to be made up of vdW interactions between the polar atoms of the COOH and $NH_2$ functional groups. These interactions were found to be relatively weak with all of them being less than 1kcal/mol, hence the very low attachment energy predicted at this surface. Compared to the strongest bulk interactions, e.g A, B and C

representing the H-bonding carboxylic acid dimers and π-π stacking interactions, the strongest interaction for this face was found to be comparatively weak and is 10th ($J^{th}$) in terms of morphological importance. Such a low attachment energy and concomitantly weak interactions at this surface would be consistent with a slow growth rate for this surface.

The surface chemistry and strongest synthons contributing to the attachment energy for the (1 0 -1) surface is shown in Figure 7-7.

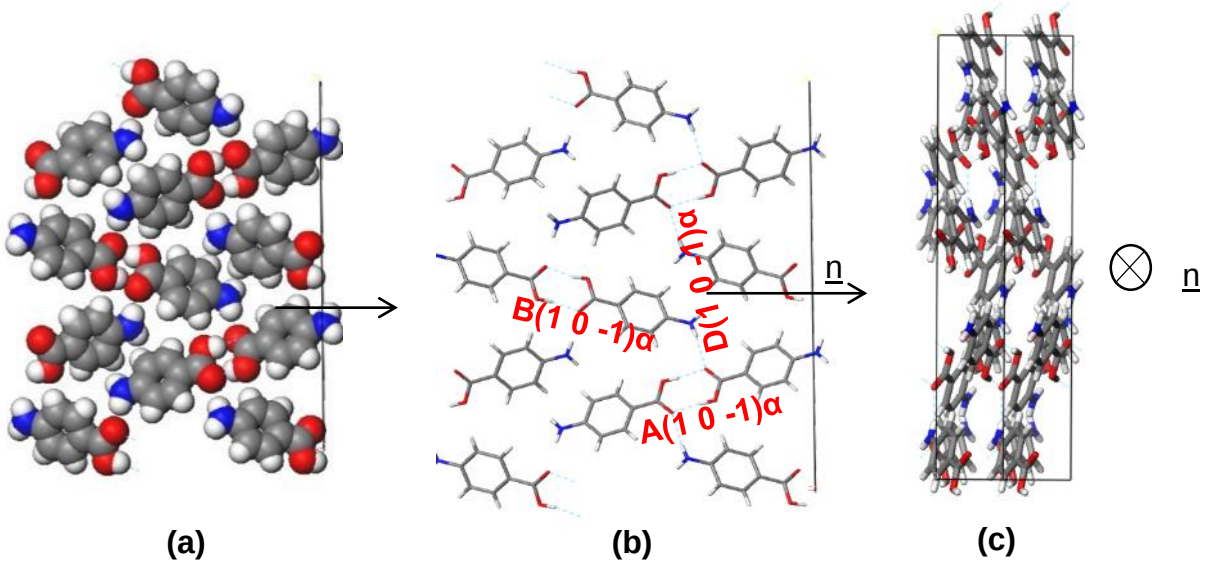


**Figure 7-7: Crystal chemistry (1 0 -1) surface of α-*p*ABA: (a) space fill model of side view; (b) stick model of side view; (c) stick model of plan view**

**Table 7-4: Extrinsic synthons contributing to the attachment energy of the α-*p*ABA (1 0 -1). Strongest interactions contributing to the attachment energy are the 1st, 2nd and 4th strongest from the bulk interactions.**

| Bond | Multiplicity | Distance (Å) | Intermolecular Energy (kcal/mol) |
|---|---|---|---|
| A(10-1)α | 1 | 8.2 | -5.7 |
| B(10-1)α | 1 | 8.3 | -5.6 |
| D(10-1)α | 2 | 7.9 | -2.3 |

Figure 7-7(a) and (b) showed that the H-bonds between the COOH groups were found to form almost parallel to the growth direction of this surface, hence promoting much faster growth in this direction when compared to that of the (1 0 1) surface. In contrast, the π-π stacking interactions were found to form almost perpendicular to the growth direction of this surface and are therefore would not be expected to strongly influence the growth of the (1 0 -1) surface.

Table 7-4 shows that the interactions contributing to the attachment energy for this surface were found to be some of the strongest bulk interactions, resulting in the attachment energy being predicted to be more than five times higher than that for the (1 0 1) surface.

The capping (0 1 -1) face was predicted to be the fastest growing of the morphologically important crystal surfaces. The surface chemistry and strongest synthons contributing to the attachment energy for the (0 1 -1) surface is shown in Figure 7-8.

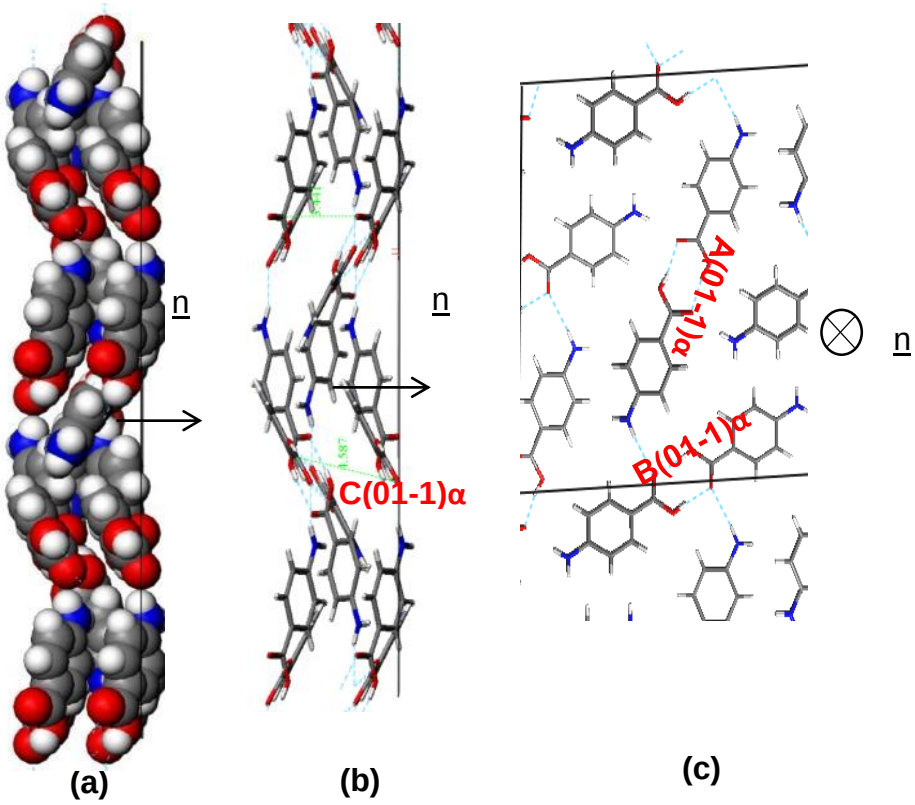


**Figure 7-8: Crystal chemistry of (0 1 -1) surface of α-*p*ABA: (a) space fill model of side view; (b) stick model of side view; (c) stick model of plan view**

**Table 7-5: Extrinsic synthons contributing to the attachment energy of the (0 1 -1) surface. Strongest interactions at (0 1 -1) are the 3 strongest from the bulk interactions**

| Bond | Multiplicity | Distance (Å) | Intermolecular Energy (kcal/mol) |
|---|---|---|---|
| A(01-1)α | 1 | 8.2 | -5.7 |
| B(01-1)α | 1 | 8.3 | -5.67 |
| C(01-1)α | 2 | 3.9 | -2.7 |

Figure 7-8(a) of the space fill model shows how the molecules were found to close pack in zig-zag chains stacking along the b direction of the structure. The molecules were found to pack more closely along this growth direction than the (1 0 1) or (1 0 -1) directions, and hence it is no coincidence that the (0 1 -1) surface was found to grow faster than the (1 0 1) or (1 0 -1) habit surfaces. Figure 7-8(b) shows the C intermolecular interaction that is dominated by π-π stacking interactions was found to be close to parallel to the direction of growth.

Table 7-5 shows that the three strongest interactions contributing to the attachment energy at this surface were found to be the same as the three strongest interactions as calculated from the bulk interactions.

The attachment energy model also predicted contribution from the OH…O intermolecular interactions between the H-bonding dimers to the growth of this surface. However, examination of the in-plane molecular packing of the (0 1 -1) surface revealed that these interactions were found not to be orientated significantly along the growth direction of this surface, which would be consistent with these interactions having a reduced role in the growth of the (0 1 -1) surface.

This molecular orientation suggests that the major interactions promoting the fast growth of the (0 1 -1) surface are the π-π stacking interactions. The close packing is favourable and coupled with the fact that the solvents used for crystallisation have strongly contrasting molecular structures, i.e. without any aromatics, would suggest that the surface/solvent interaction would be unlikely to disrupt this interaction and hence the growth process of the (0 1 -1) surface.

### 7.3.2 β-form

Figure 7-9 shows the (0 1 -1) face is the largest predicted face visible at the surface of β-*p*ABA, but it does not dominate to the same extent as the (1 0 1) face in the α form. The (1 1 0), (1 0 1) and (1 0 -1) faces also contribute significantly to the surface area of the crystal morphology. The analysis of the unsaturated synthons at the β faces present at the crystal surface was performed with the approach used for the α form.

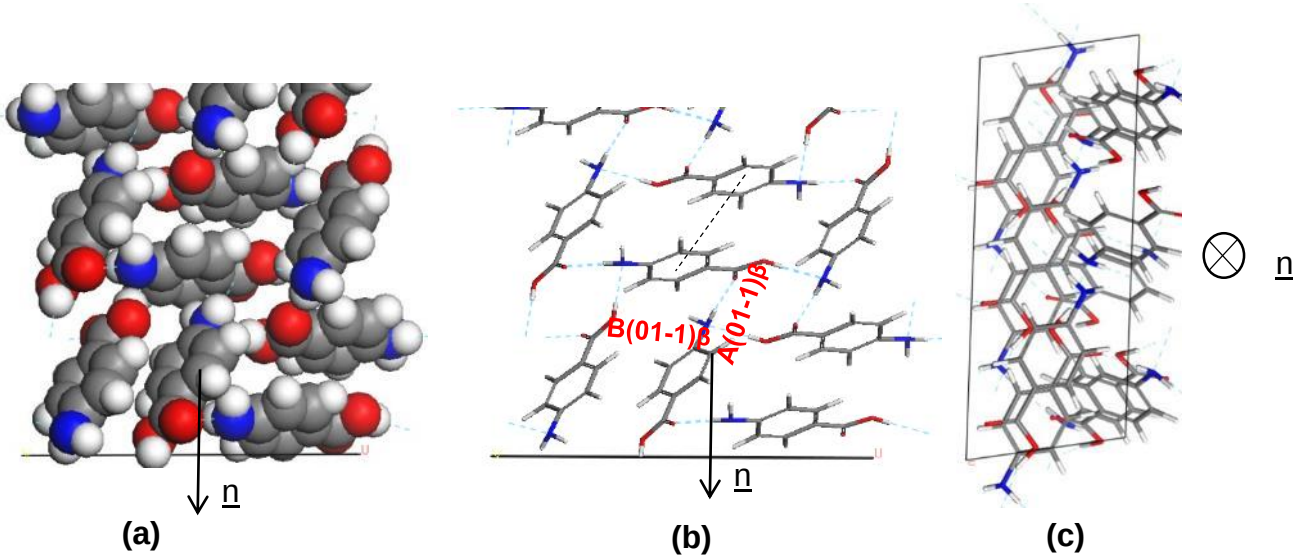


**Figure 7-9: Crystal chemistry of (0 1 -1) surface of β-*p*ABA: (a) space fill model of side view; (b) stick model of side view; (c) stick model of plan view**

**Table 7-6: Extrinsic synthons contributing to the attachment energy of the β-*p*ABA (0 1 -1) surface. Top 3 interactions contributing to the attachment energy same as the 3 strongest interactions from the bulk interactions.**

| Bond | Multiplicity | Distance (Å) | Intermolecular Energy (kcal/mol) |
|---|---|---|---|
| A(0 1 -1)β | 1 | 4.2 | -2.6 |
| B(0 1 -1)β | 2 | 8.1 | -2.5 |
| C(0 1 -1)β | 1 | 5.7 | -2.4 |

Analysis of the (0 1 -1) surface revealed that it has exposed $NH_2$ and COOH groups that form the 4-membered H-bonding ring. The molecules were also found to stack out of the plane of this face to form the head to tail π-π stacking, hence Table 7-6 shows

that the strongest interactions contributing to the attachment energy of this face were found to be the same as the strongest bulk interactions.

Figure 7-9(a) shows how the molecules actually stack in different directions. This suggests that the stacking interactions are contributing to growth in more than one direction, again highlighting the isotropic nature of the growth of this crystal. Figure 7-9(b) highlights that it is similar for the H-bonding interactions.

The surface chemistry and strongest synthons contributing to the attachment energy for the (1 0 -1) surface is shown in Figure 7-10.

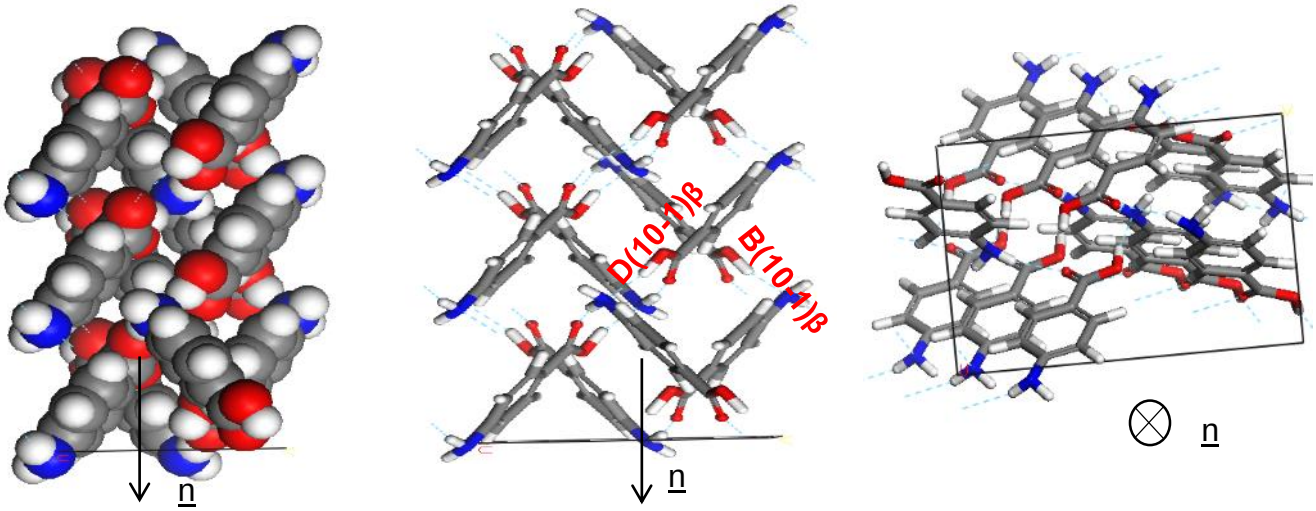


**Figure 7-10: Crystal chemistry of (1 0 -1) surface of β-*p*ABA: (a) space fill model of side view; (b) stick model of side view; (c) stick model of plan view**

**Table 7-7: Extrinsic synthons contributing to the attachment energy of the *p*ABA β (1 0 -1) surface. B and D H-bonding interactions contributing as stacking interactions are orientated away from the direction of growth.**

| Bond | Multiplicity | Distance (Å) | Intermolecular Energy (kcal/mol) |
|---|---|---|---|
| B(1 0 -1)β | 2 | 8.1 | -2.5 |
| D(1 0 -1)β | 2 | 6.7 | -1.5 |

The *p*ABA molecules were found to stack close to perpendicular to the β-(1 0 -1) surface growth direction and hence the stacking interactions were found not to

contribute to the attachment energy of this surface. The OH group and the nitrogen were found to be orientated almost parallel to the growth direction of the (1 0 -1) surface, and hence these interactions were found to dominate the growth of this surface. The surface chemistry and strongest synthons contributing to the attachment energy for the (0 0 2) surface is shown in Figure 7-11.

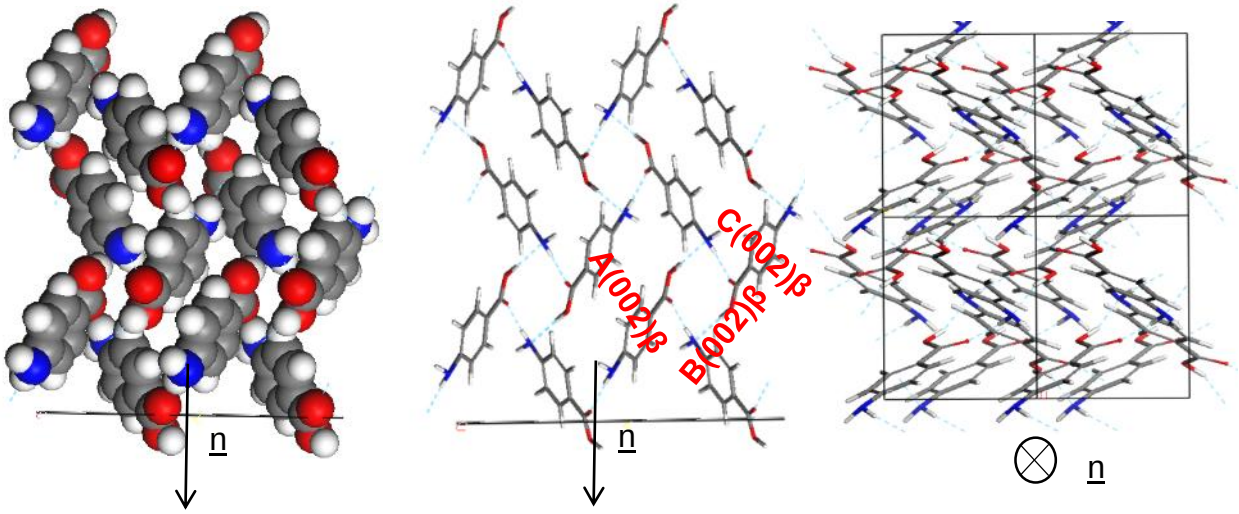


**Figure 7-11: Crystal chemistry of (0 0 2) surface of β-*p*ABA: (a) space fill model of side view; (b) stick model of side view; (c) stick model of plan view**

**Table 7-8: Extrinsic synthons contributing to the attachment energy of the β-*p*ABA (0 0 2) surface. 3 strongest interactions contributing to attachment energy are same as 3 strongest interactions from bulk structure, reflecting faster growth of this surface**

| Bond | Multiplicity | Distance (Å) | Intermolecular Energy (kcal/mol) |
|---|---|---|---|
| A(002)β | 1 | 4.2 | -2.6 |
| B(002)β | 2 | 8.1 | -2.5 |
| C(002)β | 1 | 5.7 | -2.4 |

The smaller, faster growing (0 0 2) surface was found to have contributions from the H-bonding and π-π stacking interactions to the growth of this face. The zig-zag chains of OH...N and NH...O hydrogen bonds making up the 4-membered ring structure were

observed to run closer to the growth direction of the (0 0 2) surface compared to the other important surfaces present in the β morphology.

Figure 7-11(c) reveals that the phenyl rings are found to be at about a 45° tilt away from parallel to the growth direction showing that there is some contribution to growth from the π-π stacking interactions as well as the H-bonds formed to the exposed $NH_2$ group. Table 7-8 shows that all three of the strongest bulk interactions were found to contribute to the attachment energy of this surface.

The strength and character of the extrinsic synthons associated with the major faces of the β form were found to be not dissimilar to the synthons found at the surface of the smaller faster growing faces. The more isotropic nature of the β packing which is dominated by the H-bonding ring means that the major interactions were found to be orientated in more than one crystallographic direction; hence they affect growth in different directions in 3D. The large, slow growing, (0 1 -1) and faster growing (0 0 2) surface were also found to have significant contributions from all of the 4 strongest intermolecular interactions. However, the amount of these interactions outside of the slice is found to be less in the (0 1 -1) surface than the (0 0 2) surface, hence the larger predicted area of this face at the surface. The (1 0 -1) surface has only two strong intermolecular interactions outside the slice, but there was found to be a large contribution from both interactions, hence it has a smaller area than the (0 1 -1) surface but a larger area than the (0 0 2).

### 7.3.3 Comparison between the α and β Crystal Morphologies

This isotropic nature of the distribution and strength of the synthons in 3 dimensions found within the β structure is consistent with the attachment energy prediction more closely reproducing the experimental crystal, compared to the α form where the attachment energy predicted morphology was found to be less needle-like than most experimental morphological observations[3, 192]. The difficulty in predicting needle-like morphologies using the attachment energy approach has been highlighted in previously published studies[24, 181].

The variation in nature and strength of the faces in the α form suggest that the effect of solvent binding on growth rate will vary face to face, while the interaction with solvent at the faces of the β crystal will be similar at each face, hence the experimental solvent

mediated morphology was found to be much the same as the morphology predicted in the vacuum state. If a crystal morphology is solvent dependent then the attachment energy theory cannot account for the effect of the solvent during growth, since the calculation only considers intermolecular interactions within the crystal structure. Hence, anisotropic crystal structures where the surface chemistry varies strongly face to face would require a model which can consistently and accurately predict the influence of the solvent on the growth of each crystal surface to produce accurate morphological predictions.

Experimentally it appears that the growth via π-π stacking in the α form was found to be more dominant than observed in the β form. Interestingly the amino hydrogens also showed a similar contribution for both polymorphs. This could suggest the NH…O interaction, which was not calculated to be a major synthon in the α-form, could facilitate the transition pathway between the α and β form as it is the main interaction that is found to be shared by both forms.

## 7.4 Systematic Search of Crystal Surfaces

The attachment energy calculations were all within vacuum conditions and make an assumption that molecules add layer by layer. Therefore, to simulate how a single molecule of solute or solvent may prefer to bind to a crystal surface, single probe molecules were systematically searched around the crystal surfaces of the morphologically important surfaces of α- and β-*p*ABA according to the methodology described in Section 4.4.4.

A previous study postulated a model that used the surface systematic search to predict solvent dependent morphologies of aspirin[5] (Section 3.5.3). This model calculated the competition between the solute and solvent at the crystal surface by using the strongest interaction found for the solute and solvent at the crystal surface to calculate a solution modified attachment energy. However, this approach failed to produce a morphological prediction that closely resembled the experimental solution grown needles from polar solvents such as water and ethanol.

Therefore, it could be that it is not always just the strongest binding site found from a probe molecule, but the distribution of energies found at a particular surface. If there

were a large amount of available binding sites found for a solvent probe that was not found for a solute probe at a particular surface, this could suggest that the growth of this surface would be inhibited by that solvent. Therefore, the amount of sites that were in a particular window of interaction strength were tabulated below to gain qualitative information of a crystal surfaces affinity for the solute or solvent.

The column graphs below are the sites found where the probe had an interaction energy with the surface of above 0 kcal. The data is graphed is energy range of sites on the x-axis plotted against the amount of sites found with an interaction energy within that range. Each bin is labelled with the minimum allowed energy for the bin and each bin counts all the interactions of the minimum value and 2 kcal above that value, i.e. -2 to -4 kcal.

### 7.4.1 α-*p*ABA

#### 7.4.1.1 Solute Binding

Figure 7-12 shows the distribution of energies from a probe single molecule of *p*ABA interacting with the morphologically important surfaces of α-*p*ABA. How strongly the solute molecules bind was correlated to how likely it is a molecule will be strongly adsorbed into the surface and therefore how fast growth may occur.

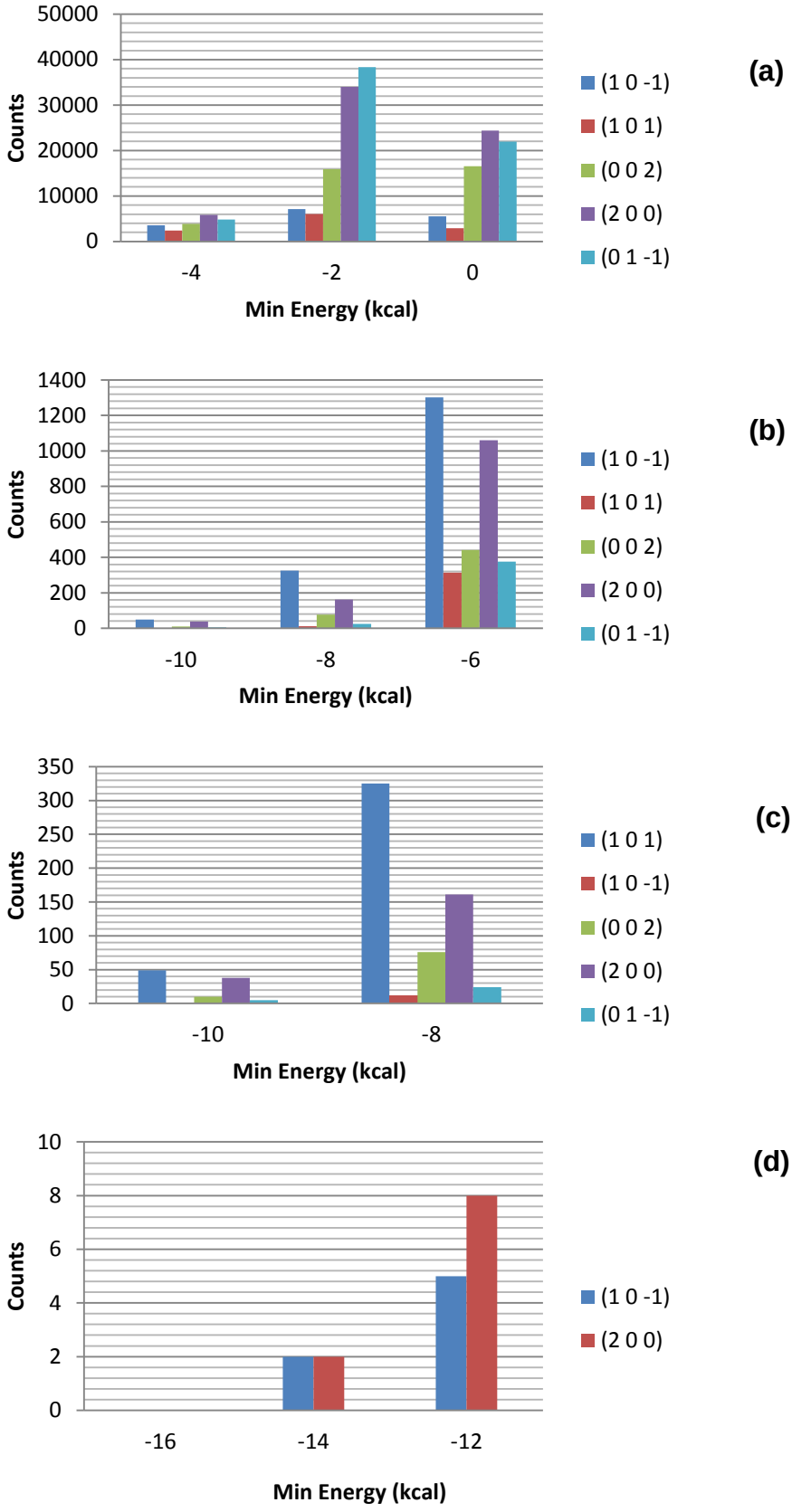


**Figure 7-12: Strength and density of the binding sites of *p*ABA molecule to the morphologically important surfaces of α-*p*ABA found from the systematic surface search: (a) 0 to -6 kcal; (b) -6 to -12 kcal; (c) -8 to -12 kcal; (d) -12 to -18 kcal**

Since it is assumed that any adsorption of *p*ABA into the surface does not involve a chemical reaction, hence no change in electronic structure, it was assumed that molecules coming from solution are only ever physisorbed rather than chemisorbed. In this case, the very weak interactions below 2 kcal can probably be discounted as the molecule is likely to be very mobile at the surface and could easily desorb back into the surrounding solution. Chapter 5 revealed that some important interactions within the α-*p*ABA crystal structure had intermolecular energies of around 2kcal and above, therefore it was assumed that molecules at sites with interaction energies above 2 kcal to a surface can potentially physisorb into the surface.

Figure 7-12(d) showed that the strongest binding sites were found to be at the (1 0 -1) and (2 0 0) surfaces, though the amount of these available sites was found to be very low. In general, Figure 7-12 showed that the (1 0 -1) and (2 0 0) surfaces were found to have the highest amount of hits for higher interaction energies (-6 kcal and above), suggesting that *p*ABA molecules bind well to these surfaces. Generally the next strongest interacting surface is the capping (0 1 -1) surface, which also has a very high amount of lower strength interaction sites between -2 and -4 kcal. Figure 7-13 shows molecular orientation at the strongest binding sites for the faces searched in Figure 7-12.

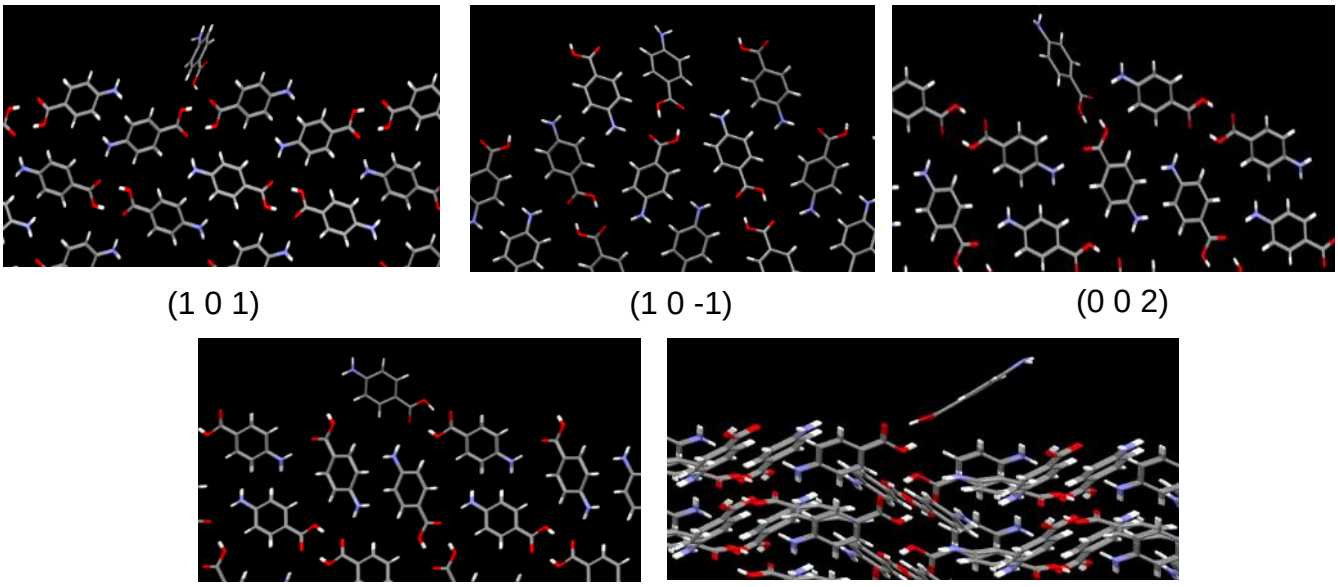


**Figure 7-13: Molecular orientation of single probe molecule of *p*ABA at the morphologically important surfaces of α-*p*ABA**

Figure 7-13 shows that at each surface the strongest binding site of a *p*ABA molecule has the major interaction being between COOH groups. The binding with the COOH group at the (0 1 -1) also results in the molecule being in an orientation that is favourable for forming the π-π stacking interactions. It was shown in Chapter 6 that the motif containing both the OH…O H-bonds and π-π stacking interaction was very stable in solution and may facilitate the self-assembly of the α-polymorph, hence this combination of synthons may also induce the fast growth of the capping face and the needle-like morphology.

A previous publication suggested that OH…O carboxylic acid dimer type interactions may form in the metastable zone prior to nucleation[229]. The modelling in chapter 6 also suggested that these interactions are very stable in most solutions, therefore the attaching growth unit may be a dimer rather than a monomer and therefore the binding energies for a carboxylic acid dimer to the morphologically important surfaces of α-*p*ABA are shown in Figure 7-14.

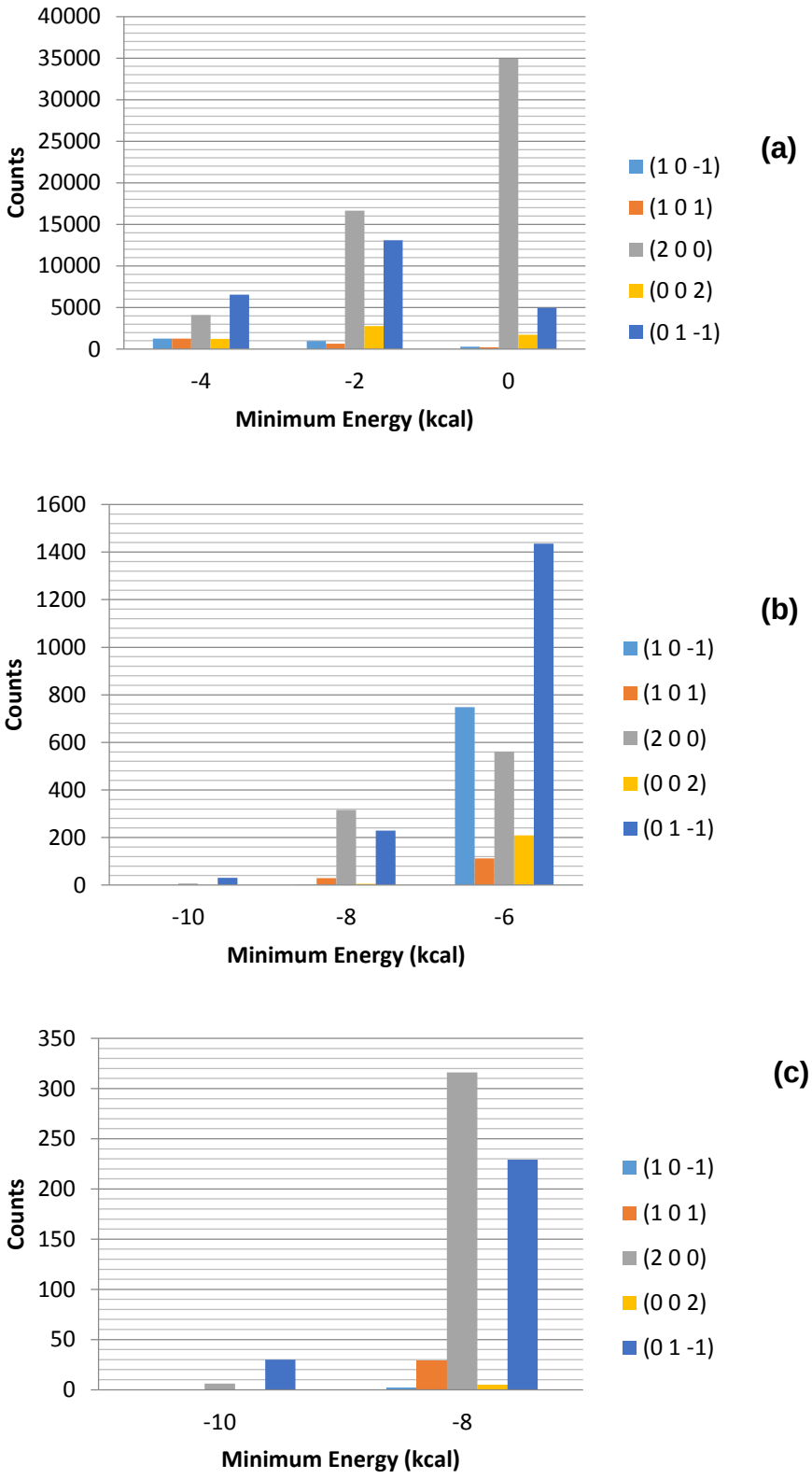


**Figure 7-14: Strength and density of the binding sites of an OH…O H-bonding *p*ABA dimer to the morphologically important surfaces of α-*p*ABA found from the systematic surface search: (a) 0 to -6 kcal; (b) -6 to -12 kcal; (c) -8 to -10 kcal; (d) -12 to -16 kcal**

Figure 7-14 shows that compared with the strength and density of the binding sites of the monomer to the morphologically important faces of α-*p*ABA, the dimer probe search found a greater amount of sites with stronger interaction energies. Since the OH...O H-bonds were not included in this calculation, the strongest interaction was between the π-π stacked molecules, therefore the increase in strong binding sites was probably due to the orientation of the molecules at the (0 1 -1) surface making the phenyl ring groups more available and hence encourage the formation of the π-π interactions. The amount of strong interactions for the (1 0 -1) surface are significantly decreased due to the decreased availability of the COOH group, suggesting that if the *p*ABA molecules attached as dimers then the molecules would more strongly prefer to attach to the capping faces than the side faces. This would probably result in an increased growth rate of the capping faces compared to the side faces.

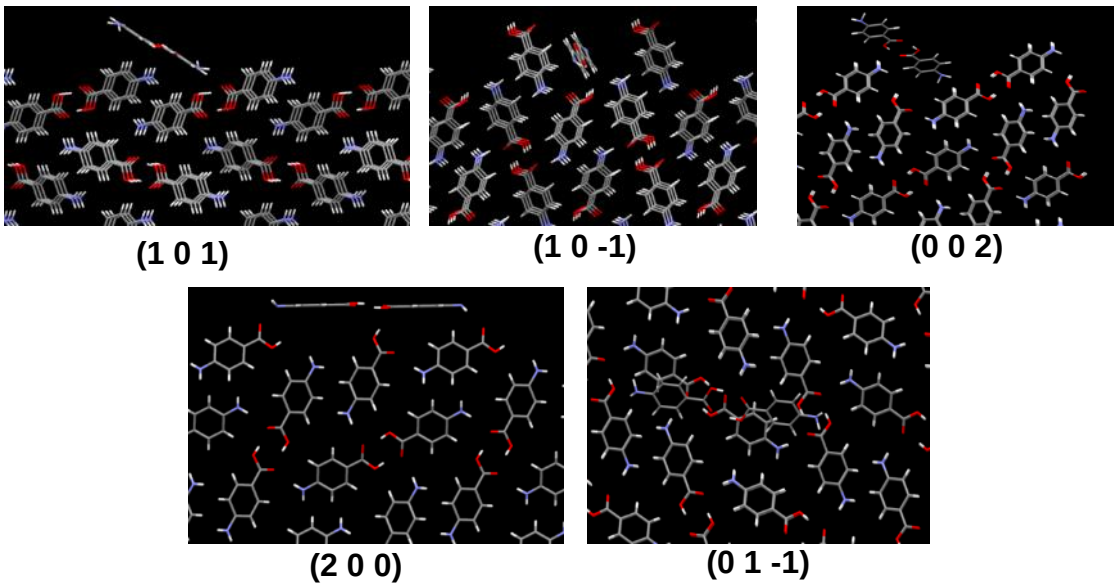


**Figure 7-15: Most favoured grid points for the carboxylic acid dimer probe at the major surfaces of α-*p*ABA**

The preferred orientation of the dimer at all surfaces was found to be more flat than the monomer, reflecting that the COOH group is satisfied prior to incorporation into the crystal lattice and that the strongest interactions that this dimer can form are π-π stacking interactions involving the phenyl ring structures. The orientation of the probe dimer at its most favourable grid point at the (0 1 -1) surface was found to be closest to the orientation that the dimer would adopt in the crystal structure, suggesting that

this dimer may relatively easily incorporate at this surface, hence facilitating fast growth.

A previous study by McCardle et al on benzoic acid suggested that the benzoic acid molecules incorporated more easily into the crystal lattice when forming π-π stacking interactions over H-bonding interactions[183], regardless if the growth unit was a monomer or dimer. Considering that the packing of α-*p*ABA is not dissimilar to that packing of benzoic acid, it could be expected that the molecules do less work when incorporating into the crystal lattice at the capping faces of the needle. The idea that the interactions that involve larger areas of the molecules interacting being more easily formed could form the basis as to why the capping faces dominated by π-π stacking interactions of α-*p*ABA grow more quickly than the side faces that are dominated by stronger H-bonding interactions. Though the strength on the synthons is greater for the H-bonds, the molecules have to be in a much more specific orientation to create these H-bonds.

#### 7.4.1.2 Solvent Binding

Since *p*ABA crystallises from polar solvents such as ethanol and water, the binding of these solvents to the crystal surfaces could potentially slow down the incorporation of *p*ABA into certain surfaces and affect the growth and morphology of α-*p*ABA. Therefore the morphologically important surfaces of α-*p*ABA were searched using ethanol and water as probe molecules. Figure 7-16 and Figure 7-17 shows the binding sites of a water molecule and then an ethanol molecule to the morphologically important surfaces of α-*p*ABA respectively, found from the systematic search.

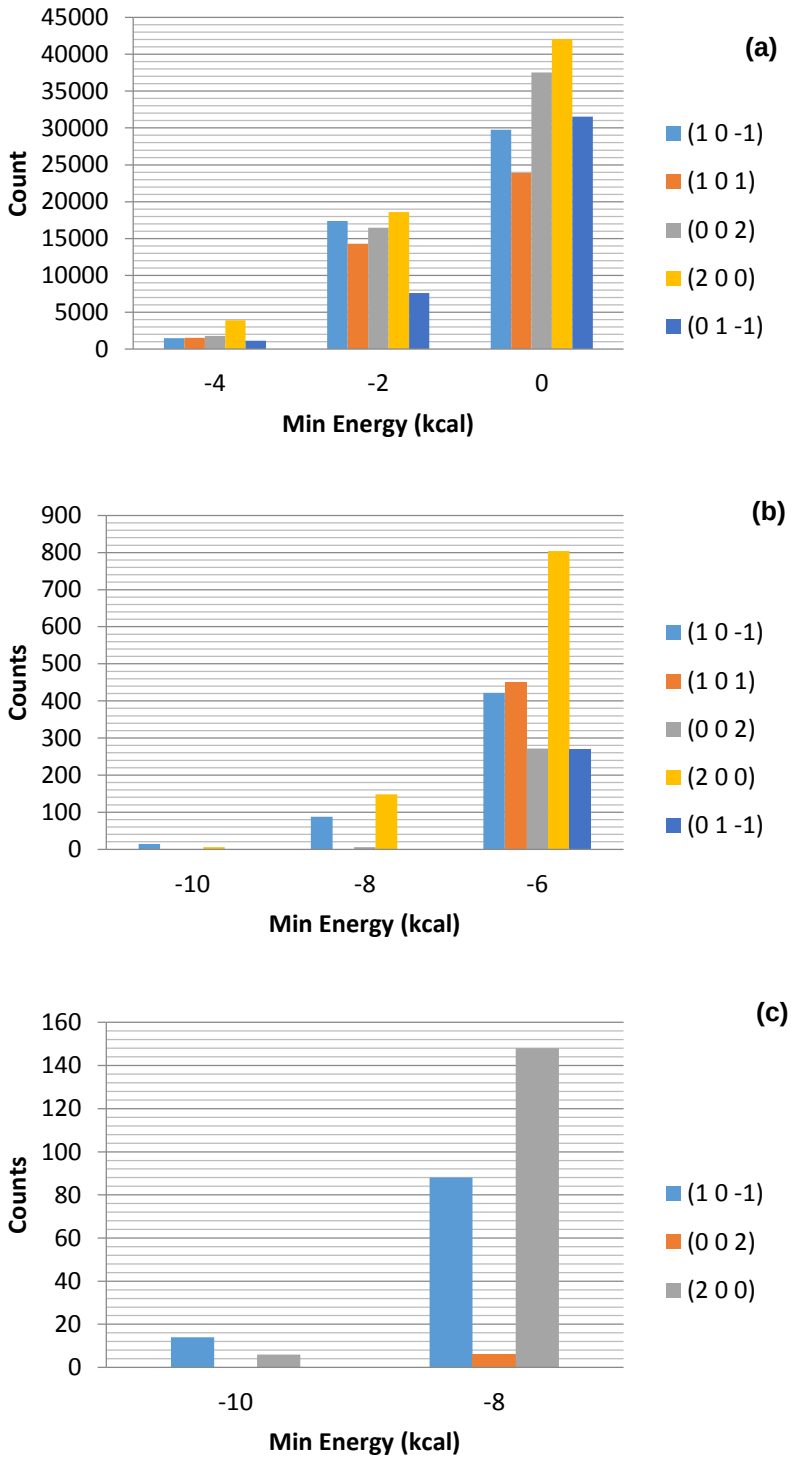


**Figure 7-16: Strength and density of the binding sites of a water molecule to the morphologically important surfaces of α-*p*ABA found from the systematic surface search: (a) 0 to -6 kcal; (b) -6 to -12 kcal; (c) -8 to -12 kcal**

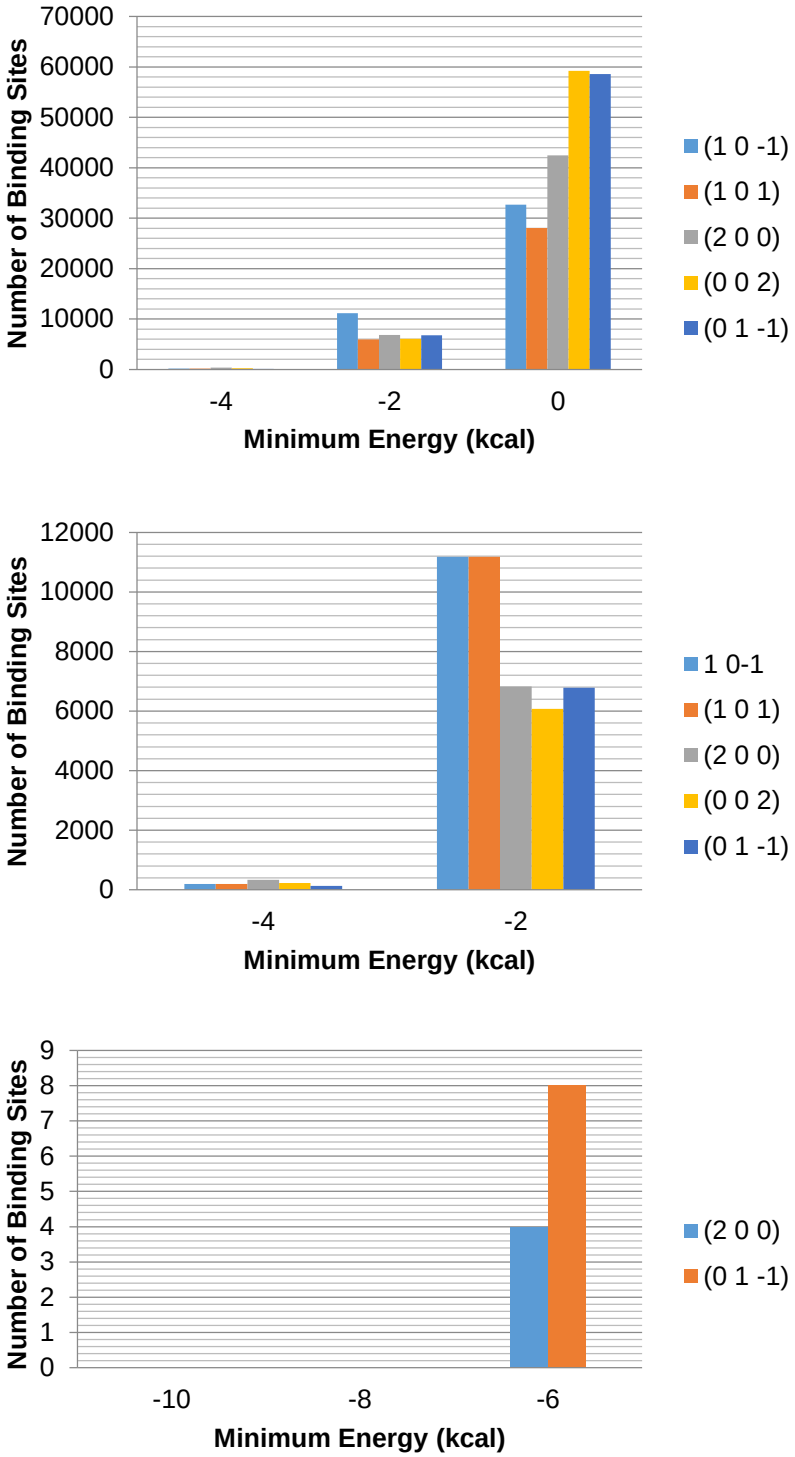


**Figure 7-17: Strength and density of the binding sites of an ethanol molecule to the morphologically important surfaces of α-*p*ABA found from the systematic surface search: (a) 0 to -6 kcal; (b) -2 to -6 kcal; (c) -6 to -12 kcal.**

Generally, it was calculated that ethanol finds significantly more binding sites at morphologically important surfaces of α-*p*ABA, than water. This is probably due to ethanol being able to form increased amounts of vdWs, as well as H-bonding interactions. However, the strongest binding sites of water to the morphologically important surfaces of α-*p*ABA were calculated to be stronger than the strongest sites calculated for ethanol. The water probe appears to form the highest amount of interactions with the side faces, the (1 0 -1) and (2 0 0) surfaces, whereas the strength of the $H_2O$ binding sites at the (0 1 -1) surface were found to be weaker and generally much lower in density. The morphology of the crystals from water solutions are the thinnest, almost hair like crystals, suggesting that the growth from the side faces is retarded, which corresponds with the water molecules binding more strongly to the (1 0 -1) and (2 0 0) surfaces compared to the capping faces, hence the water molecules are more likely to slow down the growth of the capping faces than the side faces.

### 7.4.2 β-*p*ABA

#### 7.4.2.1 Solute Binding

The explicit binding of a monomer of *p*ABA to the morphologically important surfaces of β-*p*ABA was examined. The dimer growth unit binding was not considered as there are no carboxylic H-bonding dimers present in the β-*p*ABA crystal structure. The distribution of binding sites of a single molecule of *p*ABA to the morphologically important surface of β-*p*ABA are shown in Figure 7-18.

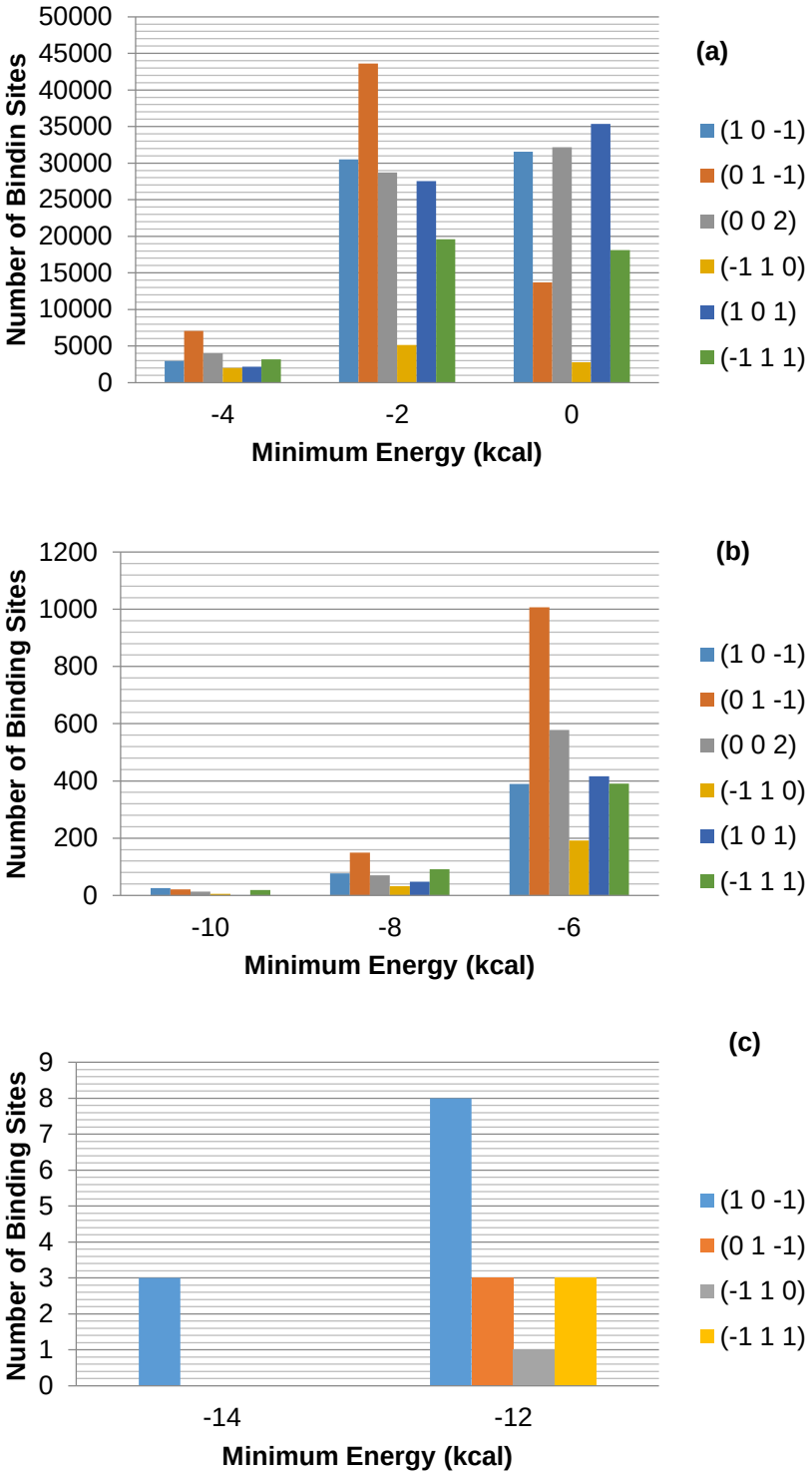


**Figure 7-18: Strength and density of binding sites of a single molecule of *p*ABA at the major faces of β-*p*ABA identified by the systematic search: (a) 0 to -6 kcal (b) -6 to -12 kcal; (c) -12 to -16 kcal**

Compared to the binding sites identified for α-*p*ABA, the amount of hits per face is more similar. This is similar to what is seen for the attachment energy calculations,

which aligns to the suggestion that the likelihood of incorporation of molecules into the different faces of β-*p*ABA is relatively isotropic compared to α-*p*ABA. It was also proposed (Section 7.3.3) that the similar strength and nature of the synthons exposed at the morphologically important faces of β-*p*ABA would result in similar solvent interaction with these surfaces. Figure 7-19 and Figure 7-20 show the strength of the binding sites of water and ethanol to the morphologically important faces of β-*p*ABA.

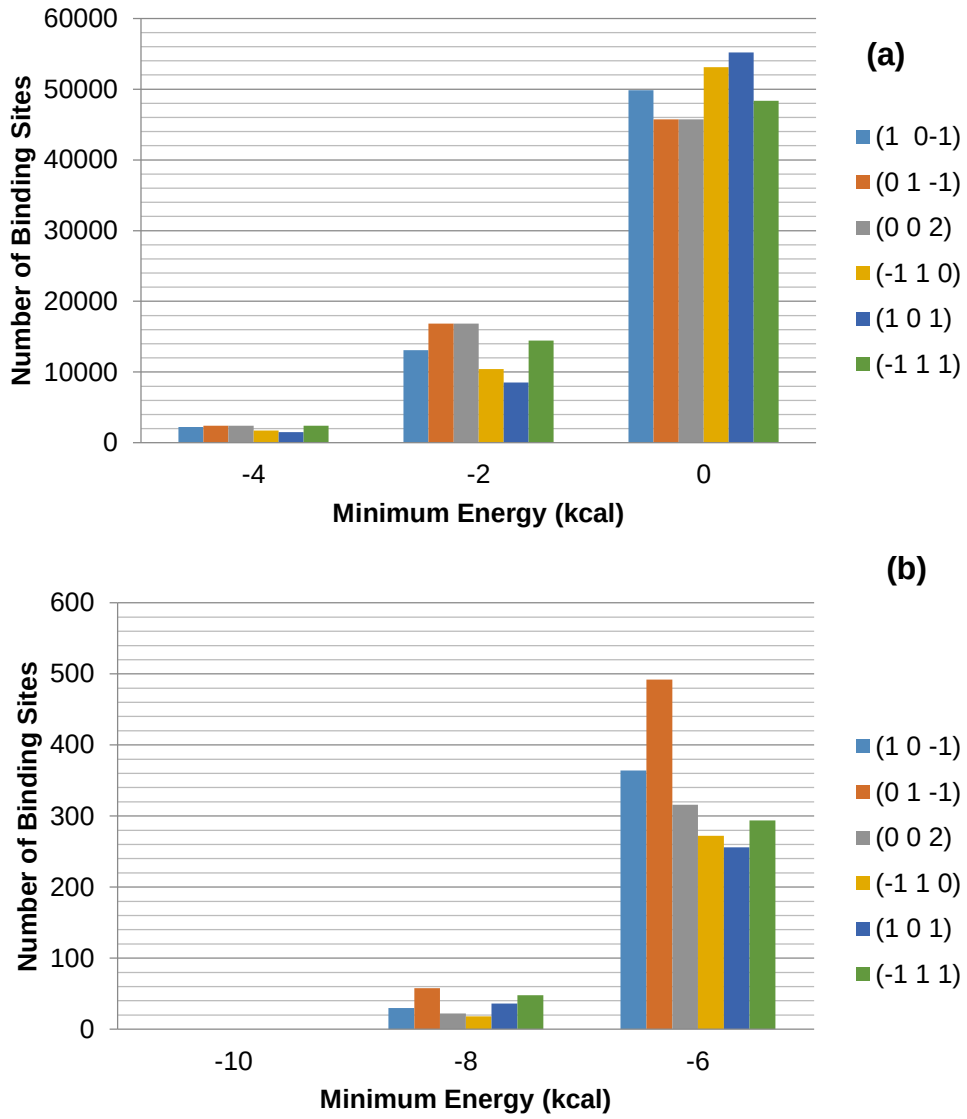


**Figure 7-19: Strength and density of the binding sites of a water molecule to the morphologically important surfaces of β-*p*ABA: (a) 0 to -6 kcal; (b) -6 to -12 kcal**

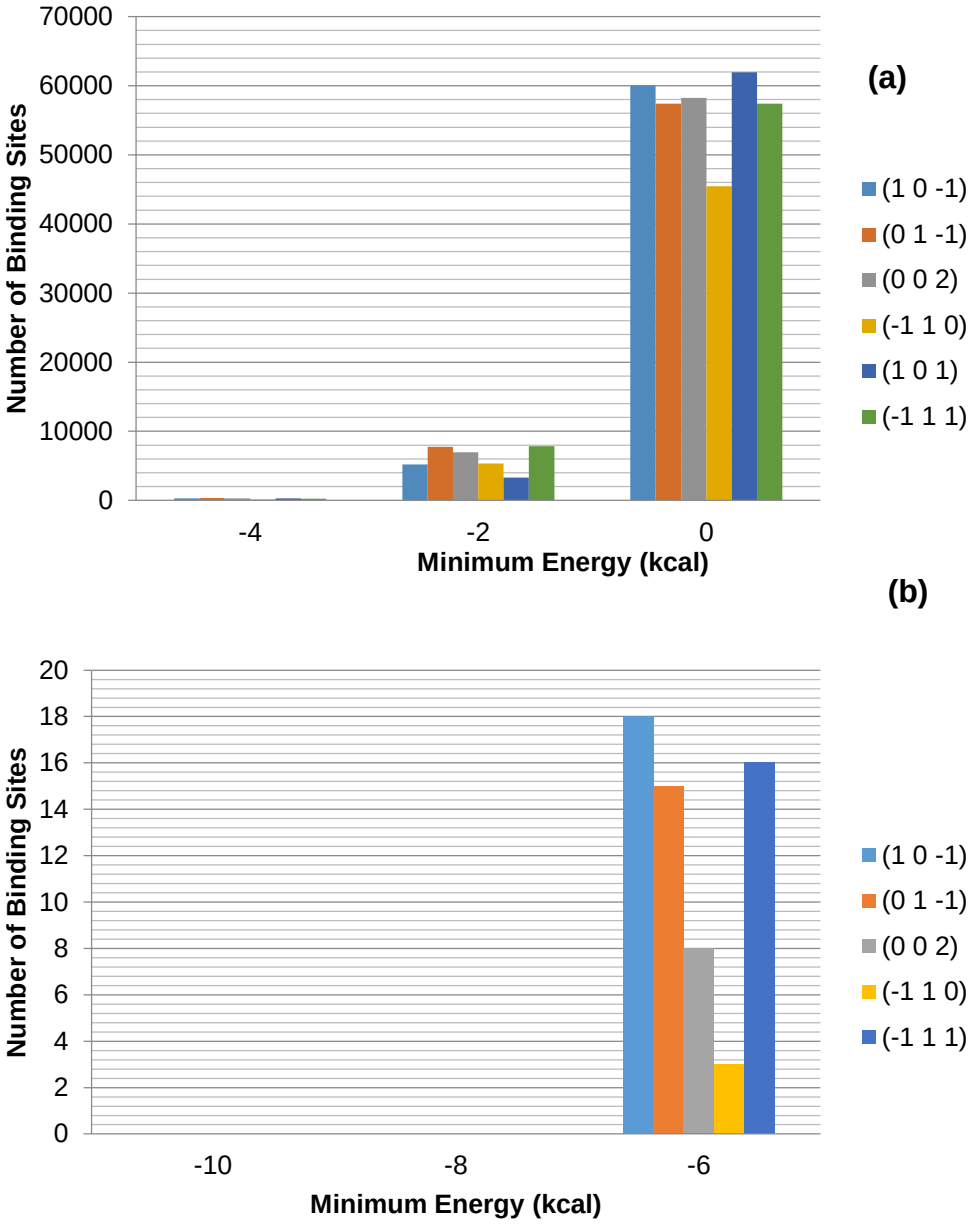


**Figure 7-20: Strength and density of the binding sites of an ethanol molecule to the morphologically important surfaces of β-*p*ABA: (a) 0 to -6 kcal; (b) -6 to -12 kcal**

The strength and density of the binding sites of water and ethanol to the morphologically important surface of β-*p*ABA was found to be much more equal than α-*p*ABA. This supports the idea that the solvent binding to each surface is more equal than for α-*p*ABA and one of the reasons why the attachment energy morphological

prediction of β-*p*ABA more closely matches the experimentally crystallised β morphology.

## 7.5 Comparison of the Morphologies of α- and β-*p*ABA

It is likely that the solvent has a greater effect on the crystal morphology of α-*p*ABA than β-*p*ABA. The appearance of a needle-like morphology as often observed for α-*p*ABA is likely to be a kinetic effect similar to what was observed in benzoic acid[183], hence the observed difference in attachment energy morphology and experimental morphologies observed from water and ethanol. The difficulty in predicting and controlling the formation of needle-like crystals is a well-studied phenomena[24, 181, 182] and remains an issue even with the advances in sophistication of calculating the solvent effect on crystal surfaces[230, 231]. This result highlights the limitations of the attachment energy calculations, since these calculations cannot account for a morphology that is changed by the solvation environment since it only calculates the synthon strength within the crystal structure. However, identifying the synthons that are dominating the growth of each surface can help identify the nature of the interactions that control the growth of certain faces, along with how the growth may be inhibited through solvent selection.

The reason behind β-*p*ABA exhibiting a morphology that matches well to the attachment energy is probably due to the fact that one face is not dominated by π-π interactions like in α-*p*ABA. It is probable that, in the polar protic solvents where the needle-like morphology of α-*p*ABA is observed from[3, 192], crystal surfaces that are dominated by π-π stacking interactions are probably more accessible to *p*ABA due to the fact that the solvation interaction is likely to be stronger to the other surfaces that are more dominated by H-bonding interactions. Though systematic searching of the crystal surfaces of aspirin resulted in a well matched solvent induced morphology prediction[5], this was not repeated with α-*p*ABA. An integrated approach that predicts the solvent binding of multiple molecules along with a prediction of the crystal growth mechanism could prove more successful when predicting a solvent induced morphology.

## 7.6 Conclusions

This chapter has revealed which of the major synthons, identified from chapter 5; influence the growth of the major surfaces of α- and β-*p*ABA through morphological prediction. Alongside this, the binding of solute and solvent to the morphologically important crystal surfaces was calculated to assess how easily a molecule may incorporate into a crystal surface. The major findings from chapter 7 are summarised in Table 7-9

**Table 7-9: Major issues addressed by chapter 7 and relevance to the study**

| Question/Problem | Answers provided by the chapter | Relevance to the study |
|---|---|---|
| How does the attachment energy morphology prediction compare to the experimentally crystallised α- and β-*p*ABA? | • β-*p*ABA morphological prediction gave closer match to experimental isotropic crystals than α-*p*ABA anisotropic experimental crystals | Attachment energy morphological prediction gives a better prediction of isotropic crystals grown at more equilibrium conditions than anisotropic crystals |
| How does the face specific surface chemistry compare between the two polymorphs? | • Strength and nature of synthons exposed at the surfaces of α-*p*ABA strongly varies per face<br>• Strength and nature of synthons exposed at the surfaces of β-*p*ABA similar per face | Variation in the strength and nature of the synthons exposed at different crystal surfaces can results in a more anisotropic, needle-like morphology for α-*p*ABA |
| How does the morphological prediction and solute/surface binding predictions change between a monomer and dimer growth unit for α-*p*ABA? | • Both monomer and dimer morphological predictions underestimate the growth rate along the long axis of the needle<br>• Binding sites at the capping faces increases with dimer growth unit, compared to side faces | The dimer growth unit favours faster growth of the capping faces since this favours π-π stacking interactions, as the OH...O H-bonding synthons would have pre-formed in solution. Prediction of the actual growth rate is more complex, may need to include growth mechanism |

| | | |
|---|---|---|
| How does ethanol and water bind to the morphologically important surfaces of α- and β-*p*ABA? | • Water and ethanol both preferentially bind to the side faces of α-*p*ABA over the capping faces<br>• Water has weakest binding to the capping surfaces<br>• Solvent binding to the morphologically important surfaces of β-*p*ABA more equal | Solvent binding may slow down the growth rate of the side faces of α-*p*ABA. Water produces the thinnest needles, hence suggesting that the lack of binding to the capping faces induces the faster growth rate for the capping face in water. The solvent binding to the morphologically important surfaces of β-*p*ABA was found to be more equal, hence the solvent effects on growth may be negated |

The greater anisotropy between the strength and nature of the synthons exposed at morphologically important surfaces of α-*p*ABA, compared to β-*p*ABA, is probably important in the fact that the attachment energy morphology prediction of β-*p*ABA more strongly resembles the solution grown crystal morphology than α-*p*ABA. The underestimation of the growth rate of the (0 1 -1) surface of α-*p*ABA is probably due to the increased ease of incorporation of growth units into that surface via π-π stacking interactions, compared to the formation of the H-bonding interactions that dominate the (1 0 -1) surface. Chapter 5 revealed that the majority of the energy of the π-π stacking synthons is on the phenyl ring, which has the greatest surface area of the molecule. This larger amount of surface area interacting to form the synthon could make it easier for the molecule to form the synthon and integrate into a surface, in comparison to a H-bonding synthon that has a relatively small area that interacts to form the synthon. In addition, chapter 6 and experimental SAXS studies{D.Toroz, 2015 #237} have suggested that the OH...O H-bonding dimer may pre-assemble in solution, which would lead to the majority of the available interaction area of the growth unit to be the phenyl rings, favouring π-π stacking interactions.

The difference between the predicted attachment energy morphology and the experimental morphology often observed for α-*p*ABA highlights the limitations of the attachment energy theory. Crystal morphologies that are strongly dependent on the

solvent the crystal was grown from are difficult to predict, since the attachment energy theory only calculates the energy of the internal synthons.

The solvent binding calculations suggested that the polar solvents, water and ethanol, bind more strongly to the (1 0 -1) surfaces than the (0 1 -1) surfaces of α-*p*ABA. This may contribute to the needle like shape observed from these solvents, since the incorporation of solute molecules into the side faces is probably more hindered than at the capping faces. The solvent binding to the β-*p*ABA surfaces was calculated to be more equal, hence the solvent influence on the morphology is probably equal over the morphologically important surfaces, resulting in a morphology that matches well to the attachment energy morphology prediction.

Using the synthonic knowledge from chapter 5 and information on the pre-assembly of molecules in solution from chapter 6, revealed that information from different parts of the crystallisation process can help predict how a crystalline material will grow. This is important with respect to finding the conditions that will produce a desirable crystalline morphology.

# Chapter 8 Experimental Crystal Growth Rate Measurements and Morphology

*Crystal growth rate measurements are used to determine the crystal growth rate mechanisms of the (0 1 -1) and (1 0 -1) surfaces. The experimental morphological variations are examined in pure ethanol and in ethanol:nitromethane mixes*

## 8.1 Introduction

The synthonic modelling of a crystal surface can be used to predict, on a molecular interaction level, how a molecule may be able to integrate into a crystal surface. However, the growth kinetics at the surface/solution interface can strongly influence the growth rate. Whether the molecules integrate at a kink sites or surface nucleation occurs and the molecules attach layer by layer, has been proven to have a strong influence on the crystal growth rate of organic materials[147-151]. Measurement of the face-specific crystal growth rates as a function of supersaturation can reveal what type of crystal growth mechanism is likely at that surface. Therefore this chapter aimed to determine the crystal growth mechanisms of the different faces of α-*p*ABA and relate them to the surface chemistry and morphology of the material.

The crystal growth rates of the capping and side faces of α-*p*ABA were measured in ethanol as a function of supersaturation and the crystal growth mechanisms were determined at these faces. The crystal growth rates and mechanisms were then related to the synthonic make-up of these surfaces determined in chapter 7.

Since the previous observations of a needle-like morphology of α-*p*ABA has been reported in polar protic solvents[3, 188, 192], it was postulated that a solvent with some π-character in the covalent bonding could disrupt the growth of the long axis of the needle. This is due to the surface chemistry of the fast growing capping faces being dominated by π-π stacking interactions (chapter 7). Therefore, the effect on the morphology of α-*p*ABA crystals in the presence of nitromethane, along with the phase diagram between α-*p*ABA and the solvate, was determined, since nitromethane contains some π-character and has no available H-bonding hydrogens. To complement this, grid-based modelling of nitromethane at the surface of α-*p*ABA was used to calculate how nitromethane may bind to the surface of α-*p*ABA and therefore affect crystal growth rates.

The work presented in this chapter contributed to the completion of objective 4. In addition, this work demonstrated a potential method for identifying a solvation environment that will produce a more desirable crystalline shape through molecular modelling of solvent/surface interactions. This method has potential applications with

respect to designing an industrial crystallisation process. The work flow associated with this chapter is shown in Figure 8-1

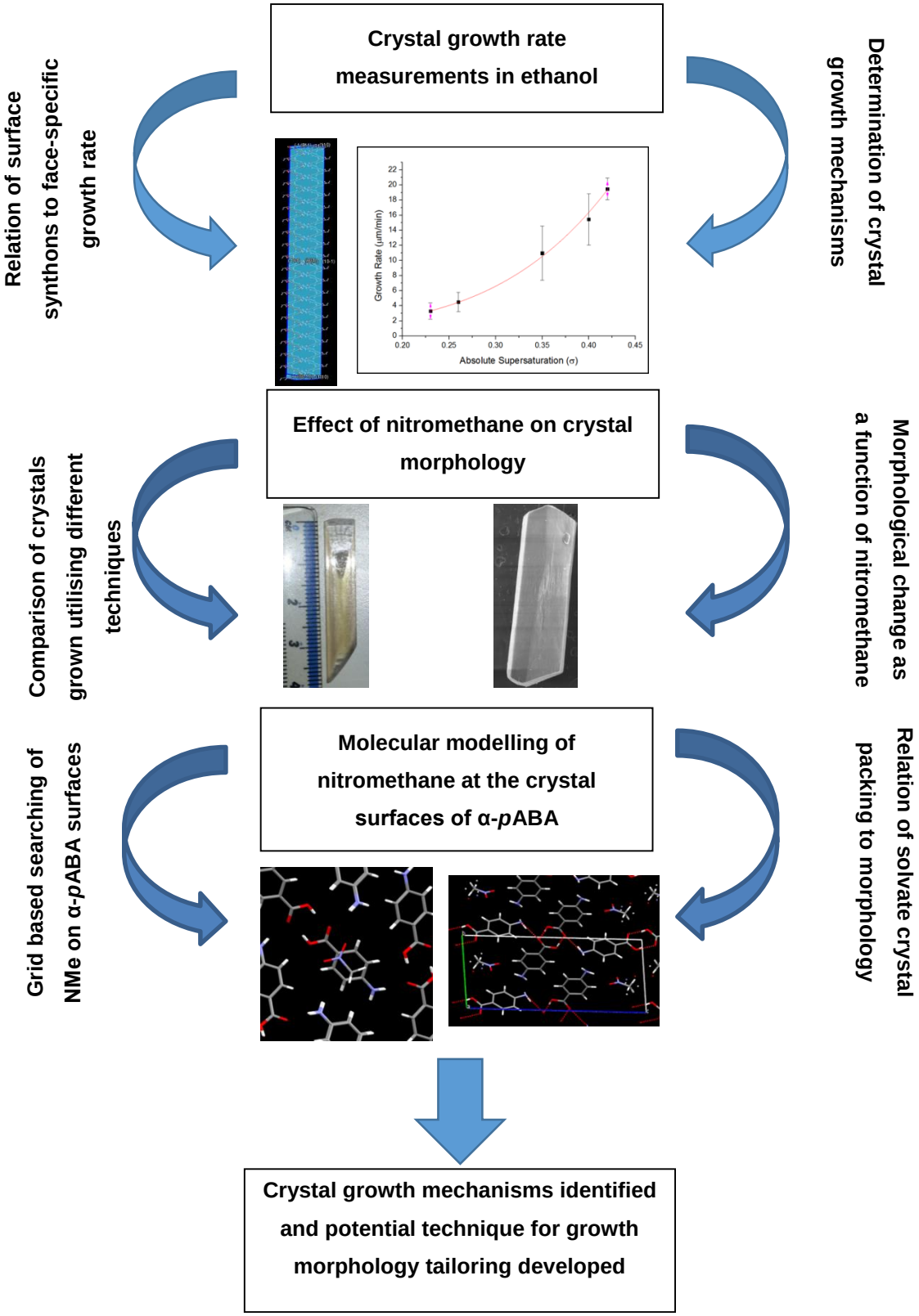


**Figure 8-1: Schematic showing work flow associated with chapter 8**

## 8.2 Crystal Growth Rate Measurements

### 8.2.1 Ethanol

The crystal growth rates along the long axis and of side faces of α-*p*ABA were measured using the techniques described in Section 4.3.3.2. Ethanol was chosen since this solvent has high solubility of α-*p*ABA and produces crystals of a reasonable size. Figure 8-2 shows the crystal growth rate vs supersaturation for the (0 1 -1) capping surface and (1 0 -1) side surface of α-*p*ABA.

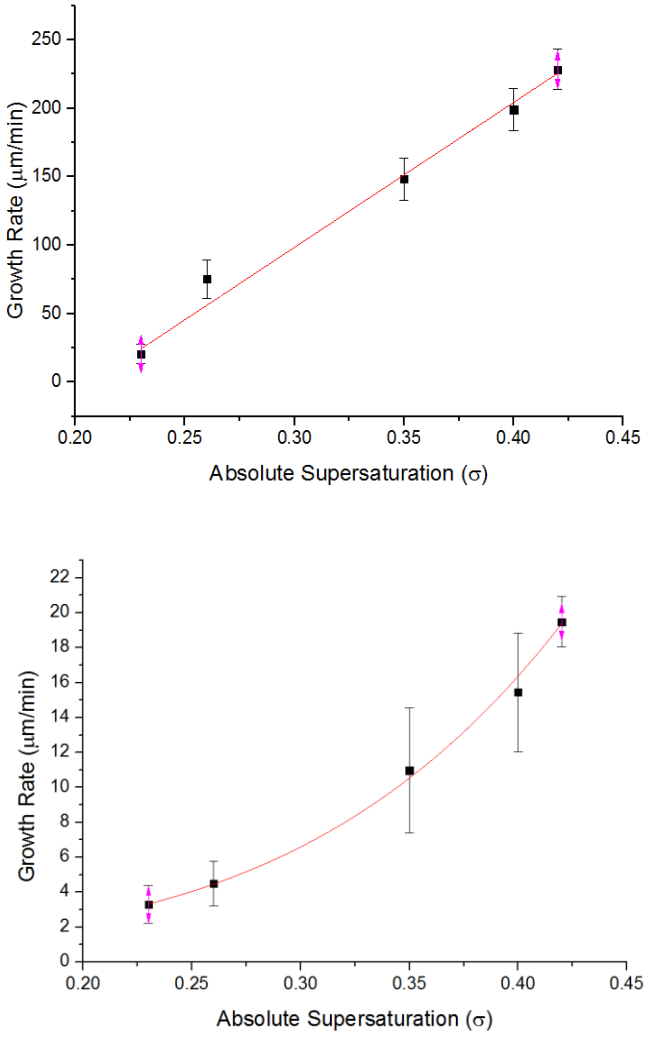


**Figure 8-2: Crystal growth rate vs absolute supersaturation for the (a) (0 1 -1) and (b) (1 0 -1) surfaces of α-*p*ABA in ethanol solutions at 20℃**

Figure 8-2 revealed that there is a dead zone up to σ = 0.23 when growing α-*p*ABA crystals at 20℃ in a stagnant, unstirred ethanol solution. Dead zones are often thought

to be as a result of immobile impurities at the crystal surface pinning down and retarding steps[233], therefore it would be interesting to observe if the dead zone would decrease if the experiments were repeated in filtered solutions. However, when the crystal started to grow, between σ = 0.23-0.42 the crystal growth rate along the long axis of the needle increased from 20.77-228.2μm/min, while the growth rate at the side faces increased from 3.29-19.48μm/min.

To identify the growth rate mechanisms, the face specific growth rate ($R_{hkl}$) and supersaturation (σ) were fitted into the growth rate equations shown in Figure 3-3, Section 3.2.4. The relationship between the change of growth rate and supersaturation that fitted closest to the relationship described by these three equations by a least sum of squares fit was assumed to be the crystal growth mechanism. The growth rate change as a function of supersaturation along the long-axis of the needle was found to be linear. This is consistent with a rough interfacial growth mechanism at this surface[150, 175]. In contrast, the crystal growth rate change as a function of supersaturation for the side (1 0 -1) surface was fit closer to an exponential relationship, consistent with a birth and spread mechanism[147]. The rough interfacial growth mechanism suggests that the energetic barrier to integration of molecules into the (0 1 -1) capping surface is low, or close to zero[133, 169, 234]. This is probably due to the phenyl rings being exposed at the (0 1 -1) surface (Chapter 7), hence a high area of the surface could form π-π stacking interactions. These interactions would be comparably less hindered by ethanol solvent molecules, since they were found to more strongly prefer to interact with the COOH and $NH_2$ groups (Figure 6-4, Chapter 6).

This method of measuring crystal growth rates has previously proven effective in elucidating the face specific growth mechanisms of ibuprofen[151]. However, the crystal growth rates are measured by a drag and measure technique within the InfinityAnalyse2 software. Hence, it was important to take several repeats and establish the results were reproducible. In addition, the 2-dimensional nature of the measurements meant that the growth rate of the face growing in the Z-direction (up towards the microscope lens) could not be measured; hence it was not possible to identify the growth rate mechanism of all the faces. However, this method did effectively identify the growth rate mechanisms of the two major surfaces.

Figure 8-3 shows a morphological sketch of the crystal morphology obtained from ethanol, filled with molecules in the orientation of the α-*p*ABA crystal structure.

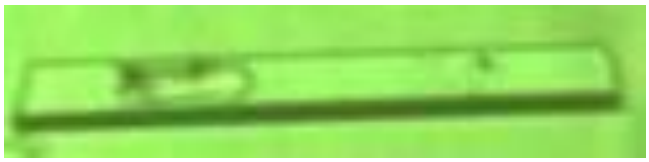

**(a)**

**(b)**

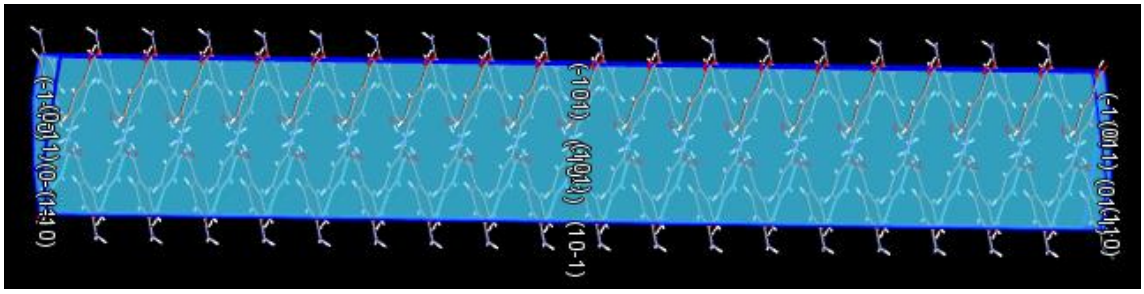


**Figure 8-3: (a) α-*p*ABA crystal grown at σ = 0.23 using the experimental method described in Section 4.3.2.2. (b) Morphological sketch of α-*p*ABA crystals sketched to more closely match experimental crystals obtained from ethanol. Sketch filled molecules in the crystal structure orientation filling the morphological sketch. Long axis of the needle orientated horizontally**

Chapter 7 determined that the growth along the long axis of the needle was dominated by π-π stacking interactions, while at the side faces the growth was dominated by H-bonding interactions. Though the π-π stacking interactions along the long axis of the needle are calculated to be weaker than the OH...O H-bonding dimer interactions, they are found to induce much faster growth in ethanol. Chapter 6 revealed how ethanol prefers to bind to the polar H-bonding $NH_2$ and COOH groups and chapter 7 revealed how ethanol is calculated to more preferentially bind to the (1 0 -1) surface compared to the (0 1 -1) surface. This probably means that both in solution and at the surface of the crystal, the COOH and $NH_2$ groups of *p*ABA are more strongly solvated than the phenyl ring. If the phenyl ring is more weakly solvated in solution compared to the COOH and $NH_2$ groups, it would mean it is more available for binding to the crystal surface, hence favouring integration at the π-π stacking dominated (0 1 -1) surface over the H-bonding dominated (1 0 -1) surface.

## 8.3 Crystal Morphology as a Function of Supersaturation in Ethanol

When attempting to control the morphology of a crystalline particle, the supersaturation as well as the solvent must be considered. Figure 8-4 shows how the morphology of α-*p*ABA changes between 2 and 8 minutes of growth from σ = 0.23-0.42.

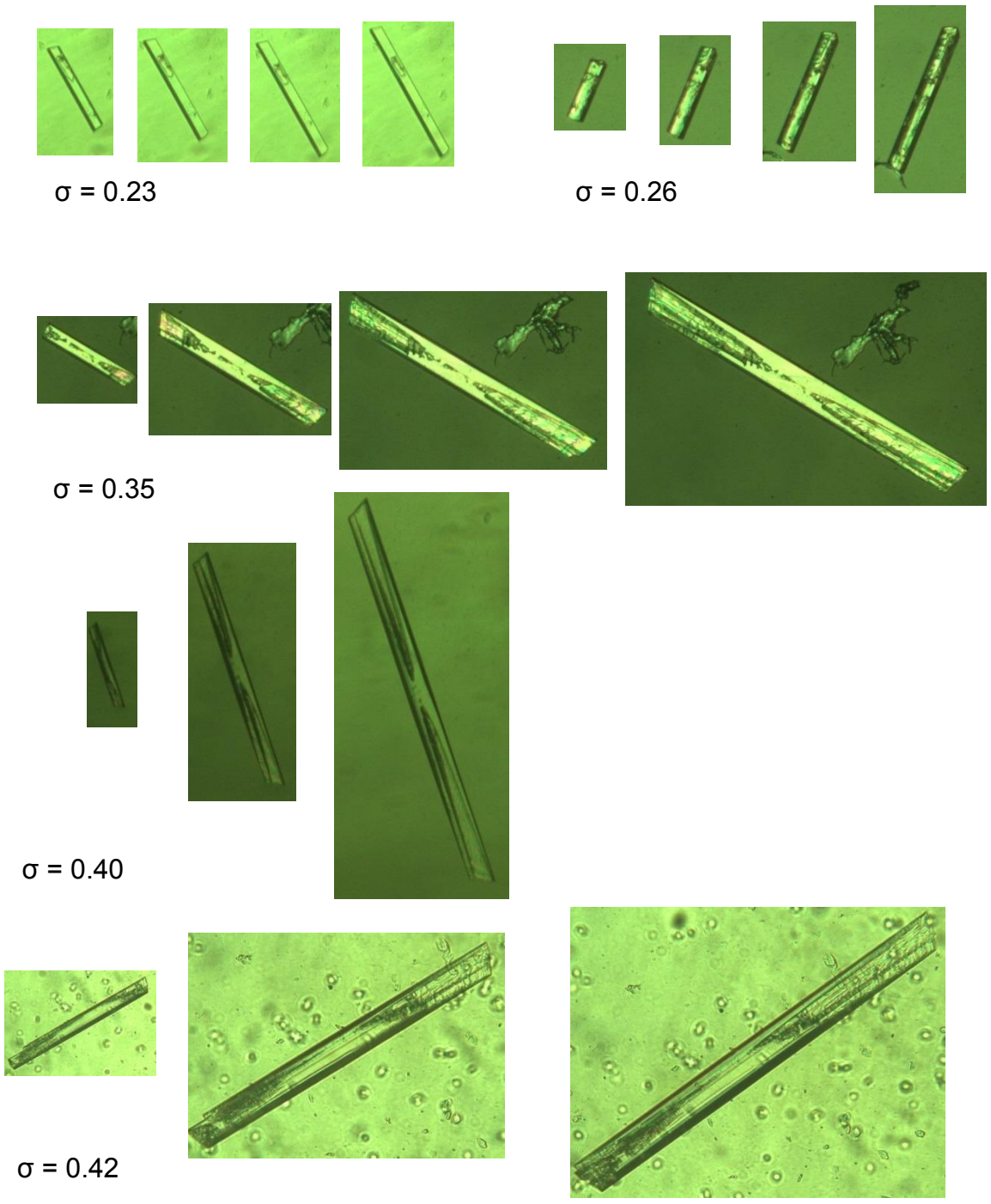


**Figure 8-4: α-pABA crystals grown in ethanol from σ = 0.23-0.42 at 20℃. Crystals grown from 2mins-8mins**

Figure 8-4 shows that α-*p*ABA crystals grown at low supersaturation were found to exhibit higher crystalline quality than the crystals grown at increased supersaturation. The crystals grown at above σ = 0.3 exhibited solvent inclusions at either end of the long axis of the needle, but is not exhibited on the side faces. This is consistent with the growth mechanism along the long axis of the needle being found to be kinetically roughened. The molecules probably incorporate very quickly into the crystal lattice along the long axis of the needle, which leads to the decreased perfection and inclusions observed. This suggests that the crystal lattice may not be perfect in these areas of the crystal, such that the molecules may not be in the exact lattice positions they should be before another layer of molecules integrates.

## 8.4 Effect of Nitromethane on the Crystallisation of α-*p*ABA

As was discussed in Chapter 7, α-*p*ABA often presents a needle-like morphology upon crystallisation from polar protic solvents. It was established from the analysis of the surface chemistry in Section 7.3 that π-π stacking interactions dominate the growth of the long axis of α-*p*ABA while H-bonding interactions dominate the growth of the side faces. Grid-based searching of the morphologically important surfaces of α-*p*ABA in Section 7.4 suggested that H-bonding solvents such as water and ethanol would have a greater propensity to bind to the side faces than the capping faces, therefore would be more likely to inhibit the growth of the side faces than the capping faces; resulting in this needle-like morphology. Therefore, NMe was chosen for crystallisation due to its lack of available protons, hence would not act as a H-bond donor like water and ethanol. In addition the π-orbital character of the $NO_2$ group would have a greater propensity to interact with the π-orbitals of the phenyl ring in *p*ABA, hence being more likely to disrupt the growth along the long axis of the needle and could result in a more isotropic crystal morphology.

## 8.4.1 Crystallisation from EtOH:NMe Solutions

### 8.4.1.1 Solubility

Since the nitromethane solvate crystals were found to have shorter aspect ratios than α-*p*ABA crystals grown from other solvents, crystallisation experiments were conducted in mixed EtOH:NMe environments to attempt to grow α-*p*ABA crystals of a large size and more desirable shape. The solubility was measured in the mixed solvents to determine the supersaturation at which to crystallise:

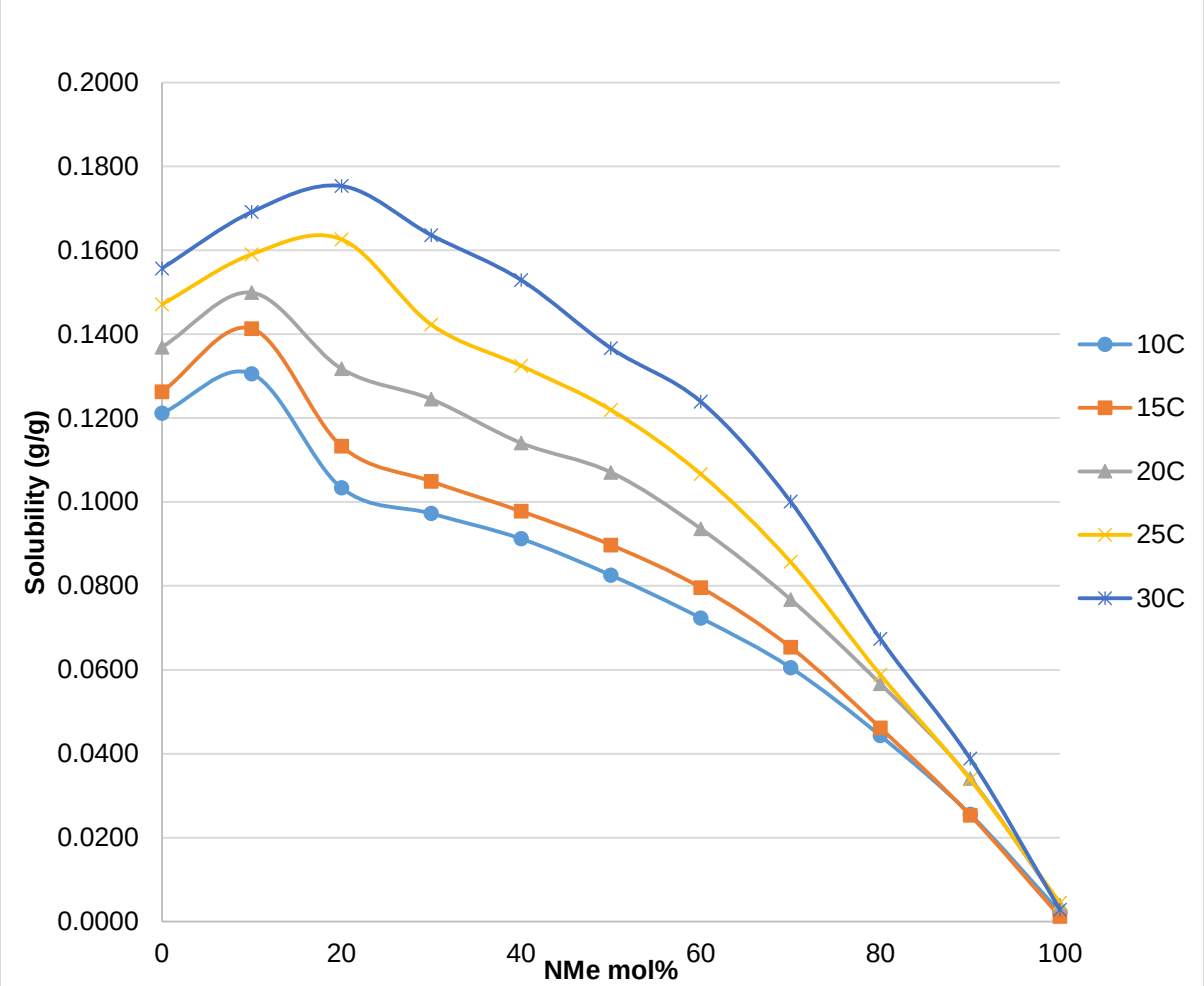


**Figure 8-5: Solubility of *p*ABA from pure EtOH to pure NMe in 10% steps by weight at different temperatures measured from gravimetric analysis**

The 90:10 EtOH:NMe solution resulted in an increase in the *p*ABA solubility compared to pure ethanol. Further addition of NMe resulted in a steady decrease up until pure nitromethane solubility. Since ethanol can act as a H-bonding donor and acceptor,

while nitromethane just as an acceptor, it is unsurprising that *p*ABA was found to have significantly lower solubility in nitromethane than ethanol.

This increase in solubility is attributed to what is known as a positive synergistic effect. These effects are known to occur with the mixing of two solvents with varying intermolecular bonding characteristics, i.e. the mixing of a strong H-bonding donor solvent with a strong H-bonding acceptor solvent[235]. In addition, the $NO_2$ group of nitromethane has some π character, which could be expected to more strongly interact with the phenyl ring than ethanol. Hence, nitromethane could be expected to solvate the phenyl ring better than the relatively hydrophobic ethanol molecule, contributing to this peak in solubility upon addition of 10% of nitromethane.

#### 8.4.1.2 Polymorphic Form

Crystallisation from the different ratios of ethanol:nitromethane yielded crystals that when examined by PXRD had peaks that were not associated with the α-*p*ABA structure. A single crystal was isolated and solved by single crystal X-ray diffraction that turned out to be a solvate, the packing diagram of the NMe solvate structure is shown below in Figure 8-6.

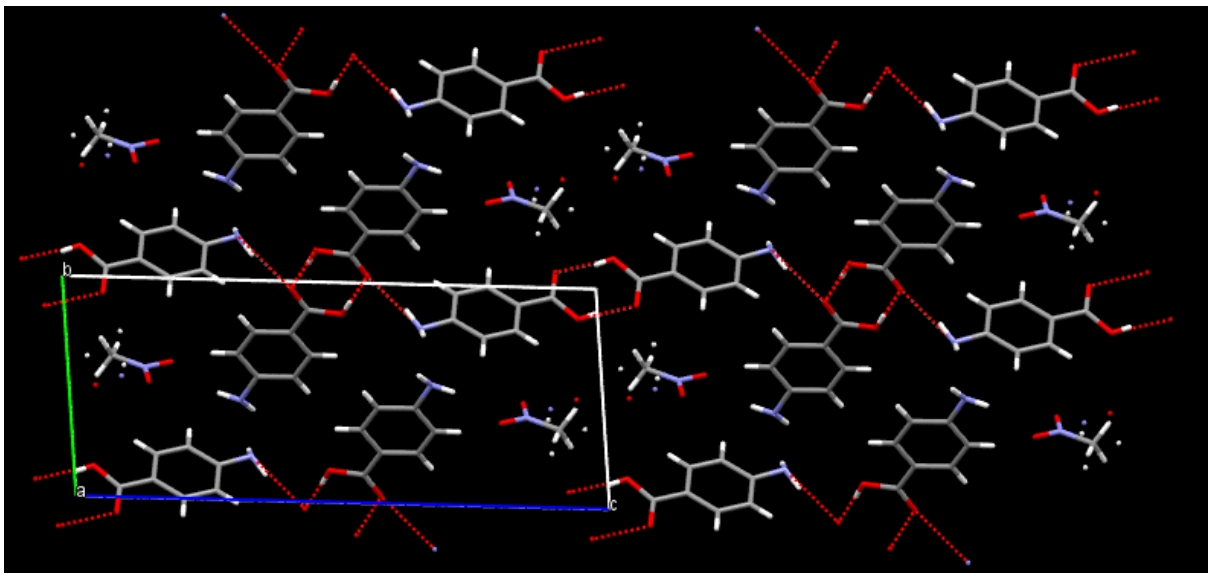


**Figure 8-6: Packing diagram of the *p*ABA:NMe solvate crystal structure solved using single crystal X-ray diffraction. Crystals grown using procedure described in Section 4.3.2.1**

The NMe solvate was found to crystallise with OH...O carboxylic acid dimers and NH...O H-bonds, similar to the α crystal structure. Though the NMe molecule was found to be disordered, from the position in the crystal structure it appears that the $NO_2$ group of the NMe molecule binds to the $NH_2$ group of the *p*ABA molecule.

Since crystals formed in pure nitromethane can form a solvate structure, the phase change between the different EtOH:NMe compositions was determined by crystallising at fixed supersaturations per composition and checking the phase by PXRD. Figure 8-7 shows a comparison of the predicted PXRD patterns for α-*p*ABA and the NMe solvate structure.

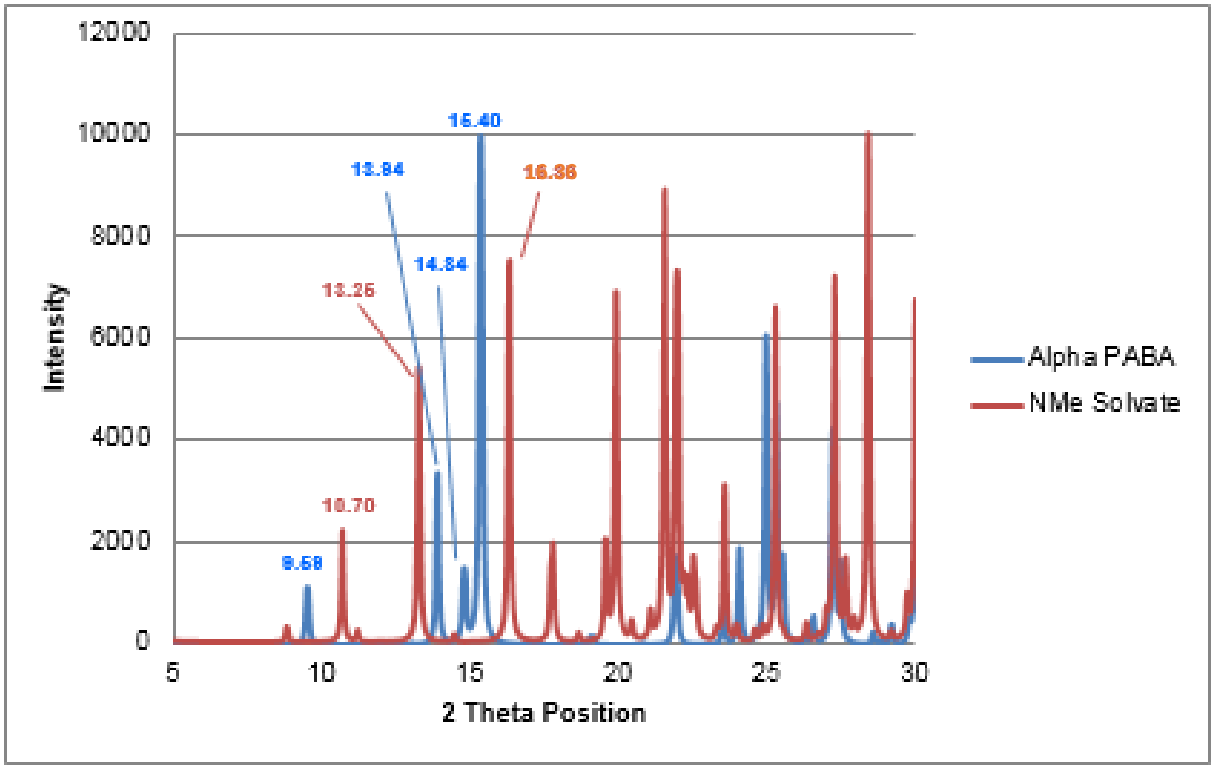


**Figure 8-7: Predicted PXRD patterns from the CIF files for α-*p*ABA (orange) and NMe solvate (purple). Predicted powder X-ray diffraction peaks taken from experimentally observed single crystal**

The major peaks from the predicted α-*p*ABA PXRD pattern are observed at 2θ = 9.59, 13.94, 14.84 and 15.40. The main peaks from the predicted NMe solvate PXRD pattern are seen at 2θ = 13.25, 16.35 and 10.70 (however this peak has shifted to the left (around 10.478)) for all of the samples containing solvate). Table 8-1 shows the calculated peak ratios for α-*p*ABA and the solvate from the samples tested by XRD.

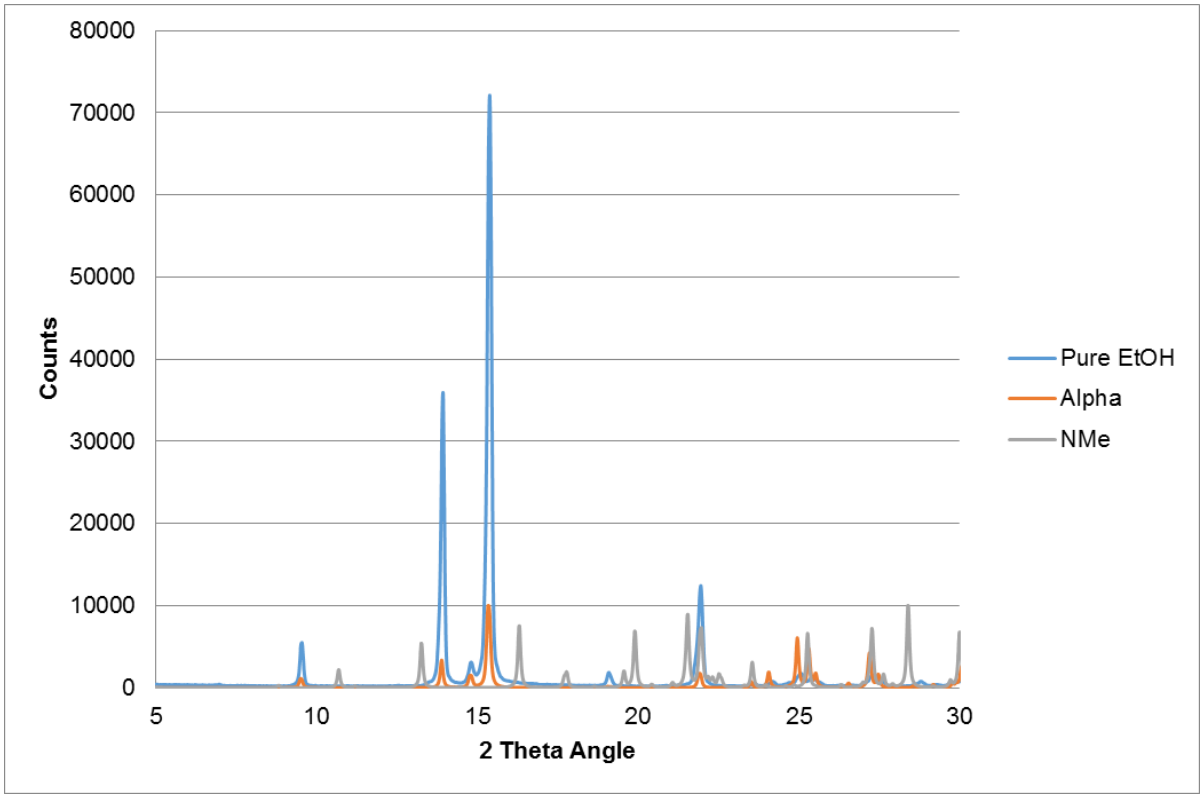


**Figure 8-8: Comparison of the experimental PXRD pattern observed from crystals obtained from cooling crystallisation of pure ethanol (blue), with the predicted patterns for the α-*p*ABA (red) and NMe solvate (green) structures. Predicted patterns obtained from the AMBNAC01 CIF file and the CIF file of the solved structure shown in Figure 8-6**

Figure 8-8 shows that the pattern observed from crystals obtained from pure ethanol contain major peaks that are associated with the α-*p*ABA structure. However crystallisation from mixed solvation environments often resulted in the appearance of peaks associated with both structures, as shown in Figure 8-9.

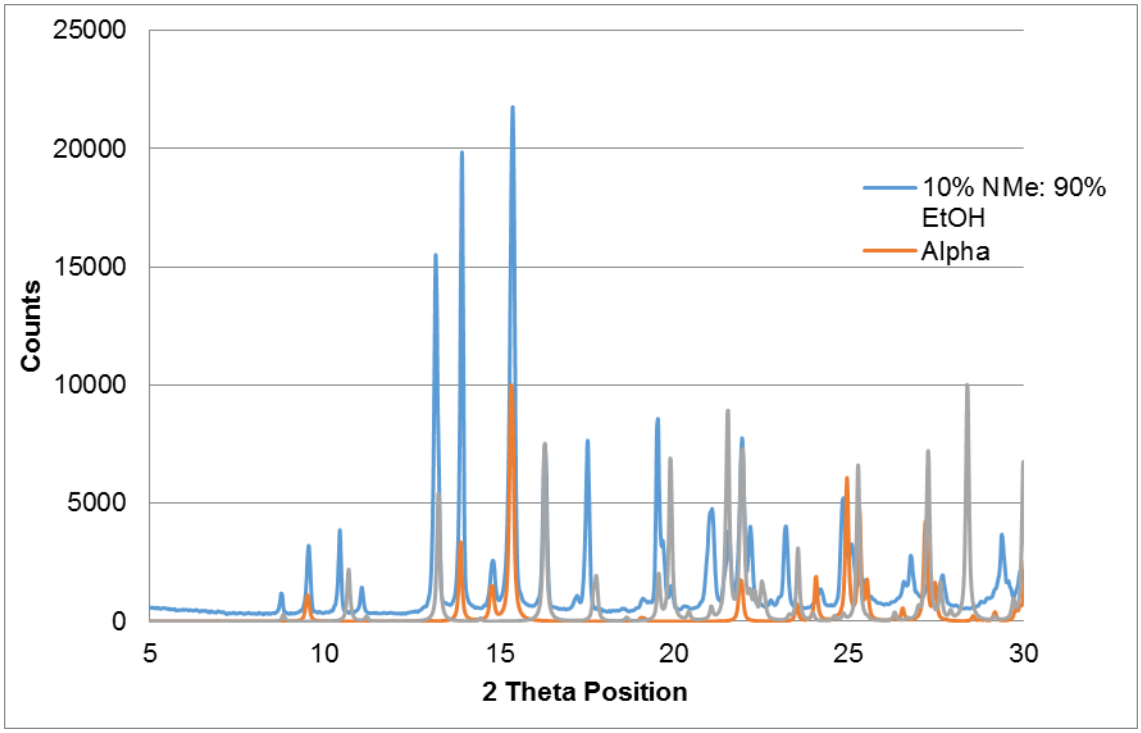


**Figure 8-9: Comparison of the experimental PXRD pattern observed from crystals obtained from cooling crystallisation of 10% NMe:90% EtOH(blue), with the predicted patterns for the α-*p*ABA (red) and NMe solvate (green) structures. Predicted patterns obtained from the AMBNAC01 CIF file and the CIF file of the solved structure shown in Figure 8-6**

The blue pattern shown in Figure 8-9 measured from crystals obtained from 10% NMe:90% EtOH solutions now clearly contains peaks associated with the α-*p*ABA and NMe solvate structures. Hence, the crystals obtained from this solution were probably a mix of pure α-*p*ABA and NMe solvate crystals.

To obtain the approximate amounts of each form in the solutions crystallised, the area under the major peaks of each form was calculated and converted into a percentage, shown in Table 8-1.

**Table 8-1: Percentage of α-*p*ABA and NMe solvate found in the crystals obtained from the mixed solvation environments, calculated from the area under the peaks associated with each structure in the PXRD patterns**

| wt% NMe | % Alpha | % Solvate |
|---|---|---|
| 10 | 66.05 | 33.95 |
| 20 | 79.77 | 20.23 |
| 30 | 92.66 | 7.34 |
| 40 | 100.00 | 0.00 |
| 50 | 91.39 | 8.61 |
| 70 | 100.00 | 0.00 |
| 80 | 100.00 | 0.00 |

Table 8-1 shows a reduction in NMe solvate content with increasing NMe content in the solvent mixture, whereby logically it might be expected that increasing the amount of nitromethane in the solution would encourage the formation of the NMe solvate. However, the induction time was observed to increase with increasing NMe content, where the crystals obtained above 50% NMe took 4-5 days to crystallise, compared to 2-3 days for the induction time of the crystals obtained from less than 50% NMe. This suggests that the NMe solvate structure is probably a metastable phase, whereby the increased induction time results in crystallisation of the more thermodynamically stable α-*p*ABA structure. This idea was tested by crystallising from pure nitromethane at increasing driving forces.

**Table 8-2: % peak areas from the PXRD of crystals obtained from pure nitromethane from simple heat/cool experiments. Saturation quoted with respect to 25°C solubility**

| Supersaturation (S) | % Peak Area α-*p*ABA | % Peak Area NMe Solvate |
|---|---|---|
| 6 | 52.10 | 47.90 |
| 8 | 66.00 | 36.00 |
| 10 | 56.21 | 43.78 |
| 20 | 32.81 | 67.19 |

Table 8-2 showed that the highest amount of solvate was found to be from the solution with the highest supersaturation, suggesting that the shorter the crystallisation time

then the increased amount of solvate. Hence this agrees with the postulation that the solvate structure is meta-stable and pure α-*p*ABA is favoured with increased induction time, since the thermodynamic form prevails due to Ostwald's ripening.

### 8.4.1.3 Crystal Morphologies from Mixed Solvation

Figure 8-10 shows SEM images of crystals grown from pure ethanol and the ethanol:nitromethane mixed solvation environments.

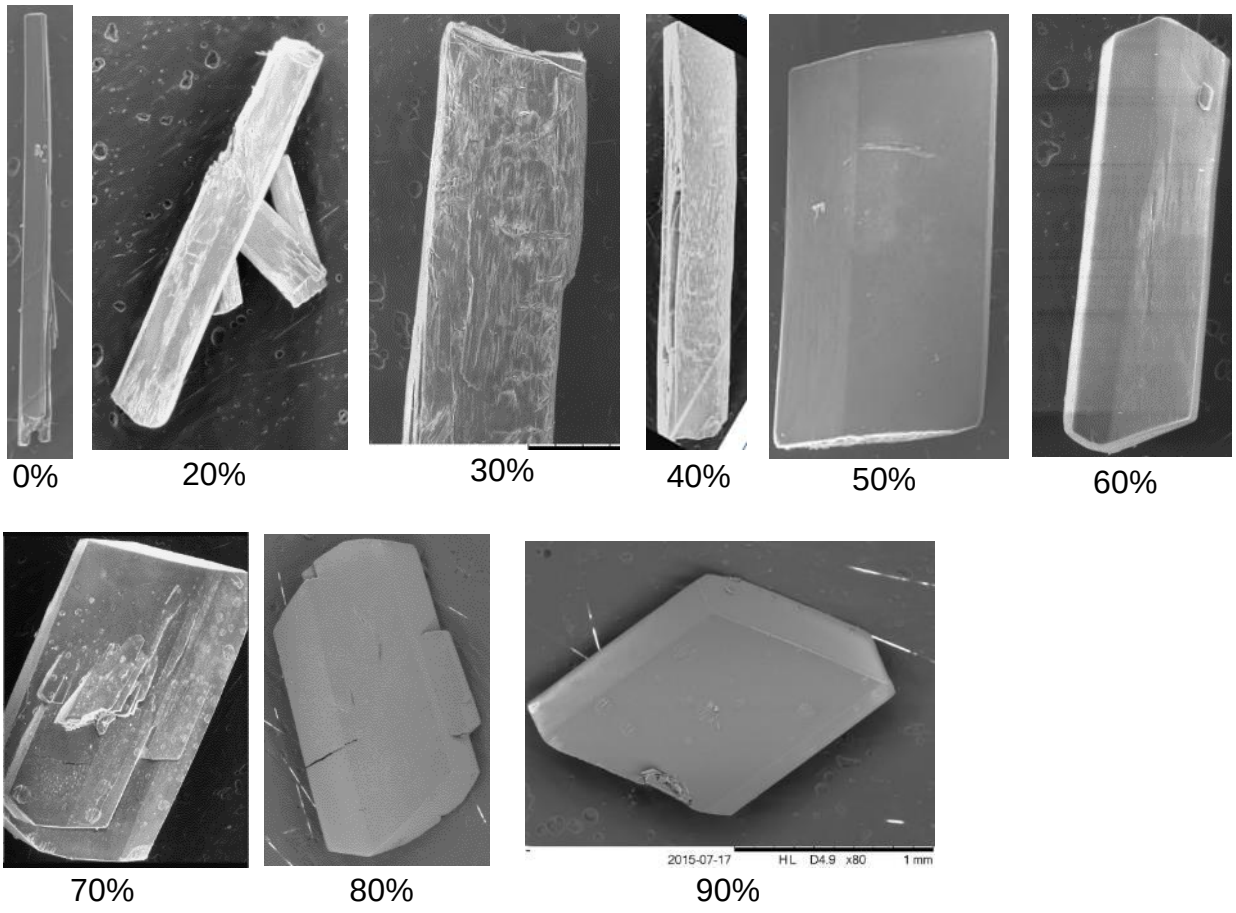


**Figure 8-10: SEM images of α-*p*ABA crystallised at S = 1.1 at 10°C from pure ethanol up to 80:20 NMe:EtOH ratio**

Figure 8-10 reveals that the morphology of the crystals became increasingly block-like upon increasing the amount of NMe present during the crystallisation process, with a significant reduction in the growth rate along the long axis of the needle. The needle-like morphology that was formed in pure ethanol became a block like crystal above around 50% nitromethane content. In addition, the crystals are generally becoming more perfect and more facetted with the increase of NMe. This is probably due to the

slowing down on the growth along the long axis of the needle. The fast unstable growth observed in ethanol probably caused many of the imperfections; hence the slowing down of the growth along this axis appears to have created higher quality and more facetted crystals.

Figure 8-11 shows that the crystals formed from the mixed solvation environment were found to be opaque, while crystals from pure ethanol were found to be transparent.

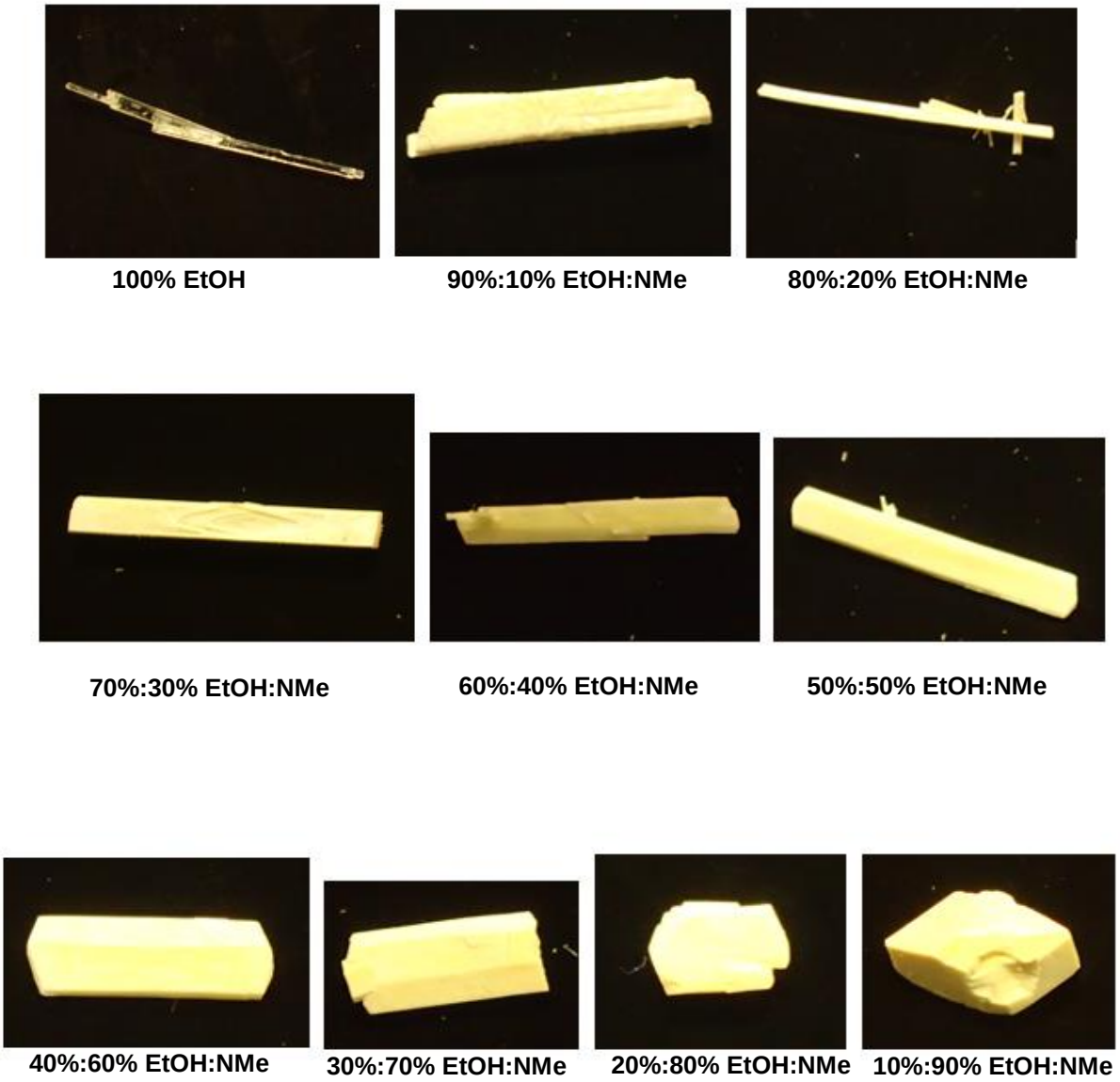


**Figure 8-11: Examples of crystals formed from pure ethanol up to pure nitromethane in 10% by weight steps**

The crystals formed from solvation environments containing any NMe were observed to be opaque, compared to the transparent crystals obtained from pure ethanol. This suggests that the crystals obtained here are polycrystalline. However, the shape of these crystals still becomes more isotropic, suggesting that the NMe does have an effect on the growth rate along the long axis of the needle.

Interestingly the crystals grown from 90:10 EtOH:NMe mixtures were significantly bigger than the crystals grown from the other mixtures. In order to obtain large single crystals for NEXAFS spectroscopy, crystals were grown from slow solvent evaporation from 90:10 EtOH:NMe mixtures.

**Figure 8-12: α-*p*ABA crystals grown from 90:10 EtOH:NMe solutions by slow solvent evaporation. Crystals took around 3 weeks to appear**

Compared to the crystals formed at 10°C in the shaker, the crystals shown in Figure 8-12 from slow solvent evaporation are far more transparent. In addition to the high quality crystals, there were other less perfect crystals that crystallised, which were used for PXRD analysis. The more transparent nature of these crystals suggests that these are in fact single crystals, compared to the polycrystalline nature of the crystals shown in Figure 8-11.

### 8.4.2 Crystal Growth Rates of α-*p*ABA in the Presence of Nitromethane

The crystal growth rates as a function of supersaturation for the capping and side faces in 95:5 ethanol:nitromethane by weight are shown in Figure 8-13.

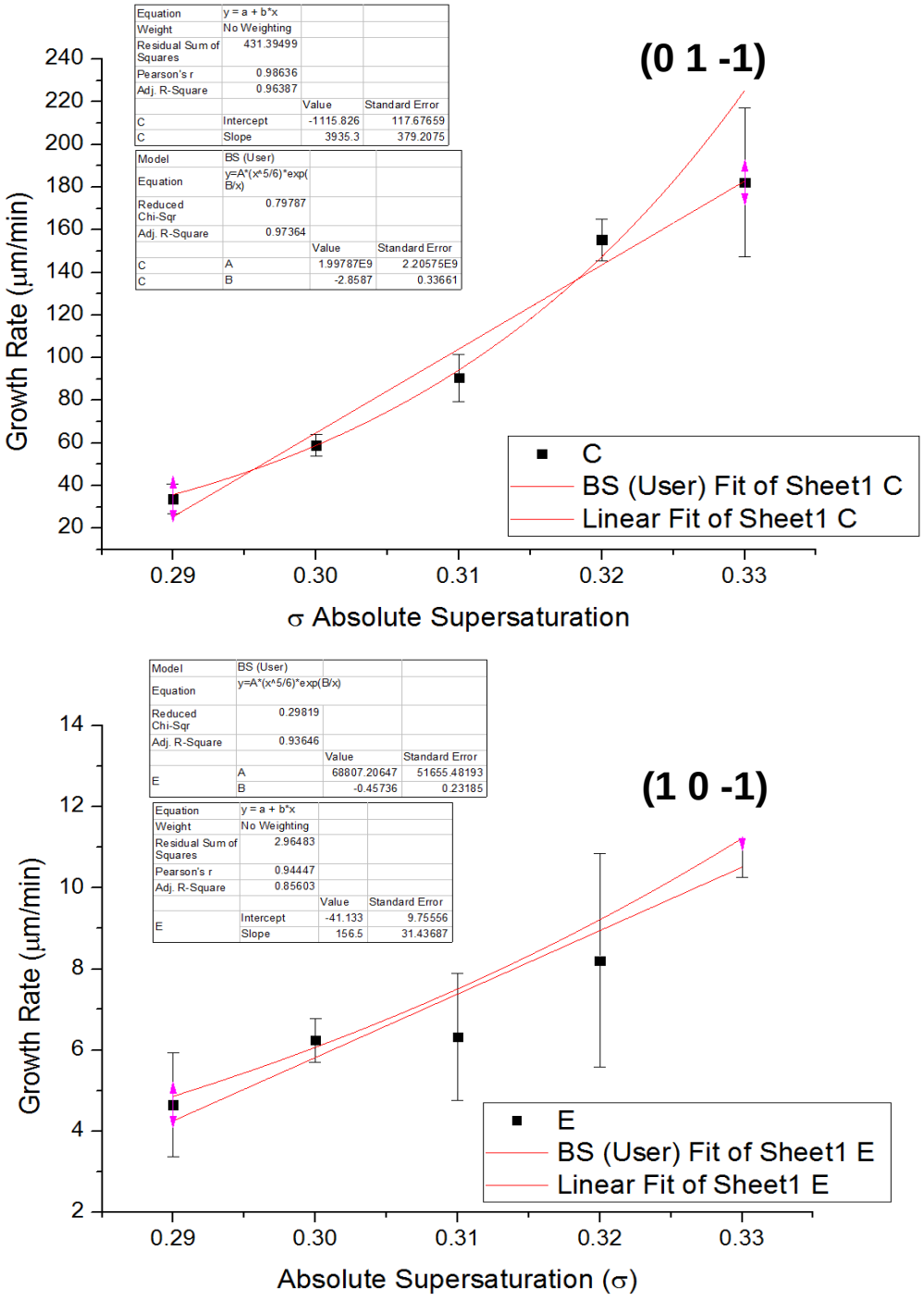


| Equation | y = a + b*x | | |
|---|---|---|---|
| Weight | No Weighting | | |
| Residual Sum of Squares | 431.39499 | | |
| Pearson's r | 0.98636 | | |
| Adj. R-Square | 0.96387 | | |
| | | Value | Standard Error |
| C | Intercept | -1115.826 | 117.67659 |
| C | Slope | 3935.3 | 379.2075 |

| Model | BS (User) | | |
|---|---|---|---|
| Equation | y=A*(x^5/6)*exp(B/x) | | |
| Reduced Chi-Sqr | 0.79787 | | |
| Adj. R-Square | 0.97364 | | |
| | | Value | Standard Error |
| C | A | 1.99787E9 | 2.20575E9 |
| C | B | -2.8587 | 0.33661 |

| Model | BS (User) | | |
|---|---|---|---|
| Equation | y=A*(x^5/6)*exp(B/x) | | |
| Reduced Chi-Sqr | 0.29819 | | |
| Adj. R-Square | 0.93646 | | |
| | | Value | Standard Error |
| E | A | 68807.20647 | 51655.48193 |
| E | B | -0.45736 | 0.23185 |

| Equation | y = a + b*x | | |
|---|---|---|---|
| Weight | No Weighting | | |
| Residual Sum of Squares | 2.96483 | | |
| Pearson's r | 0.94447 | | |
| Adj. R-Square | 0.85603 | | |
| | | Value | Standard Error |
| E | Intercept | -41.133 | 9.75556 |
| E | Slope | 156.5 | 31.43687 |

**Figure 8-13: Growth rate vs supersaturation curves for 95:5 EtOH:NMe mixture. Birth and spread and RIG growth rate vs supersaturation equations fitted to each curve**

Both the (0 1 -1) and (1 0 -1) surfaces growth rate vs supersaturation curves were found to marginally fit best to the birth and spread growth mechanism. This is interesting with respect to the capping (0 1 -1) surface changing growth mechanism upon the addition of a small amount of nitromethane. It has been observed that larger amounts of nitromethane can significantly change the morphology of the crystal by reducing the aspect ratio of the crystal; however it now also appears to show that the growth mechanism is changed upon a small addition of nitromethane. This suggests that the nitromethane stabilises the growth of the capping surfaces, possibly by more strongly binding to the surface and preventing a large build-up of solute at this surface, compared to pure ethanol. It has previously been observed that changing the ratio of mixed toluene:dietheylether environments was found to change the aspect ratio of 2,6-Dihydroxybenzoic acid crystals (2,6-DHB)[182]. The optimal ratio of the solvent mixture was found by recognising which functional groups governed the growth of the capping faces, hence predicting which solvent mixture would be likely to produce crystals of shorter aspect ratios.

In addition, the dead zone for crystal growth was found to be increased for α-*p*ABA in the 95:5 EtOH:NMe mixtures. This probably reflects the positive synergistic solubility effects observed when small amounts of nitromethane are added to ethanol, hence suggesting that this combination of solvent molecules can stabilise the *p*ABA molecules in solution and hence make more stable to remaining in solution rather than incorporating into a crystal surface.

### 8.4.3 Molecular Modelling of Nitromethane on α-*p*ABA

#### 8.4.3.1 Systematic Search of the Carboxylic Acid H-bonding Dimer

Since a previous study had used molecular modelling to identify the solvent mixture that would give desired aspect ratios of 2,6-DHB crystals, through an understanding of the solvent-solute binding at the capping surfaces[182], molecular modelling was used to attempt to understand on a molecular level how NMe affects the growth of α-*p*ABA.

The systematic searching methods described in Section 4.4.4 were employed to probe how NMe probed with the OH...O H-bonding dimer, along with the crystal surfaces of α-pABA.

The OH...O H-bonding dimer is present in both the α-*p*ABA structure and the solvate structure; therefore the binding of nitromethane, water and ethanol was compared using the systematic search.

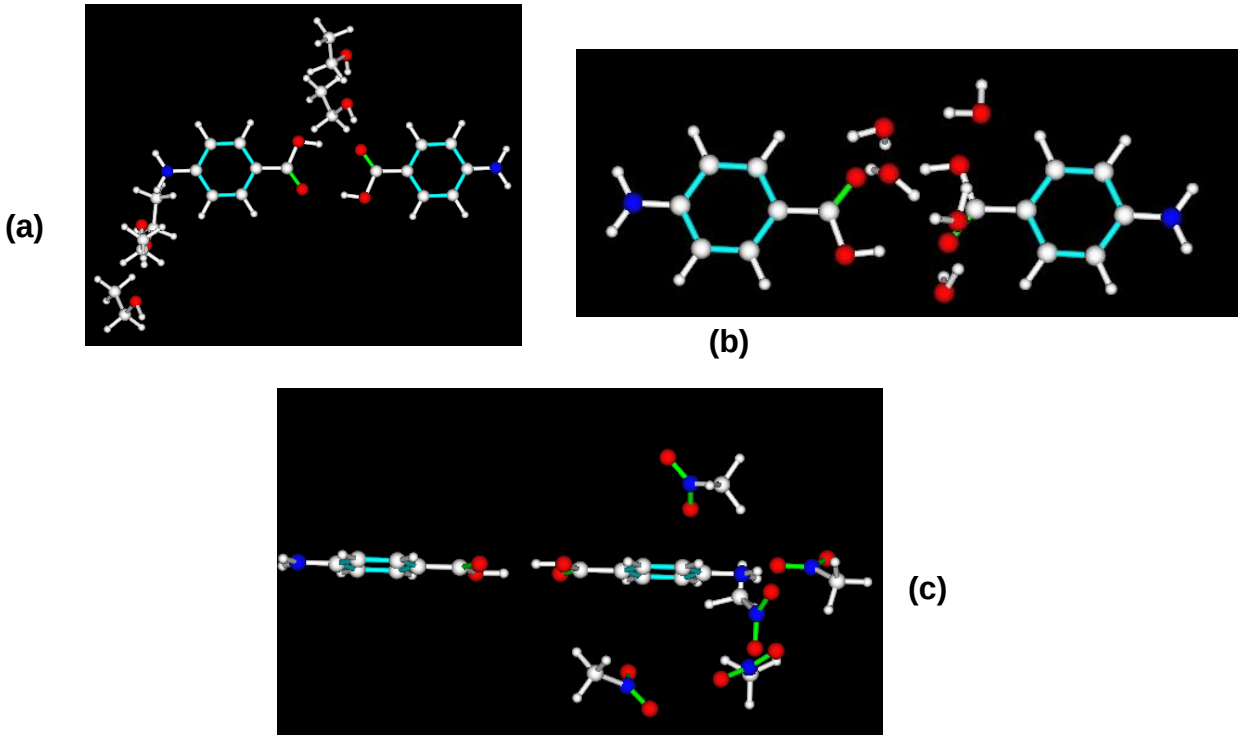


**Figure 8-14: Comparison of the sequential addition of 5 molecules of (a) ethanol, (b) water, (c) nitromethane**

Figure 8-14 showed that the ethanol molecules were found to bind to the COOH and $NH_2$ groups, the water molecules were found to bind to the COOH group and then self-associate and the nitromethane molecules were found to bind to the $NH_2$ group and the phenyl ring. The water molecules clustering around the COOH groups, while the ethanol molecules cluster around both the COOH and $NH_2$ groups, is similar to the behaviour seen in chapter 6 with respect to the systematic searching of these solvent molecules on the single molecule of *p*ABA. This reinforces the postulation the water molecules disturb the OH...O H-bonds and impede the formation of this motif and slow down the kinetic fast self-assembly of α-*p*ABA, hence promoting the thermodynamically more stable β-*p*ABA. In contrast, the ethanol molecules less closely solvate the COOH group and also have more preference to solvate the $NH_2$

group than water, therefore ethanol is probably less likely to hinder the formation of the OH...O H-bonds.

The nitromethane behaviour is more interesting with respect to crystal morphology. Nitromethane was found to solvate the $NH_2$ group and the phenyl ring, hence why the OH...O H-bonds were also found in the solvate structure. Nitomethane was the only molecule tested that was found to have any interaction with the phenyl ring, hence the observed shortening of the long axis of the needle in ethanol:nitromethane solvent mixtures, suggesting that nitromethane hinders the formation of the π-π stacking interactions that dominate growth along the long axis of the needle.

The energetic contributions to the different binding sites are shown in Figure 8-15

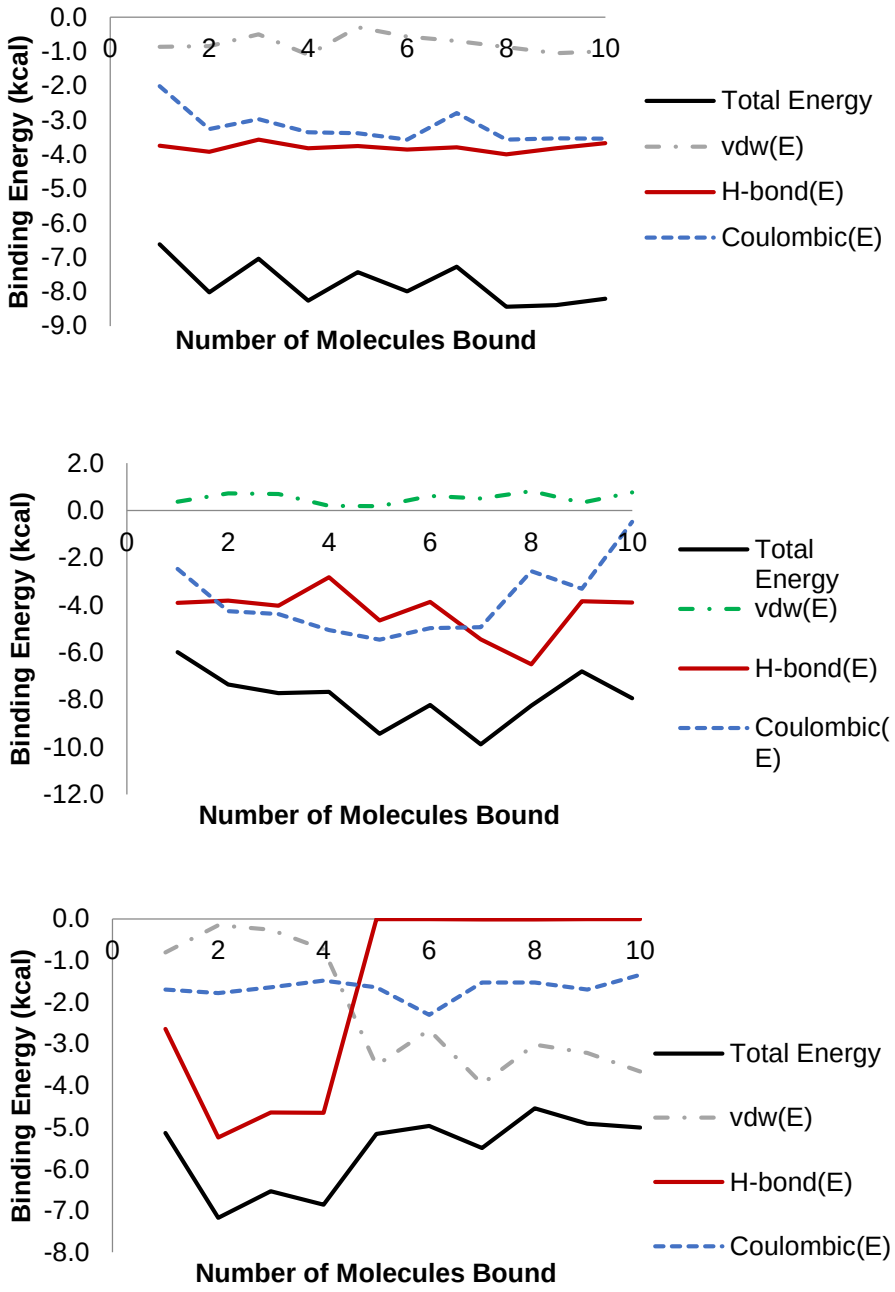


**Figure 8-15: Energetic contributions to the sequential molecular binding calculated by the systematic search for: (a) ethanol; (b) water; (c) nitromethane. Binding energy quoted is the energy of the molecule tested (mobile molecule) with the stationary cluster. Methodology is described in Section 4.4.4.1**

Figure 8-15 reveals that the vdW interactions had a relatively small contribution to the binding energy for the ethanol and water molecules. However, after the 5$^{th}$ addition of a nitromethane molecule the vdW contribution to the energy started to strongly increase, indicating the greater interaction with the phenyl ring compared to the ethanol and water molecules.

Since the systematic searching of the carboxylic acid dimer revealed that NMe has some vdW contribution when interacting with the *p*ABA molecules, the systematic searching of NMe was repeated at the crystal surfaces of α-*p*ABA using the methods described in Section 4.4.4.2.

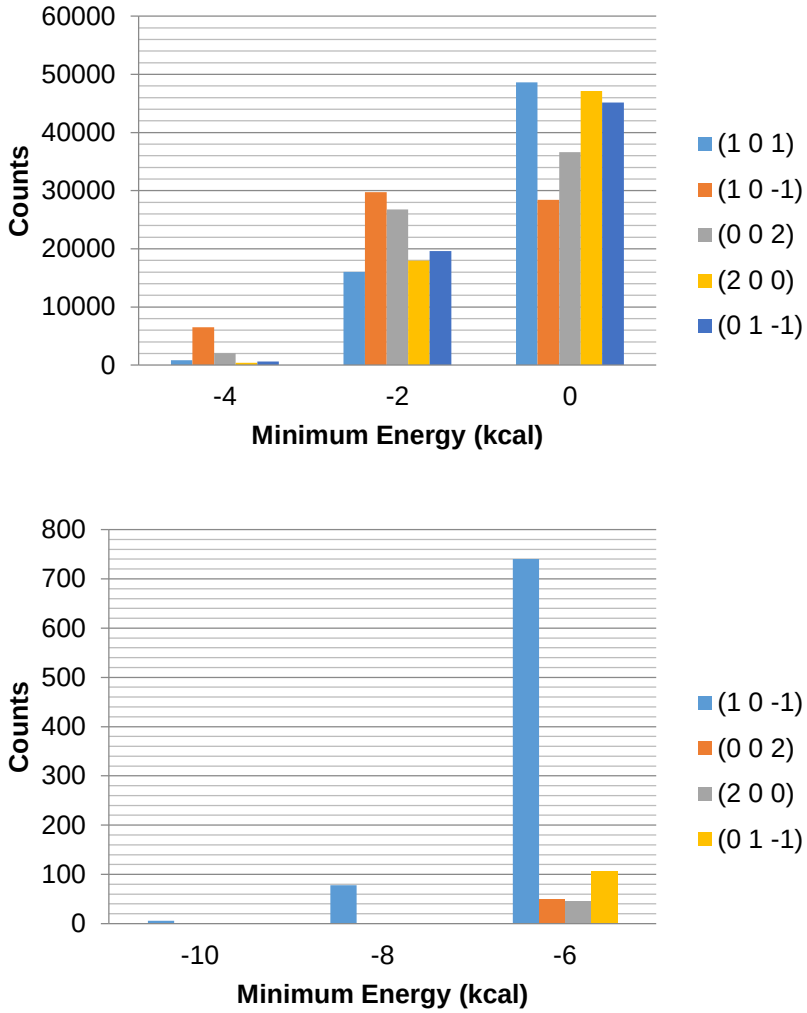


**Figure 8-16: Histogram of the amount of sites with certain energies found from the systematic search of a molecule of ethanol with the morphologically important surfaces of α-*p*ABA found from the systematic search (4.4.4.2). Energy ranges in 2kcal bins. (a) 0-6 kcal; (b) -4 to -10 kcal.**

Figure 8-16 suggests that the nitromethane molecule does not interact anymore strongly with the (0 1 -1) surface of α-*p*ABA than ethanol or even water (chapter 7). However, it is interesting to compare the most favoured orientation of the probe molecule found for these surfaces (Figure 8-17).

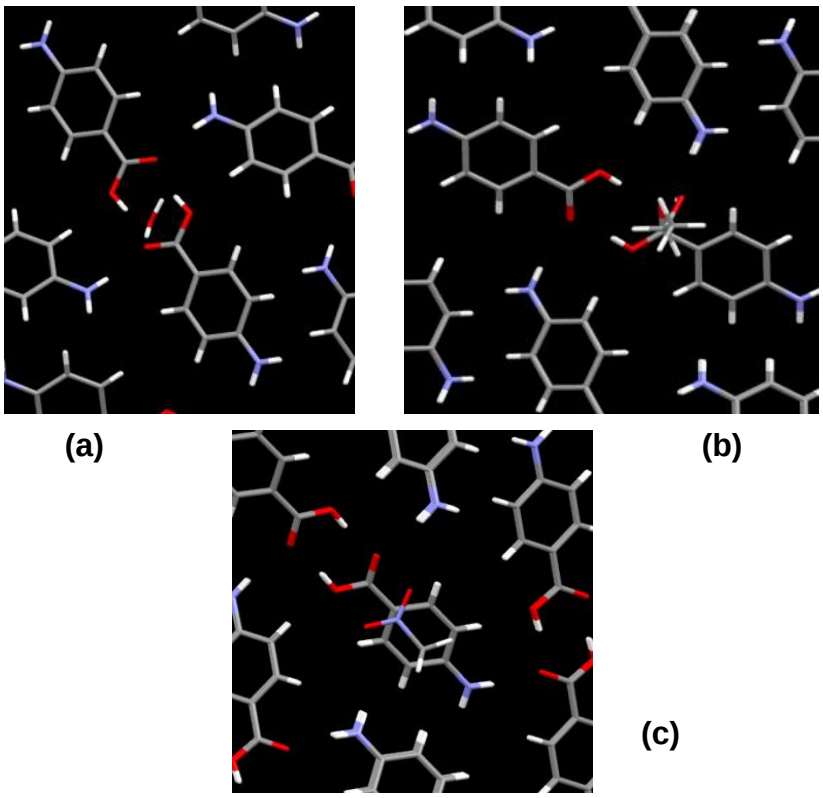


**Figure 8-17: Most favoured orientation for a probe molecule of (a) water; (b) ethanol; (c) nitromethane at the α-*p*ABA (0 1 -1) capping surface**

In Figure 8-17, the water and ethanol molecules were found to preferentially bind to the carboxylic acid groups and lie in a more upright position, especially the ethanol molecule. In contrast, the nitromethane molecule was found to lie flat at the surface on top of the phenyl ring structures. Since at the capping surface of α-*p*ABA, the *p*ABA molecules integrate into the surface by forming π-π stacking interactions between the phenyl ring structures, this preference of the nitromethane molecule to orientate in this way and interact with the ring could inhibit the formation of these π-π stacking interactions and slow down the growth of the capping face.

Though Figure 8-6 revealed that the nitromethane molecule appeared to interact most closely with the amino group of *p*ABA in the solvate structure, Figure 8-18 reveals that the nitromethane molecule also sits between the ring structures of stacked molecules of *p*ABA.

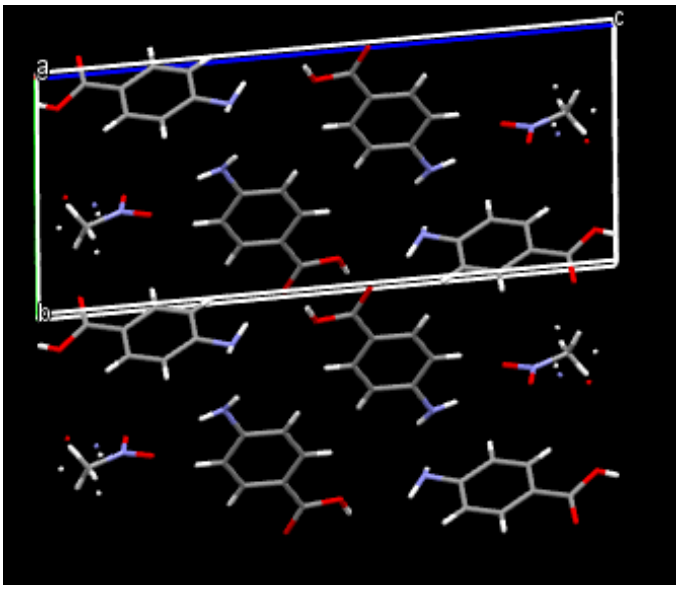


**Figure 8-18: NMe *p*ABA solvate structure viewed down the b-axis showing how the NMe molecule sits between the phenyl rings of *p*ABA**

Though the nitromethane molecule was not found to sit directly on the phenyl rings of *p*ABA, it does sit between the rings of a head to head stack of *p*ABA molecules. This type of head to head stacking interaction is seen in the α-*p*ABA structure and the disruption of this interaction is probably important in slowing down the growth along the long axis of the α-*p*ABA needle. The other stack is a head to tail stack, which is found to have a C to N distance of over 7.5Å (Figure 8-19).

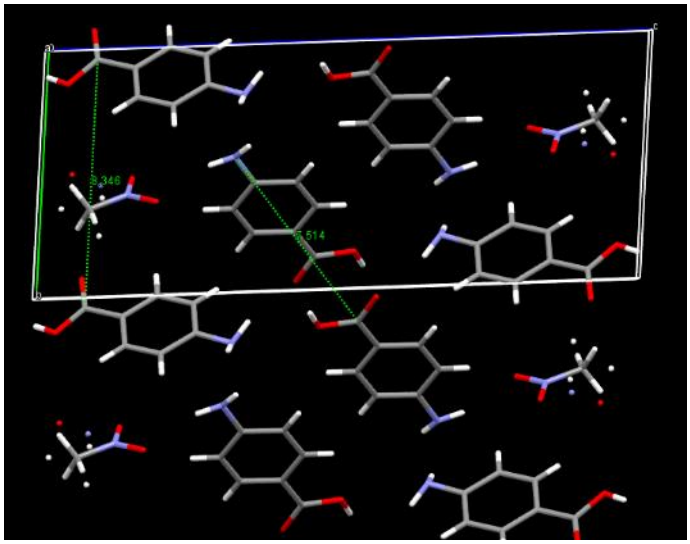

**Figure 8-19: NMe *p*ABA solvate structure showing that there is over 7.5Å between the *p*ABA molecules that have a head to tail stack**

The disruption of the head to head stacking interaction and the large distance between the head to tail stacking interaction probably results in these type of interactions having a reduced influence on the growth and morphology of these crystals.

## 8.5 Control of Crystal Morphology

Needle-like morphologies have previously shown to be challenging to predict and control, along with the problems they can cause in downstream processing[24, 181, 182]. This study has revealed the strong influence that a mixed solvation environment can have on, not only the crystal morphology, but also stabilising the crystal growth mechanism. This reinforces Bourne and Davey's work that suggests that the crystal growth mechanisms are solvent dependent. Since the nitromethane appears to disturb the stacking of molecules along the long axis of the needle, this also draws parallels to McCardle's conclusion that it is may be easier for the molecules to form these π-π stacking interactions between phenyl rings, hence facilitating fast growth[183, 184]. In chapter 6 there was a link between the area of molecule interacting and the favourability of the synthon forming, which seems to be relevant in the case of α-*p*ABA. The π-π stacking interactions do not contribute to the growth of any of the other major surfaces, therefore the influence of these interactions must draw molecules more quickly from solution and into the crystal surface than the other major faces. Hence, the capping face of α-*p*ABA has a large area of phenyl rings available to interact,

therefore the majority of the surface is open for interaction, whereas at the H-bonding (1 0 -1) surface only the specific H-bonding sites are available for interaction resulting in a smaller available area for molecules to dock onto from solution.

Crystal morphology control can be predicted and exerted using crystal growth modifying additives[134, 180, 230, 236]. However, this method of predicting a solvent environment from which the more ideal morphology may grow could be a relatively in expensive method for controlling crystal morphologies. A study into what needle like crystals have non-needle like solvates could be of interest, and as to whether a mixed solvation environment could produce a similar morphological change.

## 8.6 Conclusions

Chapter 8 revealed the crystal growth mechanisms of the side and capping faces of α-*p*ABA in ethanol and 95:5 ethanol:nitromethane mix. In addition, the effect of nitromethane on the crystal morphology of α-*p*ABA was understood by relating it to how nitromethane interacted with small clusters and the crystal surfaces of α-*p*ABA.

**Table 8-3: Major issues and outcomes arising from chapter 8**

| **Question/Problem** | **Answers Identified from this Study** | **Relevance to the study** |
|---|---|---|
| What are the growth mechanisms of the capping and side faces of α-*p*ABA in ethanol | • Growth rate of the capping faces increases linearly with supersaturation in ethanol, therefore RIG mechanism.<br>• Side face grows by a birth and spread mechanism | Roughening along the long axis of the needle results in the growth kinetics having a strong impact on crystal morphology. Probably the reason that the attachment energy morphology does not match crystals grown from ethanol |
| How does nitromethane affect the growth and morphology of α-*p*ABA? | • Addition of nitromethane shortens the aspect ratio of α-*p*ABA<br>• The longer the crystallisation time, the less solvate is formed in the sample<br>• Growth kinetics in 95:5 EtOH:NMe suggest that the growth | The morphology produced from EtOH:NMe mixtures more closely resembles the attachment energy prediction and is a more desirable morphology from an industrial perspective. The increase in α-*p*ABA over the solvate in the sample with increasing |

| | | |
|---|---|---|
| | mechanism along the long axis of the needle is becoming more birth and spread like | crystallisation time, regardless of NMe content, suggests that the solvate is strongly metastable |
| How does the binding of NMe to *p*ABA rationalise these changes in growth and morphology? | • NMe was calculated to prefer to bind more to the phenyl ring than ethanol or water<br>• Solvate crystal structure shows that the NMe molecules push the π-π stacks further apart | NMe appears to disrupt the π-π stacking interaction more than ethanol or water. Hence, this probably disrupts the solid-on-solid surface integration and slows down the growth rate of the capping faces, hence resulting in a more isotropic equilibrium like morphology |

The capping face of α-*p*ABA was found to grow by a rough interfacial growth mechanism in ethanol, while the side faces were found to grow by a birth and spread mechanism. The π-π stacking interactions identified as dominating the growth of the (0 1 -1) surface in chapter 7 probably facilitates a 'solid on solid' integration mechanism at this surface[175]. This is probably promoted by several properties of the α-*p*ABA structure, such as the larger area of available interaction in the π-π stacking synthons identified in chapter 5 that could facilitate increased ease of integration into the capping surface than the side surface. This is in addition to the calculated decreased affinity for the (0 1 -1) face than the (1 0 -1) face exhibited by ethanol molecules from the systematic search, hence the ethanol molecules would probably hinder the (1 0 -1) more than the (0 1 -1) surface.

The position of the nitromethane in the solvate structure was found to push the π-π stacking interactions further apart. The molecular modelling also showed that

nitromethane has stronger vdW interactions with the *p*ABA molecule than ethanol or water, whereby it interacts more strongly with the phenyl ring. This increased interaction with the phenyl ring probably hinders the π-π stacking interactions that result in the fast growth along the long axis of the needle, hence changing the morphology to a more equidimensional shape.

Although the geometry of the most favoured binding point on the (0 1 -1) surface (Figure 8-17) indicates that NMe would more favourably interact with the exposed phenyl rings at this surface, the distribution of energies from all the binding sites shown in Figure 8-16 does not conclusively indicate that the NMe molecule would preferentially bind to the (0 1 -1) surface over the other surfaces. It may be that molecular dynamics calculations that can account for the molecular motion at the surface may reveal more accurately whether NMe has a particular affinity for the crystal surface. However, it may just be the capability of the NMe molecule to disrupt the π-π stacking interactions more effectively than the other solvents which slows the growth of the capping face and changes the crystal morphology.

This chapter revealed how in depth knowledge of the bulk and surface synthons can result in the design of a solvation environment that produces a desired morphology, by utilising solvent molecules that hinder the synthons that promote the fastest growing surface. This procedure is of great interest to practitioners that wish to change the shape of product crystals in order to improve ease of filter or formulation. This chapter has mostly related to objective 4 but has drawn together some of the work from objectives 2 and 3. This shows how important it is to understand more of the properties of a crystal than just the surface properties, to fully be able to control the growth and morphology.

# Chapter 9 Near Edge X-Ray Absorption Fine Structure Surface Chemistry Characterisation

*This chapter carefully identifies the orientation of the molecules at the major crystal surfaces of α-pABA utilising polarisation dependent NEXAFS spectroscopy. Bulk and surface sensitive data is compared*

## 9.1 Introduction

The molecular surface chemistry can govern crystal morphology, face-specific growth rates and dissolution. The molecular orientation at the surface of crystalline materials is often assumed to be the same as if the crystal structure was terminated in that crystallographic direction. The surface specific molecular orientation can be significantly anisotropic, in-turn the crystal growth and dissolution rates can vary accordingly. It can therefore be imperative to determine, rather than assume, the molecular geometry at organic single crystal surfaces from low symmetry structures. Therefore this chapter aimed to collect surface sensitive near edge X-ray absorption fine structure data to reveal the surface molecular orientation at the morphologically important surfaces of α-*p*ABA, with respect to the predicted orientation, along with the structural homogeneity of a crystal surface.

The bulk fluorescence yield (FY) and surface sensitive partial electron yield (PEY) NEXAFS measurements provided crystallographic mapping of the orbitals associated with carbon, nitrogen and oxygen atoms, from which the molecular orientation within the bulk of the structure and at the crystal surfaces could be inferred. In addition, the nitrogen edge data was used to elucidate the intramolecular geometry of the $NH_2$ group, which had previously been of some debate.

State of the art NEXAFS imaging experiments provided data regarding the structural homogeneity of the (1 0 1) surface of α-*p*ABA. It was determined to whether the specific local geometry changes across a supposedly periodic crystal surface.

Since a lot of surface based molecular modelling is derived from termination of a crystal structure, it is important to be able to more accurately determine the molecular orientation at the crystal surface compared to the bulk. The data and conclusions drawn in this chapter further the knowledge of the molecular geometry at the crystal surfaces of α-*p*ABA and underpins the completion of objective 5. The work flow of this chapter is shown in Figure 9-1.

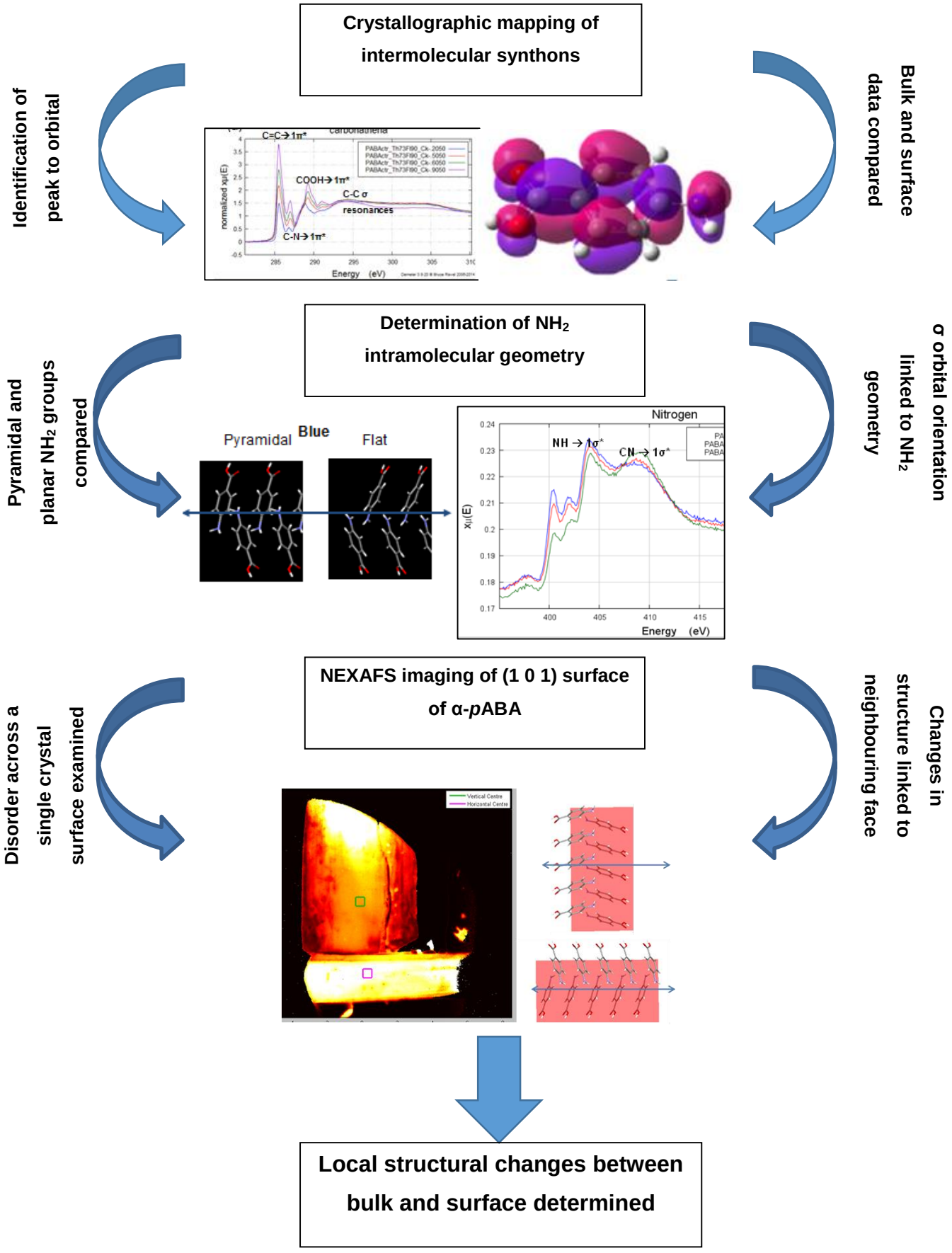


**Figure 9-1: Work flow associated with Chapter 9**

## 9.2 Crystallographic Mapping of the Intermolecular Synthons

The measurements taken in this chapter are on crystals grown from EtOH:NMe solutions (methodology Section 4.3.3.1).

### 9.2.1 (1 0 1) Surface

The large (1 0 1) surface was carefully examined by rotating a large single crystal of α-*p*ABA about three axes (Figure 9-2). Data collected in this section is all at a bias voltage of -50v, so the PEY data represents the molecular orientation at the surface through to about 10nm into the sample.

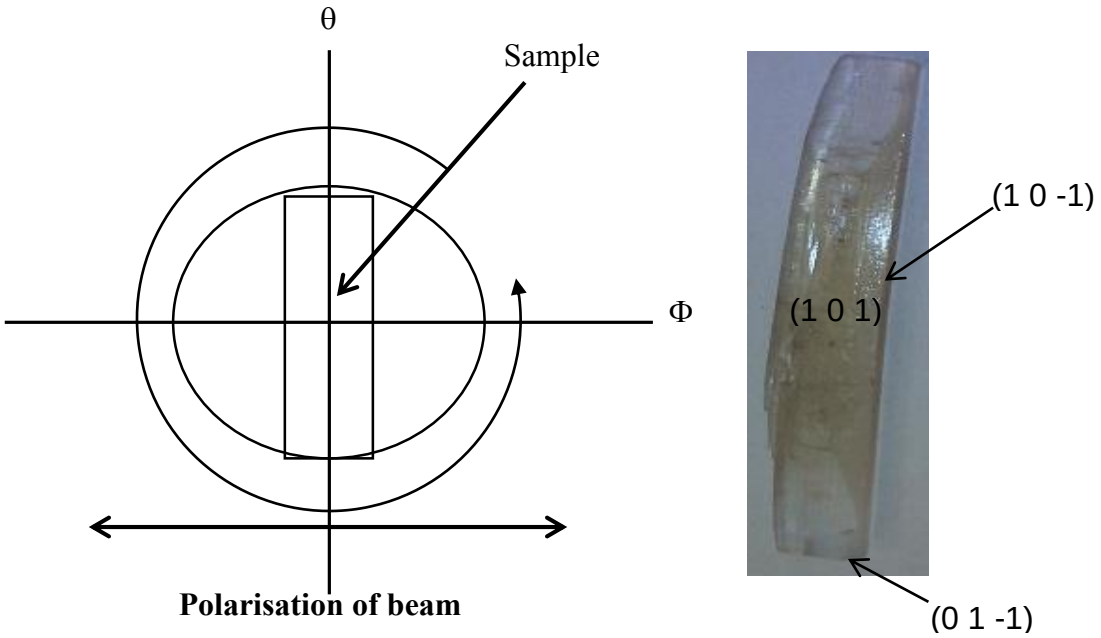


**Figure 9-2: (left) Schematic of 3-axes goniometer with mounted sample indicating the rotation of the sample available. (Right) Single crystal that was mounted for the goniometric NEXAFS spectroscopic measurements**

The beam was aligned approximately at the centre of the (1 0 1) crystal surface and the crystal was rotated initially about the in-plane azimuthal angle and measurements were taken at the C, N and O K-edge Figure 9-2.

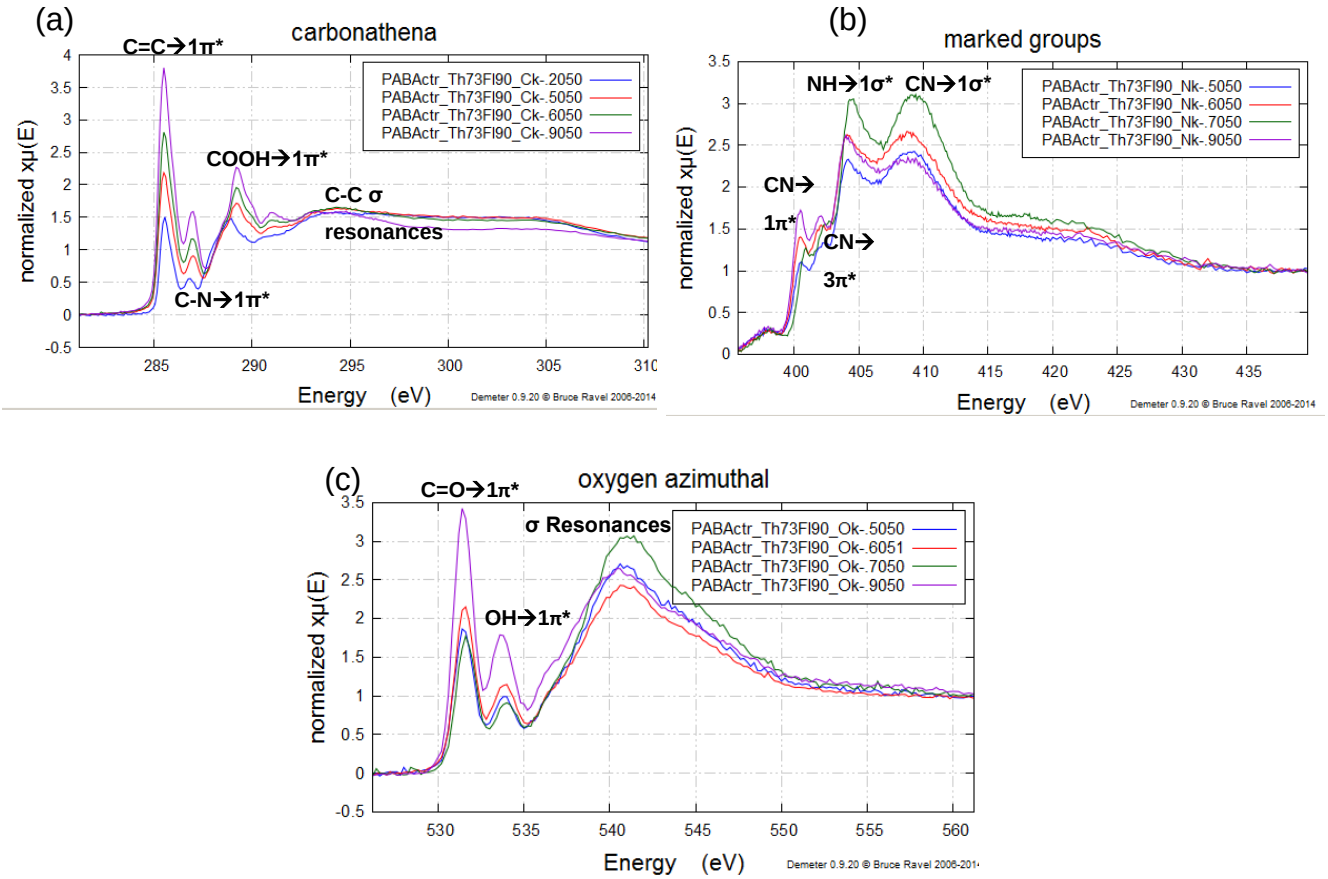


**Figure 9-3: NEXAFS spectra as a function of azimuthal scan from horizontal (purple) to close to vertical (blue) for the (a) carbon k-edge at the large (1 0 1) surface of the crystal shown in Figure 9-2; (b) nitrogen k-edge and (c) oxygen k-edge. Peaks marked with the bonding orbital the electrons are being excited from.**

The labelling of the peaks within each spectra are taken from the publication by Stevens et al[8]. These results can be compared to the crystal structure and the ground state molecular orbitals[8].

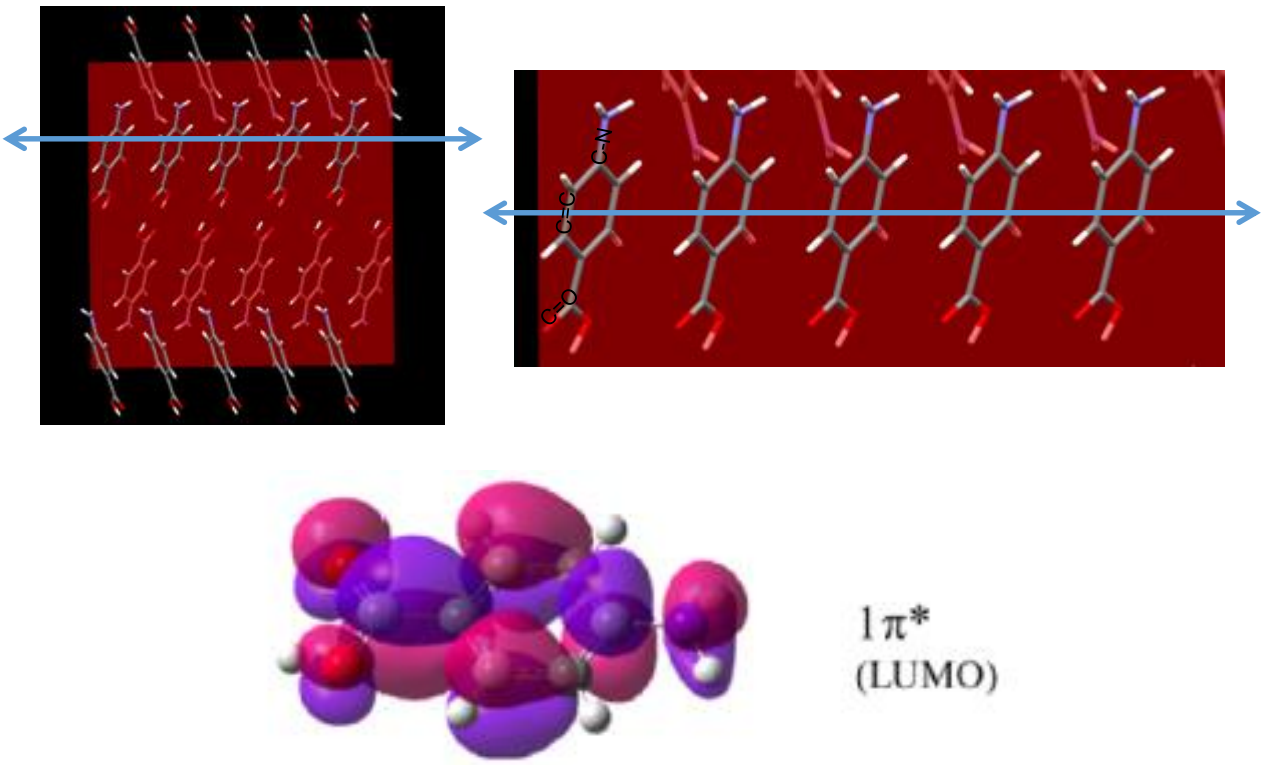


**Figure 9-4: Molecular orientation of molecules at the (1 0 1) surface of α-*p*ABA when orientated horizontal as predicted by the AMBNAC01 crystal structure. Blue line represents the polarisation vector of the beam. Below, visualisation of ground state 1π* molecular orbitals[8]**

The molecular orbital visualisation shown in Figure 9-4 was taken from the study by Stevens et al on predicting the NEXAFS spectra of α- and β-pABA. This revealed how the 1π* orbitals are above and below the plane of the covalent bonds. Therefore, when the direction of the beam polarisation is perpendicular to the covalent bonds, the transitions from core 1s orbitals into the 1π* will be at their maximum.

Figure 9-4 shows the expected orientation of the molecules at the (1 0 1) surface, when the long axis of the crystal is orientated horizontal with respect to the beam polarisation vector. The spectra measured at this orientation showed enhancement of the resonances associated with the C=C →1π*, C-N → 1π* and COOH → 1π* orbitals at around 285eV, 287eV and 289eV at the C K-edge. In chapter 5, I showed that apart from the pyramidal $NH_2$ group, it is thought that the functional groups are relatively planar with respect to the phenyl ring. Therefore, it would be expected that the π orbitals associated with the C-N bond and the COOH group would be directed in roughly the same direction as the C=C π orbitals. This resulted in the enhanced

intensity for the C-N → 1π* and COOH → 1π* resonances in the C k-edge spectra. This was mirrored in the intensities found for the π resonances in the oxygen and nitrogen spectra. The nitrogen spectra showed enhancement of the N-C → 1π* and N-C → 3π* resonances at around 401eV and 403eV respectively at the horizontal orientation, while the oxygen spectra showed enhancement of the C=O → 1π* and O-H → 1π* resonances at around 532eV and 534eV respectively.

As the crystal was rotated about the in-plane azimuthal angle, the intensity of the π and σ resonances significantly changed, highlighting the anisotropic nature of the α-*p*ABA monoclinic crystal structure. Figure 9-5 shows the predicted orientation of the molecules at the α-*p*ABA (1 0 1) surface.

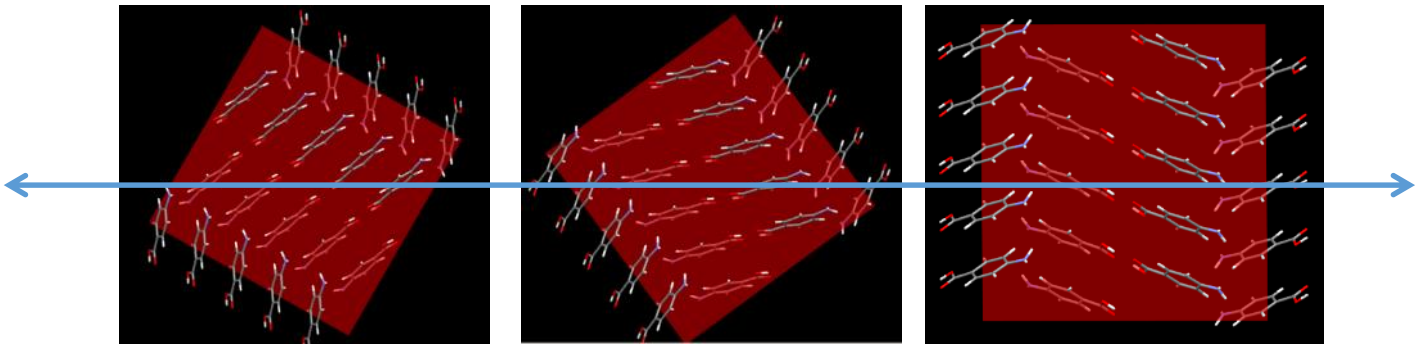

**Figure 9-5: Predicted molecular orientation of the (1 0 1) surface of α-*p*ABA as predicted by the AMBNAC01 crystal structure as the crystal is rotated from horizontal to vertical. Blue arrow represents direction of beam polarisation vector during NEXAFS experiments**

Figure 9-3 revealed that, as the crystal was rotated from horizontal to vertical, the resonances associated with the π-orbitals decreased in intensity, whilst the resonances associated with the σ orbitals increased in intensity for the carbon, nitrogen and oxygen k-edge. The broad peak at around 295eV corresponds to a C-C → 1σ* transition. The σ orbitals are in plane across the bonds of the phenyl ring, therefore Figure 9-5 shows how these orbitals become in-plane with the beam polarisation vector as the crystal is moved closer to vertical. Hence, the enhancement of the σ resonances is due to these bonds being closer to parallel to the electronic vector of the beam.

This mapping of the orbital orientation of these single crystals is useful with respect to determining molecular orientation of poorly crystalline or amorphous materials. This

proof of concept experiment revealed how the spectra associated with anisotropic molecular structures changes significantly upon rotation. If it was not possible to obtain a crystallographic structure then this technique could help, with some knowledge of the molecular structure, to determine the directionality of the molecular orbitals and covalent bonds. Hence, it should be possible to determine the molecular orientation both within the bulk and surface of the structure.

#### 9.2.1.1 Three Dimensional Mapping of the (1 0 1) Surface

The goniometer described in section 4.3.3 and shown in Figure 9-2 allowed rotation about three axes. Hence more than the in-plane orientation described Section 9.1. Hence, the crystal was tilted back about the Φ-axis to explore how the structural changes observed upon rotation in this direction, shown in Figure 9-6.

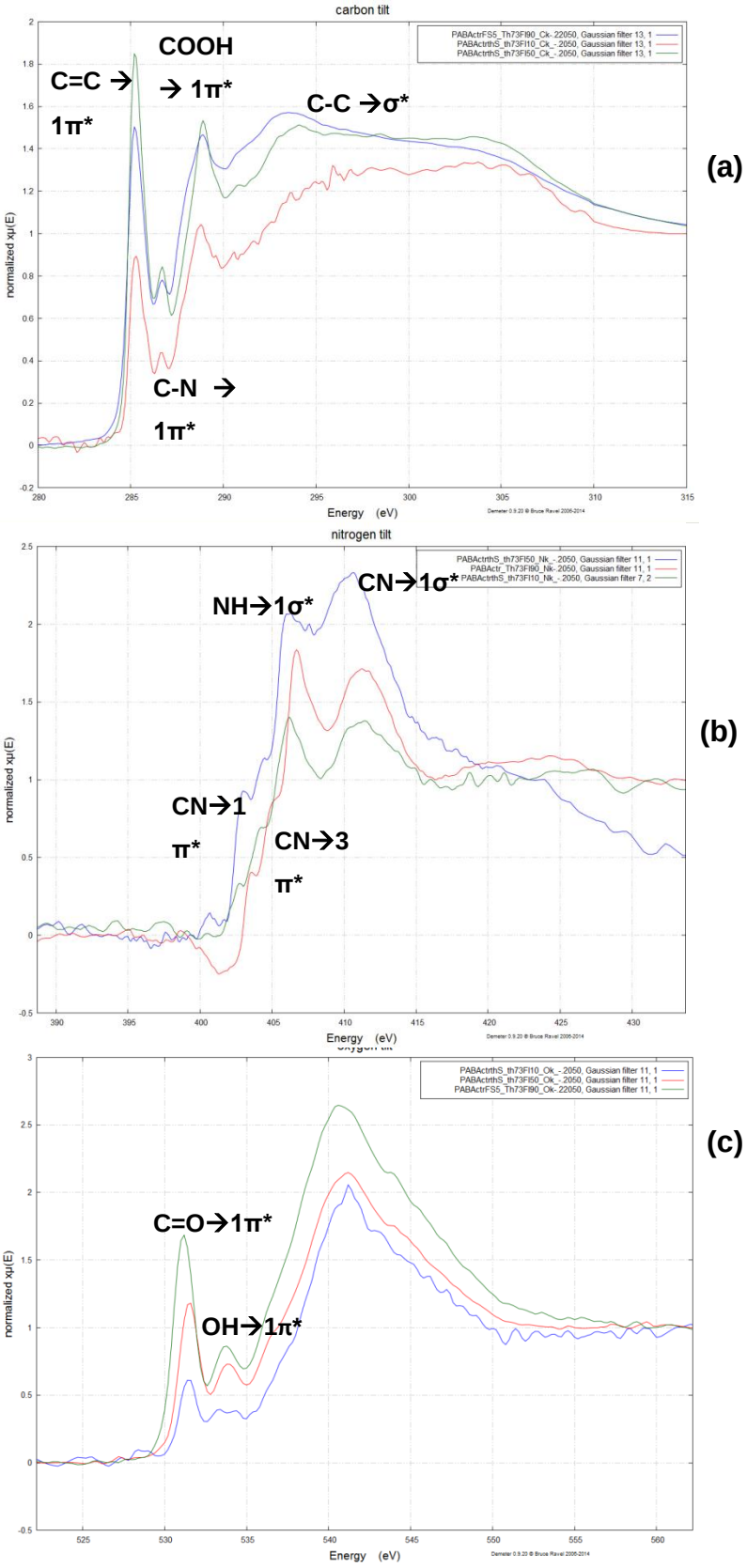


**Figure 9-6: C, N and O k-edge of vertical crystal tilted back from upright to 10° above grazing incidence about the Φ-axis**

The intensity for the grazing incidence spectra drops at each edge, which is expected as the detector picks up fewer electrons emitted. The carbon and nitrogen K-edge spectra show changes in the relative peak heights as a function of tilting, while the relative peak heights associated with the oxygen K-edge stay approximately the same. Figure 9-7 shows the expected molecular orientations for the three different tilt angles.

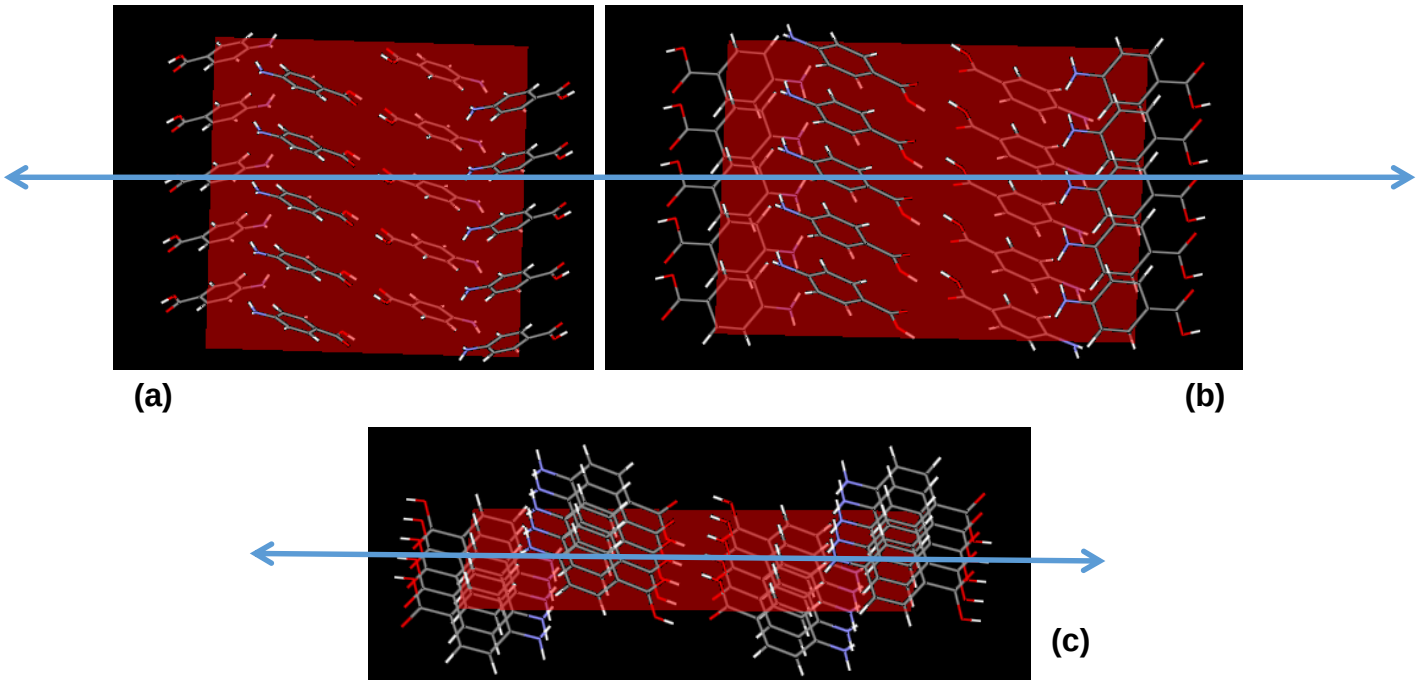


**Figure 9-7: Molecular visualisation from Mercury of the orientation at the (1 0 1) surface of an α-*p*ABA vertically orientated crystal based on the AMBNAC01 crystal structure at (a) upright; (b) 50° tilt backwards about the ϕ axis; (c) 80° tilt back about the ϕ axis. Blue arrow represents beam polarisation vector**

The enhancement of the C=C → 1π* resonance at the 50° tilt is probably due to the beam vector probing through the centre of the phenyl ring structures, more so at this angle than the other two angles Figure 9-7(b)). The vertical crystal and 80° tilt back orientation moves the molecules so that the beam polarisation is directed along, rather than through the phenyl ring. Therefore, the vector would not probe the π cloud above and below the plane of the ring.

## 9.3 Bulk Sensitive vs Surface Sensitive Data

The data presented so far has all been partial electron yield data with a bias voltage of -50V, which is thought to penetrate to around 10nm into the surface. Simultaneously, fluorescence yield data was also collected which comes from much deeper into the sample. Data was compared from both types of detection methods for the (1 0 1), (1 0 -1) and (0 1 -1) surfaces.

### 9.3.1 (1 0 1) Surface

Figure 9-8 shows the comparisons of FY and PEY data measured at the (1 0 1) surface.

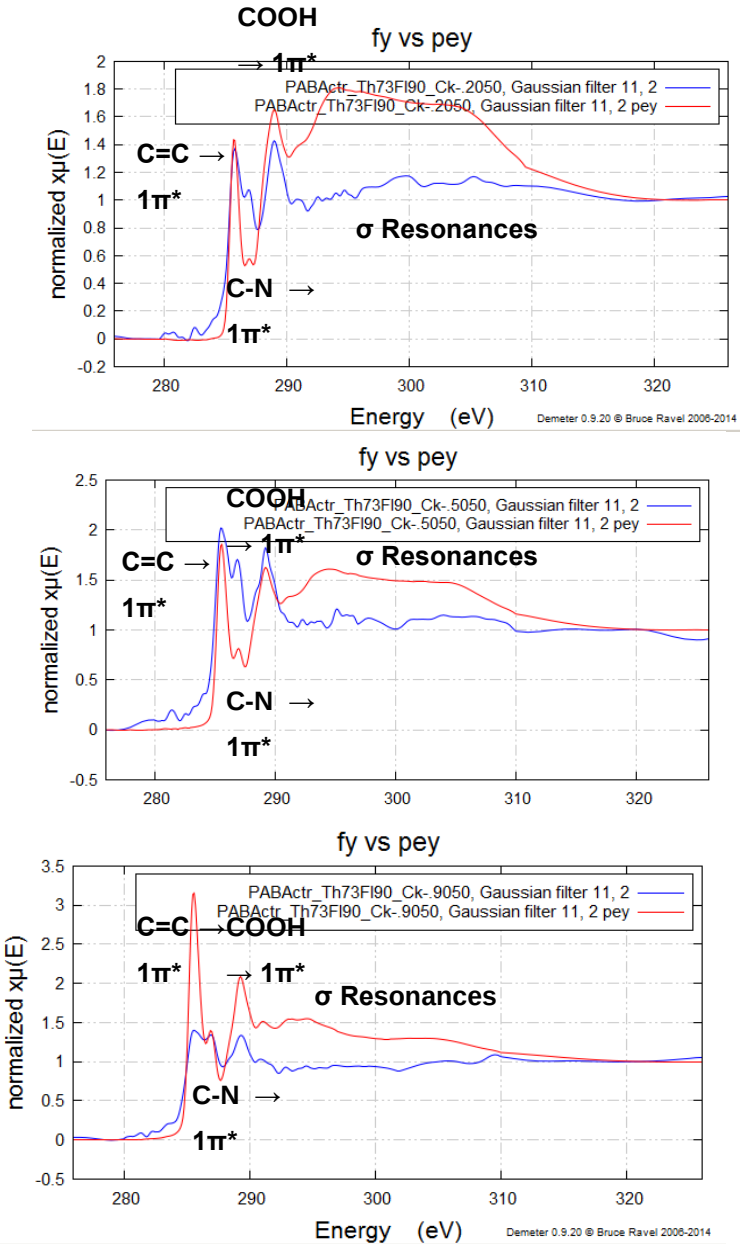


**Figure 9-8: Comparison of fluorescence yield (blue) and electron yield (red) for the carbon k-edge spectra of a flat crystal orientated (a) vertically; (b) 45° rotation about the azimuthal angle; (c) horizontally orientated (1 0 1) surface**

The relative ratios of the C=C → 1π* and C-N → 1π* peaks for both the FY and PEY data in Figure 9-8(a) and Figure 9-8(b) are found to be quite similar. In contrast, the resonances associated with the σ orbitals were found to be significantly suppressed in the FY data. In Figure 9-8c, where it would be expected that the resonances associated with the phenyl ring would be strongest, the C=C → 1π* resonance is strongly suppressed in the FY data. Since for both Figure 9-8(a) and Figure 9-8(b), the relative peak heights for the π resonances in the FY and PEY are found to be similar,

I assume that the orientation of the molecules in the bulk and closer to the surface are the same at the (1 0 1) surface. The suppression of some of the peaks in the FY data could be due to self-absorption of the fluorescence photon that is escaping from deeper into the sample.

### 9.3.2 (1 0 -1) Surface

The (1 0 -1) is predicted to have more reactive H-bonding groups exposed at the crystal surface, compared to the (1 0 1) surface. Since the OH...O H-bonding dimers are directional and strong interactions that are focussed on the COOH group of the molecule, if a COOH group was left without an available *p*ABA molecule to bind to at the next point in the lattice it could be rather unstable. At the termination of growth, it is entirely feasible that there would be 'unsatisfied' COOH groups that may rearrange to a more stable orientation. Figure 9-9 shows how the (1 0 -1) surface of α-*p*ABA is likely to have exposed COOH groups.

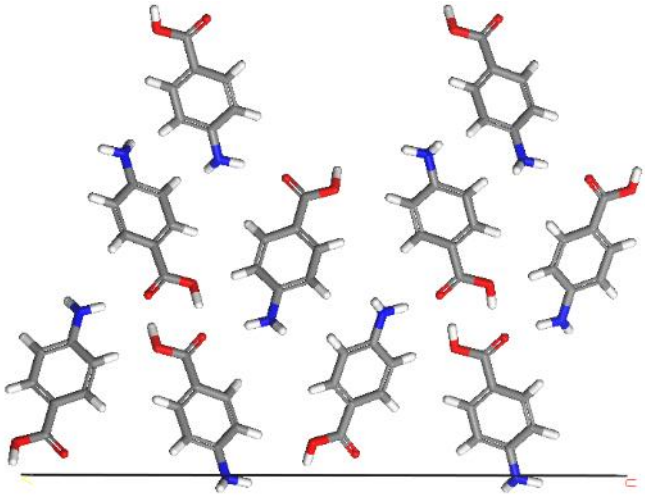

**Figure 9-9: Surface cleave of the (1 0 -1) surface of the α-*p*ABA AMBNAC01 crystal structure using the Materials Studio surface building option. The black line represents the edge of the surface**

The FY and PEY results taken at the (1 0 -1) surface were measured to identify if there were significant changes between the bulk and surface sensitive measurements. Direct evidence for surface re-construction of benzil has previously been observed utilising this technique[237], however there has been no other studies of the surface chemistry of organic crystals using this technique due to the associated difficulties with low vapour pressures of these compounds. X-ray photoelectron spectroscopic techniques have been used to identify the elemental composition at aspirin crystal surfaces[238], this technique lacks the direct measurement of molecular orientation that is provided by NEXAFS.

#### 9.3.2.1 Carbon K-Edge

Figure 9-10 shows the comparison of FY and PEY data collected at the (1 0 -1) surface.

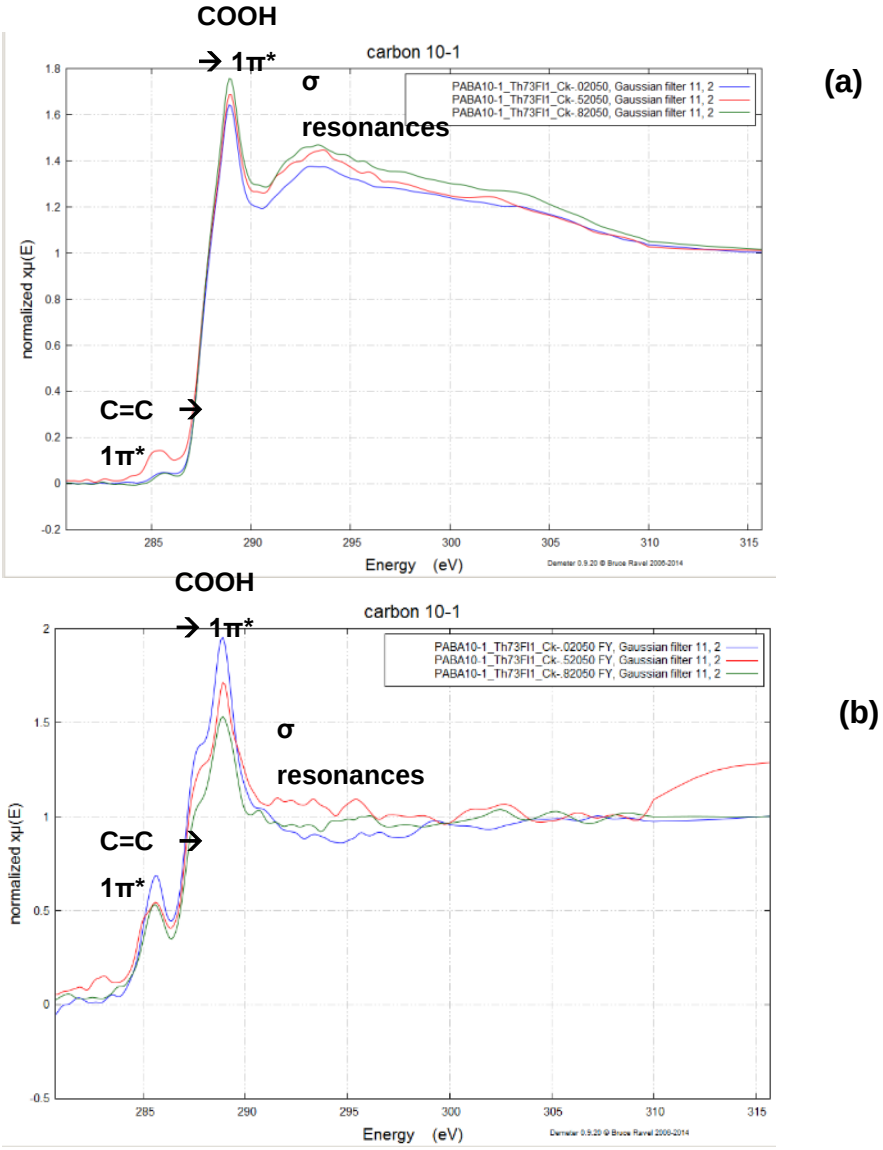


**Figure 9-10: Carbon K-edge spectra for the (1 0 -1) surface of α-*p*ABA for a crystal orientated horizontal (blue), 45° rotation in the azimuthal (red) and vertical (green). Spectra measured in (a) electron yield; (b) fluorescence yield**

Considering the relative peak heights, the spectra of both the PEY and the FY spectra were not found to change as much as may have been expected upon rotation of the (1 0 -1) surface. However, there are significant differences between the FY and TEY spectra at the same orientation. The C=C → 1π* peak is strongly suppressed in the TEY compared to the FY. In addition, there is a shoulder peak at around 287.4eV in the FY spectra that is not observed in the PEY spectra. The molecular orientation predicted by the α-*p*ABA crystal structure is shown in Figure 9-11

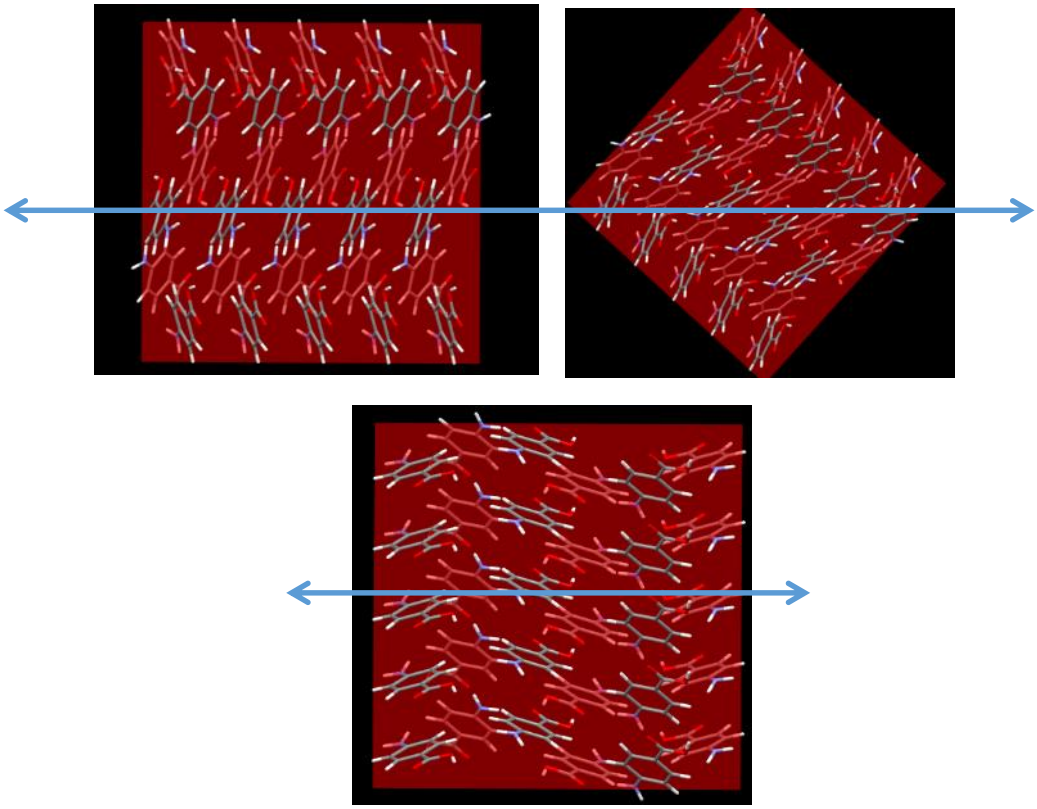

**Figure 9-11: Molecular orientation at the α-*p*ABA (1 0 -1) surface as predicted by the AMBNAC01 crystal structure at (a) horizontal; (b) 45° rotation in the azimuthal angle and (c) vertical. Blue arrow represents direction of beam polarisation**

It would be expected that, when the crystal is horizontal, there would be an intense resonance from the C=C → 1π* orbital, which would decrease upon rotation to vertical. However, this is not the case since the C=C → 1π* resonance was significantly suppressed in the PEY and a more prominent broad peak was found at about 293eV, probably associated with the σ* resonances. These significant differences in spectra suggest that the molecular orientation has changed between the bulk of the sample and the (1 0 -1) surface. The -50V bias voltage being applied to the PEY measurements would suggest that the spectra measured with the PEY method were probably still around 10nm into the sample, yet there appeared to be significant differences compared to the FY measurements. A previous study of FY and PEY measurements of benzil single crystals attributed a suppression of the π* resonances as evidence for surface reconstruction to stabilise unsaturated π-π interactions[127]. In the case of the (1 0 -1) surface of α-*p*ABA, it is thought that this surface is most likely to contain unsaturated H-bonding sites, and that the surface molecules might re-

arrange at the termination of growth to find a more stable orientation. For example, if the molecules were rotated so the ring structures were aligned in-plane at the surface, the C=C → 1π* resonance would be suppressed and rotation about the azimuthal axis would have little effect on the intensity of the peak. Though self-absorption can influence the intensity of the peaks in PEY, the fact that the degree of difference in the peaks between the FY and PEY of the (1 0 1) surface is less than the (1 0 -1) surface suggests that the changes in the peaks are more likely to be, at least in part, due to structural changes between the surface and the bulk.

#### 9.3.2.2 Oxygen K-edge

The oxygen K.-edge was also measured in partial electron yield and fluorescence yield mode at the (1 0 -1) surface shown in Figure 9-12.

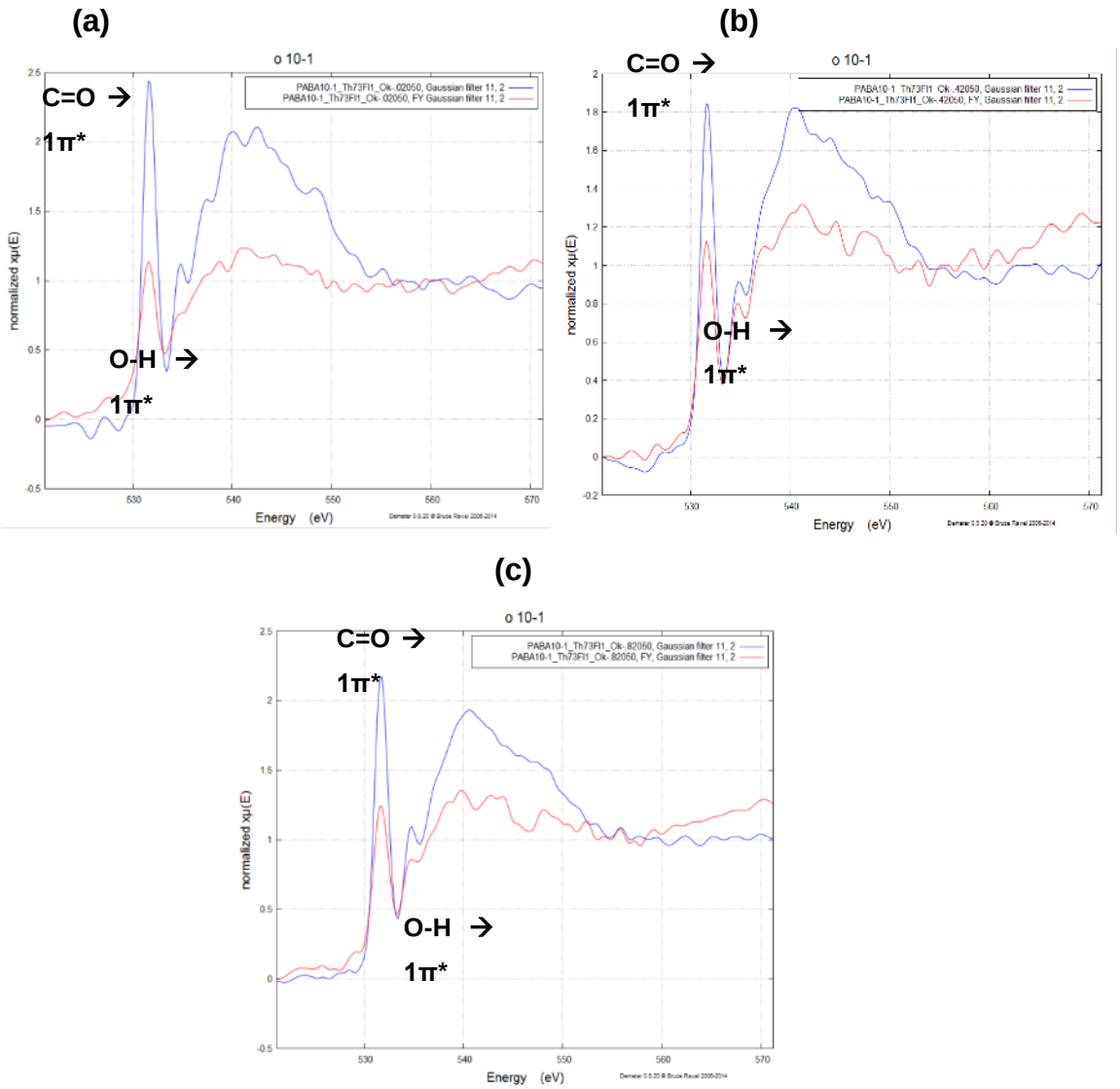


**Figure 9-12: Comparison PEY (blue) and FY (red) data at the oxygen K-edge for the (1 0 -1) surface. Orientation of surface associated with each spectrum is shown in figure 9-11**

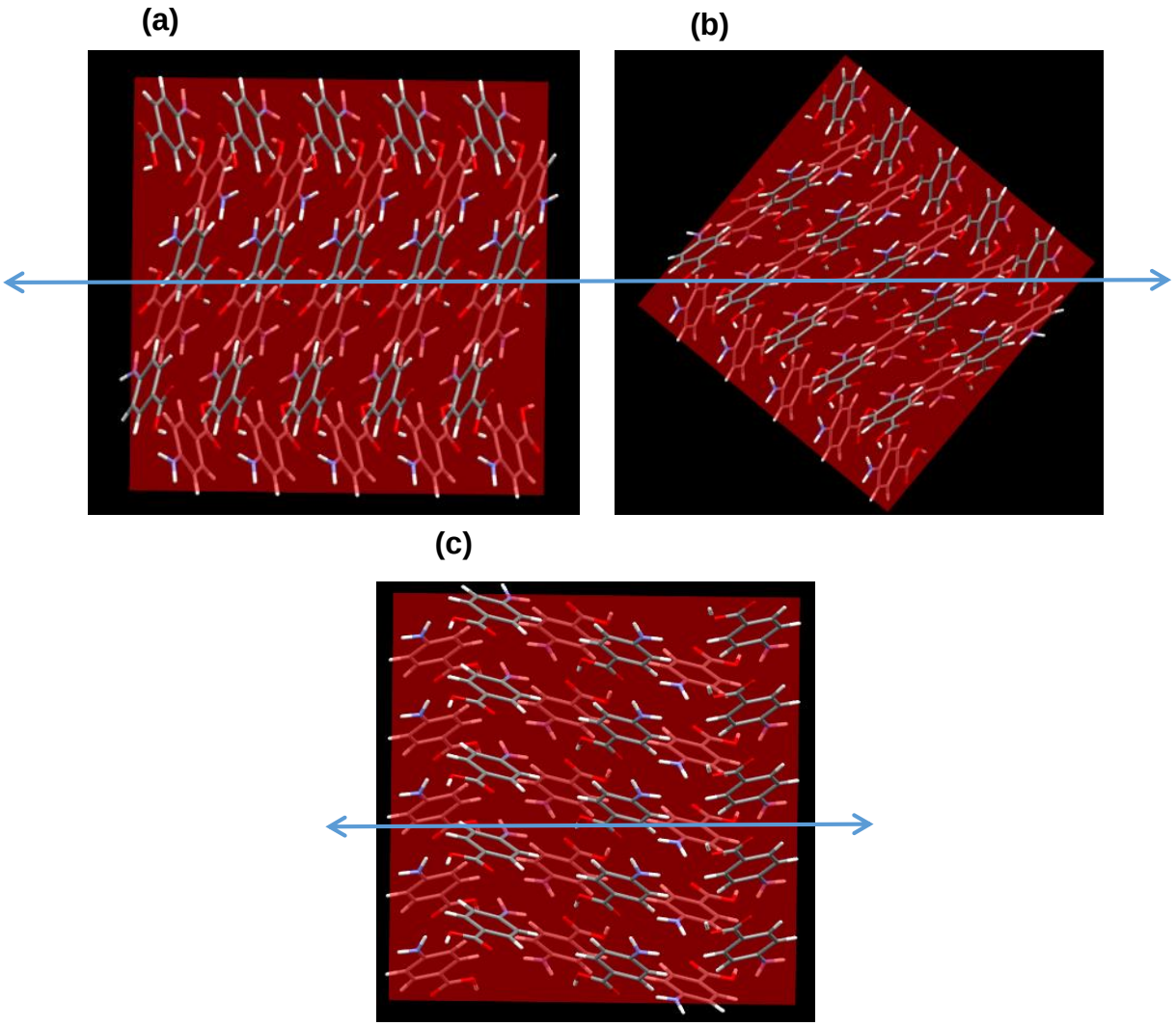


**Figure 9-13: Molecular orientation at the (1 0 -1) surface as predicted by the AMBNAC01 crystal structure. Orientations shown in (a), (b) and (c) correspond to spectra (a), (b) and (c) in Figure 9-12**

Figure 9-12 revealed that the relative peak heights in the oxygen K-edge spectra at the (1 0 -1) surface were found to change relatively little, both as a function of orientation and between the PEY and FY. Since Figure 9-13(a) shows that the out of plane π orbitals would be closer to parallel to the electronic vector of the beam than compared to Figure 9-13(b) and Figure 9-13(c), it may have been expected that the spectrum shown in Figure 9-12(a) would have significantly higher peak intensities for the C=O → 1π* and O-H → 1π* compared to the spectra shown in Figure 9-12(b) and Figure 9-12(c). However, this is not the case in either the FY or the PEY. It may be

that the molecules are somewhat more rotated than is predicted by the crystal structure, or that the COOH group is more torsioned away from the plane of the ring than previously thought, as there appears little difference in the oxygen K-edge spectra at the (1 0 -1) surface as a function of azimuthal rotation.

### 9.3.2.3 (0 1 -1) Surface

The capping surface of the α-pABA crystals are the smallest and hardest to access with the beam. However some data was collected at this surface to determine as to whether having unsaturated π-π interactions at this surface results in a change of orientation of molecules. Only a limited number of rotations could be collected in the azimuthal angle change and much of the data was found to be extremely noisy, therefore only a limited number of spectra could be compared.

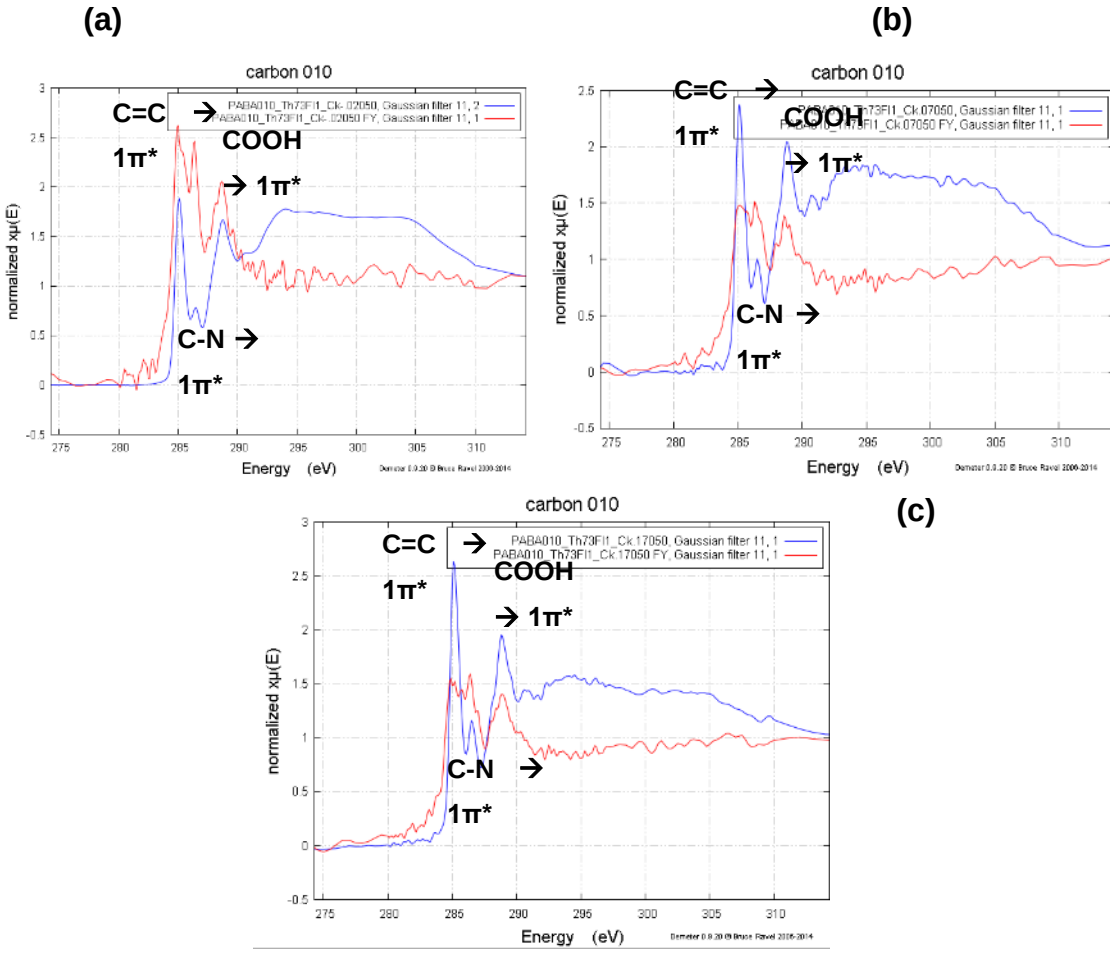


**Figure 9-14: Comparison of the FY (red) and TEY (blue) for carbon K-edge spectra at the (0 1 -1) capping face of α-*p*ABA starting from horizontal (a) and moving 5° clockwise (b) and then a further 10° clockwise (c)**

The σ resonances are found to be significantly reduced in the FY spectra, possibly due to self-absorption effects, as this was found to be a similar case for the (1 0 1) surface. Figure 9-14 shows how the PEY and FY for the (0 1 -1) surface change upon rotation in the azimuthal plane.

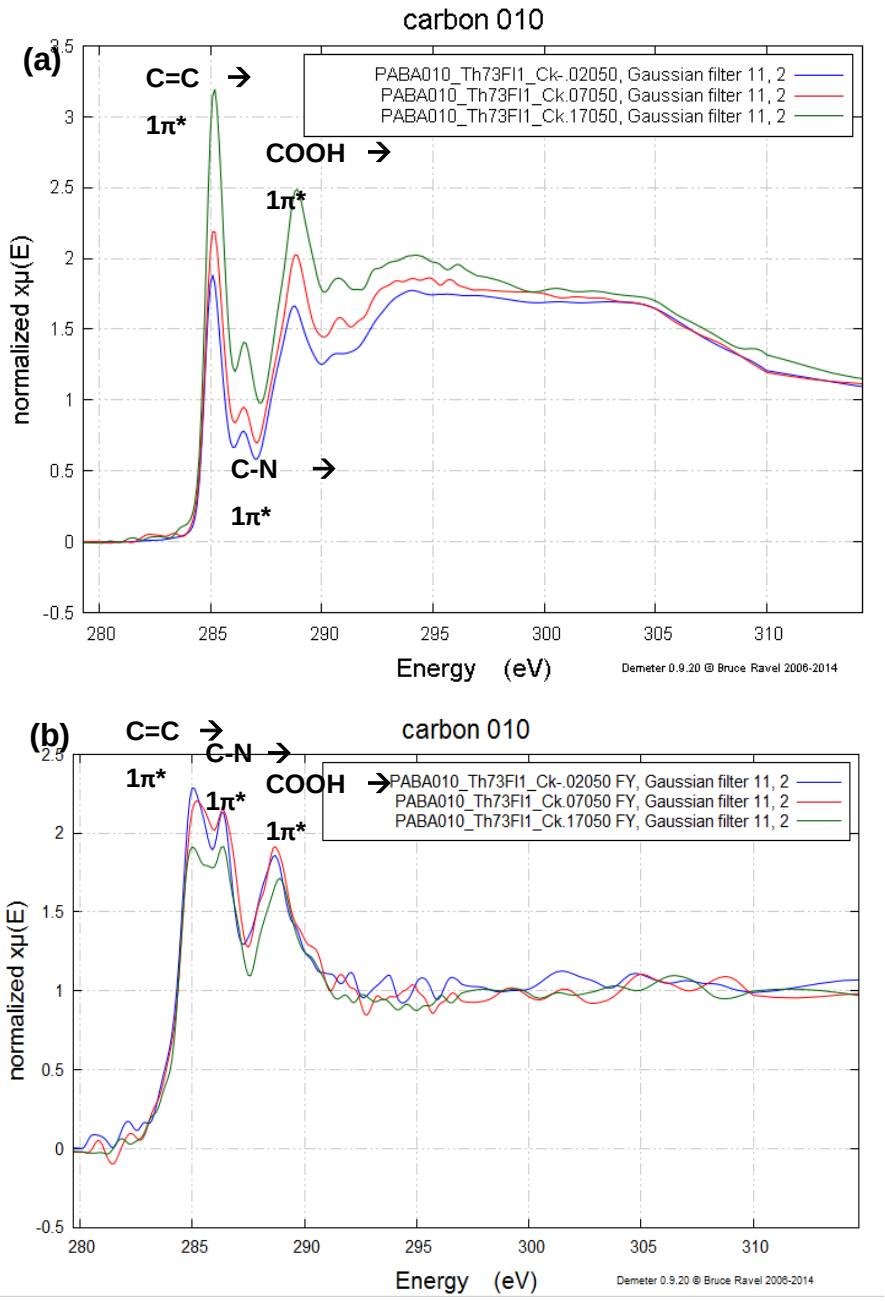


**Figure 9-15: C K-edge spectra for rotation of α-*p*ABA (0 1 -1) capping face in the in plane azimuthal angle for (a) TEY detection and (b) FY detection**

Figure 9-15(a) revealed that the PEY data showed changes in the relative peak sizes of the π and σ resonances as a function of azimuthal rotation, in contrast Figure 9-15(b) revealed that the FY data showed little change in the relative peak sizes between the π and σ resonances as a function of azimuthal rotation. However, it must be noted that the σ resonances in the FY spectra may be subject to suppression due to self-absorption effects. Figure 9-16 shows the molecular structure at the (0 1 -1) surface as it is rotated to the three azimuthal angles shown in Figure 9-15.

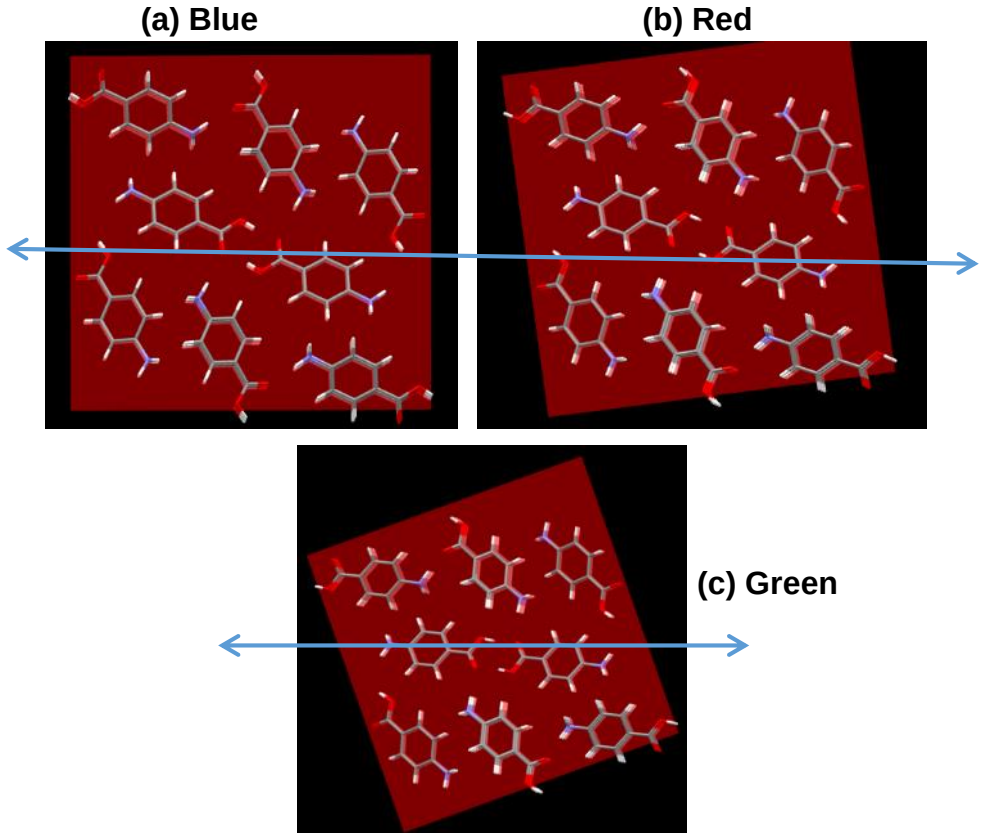


**Figure 9-16: Molecular orientation at the α-*p*ABA (0 1 -1) surface upon rotation in the azimuthal plane. Colours represent the corresponding spectra in Figure 9-15**

The green spectra shown in Figure 9-15(a) was found to have higher intensities for both the σ and π resonances, with the relative strength of the C=C → 1π* resonance being highest compared to the σ* resonances in this spectra compared to the red and blue. The observed increase in the σ* resonances is probably due to the carboxylic acid dimer motif becoming closer to parallel with the beam polarisation vector. However, from Figure 9-16 it is not immediately obvious why there should be an

increase in the π* resonances upon rotation as it appears that the molecules are flat with respect to the beam vector.

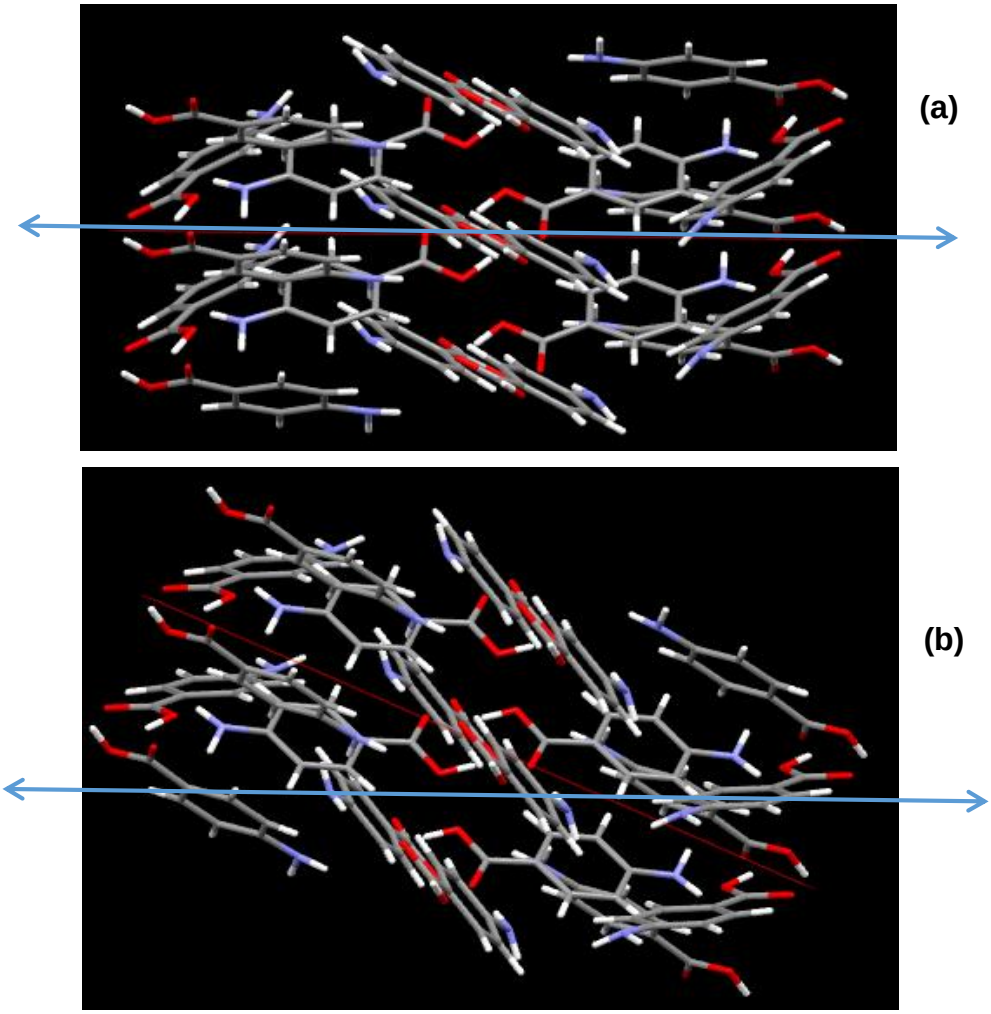


**Figure 9-17: Molecular orientation in the {0 1 -1} direction corresponding the (a) blue spectra and (b) green spectra in Figure 9-15**

Though the beam polarisation is now pointing along the direction of the OH...O carboxylic acid dimers in Figure 9-17(b), it is also now directed through the phenyl rings of the other dimer structure. This results in the out of plane π orbitals associated with the phenyl ring structures being close to parallel to the beam vector, hence the enhancement of the C=C → 1π* resonance that was observed at this orientation.

#### 9.3.2.4 What Could Affect the Surface Structure?

The changes in spectra between the bulk and surface sensitive measurements have been attributed to possible surface relaxation of molecules that do not have all their possible intermolecular interaction sites satisfied. However, it must be considered that the crystals were prepared from ethanol:nitromethane solutions. Section 8.4.1.2 suggested that ethanol could have a propensity to interact strongly with the morphologically important surfaces of α-*p*ABA, due to its H-bonding capabilities. Therefore, any surface sensitive calculations could be affected by any solvent molecules that were incorporated at the surface. Therefore, it would be interesting to attempt these measurements with crystals grown from a number of solvents to see the reproducibility of these results.

## 9.4 Intramolecular Geometry of the Amino Group

The intramolecular geometry of the amino group is of some debate in the literature as there are two published crystal structures, one with a planar $NH_2$ group[188] and one with a more pyramidal $NH_2$ group[191]. The nitrogen K-edge is sensitive to the intramolecular geometry of the amino group and can therefore reveal geometrical information for this group.

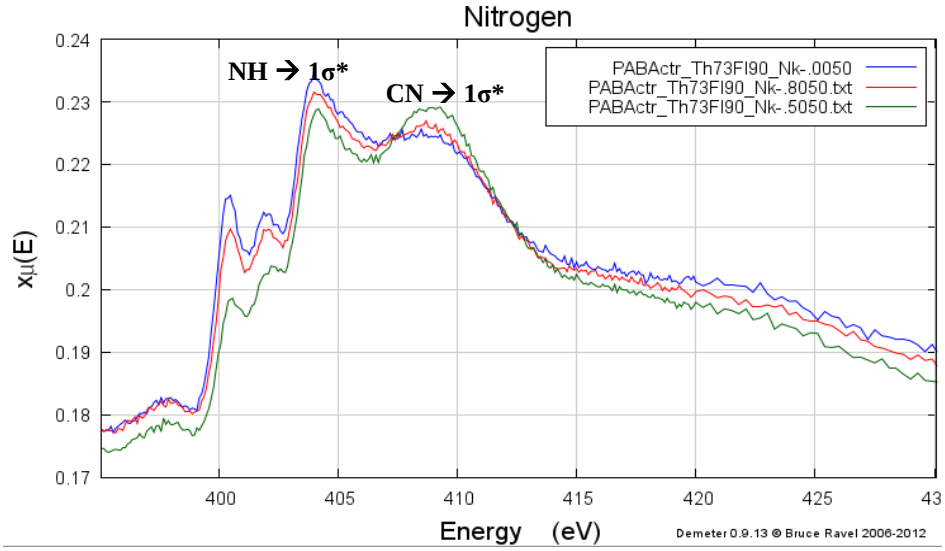


**Figure 9-18: Nitrogen K-edge spectra from azimuthal scan of (1 0 1) α-*p*ABA crystal surface**

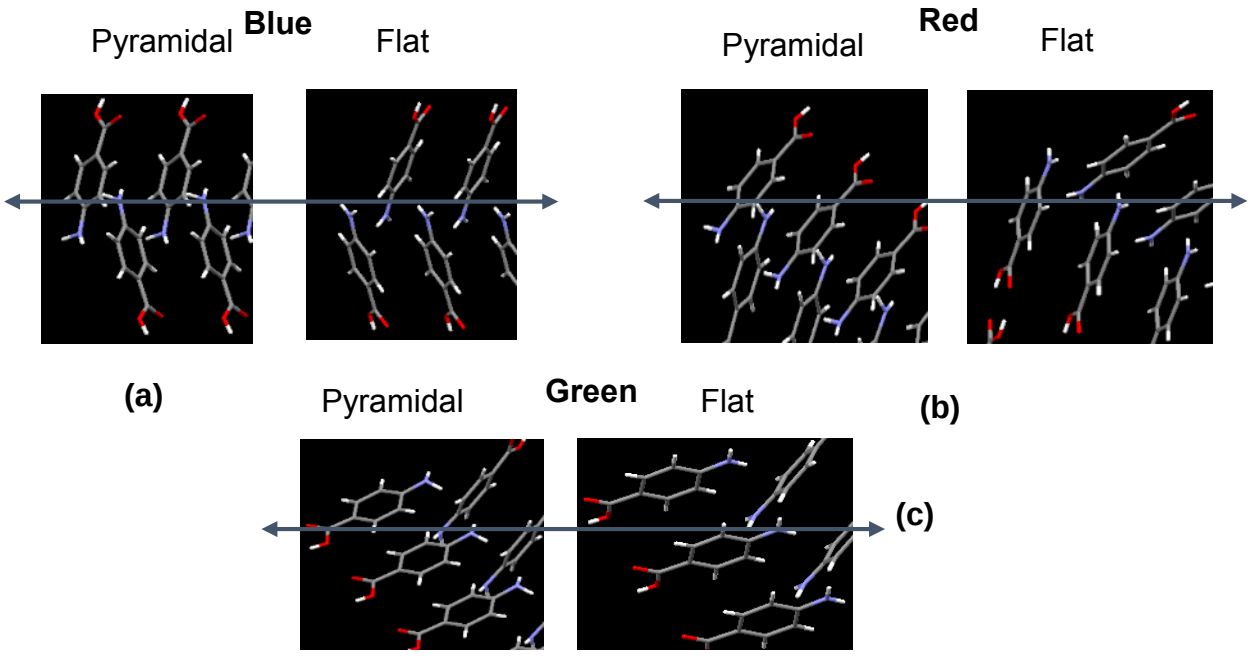


**Figure 9-19: Molecular visualisation of the predicted orientation of the α-pABA (1 0 1) surface based on the crystal structure for the orientation of the crystal for the Nitrogen K-edge measurements shown in Figure 9-18. Figures on the left have a pyramidal amino**

For the blue spectra, the crystal is orientated almost vertically and shows an intense resonance for the NH→1σ* peak. Figure 9-19(a) shows that if the amino group is pyramidal then the one of the NH bonds is close to parallel to the beam, and this could explain the intense resonance. However, if the amino group is planar, Figure 9-19(a) suggests that the NH bond would not be as parallel to the beam. The same can be said of the orientation of the crystal for the red spectra, which also shows an intense resonance for the NH→1σ*. However, the green spectra shows a relative decrease in the NH→1σ* compared to the CN→1σ*. This is consistent with the amino group being pyramidal, as Figure 9-19(c) shows that the pyramidal amino group would now be pointing downwards, and hence would not be parallel to the beam vector and a less intense resonance would be expected. This agrees well with the NEXAFS prediction of powdered structures published by Stevens et al[8]

## 9.5 Structural Homogeneity

Since a single crystal should have a periodic structure, the relative intensity of the resonances at each edge should be the same. Section 10.2.2 suggests that there are some differences in the FY and PEY spectra measured at the (1 0 -1) surface. This resulted in an investigation into the spatial homogeneity of several samples using state of the art NEXAFS microscopy.

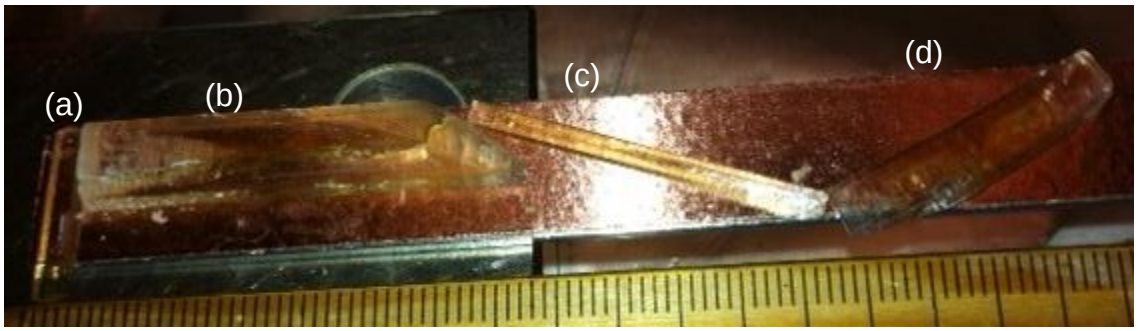


**Figure 9-20: 4 α-*p*ABA crystals mounted for the NEXAFS imaging on a copper bar. Crystals (a), (b), (c) and (d) mounted at different angles to explore if the azimuthal angle change causes any difference. All crystals prepared from slow solvent evaporation of 90:10 EtOH:NMe solutions**

Figure 9-21 shows two crystals orientated at 90° to each other. The measurement is at the carbon K-edge and normalised to the C=C → 1π* resonance.

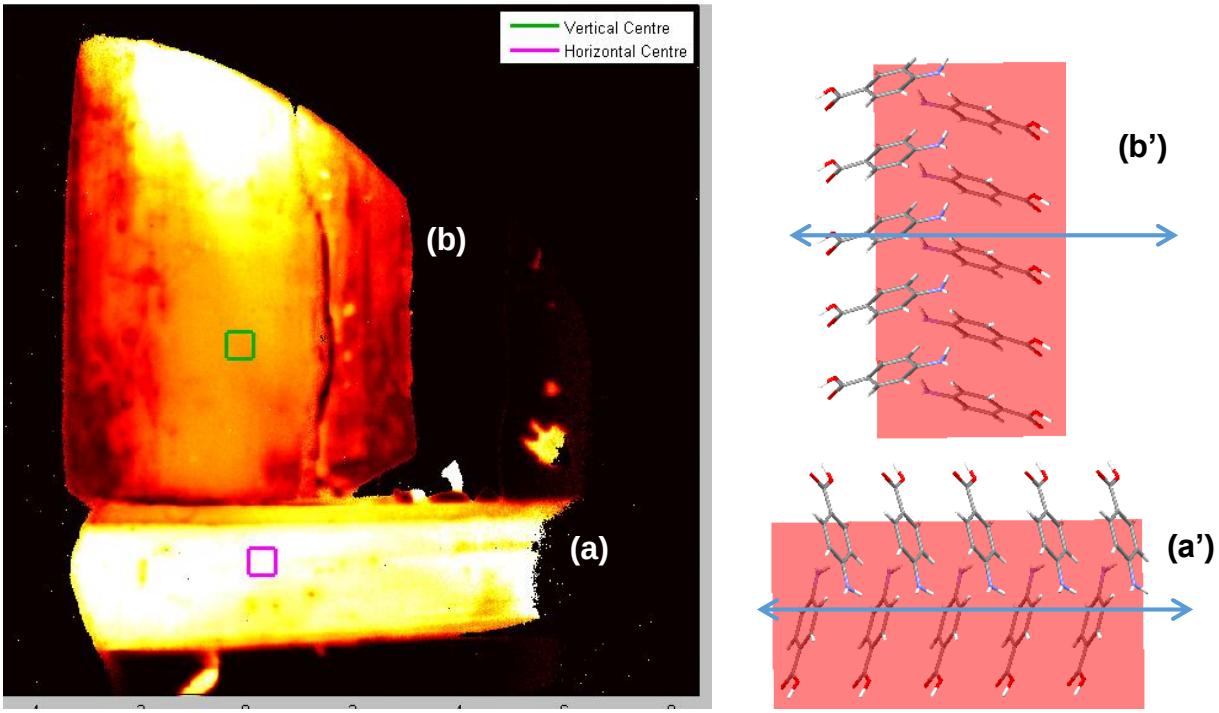


**Figure 9-21: (a) NEXAFS image of the horizontally orientated *p*ABA crystal shown in Figure 9-20(a); (a') orientation of molecules at the (1 0 1) surface of α-*p*ABA from the AMBNAC01 crystal structure at the orientation shown in Figure 9-21(a); (b) NEXAFS image of the vertically orientated crystal shown in Figure 9-20(b); (b') orientation of molecules at the (1 0 1) surface of α-*p*ABA from the AMBNAC01 crystal structure at the orientation shown in Figure 9-21(b)**

Referring to Figure 9-21, the brighter the image then the stronger the intensity of the C=C → 1π* resonance. The horizontal crystal was found to be much brighter due to the horizontal polarisation of the beam probing the out of plane π orbitals associated with the phenyl ring. Figure 9-22 shows the associated spectra from the green and purple regions of interest (ROI).

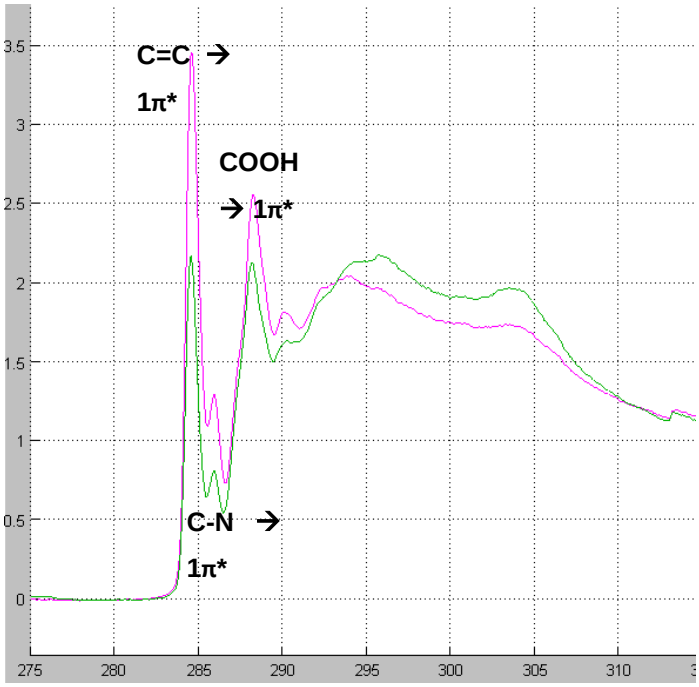


**Figure 9-22: Carbon K-edge NEXAFS spectra from the green and purple ROI's shown in Figure 9-21**

Figure 9-22 revealed that the horizontal crystal has greater enhancement of the C=C → 1π* resonance, while the horizontal crystal has greater enhancement of the σ orbital resonances. Hence, this showed the spatial resolution of NEXAFS that the NEXAFS imaging system was capable of. Therefore the studies were expanded to investigate how homogenous a crystal was by looking at the spatially resolved NEXAFS over a single crystal.

Figure 9-23 shows the vertically orientated single crystal from Figure 9-21 showing how the C K-edge changes across the (1 0 1) surface.

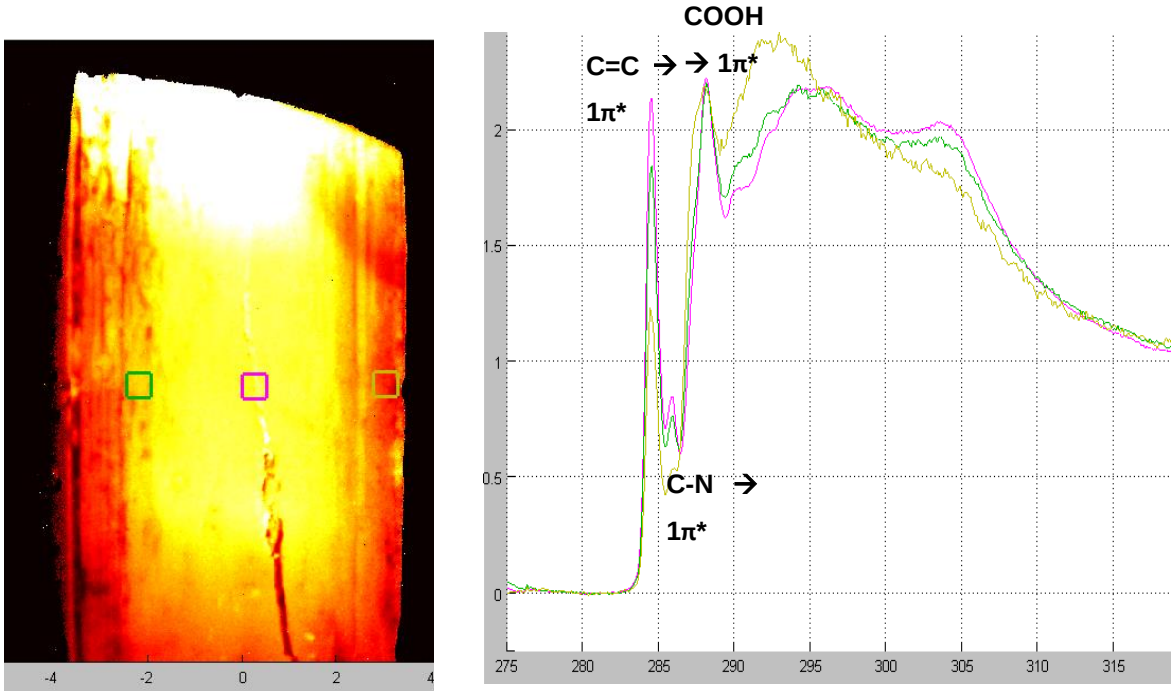


**Figure 9-23 Carbon K-edge NEXAFS spectral image of α-*p*ABA (1 0 1) surface from the crystal shown in Figure 9-20(b) with associated spectra from the three ROI's**

The purple spectra at the centre of the crystal was found to have the highest intensity for the C=C → 1π*, C-N → 1π* and COOH → 1π* resonances. The green and yellow spectra at the edges of the (1 0 1) surface showed significantly reduced π resonances and, in the yellow spectra, increase in the intensity of the σ resonances.

I think that with all of the spectra showing significant differences across a supposedly periodic crystal, it would suggest that there are changes in the local structure across the (1 0 1) surface that would not be observable using a bulk technique, such as X-ray diffraction. The changes in structure across the crystal were also investigated at the O K-edge, shown in Figure 9-24

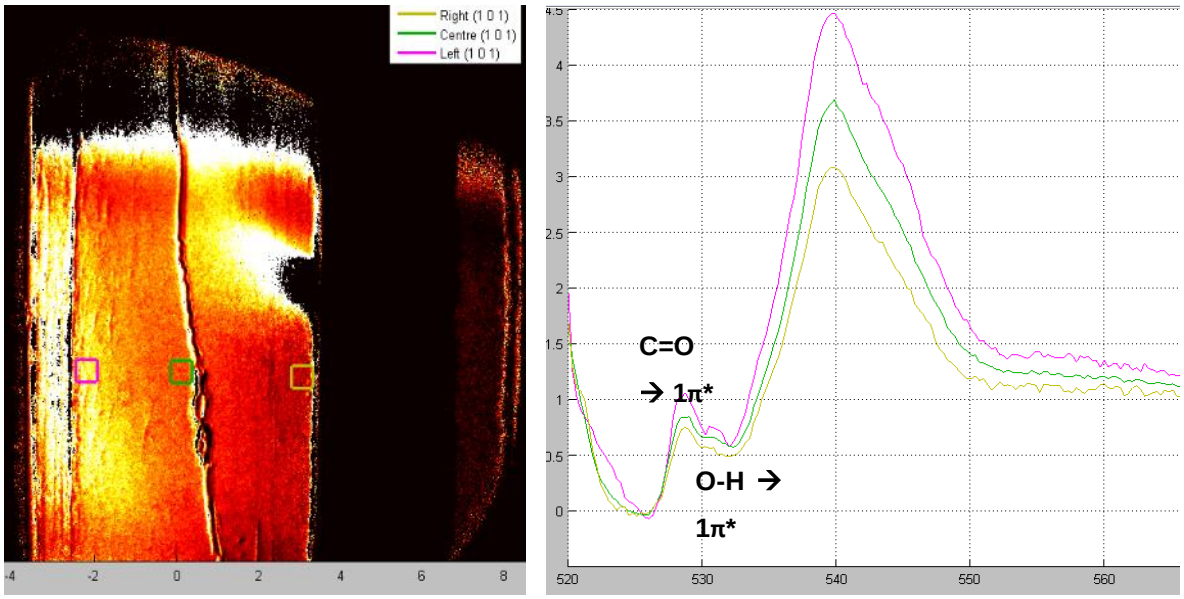


**Figure 9-24: Oxygen K-edge NEXAFS spectral image of α-*p*ABA (1 0 1) surface from the crystal shown in Figure 9-20(b)**

Though the total intensities of the spectra change at the oxygen K-edge across the crystal, the relative peak heights stay approximately the same. This suggests that the oxygen edge is not as sensitive to the potential changes in orientation observed for the carbon edge. This may suggest that the change in orientation is due to an intramolecular rotation and that the oxygen atoms remain in approximately the same orientation or that the reorientation does not affect the oxygen edge in the same way as the carbon edge.

Single crystals of α-*p*ABA show that there are obvious changes in the sector zones associated with the capping faces of the crystal compared to the centre of the crystal. Figure 9-2 shows the clear difference in colour between the centre and the end of the crystal. Therefore the differences in spectra were investigated along the length of the crystal as well.

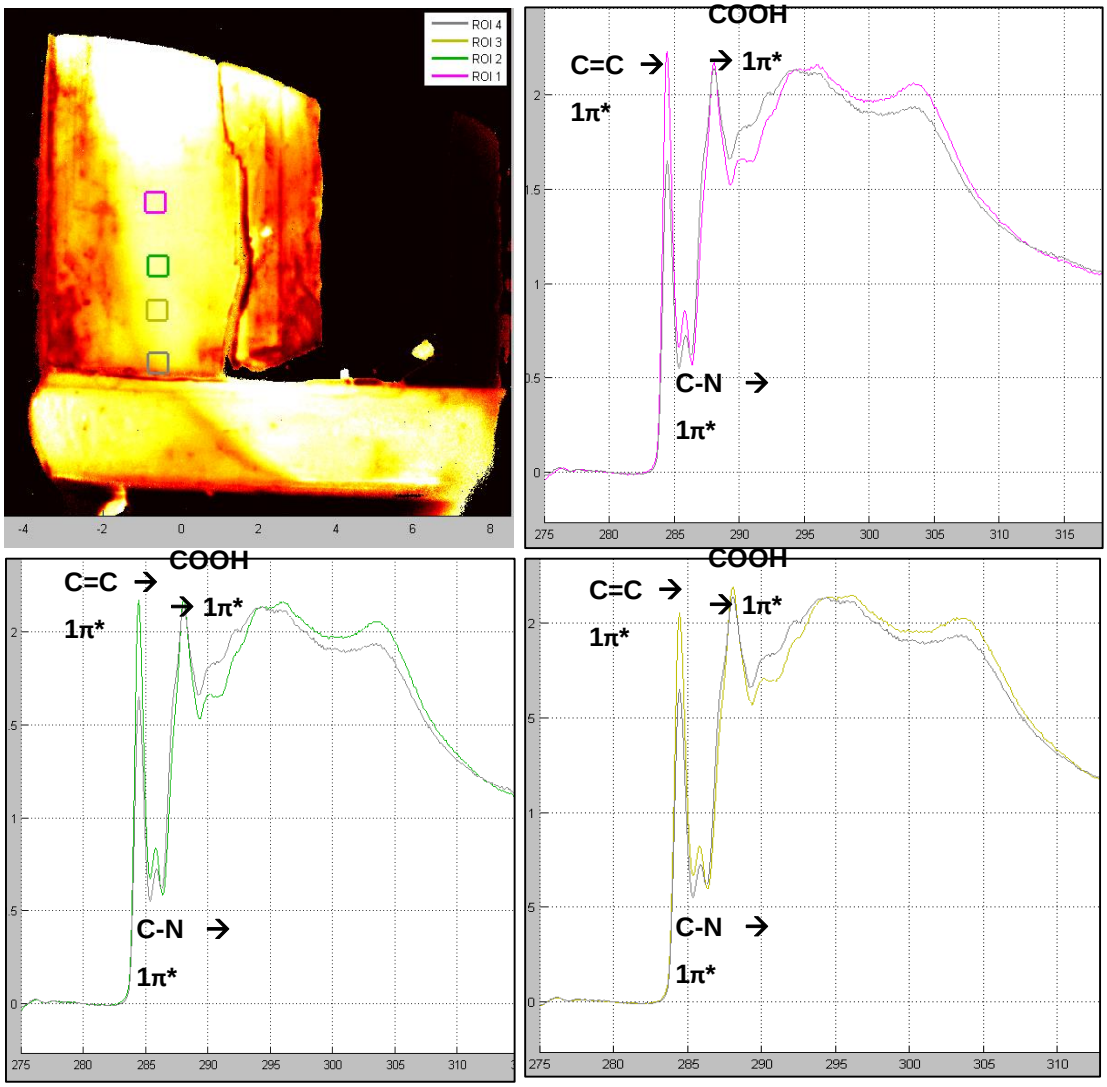


**Figure 9-25: Carbon K-edge NEXAFS spectral image of α-*p*ABA (1 0 1) surface from the crystal shown in Figure 9-20(a) and (b). Grey spectra corresponding to the ROI closest to the bottom capping surface compared to the four spectra more in the centre of the crystal**

In Figure 9-25 a clear suppression of the C=C → 1π* resonance is observed in the grey spectra associated with the ROI closest to the capping face compared to the other ROI's investigated on this crystal. In a similar way to the (1 0 -1) surface, the capping surface could be susceptible to a degree of surface relaxation due to unsaturated π-π stacking interactions, though this was not clear from the conventional NEXAFS measurements at the capping faces presented in Section 10.2.2.3.

The differences in the spectra as a function of the where across the (1 0 1) surface of α-*p*ABA the spectra were taken from was investigated in the other crystals mounted for the NEXAFS imaging.

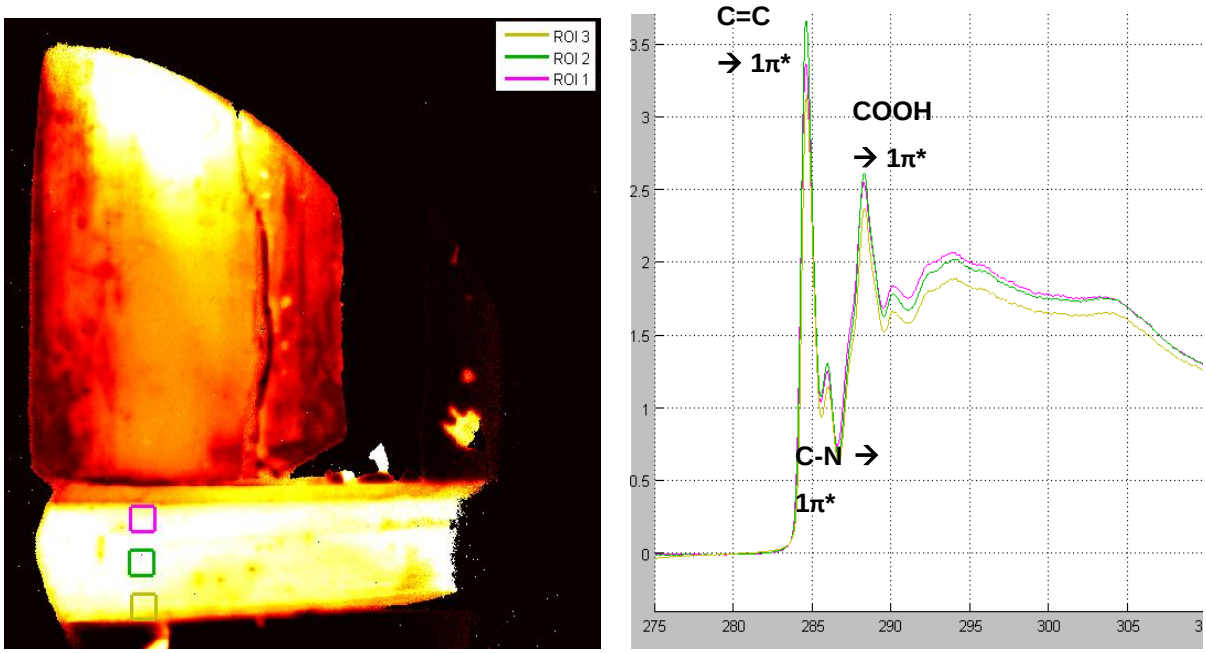


**Figure 9-26: Carbon K-edge NEXAFS spectral image of α-*p*ABA (1 0 1) surface from the crystal shown in Figure 9-20(a) and (b) with associated spectra from the three ROI's**

The amount of change between the spectra at the centre and edge of the (1 0 1) surface of the horizontal crystal was found to be less than the vertical crystal. Interestingly it was found that the intensity of the C=C → 1π* intensity decreased at the edge of the crystal close to the (1 0 -1) surface, similar to the vertical crystal. Since the crystals are orientated at 90° to each other, if the surface relaxation was the same at each crystal it would have been expected that the change in intensity of the peaks would be the opposite for the two crystals. This could mean that the suppression of the C=C → 1π* resonance is due to the edge of the crystal emitting less photons than the centre. However, it would be expected that the intensity of all the peaks would be reduced at the edge, but it seems to strongly affect the C=C → 1π* peak. It may be that the edges of the crystal become more disordered compared to the centre, and that the orientation of the molecules becomes slightly more random and hence it is not obvious to be able to predict the molecular geometry, though it appears that there is a clear difference between the bulk and the edges of the crystal. Though NEXAFS

imaging has previously been utilised to identify the orientation of self-assembled monolayers on gold[239]

Two other crystals were also mounted at differing azimuthal angles and these were also investigated to assess whether these changes in the NEXAFS spectra across the surface occur in these crystals as well.

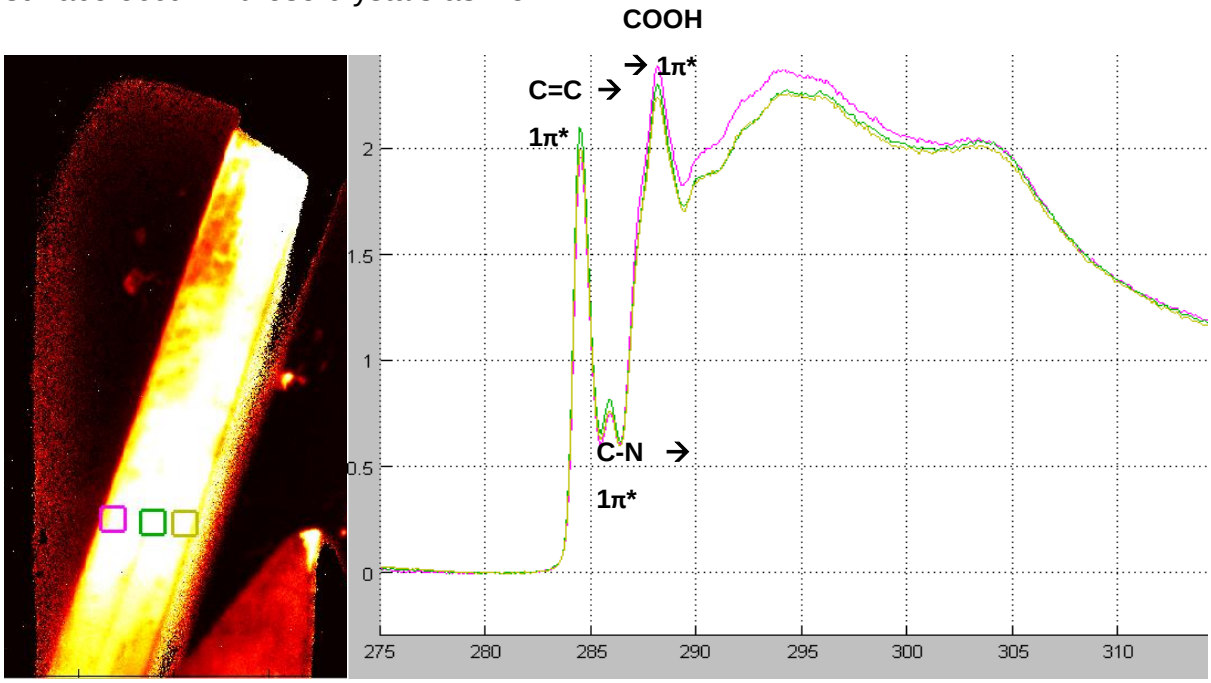


**Figure 9-27: Carbon K-edge NEXAFS spectral image of α-*p*ABA (1 0 1) surface from the crystal shown in Figure 9-20(c) with associated spectra from the three ROI's**

The differences in the spectra across the crystal shown in Figure 9-27 were found to be much more subtle, but once again a slight enhancement of the C=C → 1π* resonance was observed in the green spectrum, which was taken at the centre of the crystal. As well as showing a slight decrease in the C=C → 1π* resonance, the pink spectrum also shows an increase in the C-C → 1σ* resonance at around 293eV. Since the π and σ orbitals are directed perpendicular to each other, a fall in the peak associated with the π orbital and rise in the peak associated with the σ orbital suggests a change in orientation of the phenyl ring ROI associated with the pink resonance.

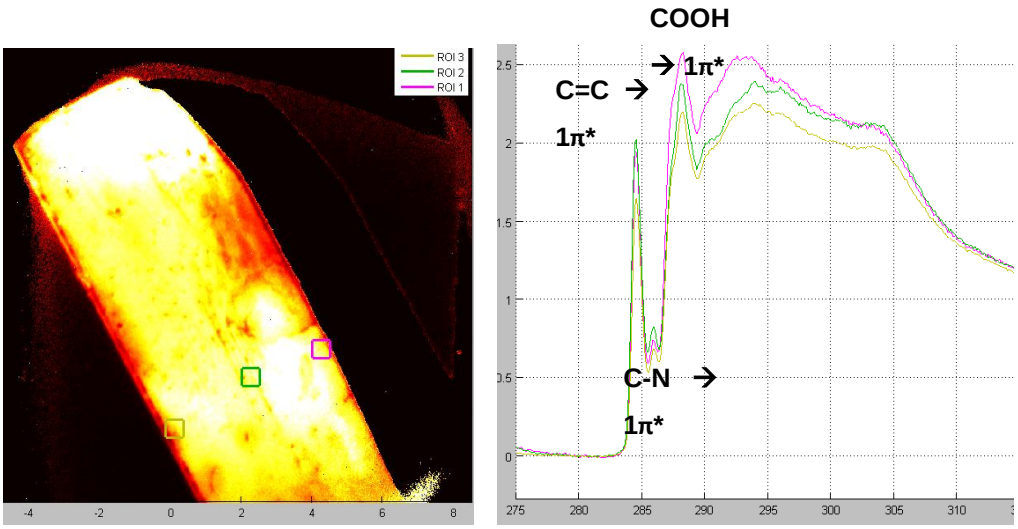


**Figure 9-28: Carbon K-edge NEXAFS spectral image of α-*p*ABA (1 0 1) surface from the crystal shown in Figure 9-20(d) with associated spectra from the three ROI's**

The changes in spectra in Figure 9-28 are similar to Figure 9-23 with the characteristic increase in the C=C → 1σ* peak rising in intensity at the expense of the C=C → 1π* peak, suggesting a change in molecular orientation.

Comparing Figure 9-28 and Figure 9-27 to Figure 9-23, there was found to be more changes in the carbon K-edge spectra across the (1 0 1) surface than in any of the other crystals. This probably suggests that this crystal is of lesser quality than the other crystals measured and therefore exhibits more disorder in the local structure compared to the other two crystals. However, all of the crystals exhibited enough changes in the carbon K-edge spectra close to the edge of the surfaces to suggest structural changes in the areas where it might be expected that there are unsaturated hydrogen bonding interactions. Nevertheless, the change in spectra was not always consistent at the edges of the crystal, suggesting that the change in structure was not a consistent molecular relaxation.

## 9.6 Local Geometry at the Crystal Surfaces of α-*p*ABA

Stohr and co-workers developed the method for elucidating the geometry of single molecules on clean substrates[120-124] by rotating the sample with respect to a polarised beam. Despite the work of Roberts et al in the 90s on developing this technique to be

relevant to single crystals[125-128, 240], this study of the surface geometry of multiple crystal faces is relatively novel work.

The surface of organic crystals can be probed using techniques such as functionalised atomic force microscopy (AFM)[241], but much of the molecular information is inferred from the surface topography of the material. The NEXAFS displayed here give molecular orientation at the atomic level with high accuracy. The NEXAFS imaging results in far more of the material being illuminated providing the spatial resolution of a crystal surface, previously lacking in the conventional NEXAFS experiments.

The surface sensitivity and high degree of accuracy of this technique means that it is the optimal tool for probing potential surface re-arrangement in molecular crystals. It could be extremely relevant to more conformationally flexible molecules that may undergo intramolecular, as well as intermolecular relaxation at a crystal surface.

## 9.7 Conclusions

Chapter 9 revealed differences between the bulk and surface sensitive NEXAFS data that could be attributed to surface relaxation due to unsaturated 'hanging' synthons. In addition, NEXAFS imaging data also suggested that the (1 0 1) surface structure may not be totally homogenous. The findings of chapter 9 are shown in Table 9-1.

**Table 9-1: Major issues and answers provided by chapter 9**

| **Question/Issue** | **Information provided by the chapter** | **Relevance to the Study** |
|---|---|---|
| Does the spectra change between the bulk FY and surface sensitive PEY? | • Spectra measured at the (1 0 -1) surface appeared to show more changes than the (1 0 1) or (0 1 -1) surfaces between the FY and PEY | Could suggest surface relaxation at the (1 0 -1) surface due to unsaturated H-bonds |
| Does the NEXAFS reveal intramolecular structural details | • Experiments at the N K-edge suggested that the $NH_2$ group is pyramidal rather than planar | Previous studies have suggested that the $NH_2$ group could be pyramidal or planar in α-*p*ABA. This suggests that it is the former |
| How does the spatially resolved structure of a single crystal surface change? | • Peak ratios of the (1 0 1) surface were found to change between the centre and the edge of the crystal, close to the (1 0 -1) surface | Could suggest that there is disorder in local geometry not detected by bulk X-ray diffraction. Also suggests that the closer to the (1 0 -1) surface then the more possibility for structural changes |

The crystallographic mapping experiments at the (1 0 1) surface of α-*p*ABA showed that the orientation of the *p*ABA molecules were in good agreement with the orientation from the crystal structure. Examination of the nitrogen K-edge data revealed that the $NH_2$ group was probably pyramidal, in good agreement with previous studies of α-*p*ABA[8].

The changes in peak ratios between the bulk FY data and surface sensitive PEY data was found to be most pronounced at the (1 0 -1) surface from the conventional NEXAFS experiments. It is thought that self-absorption effects can have some effect on the NEXAFS spectra, however it would be similar at each surface if it was having a large effect on the spectra. In addition, the problems due to the self-absorption should effect each peak similarly and has only been reported to be an issue Therefore, it seems likely that there is some differences in the surface and bulk structure, especially at the (1 0 -1) surface, which may be more susceptible to surface reconstruction due to the unsaturated H-bonds predicted at that surface.

To complement the conventional NEXAFS data, the NEXAFS imaging revealed that there are subtle differences in structure across a supposedly periodic (1 0 1) surface. There was found to be changes in the molecular orientation between the centre of the (1 0 1) surface and the edge of the (1 0 -1) surface. This supports the observations from the conventional NEXAFS that the (1 0 -1) surface appears to show changes more so than the less reactive surfaces.

This chapter revealed that NEXAFS spectroscopy is a powerful to examine surface molecular structure of crystals. This could be extremely useful for examining the molecular orientation of poorly crystalline or amorphous materials. The differences between the bulk and surface sensitive data suggested that there are more pronounced surface structural changes at surfaces containing unsaturated H-bonding interactions. In addition, the NEXAFS imaging also revealed that a supposedly periodic surface could show slightly different surface molecular orientation at the edge of the face than at the centre. This information is valuable to practitioners that rely on surface molecular models based on terminated crystal structures. This work suggests that it may be relevant to consider how likely it is for the molecular geometry to relax at the termination of growth. This work underpins objective 5 and takes structural information gained from objective 3.

# Chapter 10 Conclusions and Future Work

*The conclusions with respect to the study as a whole are summarised along with the impact with respect to what this work has achieved. The potential future studies are outlined.*

## 10.1 Conclusions

This study has revealed that an understanding of the synthonic structure that is important for the self-assembly and growth of a crystalline material can aid the selection of a crystallisation environment that gives better control over size, shape and crystal polymorphism of the product crystals.

### 10.1.1 Crystal Chemistry and Self-Assembly (Chapters 5 and 6)

The OH...O H-bonds and π-π stacking interactions calculated to be important for stabilising the lattice energy of the α-*p*ABA structure were, in turn, calculated to be important in stabilising α-like small clusters in solution and probably facilitating the fast self-assembly of this structure in solution. The head-tail π-π stacking interactions and the OH...N and NH...O H-bonds that were calculated to be important in stabilising the lattice energy of the β-*p*ABA structure were generally calculated to be less stable than α-like clusters in solution. However, in water the head-tail π-π stacking dimer was calculated to be more stable than the OH...O H-bonding dimer, along with the 4-membered ring structure being calculated to be more stable than the other α tetramers, apart from the structures containing π-π stacked OH...O H-bonding dimers. These calculations were complemented by the solvent binding calculations that showed that water strongly preferentially binds to the COOH group over any other part of the *p*ABA molecule.

These calculations suggest that the crystallisation of α-*p*ABA that often occurs in conditions where β-*p*ABA is thermodynamically stable is due to how stable the important molecular building blocks of α-*p*ABA are in solution. The stable combination of the OH...O H-bonds and π-π stacking interactions probably results in a chain reaction like fast self-assembly of the α-structure to a critical size, whereby it nucleates. Therefore, the fact that water promotes the crystallisation of the β-form more so than the other solvents is probably due to water molecules strongly solvating the COOH group and hindering the formation of the OH...O H-bonds. In addition, if the OH...O H-bonding dimers do form it was calculated that the water molecules would offer little stabilisation to the rest of the *p*ABA molecule and it seems likely that they may attack the COOH group and attempt to break the OH...O H-bonds.

Though these results seem to correlate well with the experimental crystallisation in water and ethanol, these results should only be used as a guide rather than an explicit picture of physical reality. The lack of dynamics and the need to add the molecules one by one in the SYSTsearch means that the geometry of the molecules must only be treated as approximate.

The stability of the clusters within the COSMO-RS environment is only with respect to each other. The clusters are user inputted so the results are a guide to how the molecules may cluster once the solution reaches supersaturation, it does not explicitly mean that these clusters are stable exist by themselves in solution. However, the construction of the cavities around the molecule in the solvent dielectric and the previous published work shows that this approach is a valid and useful guide for predicting the self-assembly of clusters in solution. However, more studies would further cement whether this approach is valid for a greater range of systems.

### 10.1.2 Crystal Growth and Morphology

The strength and directionality of the synthons in the crystal structure of α-*p*ABA was found to be more anisotropic than β-*p*ABA, contributing to the more anisotropic needle-like morphology of α-*p*ABA compared to the more isotropic plate-like morphology of β-*p*ABA. The strength and nature of the synthons that dominate the growth of the major morphological surfaces of α-*p*ABA were found to strongly vary between the surfaces, whereas the strength and nature of the synthons that dominated the growth of the morphologically important surfaces of β-*p*ABA were found to be much more similar. The more isotropic nature of the β-*p*ABA surfaces probably means that the solvent effects at the crystal surface are averaged and that the crystal surfaces are growing by the same growth mechanisms, hence the good match of the attachment energy morphological prediction to the experimental morphology.

For the α-*p*ABA crystals grown in ethanol, it was found that the (0 1 -1) surface grows by a rough interfacial growth mechanism, while the (1 0 -1) surface grows by a birth and spread mechanism. The greater ease of forming the π-π stacking interaction due to the greater area of the molecules interacting, combined with less hindrance from solvent binding interactions, probably results in a solid-on-solid integration mechanism at the (0 1 -1) surface and the resultant fast growth. However, the extra vdW character

of the NMe molecule resulted in solutions containing NMe resulted in retarded growth of the (0 1 -1) surface and much shorter crystals that more closely resemble the attachment energy morphological prediction.

The attachment energy theory is useful for identifying the strength and nature of the intermolecular interactions at a crystal surface; however it fails to predict solvent dependent morphologies since it only calculates the strength of the interactions within the crystal structure. Further work to correlate the strength and density of solute/solvent binding sites at particular surfaces, found by the grid based methods, into a model that can predict solvent dependent attachment energy is needed. Currently, only qualitative data can be obtained from the searching of probe molecules on crystal surfaces.

### 10.1.3 Surface Chemistry

Chapter 9 revealed that the local molecular geometry can change between the bulk and surface of the crystal. This was found to be more prominent for the (1 0 -1) surface which was predicted to be terminated with unsaturated COOH groups. The more reactive nature of these unsaturated groups may have resulted in re-arrangement of the molecules to satisfy these groups. In addition, the NEXAFS imaging experiments revealed that there were disorder and changes in local geometry across the (1 0 1) surface of the supposedly periodic crystal. This is important with respect to modelling a crystal surface, since many molecular models of a surface assume that the surface geometry is the same as the termination of a crystal structure.

## 10.2 How did the Study Satisfy the Aims and Objectives?

1. **Determine whether the formation of the intermolecular synthons affects the intramolecular conformation of *p*ABA**

Though *p*ABA is relatively inflexible, it was identified that the directional hydrogen bonds change the conformation of the COOH and $NH_2$ groups, such that the molecule adopts a higher energy conformation in the crystal structures than the global minimum. This objective was satisfied during this study.

2. **Identify the important intermolecular building blocks that influence the molecular aggregation and polymorphism in solution**

The importance of the formation of the OH...O H-bonding carboxylic acid dimers on the self-assembly of the α-form was identified. In addition, the water molecules strongly solvating the COOH group probably aids the self-assembly of the β-form in water. The addition of more dynamical modelling could probably reveal more on the exact mechanism of self-assembly in solution, however the broad aim was satisfied within this study.

3. **Ascertain the surface specific crystal chemistry and the important synthons that influence the face-specific crystal growth and predict the crystal morphology as a function of solvation environment**

The important synthons that influence the surface specific crystal growth of both polymorphs was identified and some trends observed for the calculated surface-solvent interactions. However, for the α-form it was still a challenge to calculate the crystal morphology as a function of solvent environment. The study revealed that the model to relate the solute/solvent binding energy from the grid search to crystal morphology is working progress.

4. **Elucidate the face specific crystal growth mechanisms and relate to the intermolecular interactions at the faces and crystal morphology**

The crystal growth mechanisms were identified in ethanol and 95:5 ethanol:nitromethane mixtures. Ideally the crystal growth mechanisms could be identified in a wider range of solvents to relate the solvent molecular character to growth mechanisms. Though it was identified that solvents with a lack of π-orbital bonding probably facilitates a roughening ‘solid on solid’ crystal growth mechanism, since the H-bonding solvents probably bind more strongly to the H-bonding surfaces and therefore result in the surface with π-π stacking interactions being more available.

5. **Compare predicted surface chemistry to experimental surface chemistry and relate to the face specific crystal growth**

It was identified that the H-bonding (1 0 -1) surface probably exhibits more changes in molecular geometry at the crystal surface than the other major faces of α-*p*ABA, however this study did not elucidate the exact molecular geometry at the surfaces. An extension of this work would be to identify exactly how the molecular geometry

changes between the surface and the bulk, hence this would reveal the mechanism of surface relaxation at a crystal face.

## 10.3 Impact of the Study

This study has revealed that utilising simplistic molecular modelling tools to identify important intermolecular synthons and building blocks for a crystal structure, along with their interactions with solute and solvent can rationalise a significant amount of the crystallisation behaviour of α- and β-*p*ABA. The multi-technique nature of this study has also identified which experiments can be carried out to validate and rationalise the synthonic modelling.

This approach is relevant to industrial practices looking to identify the correct conditions to crystallise highly polymorphically pure and easy to filter crystals on a large scale. The synthonic knowledge in chapters 5 and 6 resulted in being able to predict which solvents may produce a particular polymorphic form. The synthonic knowledge was then applied to surfaces to aid the prediction of solvents that will produce more desirable shaped crystals for filtration in chapter 7, along with experimental evidence collected showing the effect of the correctly selected solvent environments in chapter 8. Chapter 8 also revealed that the crystallisation time can influence the polymorphic purity of a crystallisation process. Chapter 9 revealed that the local geometry of a crystal surface cannot always be assumed to be a perfect termination of the crystal structure.

With the development of morphological population balance models that identify the correct conditions for producing crystals with a desirable crystal size distribution from a batch crystalliser, the data collected in this study on morphology and the time dependence on polymorphic purity could be inputted into the model to find the correct parameters to produce these crystals on a large scale. Figure 10-1 shows a methodology for identifying these ideal batch crystallisation conditions through this combination of molecular modelling and experimental work.

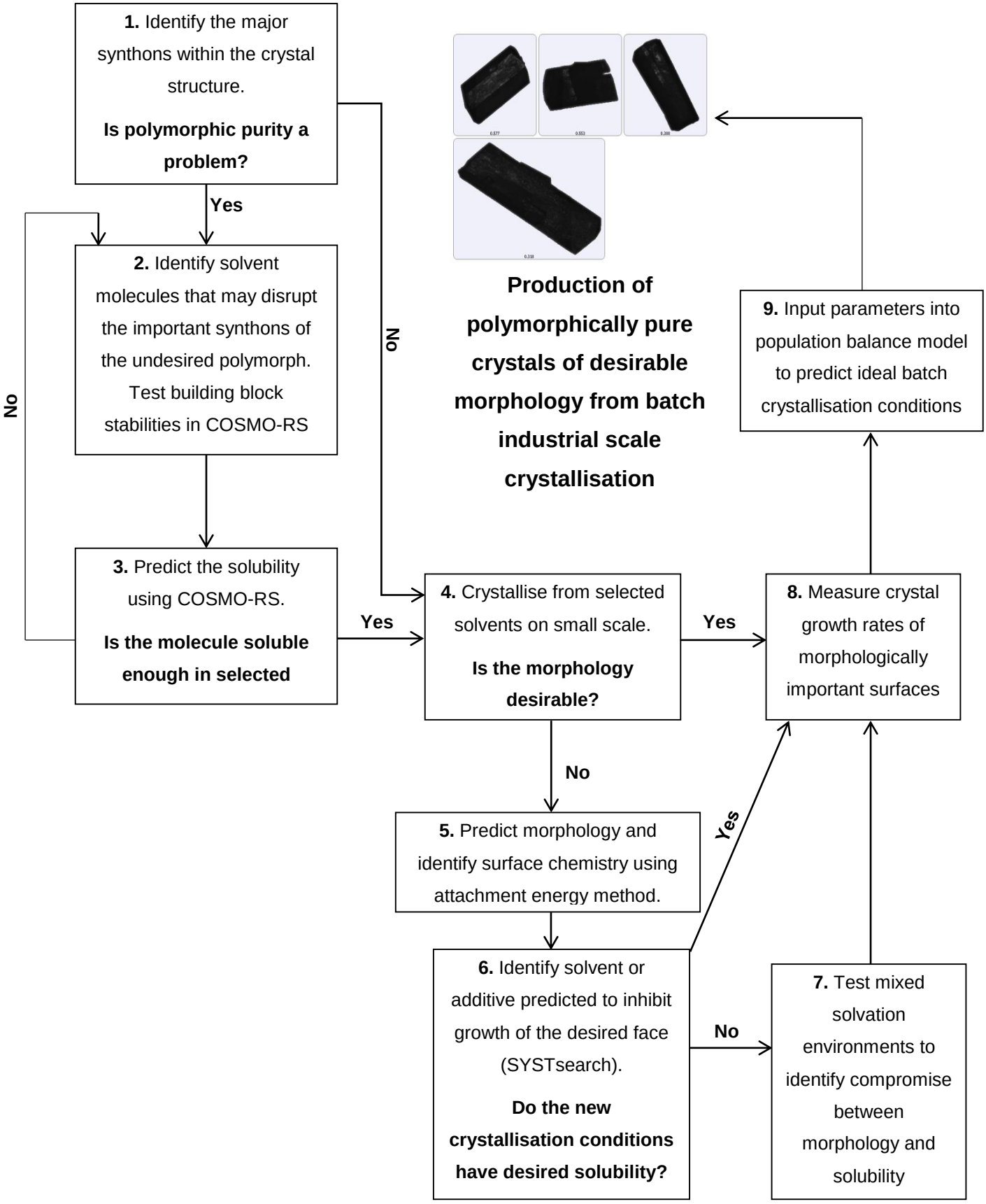


**Figure 10-1: Potential methodology for identifying the correct crystallisation conditions to produce pure crystals of a desired morphology from batch crystallisation**

The procedure shown Figure 10-1 is designed to be used as a guide for a crystallisation scientist looking to get an idea of suitable conditions for crystallisation of particles of a desirable shape. The limitations of the methodology, particularly with respect to the molecular modelling, have been highlighted in Section 10.1. However, despite these limitations the modelling does identify the chemical nature of the crystalline surfaces and how they are likely to interact with the solute and solvent. Within Figure 10-1 it has been highlighted that the predicted conditions should be rigorously tested, however this process has the potential to greatly reduce the time and effort taken to identify ideal crystallisation conditions.

## 10.4 Future Work

The final step of the methodology shown in Ffigure 10-1 is to use the morphological population balance model to identify the batch crystallisation conditions to produce a pure product with the required particle size and shape. However, this was not tested in this study and would be the logical next step would be to use the model to find the optimal conditions of batch *p*ABA crystallisation and test them at a larger scale.

This type of study would also be interesting to repeat on a molecule with increased flexibility. Many pharmaceutical drugs are large flexible molecules with many centres of rotation, whereby the conformation of the molecule in the crystal can strongly vary from the lowest energy conformation. It would therefore be of interest to study the differences between the behaviour of such a molecule and *p*ABA, especially with respect to how the surface structure may be more susceptible to surface relaxation.

Specific future work arising from the work flows that I undertook during the study are shown below, with respect to how the results found could be improved and made more relevant.

### 10.4.1 Crystal Morphology

The crystal morphology prediction using the attachment energy method gave a good prediction of the equilibrium morphology observed from crystallisation of β-*p*ABA, however gave a less accurate prediction of the more kinetic morphology associated with α-*p*ABA. The difficulty with predicting the morphology of needle-like crystals still pertains[24, 181, 182], despite improved models which attempt to account for growth

mechanism and solvent binding[5, 23]. This study has revealed that needle-like crystals of α-*p*ABA are strongly solvation environment dependent, revealing their kinetic nature. Traditional PBC and connected net approaches[172] have accurately predicted the likelihood of surface roughening from the internal structure, but this study has indicated that it is more complex than these simple models and that roughening can be a function of the external environment as well as internal.

An interesting further study would be to apply the techniques developed in this study to a range of needle-like crystals with varying degrees of structural complexity and nature. This study revealed that you can change the needle-like morphology of α-*p*ABA by understanding the synthonic nature of the fasting growing face and tweaking the solvation environment, along with reducing the interfacial roughening at this surface. It should be considered how easily a molecule may integrate into the morphologically important surfaces of a needle-like crystal, and considering the orientation that a molecule may have to take and how great the interacting area of the synthons that dominate the growth of these faces. If a large area of the molecule is interacting, such as in ring stacking interactions, it could be assumed that it would be easier for the molecules to find this type of orientation and therefore form this synthon. Considering the orientation effects and how a solvent may affect the molecules integrating into the morphologically important surfaces should improve the prediction of how likely a surface is to roughen. A more thorough measure of the growth rates of needle-like crystals when they are in conditions where they do or do not roughen could give an average indication of how much faster these crystals grow when they are surface roughened. In turn, the model could derive a scaling parameter, which could be activated in conditions whereby a surface would be thought to kinetically roughen, which would apply an increased growth rate to that surface. This model could give an attachment energy morphology prediction as a function of supersaturation that accounts for surface roughening.

### 10.4.2 Experimental Surface Chemistry Measurements

Though chapter 9 showed that there were subtle changes in local geometry between the bulk and surface of the crystal, in addition to differences across the same crystal surface, the exact nature of the directionality of these differences was not resolved.

Applying Stohr's equations from the variable orientation NEXAFS experiments should be able to resolve the exact nature of the molecular re-orientation at the surface.

The NEXAFS experiments were performed on large single crystals. Often for a pharmaceutical product it is extremely challenging, or impossible, to grow crystals of this size. Crystals of this size are also not used in formulation even if it is possible to grow to such a size. Therefore, expanding these experiments to understand the surface chemistry of much smaller particles is important to attempt to understand their growth, morphology and dissolution behaviour, which are all thought to be strongly surface chemistry dependent.

Though chapter 10 showed there were some differences in the bulk and surface structure of *p*ABA, more interesting work may come if one could solvate a crystal surface and probe the effect of solvent at the crystal surface. Flowing solvent vapour over a surface could provide more information as to how a crystal surface changes upon contact with solvent, how the solvent molecules ingress into the surface.

With the development of variable polarisation undulators, movement of the sample is no longer necessary. Schroeder and co-workers have shown that it is possible to observe structural information in solution by utilising liquid jet NEXAFS[242]. Ideally, it would be interesting to condense a layer of liquid on a crystal surface thick enough such that a small beam could be orientated just to probe the liquid layer. This could probe the degree of self-assembly of molecules in solution at a crystal surface, or whether they remain randomly orientated until they integrate into the crystal.

## 10.5 Closing Remarks

This study has revealed that the nature and strength of a couple of major synthons of a crystal structure can influence the physical properties of a crystalline material. This type of multi technique approach has resulted in much more broad interlinking of observations, especially with respect to linking the molecular modelling with experimental observations, such as crystal growth rates. Though such wide-ranging projects are time and resource consuming, the information gathered allows much more complete conclusions to be drawn on a system, rather than focussing on a small window of results. I firmly believe that in-depth characterisation of the crystallisation

behaviour of more systems using this multi-technique approach would result in more broadly applicable conclusions on how to control crystallisation behaviour being developed, that would result in more robust molecular models that could be applied to a wide range of materials.

## References


1. Mullin, *Crystallization*. 1961.
2. Cavendish Laboratory, C. X-Ray Diffraction.
3. Sullivan, R. A.; Davey, R. J., Concerning the Crystal Morphologies of the alpha and beta polymorphs of p-aminobenzoic acid. *CrystEngComm* **2015,** *17*, 1015-1023.
4. Roberts, K. J.; Sherwood, J. N.; Yoon, C. S.; Docherty, R., Understanding the Solvent-Induced Habit Modification of Benzophenone in Terms of Molecular Recognition at the Crystal/Solution Interface. *Chem Mater* **1994,** *6*, 1099-1102.
5. Hammond, R. B.; Pencheva, K.; Ramachandran, V.; Roberts, K. J., Application of grid-based molecular methods for modeling solvent-dependent crystal growth morphology: Aspirin crystallized from aqueous ethanolic solution. *Cryst Grow Des* **2007,** *7*, 1571-1574.
6. Roberts, K. J.; Docherty, R.; Bennema, P.; Jetten, L., The Importance Of Considering Growth-Induced Conformational Change In Predicting The Morphology Of Benzophenone. *J Phys D Appl Phys* **1993,** *26*, B7-B21.
7. Docherty, R.; Roberts, K. J., Modeling The Morphology Of Molecular-Crystals - Application To Anthracene, Biphenyl And Beta-Succinic Acid. *J Cryst Growth* **1988,** *88*, 159-168.
8. Stevens, J. S.; Seabourne, C. R.; Jaye, C.; Fischer, D. A.; Scott, A. J.; Schroeder, S. L. M., Incisive Probing of Intermolecular Interactions in Molecular Crystals: Core Level Spectroscopy Combined with Density Functional Theory. *J. Phys. Chem. B* **2014,** *118*, 12121-12129.
9. Docherty, R.; Clydesdale, G.; Roberts, K. J.; Bennema, P., Application Of Bravais-Friedel-Donnay-Harker, Attachment Energy And Ising-Models To Predicting And Understanding The Morphology Of Molecular-Crystals. *J Phys D Appl Phys* **1991,** *24*, 89-99.
10. Corey, E. J., General Methods for the Construction of Complex Molecules. *Pure and Applied Chemistry* **1967,** *14*, 19-39.
11. Desiraju, G.; Vittal, J. J.; Ramanan, A., *Crystal Engineering: The Design of Organic Solids*. Elsevier: 1989.
12. Hartman, P.; Perdok, W. G., On the relations between structure and morphology of crystals. I. *Acta Crystallogr* **1955,** *8*, 49-52.
13. Berkovitch-Yellin, Z., Toward an ab initio derivation of crystal morphology. *Journal of the American Chemical Society* **1985,** *107*, 8239-8253.
14. Clydesdale, G.; Docherty, R.; Roberts, K. J., HABIT - a program for predicting the morphology of molecular crystals. *Comput Phys Commun* **1991,** *64*, 311-328.
15. Clydesdale, G.; Roberts, K. J.; Walker, E. M., *The crystal habit of molecular materials: A structural perspective, G Clydesdale, K J Roberts and E M Walker, In "Molecular Solid State: Syntheses, Structure, Reactions, Applications"*. 1996; Vol. 2.
16. Etter, M. C.; Macdonald, J. C.; Bernstein, J., Graph-Set Analysis Of Hydrogen-Bond Patterns In Organic-Crystals. *Acta Crystallographica Section B-Structural Science* **1990,** *46*, 256-262.
17. Etter, M. C., Encoding And Decoding Hydrogen-Bond Patterns Of Organic-Compounds. *Accounts of Chemical Research* **1990,** *23*, 120-126.
18. Bernstein, J., *Polymorphism in Molecular Crystals*. Oxford University Press: USA, 2002.

19. Ouvrard, C.; Price, S. L., Toward Crystal Structure Prediction for Conformationally Flexible Molecules: The Headaches Illustrated by Aspirin. *Crystal Growth & Design* **2004,** *4*, 1119-1127.
20. Price, S. L., Computational prediction of organic crystal structures and polymorphism. *International Reviews in Physical Chemistry* **2008,** *27*, 541-568.
21. Price, S. L.; Leslie, M.; Welch, G. W. A.; Habgood, M.; Price, L. S.; Karamertzanis, P. G.; Day, G. M., Modelling organic crystal structures using distributed multipole and polarizability-based model intermolecular potentials. *Phys Chem Chem Phys* **2010,** *12*, 8478-8490.
22. Price, S. L.; Wibley, K. S., Predictions of crystal packings for uracil, 6-azauracil, and allopurinol: The interplay between hydrogen bonding and close packing. *J Phys Chem A* **1997,** *101*, 2198-2206.
23. Winn, D.; Doherty, M. F., A new technique for predicting the shape of solution-grown organic crystals. *Aiche Journal* **1998,** *44*, 2501-2514.
24. Lovette, M. A.; Doherty, M. F., Needle-Shaped Crystals: Causality and Solvent Selection Guidance Based on Periodic Bond Chains. *Cryst Grow Des* **2013,** *13*, 3341-3352.
25. Hamad, S.; Moon, C.; Catlow, C. R. A.; Hulme, A. T.; Price, S. L., Kinetic Insights into the Role of the Solvent in the Polymorphism of 5-Fluorouracil from Molecular Dynamics Simulations. *The Journal of Physical Chemistry B* **2006,** *110*, 3323-3329.
26. Di Tommaso, D., The molecular self-association of carboxylic acids in solution: testing the validity of the link hypothesis using a quantum mechanical continuum solvation approach. *CrystEngComm* **2013,** *15*, 6564-6577.
27. Hao, H. X.; Barrett, M.; Hu, Y.; Su, W. Y.; Ferguson, S.; Wood, B.; Glennon, B., The Use of in Situ Tools To Monitor the Enantiotropic Transformation of p-Aminobenzoic Acid Polymorphs. *Organic Process Research & Development* **2012,** *16*, 35-41.
28. Svard, M.; Nordstrom, F. L.; Hoffmann, E.-M.; Aziz, B.; Rasmuson, A. C., Thermodynamics and nucleation of the enantiotropic compound p-aaminobenzoic acid. *CrystEngComm* **2013**.
29. Datta, S.; Grant, D. J. W., Crystal structures of drugs: advances in determination, prediction and engineering. *Nat Rev Drug Discov* **2004,** *3*, 42-57.
30. Jeffrey, P. X-Ray Data Collection Course.
31. Myerson, A., *Handbook of Industrial Crystallisation*. 2001.
32. Sangwal, K., Recent developments in understanding of the metastable zone width of different solute-solvent systems. *Journal of Crystal Growth* **2011,** *318*, 103-109.
33. Davey, R. J. G., J, *From Molecules to crystallizers: An introduction to crystallization*. 2000.
34. Deglmann, P.; Schenk, S., Thermodynamics of chemical reactions with COSMO-RS: The extreme case of charge separation or recombination. *Journal of Computational Chemistry* **2012,** *33*, 1304-1320.
35. Hammond, R. B.; Pencheva, K.; Roberts, K. J., A Structural−Kinetic Approach to Model Face-Specific Solution/Crystal Surface Energy Associated with the Crystallization of Acetyl Salicylic Acid from Supersaturated Aqueous/Ethanol Solution. *Cryst Grow Des* **2006,** *6*, 1324-1334.
36. Beischer, D., Kinetik der Phasenbildung. Von Prof. Dr. M. Volmer. (Die chemische Reaktion, Bd. 4.) 220 Seiten mit 61 Abbildungen und 15 Tabellen. Format

8°. Verlag Theodor Steinkopff, Dresden 1939. Preis geb. RM 20.—, brosch. RM 19 —. *Zeitschrift für Elektrochemie und angewandte physikalische Chemie* **1940,** *46*, 327-327.
37. ter Horst, J. H.; Kashchiev, D., Determination of the nucleus size from the growth probability of clusters. *Journal of Chemical Physics* **2003,** *119*, 2241-2246.
38. White, G. M., Steady-State Random Walks with Application to Homogeneous Nucleation. *The Journal of Chemical Physics* **1969,** *50*, 4672-4678.
39. Erdemir, D.; Lee, A. Y.; Myerson, A. S., Nucleation of Crystals from Solution: Classical and Two-Step Models. *Accounts of Chemical Research* **2009,** *42*, 621-629.
40. Tajti, A.; Szalay, P. G.; Császár, A. G.; Kállay, M.; Gauss, J.; Valeev, E. F.; Flowers, B. A.; Vázquez, J.; Stanton, J. F., HEAT: High accuracy extrapolated ab initio thermochemistry. *The Journal of Chemical Physics* **2004,** *121*, 11599-11613.
41. Volmer, M.; Weber, A., Germ-formation in oversaturated figures. *Zeitschrift Fur Physikalische Chemie--Stochiometrie Und Verwandtschaftslehre* **1926,** *119*, 277-301.
42. Becker, R.; Doring, W., Kinetic treatment of germ formation in supersaturated vapour. *Annalen Der Physik* **1935,** *24*, 719-752.
43. MacDougall, F. H., Kinetic Theory of Liquids. By J. Frenkel. *The Journal of Physical and Colloid Chemistry* **1947,** *51*, 1032-1033.
44. J, Z., *Zh. Eksp. Teor. Fiz* **1942,** *12*.
45. White, D. R.; Kassner Jr, J. L., A correction to classical homogeneous nucleation theory for polar molecules exhibiting an electric double layer at the liquid surface. *Journal of Colloid and Interface Science* **1972,** *39*, 59-64.
46. Oxtoby, D. W., Homogeneous nucleation - theory and experiment. *Journal of Physics-Condensed Matter* **1992,** *4*, 7627-7650.
47. Mullin, J. W., *Crystallization*. Elsevier Butterworth-Heinemann: 2001; p 1-600.
48. Jiang, S. F.; ter Horst, J. H., Crystal Nucleation Rates from Probability Distributions of Induction Times. *Crystal Growth & Design* **2011,** *11*, 256-261.
49. Corzo, D. M. C.; Borissova, A.; Hammond, R. B.; Kashchiev, D.; Roberts, K. J.; Lewtas, K.; More, I., Nucleation mechanism and kinetics from the analysis of polythermal crystallisation data: methyl stearate from kerosene solutions. *CrystEngComm* **2014,** *16*, 974-991.
50. Wolde, P. R. t.; Frenkel, D., Enhancement of Protein Crystal Nucleation by Critical Density Fluctuations. *Science* **1997,** *277*, 1975-1978.
51. Toroz, D.; Rosbottom, I.; Turner, T. D.; Corzo, D. M. C.; Hammond, R. B.; Lai, X.; Roberts, K. J., Towards an understanding of the nucleation of alpha-para amino benzoic acid from ethanolic solutions: a multi-scale approach. *Faraday Discussions* **2015,** *179*, 79-114.
52. Vekilov, P. G., Two-step mechanism for the nucleation of crystals from solution. *Journal of Crystal Growth* **2005,** *275*, 65-76.
53. Kashchiev, D.; Vekilov, P. G.; Kolomeisky, A. B., Kinetics of two-step nucleation of crystals. *The Journal of Chemical Physics* **2005,** *122*, 244706.
54. Bonnett, P. E.; Carpenter, K. J.; Dawson, S.; Davey, R. J., Solution crystallisation via a submerged liquid-liquid phase boundary: oiling out. *Chemical Communications* **2003**, 698-699.
55. Erdemir, D.; Chattopadhyay, S.; Guo, L.; Ilavsky, J.; Amenitsch, H.; Segre, C. U.; Myerson, A. S., Relationship between self-association of glycine molecules in supersaturated solutions and solid state outcome. *Physical Review Letters* **2007,** *99*.

56. McCrone, W. C., *Physics and Chemistry of the Organic Solid State (Book 2)*. 1965.
57. Ostwald, W., *Grundiss der Allgemeinen Chemie* **1899**.
58. Brittain, H., *Polymorphism in Pharmaceutical Solids*. Marcel Dekker: USA, 1999.
59. Thompson, H. P. G.; Day, G. M., Which conformations make stable crystal structures? Mapping crystalline molecular geometries to the conformational energy landscape. *Chemical Science* **2014,** *5*, 3173-3182.
60. Bauer, J.; Spanton, S.; Henry, R.; Quick, J.; Dziki, W.; Porter, W.; Morris, J., Ritonavir: An Extraordinary Example of Conformational Polymorphism. *Pharmaceutical Research* **2001,** *18*, 859-866.
61. Tothadi, S.; Desiraju, G. R., Unusual co-crystal of isonicotinamide: the structural landscape in crystal engineering. *Philosophical Transactions of the Royal Society a-Mathematical Physical and Engineering Sciences* **2012,** *370*, 2900-2915.
62. Davey, R. J.; Blagden, N.; Potts, G. D.; Docherty, R., Polymorphism in Molecular Crystals: Stabilization of a Metastable Form by Conformational Mimicry. *J Am Chem Soc* **1997,** *119*, 1767-1772.
63. Kwokal, A.; Nguyen, T. T. H.; Roberts, K. J., Polymorph-Directing Seeding of Entacapone Crystallization in Aqueous/Acetone Solution Using a Self-Assembled Molecular Layer on Au (100). *Crystal Growth & Design* **2009,** *9*, 4324-4334.
64. Davey, R. J.; Blagden, N.; Righini, S.; Alison, H.; Ferrari, E. S., Nucleation control in solution mediated polymorphic phase transformations: The case of 2,6-dihydroxybenzoic acid. *J. Phys. Chem. B* **2002,** *106*, 1954-1959.
65. Davey, R. J.; Blagden, N.; Righini, S.; Alison, H.; Quayle, M. J.; Fuller, S., Crystal Polymorphism as a Probe for Molecular Self-Assembly during Nucleation from Solutions: The Case of 2,6-Dihydroxybenzoic Acid. *Crystal Growth & Design* **2000,** *1*, 59-65.
66. Blagden, N.; Davey, R. J., Polymorph Selection: Challenges for the Future?†. *Crystal Growth & Design* **2003,** *3*, 873-885.
67. Zurek, W. H.; Schieve, W. C., Multistep clustering and nucleation. *The Journal of Physical Chemistry* **1980,** *84*, 1479-1482.
68. Anwar, J.; Boateng, P. K., Computer Simulation of Crystallization from Solution. *Journal of the American Chemical Society* **1998,** *120*, 9600-9604.
69. Sherrill, C. D., Introduction to Molecular Mechanics. In.
70. Kettering, C. F.; Shutts, L. W.; Andrews, D. H., A Representation of the Dynamic Properties of Molecules by Mechanical Models. *Physical Review* **1930,** *36*, 531-543.
71. Wiberg, K. B., A Scheme for Strain Energy Minimization. Application to the Cycloalkanes1. *Journal of the American Chemical Society* **1965,** *87*, 1070-1078.
72. Allinger, N. L., Calculation of Molecular Structure and Energy by Force-Field Methods. In *Advances in Physical Organic Chemistry*, Gold, V.; Bethell, D., Eds. Academic Press: 1976; Vol. Volume 13, pp 1-82.
73. Momany, F. A.; Carruthers, L. M.; McGuire, R. F.; Scheraga, H. A., Intermolecular potentials from crystal data. III. Determination of empirical potentials and application to the packing configurations and lattice energies in crystals of hydrocarbons, carboxylic acids, amines, and amides. *The Journal of Physical Chemistry* **1974,** *78*, 1595-1620.
74. Nemethy, G.; Pottle, M. S.; Scheraga, H. A., Energy parameters in polypeptides. 9. Updating of geometrical parameters, nonbonded interactions, and

hydrogen bond interactions for the naturally occurring amino acids. *J Phys Chem* **1983,** *87*, 1883-1887.
75. Mayo, S. L.; Olafson, B. D.; Goddard, W. A., Dreiding - A Generic Force-Field For Molecular Simulations. *J Phys Chem* **1990,** *94*, 8897-8909.
76. Rappe, A. K.; Casewit, C. J.; Colwell, K. S.; Goddard, W. A.; Skiff, W. M., UFF, a full periodic table force field for molecular mechanics and molecular dynamics simulations. *Journal of the American Chemical Society* **1992,** *114*, 10024-10035.
77. Hamaker, H. C., The London - Van Der Waals attraction between spherical particles. *Physica* **1937,** *4*, 1058-1072.
78. Buckingham, R. A.; Corner, J., Tables of Second Virial and Low-Pressure Joule-Thomson Coefficients for Intermolecular Potentials with Exponential Repulsion. *P Roy Soc Lond A Mat* **1947,** *189*, 118-129.
79. Price, S. L., Computed Crystal Energy Landscapes for Understanding and Predicting Organic Crystal Structures and Polymorphism. *Accounts of Chemical Research* **2009,** *42*, 117-126.
80. Meller, J., Molecular Dynamics. In *Encyclopedia of Life Sciences*, Nature Publishing Group: 2001.
81. Anwar, J.; Zahn, D., Uncovering Molecular Processes in Crystal Nucleation and Growth by Using Molecular Simulation. *Angewandte Chemie International Edition* **2011,** *50*, 1996-2013.
82. Anwar, J.; Boateng, P. K.; Tamaki, R.; Odedra, S., Mode of Action and Design Rules for Additives That Modulate Crystal Nucleation. *Angewandte Chemie International Edition* **2009,** *48*, 1596-1600.
83. Raiteri, P.; Demichelis, R.; Gale, J. D.; Kellermeier, M.; Gebauer, D.; Quigley, D.; Wright, L. B.; Walsh, T. R., Exploring the influence of organic species on pre- and post-nucleation calcium carbonate. *Faraday Discussions* **2012,** *159*, 61-85.
84. Heitler, W., Fault energy and exchange at the multibody problem. *Z. Phys.* **1927,** *46*, 47-72.
85. Davies, U. C. ChemWiki, Valence Bond Theory.
86. Pauling, L., The rotational motion of molecules in crystals. *Physical Review* **1930,** *36*, 0430-0443.
87. Mulliken, R. S., The assignment of quantum numbers for electrons in molecules I. *Physical Review* **1928,** *32*, 0186-0222.
88. Mulliken, R. S., The assignment of quantum numbers for electrons in molecules. II. Correlation of molecular and atomic electron states. *Physical Review* **1928,** *32*, 0761-0772.
89. Mulliken, R. S., The assignment of quantum numbers for electrons in molecules. III. Diatomic hydrides. *Physical Review* **1929,** *33*, 0730-0747.
90. Hartree, D. R., The wave mechanics of an atom with a non-Coulomb central field Part I theory and methods. *Proceedings of the Cambridge Philosophical Society* **1928,** *24*, 89-110.
91. Fock, V., Approximation method for the solution of the quantum mechanical multibody problems. *Z. Phys.* **1930,** *61*, 126-148.
92. Hartree, D. R.; Hartree, F. R. S.; Hartree, W., Self-consistent field, with exchange, for beryllium. *Proceedings of the Royal Society of London Series a-Mathematical and Physical Sciences* **1935,** *150*, 0009-0033.
93. Dovesi, R.; Orlando, R.; Erba, A.; Zicovich-Wilson, C. M.; Civalleri, B.; Casassa, S.; Maschio, L.; Ferrabone, M.; De La Pierre, M.; D'Arco, P.; Noel, Y.;

Causa, M.; Rerat, M.; Kirtman, B., CRYSTAL14: A Program for the Ab Initio Investigation of Crystalline Solids. *International Journal of Quantum Chemistry* **2014,** *114*, 1287-1317.
94. Pisani, C.; Dovesi, R., Exact-exchange hartree-fock calculations for periodic-systems .1. Illustration of the method. *International Journal of Quantum Chemistry* **1980,** *17*, 501-516.
95. Dovesi, R.; Civalleri, B.; Orlando, R.; Roetti, C.; Saunders, V. R., Ab initio quantum simulation in solid mate chemistry. In *Reviews in Computational Chemistry, Vol 21*, Lipkowitz, K. B.; Larter, R.; Cundari, T. R., Eds. 2005; Vol. 21, pp 1-125.
96. Kohn, W.; Sham, L. J., Self-consistent equations including exchange and correlation effects. *Physical Review* **1965,** *140*, 1133-&.
97. Grimme, S., Density functional theory with London dispersion corrections. *Wiley Interdisciplinary Reviews: Computational Molecular Science* **2011,** *1*, 211-228.
98. Zhao, Y.; Truhlar, D. G., The M06 suite of density functionals for main group thermochemistry, thermochemical kinetics, noncovalent interactions, excited states, and transition elements: two new functionals and systematic testing of four M06-class functionals and 12 other functionals. *Theoretical Chemistry Accounts* **2008,** *120*, 215-241.
99. Tomasi, J.; Mennucci, B.; Cammi, R., Quantum Mechanical Continuum Solvation Models. *Chemical Reviews* **2005,** *105*, 2999-3094.
100. Tomasi, J.; Persico, M., Molecular Interactions in Solution: An Overview of Methods Based on Continuous Distributions of the Solvent. *Chemical Reviews* **1994,** *94*, 2027-2094.
101. Bell, R. P., The electrostatic energy of dipole. *Transactions of the Faraday Society* **1931,** *27*, 0797-0802.
102. Born, M., Volumes and hydration warmth of ions. *Z. Phys.* **1920,** *1*, 45-48.
103. Kirkwood, J. G., On the Theory of Strong Electrolyte Solutions. *Journal of Chemical Physics* **1934,** *2*.
104. Onsager, L., Electric Moments of Molecules in Liquids. *Journal of the American Chemical Society* **1936,** *58*, 1486-1493.
105. Klamt, A.; Schuurmann, G., COSMO: a new approach to dielectric screening in solvents with explicit expressions for the screening energy and its gradient. *Journal of the Chemical Society, Perkin Transactions 2* **1993,** *0*, 799-805.
106. Klamt, A., Conductor-like screening model for real solvents - a new approach to the quantitative calculation of solvation phenomena. *Journal of Physical Chemistry* **1995,** *99*, 2224-2235.
107. Klamt, A.; Eckert, F. *COSMOtherm*, 3.0. Release 15.01; COSMO*logic* GMBH & Co. KG: Leverkusen, Germany, 2014.
108. Eckert, F.; Klamt, A., Fast solvent screening via quantum chemistry: COSMO-RS approach. *Aiche Journal* **2002,** *48*, 369-385.
109. Klamt, A.; Eckert, F.; Hornig, M.; Beck, M. E.; Burger, T., Prediction of aqueous solubility of drugs and pesticides with COSMO-RS. *Journal of Computational Chemistry* **2002,** *23*, 275-281.
110. Palomar, J.; Ferro, V. R.; Torrecilla, J. S.; Rodriguez, F., Density and molar volume predictions using COSMO-RS for ionic liquids. An approach to solvent design. *Industrial & Engineering Chemistry Research* **2007,** *46*, 6041-6048.
111. Buggert, M.; Cadena, C.; Mokrushina, L.; Smirnova, I.; Maginn, E. J.; Arlt, W., COSMO-RS Calculations of Partition Coefficients: Different Tools for Conformation Search. *Chemical Engineering & Technology* **2009,** *32*, 977-986.

112. Stock, B. D. C. a. S. R., *Elements of X-Ray Diffraction*. 3rd ed.; Prentice Hall International: 2001.
113. Ladd, M.; Palmer, R., *Structure Determination by X-ray Crystallography*. Springer: New York, USA, 1977.
114. Aslanov, L. A.; Fetisov, G. V.; Howard, J. A. K., *Crystallographic Instrumentation*. Oxford University Press: New York, USA, 1998.
115. Hasegawa, K., Introduction to Single Crystal X-Ray Analysis 1. What is X-Ray Crystallography? *Rigaku Journal* **2012,** *28*, 14-18.
116. Stohr, J., *NEXAFS Spectroscopy*. Springer-Verlag: Berlin, Germany, 1991.
117. Catlow, R. A.; Greaves, G. N., *Applications of Synchrotron Radiation*. Springer: 1990.
118. Stohr, J.; Sette, F.; Johnson, A. L., NEAR-EDGE X-RAY-ABSORPTION FINE-STRUCTURE STUDIES OF CHEMISORBED HYDROCARBONS - BOND LENGTHS WITH A RULER. *Physical Review Letters* **1984,** *53*, 1684-1687.
119. Solomon, J. L.; Madix, R. J.; Stohr, J., ORIENTATION AND ABSOLUTE COVERAGE OF BENZENE, ANILINE, AND PHENOL ON AG(110) DETERMINED BY NEXAFS AND XPS. *Surface Science* **1991,** *255*, 12-30.
120. Stohr, J.; Baberschke, K.; Jaeger, R.; Treichler, R.; Brennan, S., ORIENTATION OF CHEMISORBED MOLECULES FROM SURFACE-ABSORPTION FINE-STRUCTURE MEASUREMENTS - CO AND NO ON NI(100). *Physical Review Letters* **1981,** *47*, 381-384.
121. Norman, D.; Stöhr, J.; Jaeger, R.; Durham, P. J.; Pendry, J. B., Determination of local atomic arrangements at surfaces from near-edge x-ray-absorption fine-structure studies: O on Ni(100). *Physical Review Letters* **1983,** *51*, 2052-2055.
122. Koestner, R. J.; Stöhr, J.; Gland, J. L.; Horsley, J. A., Orientation and bonding of ethylene and ethylidyne on Pt(111) by means of near-edge x-ray absorption fine structure spectroscopy. *Chemical Physics Letters* **1984,** *105*, 332-335.
123. Horsley, J. A.; Stöhr, J.; Koestner, R. J., Structure and bonding of chemisorbed ethylene and ethylidyne on Pt(111) from near edge x-ray absorption fine structure spectroscopy and multiple scattering calculations. *The Journal of Chemical Physics* **1985,** *83*, 3146-3153.
124. Stöhr, J.; Outka, D. A., Determination of molecular orientations on surfaces from the angular dependence of near-edge x-ray-absorption fine-structure spectra. *Physical Review B* **1987,** *36*, 7891-7905.
125. Hastie, G. P.; Johnstone, J.; Roberts, K. J.; Fischer, D., Examination of the structure and melting behaviour of thin film n-alkanes using ultra-soft polarised near-edge X-ray absorption spectroscopy. *J. Chem. Soc.-Faraday Trans.* **1996,** *92*, 783-789.
126. Hastie, G. P.; Johnstone, J.; Roberts, K. J.; Fischer, D., Application of polarised ultra-soft X-ray absorption near-edge spectroscopy to the characterisation of the structure of molecular interfaces. *Journal of Crystal Growth* **1996,** *166*, 67-71.
127. Hastie, G. P.; Johnstone, J.; Walker, E. M.; Roberts, K. J., Direct evidence for surface reconstruction on organic solid surfaces: benzil (0001). *Journal of the Chemical Society, Perkin Transactions 2* **1996,** *0*, 2049-2050.
128. Hastie, G. P.; Johnstone, J.; Roberts, K. J., A NEXAFS spectroscopic examination of the supramolecular organization of a red reactive Azo dye adsorbed onto cellulose substrates. *Journal of Materials Science Letters* **1998,** *17*, 1871-1874.
129. Johnstone, J.; Roberts, K. J., Structural Characterisation of Condensed Molecular Materials using Polarised NEXAFS Spectroscopy. *Molecular Crystals and*

*Liquid Crystals Science and Technology Section a-Molecular Crystals and Liquid Crystals* **1998,** *313*, 39-53.
130. Stevens, J. S.; Byard, S. J.; Seaton, C. C.; Sadiq, G.; Davey, R. J.; Schroeder, S. L. M., Crystallography Aided by Atomic Core-Level Binding Energies: Proton Transfer versus Hydrogen Bonding in Organic Crystal Structures. *Angewandte Chemie-International Edition* **2011,** *50*, 9916-9918.
131. Bisti, F.; Stroppa, A.; Perrozzi, F.; Donarelli, M.; Picozzi, S.; Coreno, M.; de Simone, M.; Prince, K. C.; Ottaviano, L., The electronic structure of gas phase croconic acid compared to the condensed phase: More insight into the hydrogen bond interaction. *The Journal of Chemical Physics* **2013,** *138*, 014308.
132. Tu, G.; Tu, Y.; Vahtras, O.; Ågren, H., Core electron chemical shifts of hydrogen-bonded structures. *Chemical Physics Letters* **2009,** *468*, 294-298.
133. Bennema, P., Growth and Morphology of Crystals: Integration of Theories of Roughening and Hartmann-Perdok Theory. In *Handbook of Crystal Growth*, Hurle, D. T. J., Ed. 1993; Vol. 1.
134. Clydesdale, G.; Roberts, K. J.; Docherty, R., Modelling the morphology of molecular crystals in the presence of disruptive tailor-made additives. *J Cryst Growth* **1994,** *135*, 331-340.
135. Hammond, R. B.; Roberts, K. J.; Smith, E. D. L.; Docherty, R., Application of a Computational Systematic Search Strategy to Study Polymorphism in Phenazine and Perylene. *The Journal of Physical Chemistry B* **1999,** *103*, 7762-7770.
136. Noyes, A. A.; Whitney, W. R., The rate of solution of solid substances in their own solutions. *J Am Chem Soc* **1897,** *19*, 930-934.
137. Garside, J.; Mesmann, A.; Nyvlt, J., *Measurement of Crystal Growth and Nucelation Rates*. IChemE: 2002.
138. Randolph, A. D.; White, E. T., Modeling size dispersion in the prediction of crystal-size distribution. *Chemical Engineering Science* **1977,** *32*, 1067-1076.
139. Randolph, A. D.; Larson, M. A., *Theory of Particulate Processes, 2nd ed*. Academic Press: New York, 1988.
140. Ristić, R. I.; Sherwood, J. N.; Wojciechowski, K., Assessment of the strain in small sodium chlorate crystals and its relation to growth rate dispersion. *Journal of Crystal Growth* **1988,** *91*, 163-168.
141. Garside, J.; Ristic, R. I., GROWTH-RATE DISPERSION AMONG ADP CRYSTALS FORMED BY PRIMARY NUCLEATION. *Journal of Crystal Growth* **1983,** *61*, 215-220.
142. Judge, R. A.; Forsythe, E. L.; Pusey, M. L., Growth Rate Dispersion in Protein Crystal Growth. *Crystal Growth & Design* **2010,** *10*, 3164-3168.
143. White, E.; Wright, P., *Magnitude of Size Dispersion Effects in Crystallisation*. American Institute of Chemical Engineers: New York, 1971; Vol. 110.
144. Wang, S.; Mersmann, A., Initial-size-dependent growth rate dispersion of attrition fragments and secondary nuclei. *Chemical Engineering Science* **1992,** *47*, 1365-1371.
145. Mitrović, M. M., Influence of initial crystal size on growth rate of crystals from solutions. *Journal of Crystal Growth* **1994,** *139*, 332-335.
146. Daudly, P. J. Crystallisation of ammonium sulfate. Delft University of Technology, Netherlands, 1987.
147. Burton, W. K.; Cabrera, N.; Frank, F. C., The Growth Of Crystals And The Equilibrium Structure Of Their Surfaces. *Philos T Roy Soc A* **1951,** *243*, 299-358.
148. Ohara, M.; Reid, R. C., *Modelling Crystal Growth Rates*. 1974.

149. Bourne, J. R.; Davey, R. J., The role of solvent-solute interactions in determining crystal growth mechanisms from solution. *J Cryst Growth* **1976,** *36*, 278-286.
150. Bourne, J. R.; Davey, R. J., The role of solvent-solute interactions in determining crystal growth mechanisms from solution: II. The growth kinetics of hexamethylene tetramine. *J Cryst Growth* **1976,** *36*, 287-296.
151. Nguyen, T. T. H.; Hammond, R. B.; Roberts, K. J.; Marziano, I.; Nichols, G., Precision measurement of the growth rate and mechanism of ibuprofen {001} and {011} as a function of crystallization environment. *CrystEngComm* **2014,** *16*, 4568-4586.
152. Haüy, *Traité de Minéralogie*. 1801.
153. Dowty, E., Computing and drawing crystal shapes. *Am. mineral* **1980,** *65*, 465-472.
154. Bruno, I. J.; Cole, J. C.; Edgington, P. R.; Kessler, M.; Macrae, C. F.; McCabe, P.; Pearson, J.; Taylor, R., New software for searching the Cambridge Structural Database and visualizing crystal structures. *Acta Crystallogr B* **2002,** *58*, 389-397.
155. Hagler, A. T.; Lifson, S.; Dauber, P., Consistent Force-Field Studies Of Inter-Molecular Forces In Hydrogen-Bonded Crystals .2. Benchmark For The Objective Comparison Of Alternative Force-Fields. *Journal of the American Chemical Society* **1979,** *101*, 5122-5130.
156. Lifson, S.; Hagler, A. T.; Dauber, P., Consistent Force-Field Studies Of Inter-Molecular Forces In Hydrogen-Bonded Crystals .1. Carboxylic-Acids, Amides, And The C=O...H- Hydrogen-Bonds. *J Am Chem Soc* **1979,** *101*, 5111-5121.
157. Zhao, Y.; Truhlar, D. G., A new local density functional for main-group thermochemistry, transition metal bonding, thermochemical kinetics, and noncovalent interactions. *J. Chem. Phys.* **2006,** *125*.
158. Williams, D. E., Nonbonded potential parameters derived from crystalline aromatic hydrocarbons. *J. Chem. Phys.* **1966,** *45*, 3770-&.
159. Wang, J. M.; Wolf, R. M.; Caldwell, J. W.; Kollman, P. A.; Case, D. A., Development and testing of a general amber force field. *Journal of Comput Chem* **2004,** *25*, 1157-1174.
160. Gale, J. D.; Henson, N. J., Derivation Of Interatomic Potentials For Microporous Aluminophosphates From The Structure And Properties Of Berlinite. *J Am Chem Soc Faraday T* **1994,** *90*, 3175-3179.
161. Copley, R. C. B.; Deprez, L. S.; Lewis, T. C.; Price, S. L., Computational prediction and X-ray determination of the crystal structures of 3-oxauracil and 5-hydroxyuracil - an informal blind test. *CrystEngComm* **2005,** *7*, 421-428.
162. Day, G. M.; Cooper, T. G.; Cruz-Cabeza, A. J.; Hejczyk, K. E.; Ammon, H. L.; Boerrigter, S. X. M.; Tan, J. S.; Della Valle, R. G.; Venuti, E.; Jose, J.; Gadre, S. R.; Desiraju, G. R.; Thakur, T. S.; van Eijck, B. P.; Facelli, J. C.; Bazterra, V. E.; Ferraro, M. B.; Hofmann, D. W. M.; Neumann, M. A.; Leusen, F. J. J.; Kendrick, J.; Price, S. L.; Misquitta, A. J.; Karamertzanis, P. G.; Welch, G. W. A.; Scheraga, H. A.; Arnautova, Y. A.; Schmidt, M. U.; van de Streek, J.; Wolf, A. K.; Schweizer, B., Significant progress in predicting the crystal structures of small organic molecules - a report on the fourth blind test. *Acta Crystallographica Section B-Structural Science Crystal Engineering and Materials* **2009,** *65*, 107-125.

163. D'Oria, E.; Karamertzanis, P. G.; Price, S. L., Spontaneous Resolution of Enantiomers by Crystallization: Insights from Computed Crystal Energy Landscapes. *Crystal Growth & Design* **2010,** *10*, 1749-1756.
164. Brunsteiner, M.; Price, S. L., Morphologies of organic crystals: Sensitivity of attachment energy predictions to the model intermolecular potential. *Cryst Grow Des* **2001,** *1*, 447-453.
165. Bravais, A., *Etudes Crystallographiques*. Gauthiers Villars: Paris, 1886.
166. Donnay, J. D. H.; Harker, D., A new law of crystal morphology extending the law of bravais. *Am Mineral* **1937,** *22*, 446-467.
167. Friedel, G., *Bulletin De La Societe Francaise De Mineralogie Et De Crystallographie* **1907,** *30*, 326.
168. Docherty, R.; Roberts, K. J.; Dowty, E., Morang — A computer program designed to aid in the determinations of crystal morphology. *Comput Phys Commun* **1988,** *51*, 423-430.
169. Human, H. J.; Van Der Eerden, J. P.; Jetten, L. A. M. J.; Odekerken, J. G. M., On the roughening transition of biphenyl: Transition of faceted to non-faceted growth of biphenyl for growth from different organic solvents and the melt. *J Cryst Growth* **1981,** *51*, 589-600.
170. Hartman, P., *Crystal Growth: An Introduction*. Elsevier: Amsterdam, Netherlands, 1973.
171. Bennema, P., Morphology of Crystals: Past and Present. In *Science and Technology of Crystal Growth*, van der Earden, J. P.; Bruinsma, O. S. L., Eds. Kluwer: Netherlands, 1995.
172. Meekes, H.; Bennema, P.; Grimbergen, R. F. P., On the Prediction of Crystal Morphology. II. Symmetry Roughening of Pairs of Connected Nets. *Acta Crystallogr A* **1998,** *54*, 501-510.
173. Grimbergen, R. F. P.; van Hoof, P. J. C. M.; Meekes, H.; Bennema, P., Morphology of orthorhombic n-paraffin crystals: the influence of multiple connected nets. *J Cryst Growth* **1998,** *191*, 846-860.
174. Onsager, L., Crystal Statistics. I. A Two-Dimensional Model with an Order-Disorder Transition. *Phys Rev* **1944,** *65*, 117-149.
175. Gilmer, G. H.; Bennema, P., Simulation of Crystal Growth with Surface Diffusion. *J Appl Phys* **1972,** *43*, 1347-1360.
176. Hartman, P.; Bennema, P., The attachment energy as a habit controlling factor: I. Theoretical considerations. *J Cryst Growth* **1980,** *49*, 145-156.
177. Jackson, K. A., *Mechanism of Growth in Liquid Metals and Solidification*. Cleveland, 1958.
178. Berkovitch-Yellin, Z.; Van Mil, J.; Addadi, L.; Idelson, M.; Lahav, M.; Leiserowitz, L., Crystal morphology engineering by "tailor-made" inhibitors; a new probe to fine intermolecular interactions. *J Am Chem Soc* **1985,** *107*, 3111-3122.
179. Weissbuch, I.; Addadi, L.; Lahav, M.; Leiserowitz, L., Molecular Recognition at Crystal Interfaces. *Science* **1991,** *253*, 637-645.
180. Clydesdale, G.; Roberts, K. J.; Lewtas, K.; Docherty, R., Modelling the morphology of molecular crystals in the presence of blocking tailor-made additives. *J Cryst Growth* **1994,** *141*, 443-450.
181. Panina, N.; van de Ven, R.; Janssen, F. F. B. J.; Meekes, H.; Vlieg, E.; Deroover, G., Study of the Needle-Like Morphologies of Two beta-Phthalocyanines. *Cryst Grow Des* **2009,** *9*, 840-847.

182. Chen, J.; Trout, B. L., Computer-Aided Solvent Selection for Improving the Morphology of Needle-like Crystals: A Case Study of 2,6-Dihydroxybenzoic Acid. *Crystal Grow Des* **2010,** *10*, 4379-4388.
183. McArdle, P.; Hu, Y.; Lyons, A.; Dark, R., Predicting and understanding crystal morphology: the morphology of benzoic acid and the polymorphs of sulfathiazole. *CrystEngComm* **2010,** *12*, 3119-3125.
184. Walshe, N.; Crushell, M.; Karpinska, J.; Erxleben, A.; McArdle, P., Anisotropic Crystal Growth in Flat and Nonflat Systems: The Important Influence of van der Waals Contact Molecular Stacking on Crystal Growth and Dissolution. *Crystal Grow Des* **2015,** *15*, 3235-3248.
185. Walker, E. M.; Roberts, K. J.; Maginn, S. J., A Molecular Dynamics Study of Solvent and Impurity Interaction on the Crystal Habit Surfaces of ε-Caprolactam. *Langmuir* **1998,** *14*, 5620-5630.
186. Lu, J. J.; Ulrich, J., An improved prediction model of morphological modifications of organic crystals induced by additives. *Cryst Res Technol* **2003,** *38*, 63-73.
187. Duan, X.; Wei, C.; Liu, Y.; Pei, C., A molecular dynamics simulation of solvent effects on the crystal morphology of HMX. *J Hazard Mater* **2010,** *174*, 175-180.
188. Athimoolam, S.; Natarajan, S., 4-carboxyanilinium (2R, 3R)-tartrate and a redetermination of the mu-polymorph of 4-aminobenzoic acid. *Acta Crystallographica Section C-Crystal Structure Communications* **2007,** *63*, O514-O517.
189. Gracin, S.; Fischer, A., Redetermination of the beta-polymorph of p-aminobenzoic acid. *Acta Crystallographica Section E-Structure Reports Online* **2005,** *61*, O1242-O1244.
190. Benali-Cherif, R.; Takouachet, R.; Bendeif, E.-E.; Benali-Cherif, N., The structural properties of a noncentrosymmetric polymorph of 4-aminobenzoic acid. *Acta Crystallographica Section C* **2014,** *70*, 323-325.
191. Lai, T. F.; Marsh, R. E., The crystal structure of p-aminobenzoic acid. *Acta Crystallographica* **1967,** *22*, 885-893.
192. Gracin, S.; Rasmuson, Å. C., Polymorphism and Crystallization of p-Aminobenzoic Acid. *Crystal Growth & Design* **2004,** *4*, 1013-1023.
193. Groth, P., *Chemishe Krystalographie, Leipzig: Engelmann* **1908,** *4*, 509.
194. Prasad, M.; Kapadia, M. R.; Thakar, V. C., *J. Univ. Bombay Sci.* **1939,** *8*, 667-669.
195. Alleaume, M.; Salascim.G; Decap, J., Structure de lacide para-aminobenzoique (pab). *Comptes Rendus Hebdomadaires Des Seances De L Academie Des Sciences Serie C* **1966,** *262*, 416-&.
196. Killean, R. C. G.; Tollin, P.; Watson, D. G.; Young, D. W., Twinning in p-aminobenzoic acid. *Acta Crystallographica* **1965,** *19*, 482-483.
197. Kuhnertb.M; Grimm, H., SOLVENT INCLUSIONS IN CRYSTALS OF P-SUBSTITUTED BENZOIC ACID DERIVATIVES. *Mikrochimica Acta* **1969**, 1208-&.
198. Fischer, D.; Jaye, C.; Scammon, K.; Sobol, P.; Principe, E., A Novel Large Area Imaging NEXAFS Spectrometer for Combinatorial Chemical and Structural Analysis. *Microscopy and Microanalysis* **2010,** *16*, 380-381.
199. Konicek, A. R.; Jaye, C.; Hamilton, M. A.; Sawyer, W. G.; Fischer, D. A.; Carpick, R. W., Near-edge X-ray absorption fine structure imaging of spherical and flat counterfaces of ultrananocrystalline diamond tribological contacts: A correlation of surface chemistry and friction. *Tribology Letters* **2011,** *44*, 99-106.

200. Newville, M., IFEFFIT: interactive XAFS analysis and FEFF fitting. *Journal of Synchrotron Radiation* **2001,** *8*, 322-324.
201. Ravel, B.; Newville, M., ATHENA, ARTEMIS, HEPHAESTUS: data analysis for X-ray absorption spectroscopy using IFEFFIT. *Journal of Synchrotron Radiation* **2005,** *12*, 537-541.
202. Technologies, A. *CrysAlisPro* 2013.
203. Inc, A. S. *Materials Studio* 5.5; San Diego, 2011.
204. Delley, B., An all-electron numerical-method for solving the local density functional for polyatomic-molecules. *Journal of Chemical Physics* **1990,** *92*, 508-517.
205. Delley, B., From molecules to solids with the DMol(3) approach. *Journal of Chemical Physics* **2000,** *113*, 7756-7764.
206. Clydesdale, G.; Roberts, K. J.; Docherty, R., HABIT95 — a program for predicting the morphology of molecular crystals as a function of the growth environment. *Journal of Crystal Growth* **1996,** *166*, 78-83.
207. Dalgarno, A., Atomic polarizabilities and shielding factors. *Advances in Physics* **1962,** *11*, 281-315.
208. McGuire, R. F.; Momany, F. A.; Scheraga, H. A., Energy parameters in polypeptides. V. Empirical hydrogen bond potential function based on molecular orbital calculations. *The Journal of Physical Chemistry* **1972,** *76*, 375-393.
209. Frisch, M. J.; Trucks, G. W.; Schlegel, H. B.; Scuseria, G. E.; Robb, M. A.; Cheeseman, J. R.; Scalmani, G.; Barone, V.; Mennucci, B.; Petersson, G. A.; Nakatsuji, H.; Caricato, M.; Li, X.; Hratchian, H. P.; Izmaylov, A. F.; Bloino, J.; Zheng, G.; Sonnenberg, J. L.; Hada, M.; Ehara, M.; Toyota, K.; Fukuda, R.; Hasegawa, J.; Ishida, M.; Nakajima, T.; Honda, Y.; Kitao, O.; Nakai, H.; Vreven, T.; Montgomery Jr., J. A.; Peralta, J. E.; Ogliaro, F.; Bearpark, M. J.; Heyd, J.; Brothers, E. N.; Kudin, K. N.; Staroverov, V. N.; Kobayashi, R.; Normand, J.; Raghavachari, K.; Rendell, A. P.; Burant, J. C.; Iyengar, S. S.; Tomasi, J.; Cossi, M.; Rega, N.; Millam, N. J.; Klene, M.; Knox, J. E.; Cross, J. B.; Bakken, V.; Adamo, C.; Jaramillo, J.; Gomperts, R.; Stratmann, R. E.; Yazyev, O.; Austin, A. J.; Cammi, R.; Pomelli, C.; Ochterski, J. W.; Martin, R. L.; Morokuma, K.; Zakrzewski, V. G.; Voth, G. A.; Salvador, P.; Dannenberg, J. J.; Dapprich, S.; Daniels, A. D.; Farkas, Ö.; Foresman, J. B.; Ortiz, J. V.; Cioslowski, J.; Fox, D. J. *Gaussian 09*, Gaussian, Inc.: Wallingford, CT, USA, 2009.
210. Hammond, R. B.; Ma, C.; Roberts, K. J.; Ghi, P. Y.; Harris, R. K., Application of Systematic Search Methods to Studies of the Structures of Urea−Dihydroxy Benzene Cocrystals. *The Journal of Physical Chemistry B* **2003,** *107*, 11820-11826.
211. Hammond, R. B.; Hashim, R. S.; Ma, C.; Roberts, K. J., Grid-based molecular modeling for pharmaceutical salt screening: Case example of 3,4,6,7,8,9-hexahydro-2H-pyrimido (1,2-a) pyrimidinium acetate. *Journal of Pharmaceutical Sciences* **2006,** *95*, 2361-2372.
212. Gavezzotti, A.; Filippini, G., Computer prediction of organic crystal structures using partial X-ray diffraction data. *Journal of the American Chemical Society* **1996,** *118*, 7153-7157.
213. Ramachandran, V.; Murnane, D.; Hammond, R. B.; Pickering, J.; Roberts, K. J.; Soufian, M.; Forbes, B.; Jaffari, S.; Martin, G. P.; Collins, E.; Pencheva, K., Formulation Pre-screening of Inhalation Powders Using Computational Atom–Atom Systematic Search Method. *Molecular Pharmaceutics* **2014,** *12*, 18-33.
214. Nabavian, M.; Sabbah, R.; Chastel, R.; Laffitte, M., Thermodynamics Of Nitrogen-Compounds .2. Thermochemistry Of Aminobenzoic Acids, Pyrimidine,

Uracil And Thymine. *Journal De Chimie Physique Et De Physico-Chimie Biologique* **1977,** *74*, 115-126.
215. de Kruif, C. G.; Voogd, J.; Offringa, J. C. A., Enthalpies of sublimation and vapour pressures of 14 amino acids and peptides. *The Journal of Chemical Thermodynamics* **1979,** *11*, 651-656.
216. Karamertzanis, P. G.; Kazantsev, A. V.; Issa, N.; Welch, G. W. A.; Adjiman, C. S.; Pantelides, C. C.; Price, S. L., Can the Formation of Pharmaceutical Cocrystals Be Computationally Predicted? 2. Crystal Structure Prediction. *Journal of Chemical Theory and Computation* **2009,** *5*, 1432-1448.
217. Etter, M. C., Hydrogen bonds as design elements in organic chemistry. *The Journal of Physical Chemistry* **1991,** *95*, 4601-4610.
218. Clydesdale, G.; Roberts, K. J.; Telfer, G. B.; Grant, D. J. W., Modeling the crystal morphology of α-lactose monohydrate. *Journal of Pharmaceutical Sciences* **1997,** *86*, 135-141.
219. Feyereisen, M. W.; Feller, D.; Dixon, D. A., Hydrogen Bond Energy of the Water Dimer. *The Journal of Physical Chemistry* **1996,** *100*, 2993-2997.
220. Dunitz, J. D.; Filippini, G.; Gavezzotti, A., Molecular Shape and Crystal Packing: a Study of C12H12 Isomers, Real and Imaginary. *Helvetica Chimica Acta* **2000,** *83*, 2317-2335.
221. Nyman, J.; Day, G. M., Static and lattice vibrational energy differences between polymorphs. *CrystEngComm* **2015,** *17*, 5154-5165.
222. Raabe, G., The use of quantum chemical semiempirical methods to calculate the lattice energies of organic molecular crystals. Part I: The three polymorphs of glycine. *Z. Naturfors. Sect. A-J. Phys. Sci.* **2000,** *55*, 609-615.
223. Raabe, G., The use of quantum-chemical semiempirical methods to calculate the lattice energies of organic molecular crystals. Part III: The lattice energy of borazine (B3N3H6) and its packing in the solid state. *Z. Naturfors. Sect. A-J. Phys. Sci.* **2004,** *59*, 609-614.
224. Black, J. F. B.; Davey, R. J.; Gowers, R. J.; Yeoh, A., Ostwald's rule and enantiotropy: polymorph appearance in the crystallisation of p-aminobenzoic acid. *CrystEngComm* **2015,** *17*, 5139-5142.
225. Mokrushina, L.; Buggert, M.; Smirnova, I.; Arlt, W.; Schomacker, R., COSMO-RS and UNIFAC in prediction of micelle/water partition coefficients. *Industrial & Engineering Chemistry Research* **2007,** *46*, 6501-6509.
226. Nguyen, T. T. H. Influence of Crystallisation Environment on the Nucleation and Growth of Single Crystals of (RS)-Ibuprofen. University of Leeds, Leeds, UK, 2014.
227. Di Tommaso, D.; Watson, K. L., Density Functional Theory Study of the Oligomerization of Carboxylic Acids. *The Journal of Physical Chemistry A* **2014,** *118*, 11098-11113.
228. Vekilov, P. G., Nucleation. *Crystal Growth & Design* **2010,** *10*, 5007-5019.
229. Toroz, D.; Rosbottom, I.; Turner, T. D.; Corzo, D. M. C.; Hammond, R. B.; Lai, X.; Roberts, K. J., Towards an understanding of the nucleation of alpha-para amino benzoic acid from ethanolic solutions: a multi-scale approach. *Faraday Discuss* **2015,** *179*, 79-114.
230. ter Horst, J. H.; Geertman, R. M.; van Rosmalen, G. M., The effect of solvent on crystal morphology. *Journal of Crystal Growth* **2001,** *230*, 277-284.

231. Singh, M. K.; Banerjee, A., Role of Solvent and External Growth Environments to Determine Growth Morphology of Molecular Crystals. *Crystal Growth & Design* **2013,** *13*, 2413-2425.
232.
233. B, J.; P, M., *Growth Dissolution and Pattern Formation in Geosystems*. Springer: 2013.
234. Jetten, L. A. M. J.; Human, H. J.; Bennema, P.; Van Der Eerden, J. P., On the observation of the roughening transition of organic crystals, growing from solution. *Journal of Crystal Growth* **1984,** *68*, 503-516.
235. Cook, J. L.; Hunter, C. A.; Low, C. M. R.; Perez-Velasco, A.; Vinter, J. G., Preferential Solvation and Hydrogen Bonding in Mixed Solvents. *Angewandte Chemie International Edition* **2008,** *47*, 6275-6277.
236. Schmidt, C.; Ulrich, J., Predicting Crystal Morphology Grown from Solution. *Chemical Engineering & Technology* **2012,** *35*, 1009-1012.
237. Hastie, G. P.; Johnstone, J.; Walker, E. M.; Roberts, K. J., Direct evidence for surface reconstruction on organic solid surfaces: Benzil (0001). *Journal of the Chemical Society. Perkin Transactions 2* **1996,** *10*, 2049-2050.
238. Heng, J. Y. Y.; Bismarck, A.; Lee, A. F.; Wilson, K.; Williams, D. R., Anisotropic surface chemistry of aspirin crystals. *Journal of Pharmaceutical Sciences* **2007,** *96*, 2134-2144.
239. Baio, J. E.; Jaye, C.; Fischer, D. A.; Weidner, T., High-Throughput Analysis of Molecular Orientation on Surfaces by NEXAFS Imaging of Curved Sample Arrays. *ACS Combinatorial Science* **2014,** *16*, 449-453.
240. Johnstone, J.; Peacock, C.; Roberts, K. J., Application of polarised NEXAFS spectroscopy to the structural characterisation of condensed molecular surfaces and interfaces. *Journal of Crystal Growth* **1999,** *198*, 275-281.
241. Overney, R. M.; Howald, L.; Frommer, J.; Meyer, E.; Brodbeck, D.; Güntherodt, H. J., Molecular surface structure of organic crystals observed by atomic force microscopy. *Ultramicroscopy* **1992,** *42–44, Part 2*, 983-988.
242. Stevens, J. S.; Gainar, A.; Suljoti, E.; Xiao, J.; Golnak, R.; Aziz, E. F.; Schroeder, S. L. M., Chemical Speciation and Bond Lengths of Organic Solutes by Core-Level Spectroscopy: pH and Solvent Influence on p-Aminobenzoic Acid. *Chemistry – A European Journal* **2015,** *21*, 7256-7263.